Discrete Mathematical Models For Electrical Impedance Tomography

Husein Perez

Department of Mechanical Engineering and Mathematical Sciences
Faculty of Technology, Design and Environment
Oxford Brookes University

A thesis submitted in partial fulfilment of the requirements of
Oxford Brookes University for the degree of
Doctor of Philosophy

January 20, 2016

Acknowledgements

Undertaking my PhD has been a truly life-changing experience. It would not have been possible without the support and guidance that I received from many people.

Firstly, I would like to express my sincere gratitude to my Director of Studies Dr. Cristiana Sebu for the continuous support of my PhD study and related research, for her patience, motivation, and immense knowledge. Her guidance helped me in all the time of research and writing of this thesis. I could not have imagined having a better supervisor and mentor for my PhD study.

I would like to express my special appreciation and thanks to Prof. Khaled Hayatleh, whom, despite his many other academic and professional commitments, he undertook to act as my Co-Director of Studies. His wisdom, knowledge and commitment to the highest standards inspired and motivated me.

Many thanks also to our collaborators at Johannes Gutenberg University of Mainz, especially Prof. Karl Schilcher who made it possible for me to pursue my doctoral degree. I would like to thank you all for encouraging my research and for allowing me to grow as a research scientist. Your advice on both research as well as on my career have been priceless. You have been all a tremendous mentors for me.

I am particularly indebted to MEMS staff Prof. Gareth Neighbour, Prof. John Durodola, Prof Michael Pidcock, Steve Barker, Dr. Rob Beale, my lab mates Mohamed Ben-Esmael, Srisivane Sivanesan and Jill Organ from the Graduate Office. They have all been exceptionally supportive. I apologize had I, unintentionally, forgotten to mention other names.

A sincere and very special gratitude to my family, especially, my dearest father and my brother and sisters. Words cannot express how grateful I am to you all. Your prayers, support and caring for me was what sustained me thus far.

Lastly but, certainly, not least, to express my greatest appreciation to my beloved wife and my children Ibrahim , Ala, Aya, and my little angel Dania, who spent sleepless nights with me and was always my support in the moments when there was no one to answer my queries. To all I say thank you.

Husein PEREZ

Oxford Brookes University
Oxford
January, 2016

Discrete Mathematical Models For Electrical Impedance Tomography

Submitted for the degree of Doctor of Philosophy

Husein Perez, 2015

Abstract

Electrical Impedance Tomography (EIT) is a non-invasive, portable and low-cost medical imaging technique. Different current patterns are injected to the surface of a conductive body and the corresponding voltages are measured also on the boundary. These measurements are the data used to infer the interior conductivity distribution of the object. However, it is well known that the reconstruction process is extremely ill-posed due to the low sensitivity of the boundary voltages to changes in the interior conductivity distribution. The reconstructed images also suffer from poor spatial resolution. In tomographic systems, the spatial resolution is related to the number of applied current patterns and to the number and positions of electrodes which are placed at the surface of the object under examination.

Two mammographic sensors were recently developed at the University of Mainz in collaboration with Oxford Brookes University. These prototypes consist of a planar sensing head of circular geometry with twelve large outer (active) electrodes arranged on a ring of radius 4.4cm where the external currents are injected and a set of, respectively thirty six and fifty four point-like high-impedance inner (passive) electrodes arranged in a hexagonal pattern where the induced voltages are measured. Two 2D reconstruction methods were proposed for these devices, one based on resistor network models and another one which uses an integral equation formulation. The novelty of the device and hence of these imaging techniques consists exactly in the distinct use of active and passive electrodes.

The 2D images of the conductivity distribution of the interior tissue of the breast provide only information about the existence and location of the tumour. In this thesis different circular designs for the sensing head of this EIT device were analysed. The 2D resistor network approach was adapted to the different data collection geometries and the sensitivity of the reconstructions with respect to errors in the simulate data were investigated before any modifications to the original design were made.

A novel 3D reconstruction algorithm was also developed for a simpler geometry of the sensing head which consisted of a rectangular array of thirty six electrodes (twenty active + sixteen passive). This electrode configuration as well as the proposed imaging technique are intended to be used for breast cancer detection. The algorithm is based on linearizing the conductivity about a constant value and allows real-time reconstructions. The performance of the algorithm was tested on numerically simulated data and small inclusions with conductivities three or four times the background lying beneath the data collection surface were successfully detected. The results were fairly stable with respect to the noise level in the data and displayed very good spatial resolution in the plane of electrodes.

Keywords: Breast cancer, Electrical Impedance Tomography, Inverse conductivity problem, non-invasive measuring technique, discrete resistor networks, reconstruction algorithm.

Contents

List of Figures

List of Tables

Definitions, Abbreviations and Symbols

Definitions

Admittance A measure of how easily a circuit or device will allow a current to flow. It is defined as the inverse of impedance.

Angular frequency A scalar measure of rotation rate.

Conductance A measure of the ease with which current can flow in a material. It depends on the physical parameters of the material such as length, area of cross section as well as the conductivity of the material.

Current density Is the electric current per unit area of cross section.

Electrical conductivity A measure of the ability of a material to conduct an electric current.

Impedance A measure of the opposition that a circuit presents to a current when a voltage is applied

In vitro An examination performed with cells or biological molecules are outside their normal biological environment.

In vivo An examination performed using living organism.

Magnetisation The density of magnetic field in a magnetic material

Permeability A measure of the degree of magnetisation that a material obtains in response to an applied magnetic field

Permittivity A measure of the resistance that is encountered when forming an electric field in a medium.

Spatial frequency A measure of how often sinusoidal components repeat per unit of distance.

List of Abbreviations

ADC Analog-to-Digital Converter

AC Alternating Current

CAT Computerised Axial Tomography

CT Computerised Tomography

DC Direct Current

ECT Electrical Capacitance Tomography

EIDORS Electrical Impedance Tomography and Diffuse Optical Tomography Reconstruction

EIS Electrical Impedance Scanning

EIT Electrical Impedance Tomography

ERT Electrical Resistance Tomography

EMT Electromagnetic Tomography

FEM Finite Elements Method

MRI Magnetic Resonance Imaging

MCS Multiple Current Source

PDE Partial Differential Equation

SCS Single Current Source

SVS Single Voltage Source

List of Symbols

γ Admitivity

Ω Domain

$\partial\Omega$	Boundary of a domain Ω
I	Electric Current
j	Current Density
σ	Conductivity
C_m	Capacitance of the cell membrane
ρ	Electric charge density
ϵ	Electrical permittivity of the free space
ω	Angular frequency
$\mathbf{B}$	Magnetic Field
$\mathbf{D}$	Electric Displacement
$\mathbf{E}$	Electric Field
$\mathbf{H}$	Magnetic Flux
S	Conductance
R_e	Extra Cellular Resistance
Z	Impedance
R_i	Intra Cellular Resistance
R	Resistance
V	Voltage

Mathematical Symbols

$\nabla \cdot \mathbf{F}$	Divergence of a vector field $\mathbf{F}$
∇f	Gradient of a scalar field f
$\int_\Omega$	Integral over the domain Ω
$\int_{\partial\Omega}$	Integral over the boundary of a domain Ω
$\nabla^2 f$	Laplace operator
iff	Mathematical notation means if and only if

Chapter 1

Introduction

Medical imaging refers to the process of constructing images of the human body or parts of it for clinical purposes, such as diagnosis of diseases or screening of the human organs and tissues. The term is used to define non-invasive techniques which generate images of internal parts of the body [1]. Non-invasive medical imaging does not physically penetrate the skin, but rather transmits electric current, electromagnetic or ultrasonic fields into the body, which in themselves could be quite invasive. The technique then measures the response of the inner tissue to this signal. The measured responses on the surface of the skin are then used as synthetic data by an inversion algorithm to image relevant physical properties of the internal tissues, e.g. electrical conductivity, magnetisation, density, etc.

There is a large variety of non-invasive imaging techniques used nowadays in medicine. For instance, X-rays mammography which uses short-wave electromagnetic radiation is used to detect any suspicious lesions in breast tissue [2]. Ultrasound (also called sonography) is an imaging technique that uses ultrasonic waves which bounce off tissues and internal organs. The echoes produce a picture called a sonogram which is used for visualizing soft body tissues including tendons, muscles, blood vessels

and internal organs [3]. Computed tomography (also known as a CT or CAT) uses computer reconstruction techniques to create cross-sectional images of the body from X-rays. The image from a CT scan can be enhanced several times to show detailed internal structures and to offer accurate information about the location of lesions which could be used for future surgery [4]. Magnetic resonance imaging (MRI), is another medical imaging technique, mainly used in radiology to investigate the anatomy of the body. MRI scanners use strong magnetic fields and radio-waves to construct images of the body [5].

Most of these medical imaging systems utilise radioactive sources, which may cause side effects in a patient, especially after long-term exposure. The other feature which all these modalities have in common is that the transmission of large signals into the body follows a straight line pattern. Therefore, X-ray CT, Ultrasound and MRI are also known as hard-field imaging techniques [6].

Early detection and treatment of breast cancer plays a crucial role in reducing mortality rates among patients. Unfortunately, classical screening techniques have limitations in their ability to determine lesion types in addition to their inefficiency to detect carcinoma in dense breast tissue which is more common among young women [7, 8]. As a result, the practicality of these imaging techniques in detecting breast cancer has become questionable due to the high rate of positive mammograms results which are followed by a negative biopsy diagnostic of cancer. In Europe, for instance, 80% of benign lesion findings have been recorded after biopsy examination [9], meaning that only one tissue sample out of every five patients undergoing a biopsy leads to malignant histopathological diagnosis. Moreover, clinical studies have shown that X-ray mammography which is the standard screening method in detecting breast cancer still does not offer the adequate specificity. For example, in a study by Elmore and co-workers [10] based on 9762 screening mammograms, the authors estimated the

accumulative risk of a false-positive results after ten mammography examinations to be 49.1%. Similar results were also presented in [11], where the sensitivity of X-ray mammography was reported to be 74% with a specificity of 60%, which means a 26% false-negative rate and 40% false-positive. According to Martin *et al*, the results from both latter studies demonstrate the growing problem of the biopsy diagnostic of cancer which is becoming a matter of deep concern [12].

The area of research of this thesis is a medical imaging technique called Electrical Impedance Tomography(EIT) and its applications in early detection of breast cancer. The word *tomograph* comes from the Greek word $\tau o \mu \eta$ (tome), which means a slice or a cross-section. The technique is relatively new, but it is increasingly attracting more attention as a low-cost, non-invasive, and a non-radiative imaging technique with a wide range of medical, industrial and geophysical applications [13]. EIT belongs to a family of electromagnetic imaging techniques which also include electrical capacitance tomography (ECT), electromagnetic tomography (EMT), and magnetic induction tomography (MIT) [14].

Unlike hard-field modalities, EIT belongs to the soft-field imaging techniques which also include other modalities such as the Optical Tomography(OT). The difference between hard- and soft-field imaging is that in soft-field imaging the transmitting field does not follow the straight line pattern of hard-field modalities. Instead, the signal distribution (e.g. electric current) tends to follow random paths inside the body. In this sense, the nature of soft field is much more complex than that of hard-field, which produces the great difficulty when designing the image reconstruction algorithms [6].

EIT creates images of the interior of an object by injecting current to the surface of the skin above the area under examination. During the injection, readings of induced

voltages on the surface of the skin are collected either at the same electrodes used for current injection (active) or at additional (passive) ones [15]. These measured potentials are used afterwards by a reconstruction algorithm to create an image of the determined conductivity distribution inside the body [16, 17].

The reconstructed EIT images offer information about the impedance properties of internal tissues which may not be obtained by other image devices. Therefore, EIT might be able to diagnose benign or malignant tumours. Moreover, clinical studies have shown that EIT examination offers high sensitivity for the differential diagnosis of suspicious breast lesions compared to other classical diagnosis modalities. Therefore, scientists nowadays are exploiting this useful feature as an additional value, by using EIT as an adjacent to other diagnostic techniques [18].

Safety and portability are yet another advantageous features of EIT over classical imaging techniques. Since EIT applies low voltages at the surface of the skin and currents are only injected locally over the area under investigation [19], there are no known risks during EIT examination. Additionally, EIT systems are significantly less expensive than other imaging techniques, since they require no more computing power other than that of a standard PC [20]. Moreover, the ability to make repeated measurements of changes in the internal organs (i.e. lungs or brain) makes EIT the only bed-side modality where images are reconstructed in real-time [21] . Therefore, EIT has already been used as monitoring tool in a variety of applications in clinical care medicine, including monitoring of ventilation distribution [22], assessment of lung functionality [23, 24], and detection of pneumothorax [25, 26].

In the mathematical sense, it is well established that image reconstruction in EIT is a challenging problem, being extremely ill-posed, and require solving a system of non-linear equations. The ill-posedness of this inverse conductivity problem comes

from the fact that large changes in the conductivity distribution inside the body can only correspond to very small changes in voltage data measured at the surface of the skin. Furthermore, in the physical problem, data could also be lost because the measurement precision is finite.

The inverse problem related to EIT is known as the inverse conductivity problem and it was first considered in 1980 by Calderón in [27] about inverse boundary value problem. In this research the author investigated whether one can determine the electrical conductivity of a medium by making voltage and current measurements at the boundary of the medium. In his study, Calderón concluded that the conductivity can be uniquely determined in domains with simply connected boundary if the conductivity is smooth and isotropic in some interior areas of the domain.

Since this first approach by Calderón, much theoretical work has been undertaken concerning the uniqueness and existence of the conductivity inside a region from full or partial knowledge of the Neumann-to-Dirichlet mapping which relates the distribution of the injected currents to the boundary values of the induced potentials [28]. Calderón pioneer contribution motivated many developments to solve other inverse problems.

Although significant progress has been achieved both in the theoretical and the practical aspects of this technique [16], there are still many challenges in EIT imaging such as the computational complexity of the reconstruction algorithm and the diagnostic capability of EIT in detecting breast cancer which is limited by the design of the system. For example, the spatial resolution of a tomographic system is determined by the number and the positions of the electrodes which can be attached to a patient and by the injected current patterns used by the EIT system [29, 30]. Another example is the sensitivity of an EIT system which depends on the distance between the

electrode and the target object, and on the amplitude of the injected current. The accuracy of EIT system, on the other hand, is determined by the amount of noise in the measurements, the number of electrodes and the applied regularisation methods. Other practical issues such as errors in electrode positions or boundary shape [25], high and uncontrollable contact impedance of the skin can also significantly influence the degree of accuracy [31]. In experimental tests, accuracy is usually optimised, since less regularisation is required. In practice, however, EIT measurements are subject to noise and wrong assumptions of the shape of the body.

Moreover, since most of the image reconstruction algorithms require the solution of two problems; forward and inverse problem, accurate information about the electrode positions and boundary of the body surface is very important. Any incompatible information from electrode positions to the body surface boundary can cause mismatching between real and simulated data [32].

Before manufacturing an EIT system, theoretical studies and simulations are usually carried out to anticipate the performance of the system. In these studies, mathematical techniques such as methods for solving the forward problem based on finite elements for example, and modelling of the physical laws of electromagnetism applied to the EIT problem are investigated in order to generate simulated synthetic data [33, 34]. Image reconstruction and analysis may follow after generating the simulated data to verify whether the system could produce images with sufficient information about the conductivity distribution inside the object under investigation.

Image reconstruction algorithms of EIT can be categorised into two main types: iterative and non-iterative (direct) algorithms. In the first type, the conductivity of the anomalies is assumed to differ slightly from the background. The computed value of the internal electrical potential corresponding to the background electrical prop-

erty is used by linearisation methods in order to approximate the unknown internal potentials. This procedure is quite fast, but produces a non-negligible error in the reconstruction, however, accurate results could be obtained if the solution is updated multiple times.

Iterative methods generally suffer from the ill-posedness nature of the EIT problem in addition to the computational cost of solving the forward problem in each updating step [35]. Moreover, these methods are inadequate in some applications where the variations of conductivity are considerably large such as the detection of breast cancer which is up to four times more conductive than normal breast tissues [36]. Additionally, iterative algorithms which are based on output least-squares or statistical inversion, which although promising for obtaining accurate reconstructed values, are computationally slow. Examples of iterative methods include back-projection [37], Calderon's approach [38], and one-step Newton method [39].

The second common approach is the direct or non-iterative reconstruction algorithms. Non-linear problems are solved faster with the potential to infer the conductivity values with higher precision. Examples of non-iterative algorithms are those based on resistor networks modelling [40, 41] and Muller's method proposed in [42].

The EIT devices developed by the Institut für Physik, Universität, Mainz, Germany in collaboration with Oxford Brookes University, consist of a planar sensing head of circular geometry. All the tomographic systems are primarily designed for medical applications where measurements in this case can only be taken from one side of the patient's body (e.g. mammography or skin cancer detection). In this application the device is much smaller than the human body to which it is applied. If a breast tumour is allocated at a shallow depth under the surface of the skin, one can extract sufficient information about the existence and location of the cancer only by reconstructing the

conductivity at the surface of the skin. The reconstruction algorithms for this mammography are based on a resistor network model or on integral equations approach. Hence, the conductivity of a two-dimensional circular domain from boundary measurements of currents and interior measurements of the potential is determined if the measurement area is modelled as a resistor network of regular geometric pattern. The novel design of Mainz-Brookes mammographs is in the distinct use of active and passive electrodes. Since high impedance voltage measurements are taken only at the inner electrodes the problem of contact impedance does not arise.

1.1 Justification

The proposed research in this thesis is concerned with the inverse conductivity problem which has practical applications in medicine, geophysics and industry in the form of Electrical Impedance Tomography (EIT). The project explores the possibility of using EIT as an aid for detecting breast cancer in its earliest stages of development. The advantages (low cost, minimal patient discomfort and no known side effects) of an impedance imaging system over traditional X-ray mammography make this technology a useful addition to available technologies for the fight against breast cancer.

Since the 1920s, numerous researchers performed *in vitro* impedance measurements on both normal and cancerous human breast tissues [43]. *In vitro* studies have shown that there is a difference of three time or more in the electrical conductivity between healthy and cancerous tissues, and hence, imaging the electrical properties of the breast tissue would result in potential information which could improve the diagnosis of early cancer detection. Additionally, EIT can play the role of a regular

screening method. The technique could be capable of providing the physician with the sufficient information to decide whether the patient needs further diagnosis, in case of any suspicious abnormalities. This will prevent unnecessary regular exposure to radiation or the need for biopsy samples, and can significantly reduce the health-care cost. However, to achieve clinical acceptance, the theoretical developments of reconstruction methods should be closely connected with laboratory experiments and studies on real data. The research presented in this thesis will address this need by developing non-iterative reconstruction algorithms based on discrete models to be tested with real data obtained by the EIT group at Mainz University, Germany.

1.2 Research Aims and Objectives

The goal of this research project is to implement in Matlab two-dimensional discrete resistor network models for Electrical Impedance Tomography (EIT) intended to be used for conductivity imaging with real data obtained from planar EIT devices designed by Oxford Brookes University in collaboration with the EIT group at University of Mainz, Germany. This two-dimensional inversion technique is direct (non-iterative) which will enable conductivity reconstructions in real time.

This research also investigates the optimal geometry of the planar array of electrodes for the design of a new sensing head of the EIT device for breast cancer detection by introducing additional electrodes for measuring voltages and/or by increasing the number of electrodes for current injection.

Numerical experiments using simulated data and the two-dimensional image reconstruction algorithm showed that a map of the conductivity at the surface provides

enough information on the existence and location of a breast tumour, but only if the latter is either large or situated at shallow depths. Additional information about the depth of the tumour and its real size can only be obtained by extending the existing two-dimensional inversion technique to address the full three-dimensional problem.

Since EIT devices are generally much smaller than the human body to which they are applied, the imaging of the conductivity distribution of the three-dimensional half space is, therefore, required from electrical measurements performed on its surface. Therefore, this research also extended to the development of a three-dimensional reconstruction algorithm based on a set of discrete voxels to model a full three-dimensional space. This non-iterative three-dimensional reconstruction algorithm enables the detection of smaller and deeper tumours, and hence, improved the specificity of the results.

1.3 Structure of the Thesis

The second chapter begins with an introduction to Electrical Impedance Tomography (EIT), followed by examples of medical and industrial applications of EIT. A closer look at medical EIT systems can be also found in this chapter. Mathematical formulation of the continuum model, including the derivation of the governing equation and both the forward and inverse problem is presented in this chapter too. Finally, this chapter also include a discussion about the most common electrode modelling in addition to defining an optimal current patterns for EIT.

The main focus of the third chapter is on Electrical Impedance Tomography in diagnosing breast cancer. In this chapter definitions of accuracy, specificity, and sensitivity

are introduced. Additionally, *in vitro* and *in vivo* methods for measuring the conductivities of human breast tissues are explained with some experimental results giving various measurements of the electrical properties of different human tissues. The chapter also includes clinical trials of EIT for detecting breast cancer, with a focus on evaluating the sensitivity and specificity. Finally, clinical trails using EIT as an adjunct to other imaging modalities (mainly x-ray mammography) are also presented.

In chapter four, a two-dimensional reconstruction algorithm based on discrete resistor network is presented. The algorithm is intended to be used for conductivity imaging, with data obtained from a planar electrical impedance tomography device developed by Brookes University in collaboration with Mainz University in Germany for breast cancer detection. In this chapter, the investigation of different proposed geometries for the prototypes is also presented. The chapter concludes by two-dimensional numerical reconstructions obtained from these different prototypes.

Chapter five presents a novel three-dimensional reconstruction algorithm for electrical impedance imaging, which is suitable for determining the conductivity distribution beneath the surface of a medium, given surface voltage data measured on a rectangular array of electrodes. The electrode configuration in this approach is desirable for using electrical impedance tomography to detect tumours in the human breast. The algorithm is based on linearising the conductivity about a constant value. The chapter also concludes with numerical reconstructions using EIDORS (see Subsection 4.3.3 for a detailed description of this forward solver) and Matlab for inclusions with different conductivities and dimensions placed at various positions and depths from surface electrodes.

Finally, chapter six is devoted to the discussion and conclusion of the work in this research, followed by suggestions for future research paths related to this work.

Chapter 2

Electrical Impedance Tomography

2.1 Introduction

The principle of Electrical Impedance Tomography (EIT) is to infer the conductivity distribution inside a conductive object when access is limited to its boundary. This can be achieved by injecting current patterns and performing simultaneous measurements of the potentials on the boundary of that object.

The physical domain under investigation in this case is a material with regions of different electrical conductivities. Mathematically, it is a subset of the Euclidean spaces $\mathbb{R}^2$ or $\mathbb{R}^3$ and it is denoted by Ω. The domain Ω is considered to be an open, and simply connected set. If Ω is a subset of $\mathbb{R}^n, n = 2$ or 3, then the notation $\overline{\Omega}$ defines its closure. The boundary of the domain, denoted by $\partial\Omega$, is defined as $\partial\Omega = \partial\left(\mathbb{R}^n \backslash \overline{\Omega}\right)$. In medical EIT, Ω refers to the human body and $\partial\Omega$ refers to the surface of the skin. The governing equation for EIT is the generalised Laplace equation, which is an elliptic partial differential equation (PDE). To reconstruct the conductivity, boundary conditions and/or initial conditions for the governing PDE must be enforced. Depending on the technique used in EIT, the two most common boundary

conditions associated with EIT are the Dirichlet and the Neumann boundary conditions. A Dirichlet condition is enforced by specifying the value of the solution on the boundary. In practice this corresponds to fixing the voltage on the boundary $\partial\Omega$ and measuring the current. The Neumann condition, on the other hand, specifies the normal derivative of the solution on the boundary, which in practice corresponds to applying the current density j on $\partial\Omega$ and measuring the voltages. The mathematical formulation of the EIT problem with Dirichlet and Neumann boundary conditions is presented in Subsection 2.4.1)

2.2 Applications of EIT

The concept of EIT imaging is motivated by the fact that various materials exhibit different electrical properties (see Tables 2.1 and 2.2). Hence, a map of the electrical conductivity can be used to infer the interior structure of an object under investigation.

Table 2.1: Electrical properties of some biological tissues measured at frequency $100kHz$ [16, 44]

Tissue	Conductivity (mS/cm)	Permittivity (μ F/m)
Blood	6.70	0.05
Liver	2.80	0.49
Bone	0.06	0.0027
Cardiac Muscle	6.30 (longitudinal)	0.88
	2.30 (transversal)	0.36
	1.00 (expiration)	0.44
	0.40 (inspiration)	0.22
Fat	0.36	0.18
Skin	0.0012	0.0144

With such characteristics, EIT has important applications in medicine (lung function monitoring, detection of pulmonary emboli, monitoring of heart functions, blood

Table 2.2: Resistivity of some rocks and fluids [45–47]

.

Rocks or fluids	Resistivity ($1/\sigma$ *in* Ωm)
Marine sand, shale	1-10
Terrestrial sands, claystone	15-50
Volcanic rocks, basalt	10-200
Granite	500-2000
Limestone dolomite, anhydrite	500-5000
Chloride water from oil fields	0.16
Sulphate water from oil fields	1.2

flow, breast cancer detection), in geophysics (detection of underground minerals, detection of leaks in underground storage tanks, monitoring flows of injected fluids into the earth, exploring of underground resources of water, and monitoring volcano activities), in industry (industrial process monitoring) and non-destructive testing (detection of corrosion and of small defects in metals) [16, 48]. Moreover EIT has applications in the identification of cracks, materials composites, and their geometry in inaccessible locations [49].

In the next subsection, different medical applications of EIT developed by a number of research groups are presented in more details, followed by a subsection about industrial and geophysical applications of EIT.

2.2.1 Medical Applications

Impedance imaging has been widely studied for the past two decades. It is estimated that the number of studies conducted in the field of medical imaging is approximately 5 billion worldwide [50].

Although significant progress has been achieved both in the theoretical and in the

practical aspects of this imaging technique [16], the success of EIT as a medical application has been rather limited; partially, because of its theoretical limitations such as ill-posedness and poor spatial resolution when compared to other imaging technologies. The sensitivity of the boundary data to changes in the interior conductivity of an object has been proven to be very low resulting in images with a resolution which deteriorates as the distance from the boundary increases [31, 51]. There are also practical problems associated with reconstructing images in EIT for medical applications which are mainly due to errors in electrode positions or boundary shape, and to the high and uncontrollable contact impedance of the skin. As a result, EIT has not made yet the transition to be used widely as a clinical diagnosis routine. However, many research groups are actively working on the development of various medical EIT applications. Some examples of such groups are given next.

The research group at the University College of London (UCL) has been experimenting ways to adjust medical EIT systems for imaging changes in the brain following medical conditions such as stroke, epilepsy or normal physiological brain function [52]. According to this group, the portability and low cost of such systems would offer unique and practical advantages over existing methods for imaging brain functions such as functional MRI (fMRI). The group also claims that such an EIT system has the potential of producing images in milliseconds for fast neural activity in the brain. The UCL group also believe that this system would offer a revolutionary advance in neuroscience technology [53]. Some of the challenges in this work are mainly due to the fact that skull is resistive and tends to divert current. Hence, the signal to noise ratio is low. However, the researchers at UCL claim that the developed hardware and image reconstruction algorithms are capable of producing non-invasive images inside tanks which mimic the human head, and also on experimental animals with electrodes on the brain [54]. Currently, the UCL group is investigating the possibility

of collecting clinically relevant images on human subjects.

Cherepenin *et al* from Kotel'nikov Institute of Radioengineering and Electronics, (RAS), Moscow, Russia developed an EIT system for gynaecological applications. The system has 48 electrodes embedded on a small space inside a hand-held probe used for vaginal examinations. According to this study, the system offers a near real-time three dimension visualisation of the interior spatial distribution of the electrical conductivity of the cervix tissue [55]. The ability of producing a near real-time visualization is due to relatively small number of measurement electrodes which enables a few frames to be reconstructed per second. However, due to the small number of electrodes, the reconstructed images have quite poor resolution. Additionally, the device is also capable of producing the three-dimensional images up to a depth of 8mm inside the cervix. This group claims that the device is independent on an external PC, thus it could be designed as self-contained and therefore could be used for clinical gynaecological screening usage. Further developments including optimising the measuring head for regular use and improving sterilisation for a proper frequent use are still under consideration.

The research group at RAS also developed a new medical imaging system which consists of a planar array with 256 electrodes. The system is capable of obtaining three-dimensional images of the conductivity distribution in regions below the skin surface up to a depth of several centimetres. According to their studies, both the measuring system and the image reconstruction algorithm can be used for breast tissue imaging, particularly, for detecting malignant tumours. Since mammary glands change with physiological conditions such as menstrual cycle, pregnancy, lactation, and postmenopause, the purpose of this device is to investigate the state of mammary glands among women with different hormonal status. This study showed that electrical impedance mammograms from different groups of patients had clear vi-

sual distinctions of mammary glands and statistically showed significant differences in their conductivities. The group, hence, concluded that data on conductivity distribution in the mammary gland during different physiological periods could be used for further research on mammary glands with different pathology [56].

The group at the Respiratory Intensive Care Unit, São Paulo School of Medicine, Brazil, proposed an EIT-based method to monitor pneumothorax complication during mechanical ventilation [21]. The purpose of their study was to identify characteristic changes in the EIT signals associated with pneumothoraces. The focus of their research was to develop a fine-tune algorithm for automatic detection of pneumothoraces, and consequently analyse the sensitivity and specificity of their algorithm in real-time. Results have showed that pneumothoraces as small as 20ml could be detected with a sensitivity of 100% and specificity 95% and could be easily distinguished from other lung diseases. The locations of pneumothoraces were also correctly identified in all cases, with a total delay of only three respiratory cycles. This study concluded that the EIT-based system which they developed is capable of detecting early signs of pneumothoraces in high-risk situations, and also identifying their locations. According to the group, this technique opens opportunities for improving patient safety during mechanical ventilation [25].

Another medical application of EIT is the measurement of cardiac parameters which was investigated in [29], with a focus on the measurement of the volume of the heart stroke mainly on the right ventricular diastolic function. According to this research, such application of EIT can be used in an intensive care unit as a non-invasive technique to measure heart stroke volume in real-time.

In Section 2.3 the general characteristics of EIT systems designed for medical applications will be further discussed. Section 3.5 focuses on medical EIT systems designed

specifically for detecting breast cancer and also mentions the outcomes of clinical trials. The next subsection is about the industrial and geophysical applications of EIT.

2.2.2 Industrial and Geophysical Applications

One important non-medical application of EIT is in Industrial Process Imaging, or Industrial Process Tomography (IPT) [57]. IPT is a non-destructive, non-invasive imaging technique used in a variety of industrial applications to scan inaccessible containers such as pressure vessel and pipelines and construct a cross-sectional image in real-time. Since measurements of the contents of closed containers cannot be made using optical instrumentation or higher energy radiation methods, the density and velocity distribution of the contents can be tomographically imaged instead, offering a more structured approach to modelling, designing, and operating opaque and fast moving dispersions [58]. IPT technique can also offer continuous system measurements allowing a better understanding and an improved monitoring of industrial processes. The technique can be used as an on-line control of processes including fault detection and system malfunction. In addition to above, the analytical information provided by IPT allows a robust experimental means for the optimisation of process vessel design and operation through model development and validation [59].

Electrical Resistivity Tomography (ERT) is a geophysical technique to image subsurface structures, which works by performing electrical resistivity measurements at the earth surface, or inside boreholes drilled in the soil. The deeper the boreholes, the lower earth layers can be investigated. The concept of ERT is similar to that of the EIT in the sense that ERT exploits the differences in the resistivity of different

materials in order to reconstruct an image for the sub-layers structure of the earth. However, in geophysical applications of EIT, either direct current or alternating current of low frequency (typically about 20Hz) are applied. [60]. Additional applications of ERT include: fault inspection, allocation of ground water, soil moisture content detection, etc. [61].

Resistivity tomographic imaging can also be applied to monitoring transport pipelines. Early work was concerned with measuring two-phase flow in industrial pipelines, especially oil/gas and oil/water flows from offshore oil wells [62]. Since the behaviour of two-phase flow is extremely complex, it presents a great challenge to the study of flow mechanism. Measurements of pressure gradients and any possible void fractions are very important for safety and quality assurance purposes in industry. ERT, therefore, provides a simple, non-iterative and a fast response method for measuring pressure and void fractions. Additionally, ERT can display a cross-sectional electrical conductivity distribution of the mixture within the pipe [63, 64].

Induced Polarisation is another application of EIT which is a geophysical imaging modality used to detect sub-surface materials such as steel. The technique measures the slow decay of voltage in the ground after an excitation current pulse is applied. The induced polarisation is an indicator for the ability of sub-surface materials to store electric charges. When a current is injected, the decay with time of the difference in the measured potential is observed. The rate of decay of this potential (induced polarization potential) depends on the general physical characteristics of rocks, their pore geometries and degree of water saturation [65–67].

2.3 Medical EIT Systems

Impedance measurements have been used in many areas of medical diagnosis in the past, but not as imaging tools. For example, measurements of the impedance of the thorax were used to examine intra-thoracic fluid to diagnose any cardio-pulmonary diseases. Impedance measurements are also used to monitor respiration; a technique called Impedance Pneumograghy [21]. With electrodes attached to the head, impedance measurements can also be used to study cerebral haemodynamics, particularly, as a technique applied to newborns [68]. The measurements obtained by impedance pneumograghy can be used as an indicator of a wide range of neurological diseases and to detect traumatic brain injuries [69].

The discovery of EIT as a medical imaging modality is attributed to John G. Webster in 1978 [70]. The first medical EIT system, however, was developed in 1984 by David C. Barber and Brian H. Brown [71]. In their published work [72] in year 1984, together, Brown and Barber attempted to visualise the cross section of a human forearm by placing a set of 16 electrodes around the boundary of the area being examined. The aim was to image the distribution of resistances within the slice defined by placing the electrodes around the boundary of forearm.

There are two categories of medical EIT systems based on the placement of the electrodes: planar systems, also known as mapping systems and circular tomographic systems which use a belt-like set of electrodes used to wrap the area under investigation, see Figure 2.1.

(a) Planar (mapping) EIT system [73]

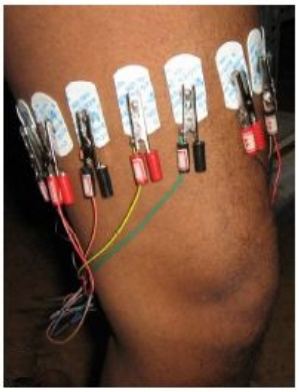

(b) Circular tomographic system [74]

Figure 2.1: Medical EIT systems.

Planar (mapping) systems are typically used for breast, skin and prostate cancer screening. For example, during medical examination of the breast, the plate with the electrodes is pressed against the skin which, hence, presses the breast against the chest wall as shown in Figure 2.1(a). As a result, all electrodes are in contact with the breast and the examined area constitutes a relatively shallow region between the measuring electrodes and the chest wall. Currents or voltages are then applied through electrodes in the array.

In circular tomographic systems, electrodes are in a belt-like arrangement. During examination, electrodes are attached to the patient's body in such a way they surround the region to be imaged as shown in Figure 2.1(b). The circular arrangement of the electrodes around the body creates a cross-sectional plane of intersection were the electrical conductivity distribution is determined. In the case when more than one layer is examined, the enclosed region of interest is a volume, not a cross-sectional plane and more circular arrays of electrodes are generally placed around the examined area.

Typical medical EIT systems as the one shown in Figure 2.2 apply alternating currents of low frequency in the range between 10Hz-10MHz. This range of frequencies is selected for minimizing the capacitive effects of the human tissues [75]. However,

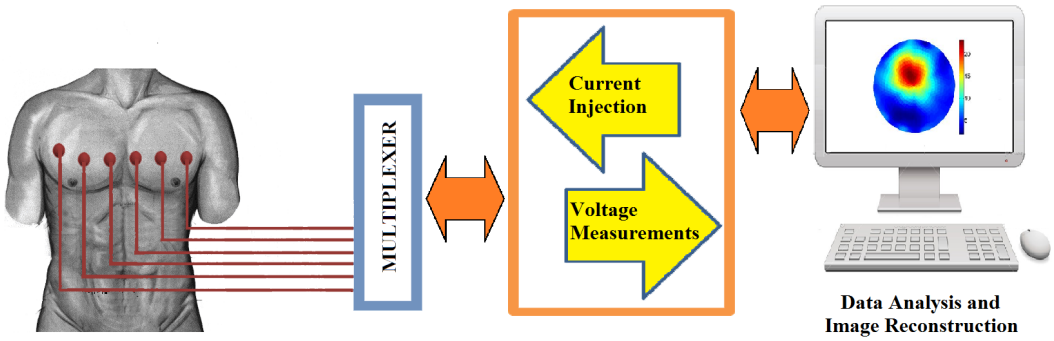

Figure 2.2: Typical medical EIT system [76]

according to Romsauerova *et al*, for EIT brain imaging, the frequency of the applied current should be below 100Hz as higher frequencies could stimulate cutaneous nerve endings. In this research [77], Romsauerova and co-workers attempted to find the most suitable current patterns which could be employed for brain imaging. When a current pattern with frequency in the range of 20Hz - 1.6MHz was applied to the forefront of the head in four healthy volunteers with the same current amplitude of 0.28mA, for each frequency, an unpleasant tingling sensation was perceived. According to this study, the sensation reduced or disappeared when frequencies below 100Hz were applied. They conclude that, the optimal compromise for brain imaging with absence of sensation was a current pattern of frequency of 40Hz. For current patterns of frequencies of 80Hz and 20Hz, the sensation was reduced by 75% and 50%, respectively.

For planar EIT systems, there are three main current excitation methods:

1. Single Voltage Source (SVS), which fixes a constant voltage to a planar array of

electrodes pressed against the body, with reference to a single hand-held electrode. Then the induced currents are measured at each of the other electrodes on the array.

2. Single Current Source (SCS), which injects a current through each electrode sequentially, and measures the induced voltage on all other electrodes.

3. Multiple Current Sources (MCS) uses both fixed current patterns as well as adjustable pre-defined patterns of currents [78].

For circular EIT systems used to reconstruct cross-sectional images, there are also three techniques for current injection and voltage measurement [79,80]. These include:

1. Adjacent Drive which is the most common technique to drive current. In this procedure, the current is injected through adjacent electrodes and the voltage differences are measured sequentially at all remaining adjacent pair of electrodes.

2. Opposite, a technique which is mostly used in brain EIT imaging. In this procedure, the current is applied through electrodes that are 180° apart, while voltage differences are measured on the remaining electrodes.

3. Trigonometric, a technique, where spatial frequency currents are injected and voltages are measured at all electrodes. Because current flows through all electrodes simultaneously, many assigned current injectors are needed, e.g. a 16-electrode EIT system requires 16 current injectors. In the trigonometric procedure, the boundary potentials are measured with reference to a single grounded electrode. Therefore, for each current pattern only 15 voltage measurements can be taken for a 16-electrode EIT system [81].

2.3.1 Challenges of medical EIT

In conventional medical imaging technologies such as the X-ray CT, a collimated beam of radiation passes through the body in straight lines. The attenuation in this case is affected only by the tissue laying in the path of the beam [82]. Such techniques are said to have a local property. Contrary to this, the non-local property of EIT is due to the fact that injected currents scatter inside the body. This is one of the reasons why imaging the conductivity distribution inside an object is such difficult.

Furthermore, the sensitivity of electrical impedance imaging to changes in electrical properties of internal tissues is inversely proportional with the distance from the nearest electrode. For example, in the circular array arrangement, the parts towards the centre of the imaged area have the least sensitivity. In the case of planar systems, the sensitivity of the reconstructed image decreases as the distance between the examined tissue and the electrodes plane increases.

As mentioned earlier, in addition to the high sensitivity to noise, the impedance imaging techniques also suffer from poor spatial resolution if compared with other imaging techniques such as X-ray mammography. Such poor resolution might be one of the drawbacks of EIT as medical imaging technique. While high resolution might not be an issue in other applications of EIT such as ERT, it is however, very important in most medical applications [29]. According to [83], the electrode arrangements, the number of electrodes used to inject current and the number of different current patterns which are injected, could also influence the resolution of the image reconstructed by impedance imaging systems.

2.4 EIT Continuum Model

The reconstruction of the conductivity distribution in EIT requires a way of calculating the potential u, of the electric field $\mathbf{E} = -\nabla u$, from given boundary conditions and measurements. Electromagnetic fields are governed by four fundamental partial differential equations called Maxwell's equations (2.1-2.4). These equations explain how electric and magnetic fields propagate, interact, how they are influenced by objects and how they change in time [84]. They were stated in their final form by the physicist James Clerk Maxwell between 1861 and 1862. The basic quantities in Maxwell's equations are the electric field $\mathbf{E}$ and the magnetic field $\mathbf{H}$. Both are represented as vector functions of time and space. When the fields $\mathbf{E}$ and $\mathbf{H}$ are applied to a material, they induce an electrical displacement $\mathbf{D}$ and a magnetic flux $\mathbf{B}$, respectively [85]. Together, the set of four equations define the spatial and temporal relationship between the two fields $\mathbf{E}$ and $\mathbf{H}$ as follows:

$$\nabla \times \mathbf{E}(x,t) = -\frac{\partial \mathbf{B}(x,t)}{\partial t} \qquad \text{(Faraday's law)}, \tag{2.1}$$

$$\nabla \times \mathbf{H}(x,t) = \mathbf{j}(x,t) + \frac{\partial \mathbf{D}(x,t)}{\partial t} \qquad \text{(Ampere's law)}, \tag{2.2}$$

$$\nabla \cdot \mathbf{B}(x,t) = 0 \qquad \text{(Gauss' law for magnetism)}, \tag{2.3}$$

$$\nabla \cdot \mathbf{D}(x,t) = \rho \qquad \text{(Gauss' law)}. \tag{2.4}$$

where ρ is the charge density. In the special case of a linear medium, Ohm's law states that the current density $\mathbf{j}$ in equation 2.2 can be given at any point(x) and time(t) by:

$$\mathbf{j} = \sigma \mathbf{E}(x,t), \tag{2.5}$$

where σ is the electric conductivity. Moreover, in the linear approximation and for isotropic media, there is a direct relationship between fields and their fluxes [86]

$$\mathbf{D} = \epsilon(x, \omega)\mathbf{E}, \tag{2.6}$$

$$\mathbf{B} = \mu(x, \omega)\mathbf{H}. \tag{2.7}$$

where ϵ and μ are the permittivity and permeability of the medium respectively.

2.4.1 Mathematical Formulation

In practice, EIT systems use alternating currents patterns at a fixed angular frequency ω over time t. Therefore, the electric and magnetic fields, $\mathbf{E}(x,t)$ and $\mathbf{H}(x,t)$, and their corresponding fluxes, $\mathbf{B}(x,t)$ and $\mathbf{D}(x,t)$, respectively, are time-harmonic and can be written as:

$$\mathbf{E}(x,t) \longmapsto \mathbf{E}(x)e^{i\omega t}, \qquad \mathbf{B}(x,t) \longmapsto \mathbf{B}(x)e^{i\omega t} \tag{2.8}$$

$$\mathbf{H}(x,t) \longmapsto \mathbf{H}(x)e^{i\omega t}, \qquad \mathbf{D}(x,t) \longmapsto \mathbf{D}(x)e^{i\omega t}. \tag{2.9}$$

Using the expressions above, equations (2.1) and (2.2), become:

$$\nabla \times \mathbf{E}(x) \quad = -i\omega\mu(x)\mathbf{H}(x), \tag{2.10}$$

$$\nabla \times \mathbf{H}(x) \quad = (\sigma(x) + i\omega\epsilon(x))\mathbf{E}(x). \tag{2.11}$$

Since EIT uses relatively low current frequency ω, and the technique is applied to objects with lengths L which generally satisfy $\omega\mu|\gamma|L^2 \ll 1$, where $\gamma(x) = \sigma(x) + i\epsilon\omega(x)$ is the admittivity of the medium, then equation (2.10) and (2.11) can be

approximated by:

$$\nabla \times \mathbf{E}(x, \omega) = 0, \tag{2.12}$$

$$\nabla \times \mathbf{H}(x, \omega) = \gamma(x, \omega)\mathbf{E}(x, \omega), \tag{2.13}$$

The electric potential at a point x in an electric field $\mathbf{E}$, can be defined as:

$$u(x) = -\int_C \mathbf{E} \cdot d\ell,$$

where C is an arbitrary path connecting the point with zero potential to x. When $\nabla \times \mathbf{E} = 0$, the line integral above does not depend on C any more [87], but only on the endpoint x. In this case, the electric field is said to be conservative and can be determined by the gradient of the potential:

$$\mathbf{E} = -\nabla u(x). \tag{2.14}$$

Moreover, if there are no internal current sources, the time-harmonic electric current density is defined as

$$\nabla \times \mathbf{H} = j(x). \tag{2.15}$$

Hence, from equation (2.14) and (2.15), we see that

$$j(x) = -\gamma \nabla u(x), \tag{2.16}$$

which is Ohm's law.

Since the divergence of a curl is zero, we can re-write equation (2.13) as:

$$\nabla \cdot (\nabla \times \mathbf{H}) = \nabla \cdot [\gamma(x)\mathbf{E}] = 0. \tag{2.17}$$

Substituting (2.14) into (2.17), we arrive at the generalised Laplace equation

$$\nabla \cdot [\gamma(x)\nabla u(x)] = 0. \tag{2.18}$$

The Forward Problem of EIT

The forward problem of EIT is to find the solution $u(x)$, $x \in \Omega$, of equation (2.18) given the admittivity distribution $\gamma(x)$, $x \in \Omega$, subject to either a Dirichlet boundary condition

$$u(x) = V(x), \qquad x \in \partial\Omega \tag{2.19}$$

or Neumann boundary condition

$$\gamma(x)\frac{\partial u}{\partial n} \equiv \gamma(x)\nabla u(x) \cdot \mathbf{n}(x) = j(x) \qquad \text{at } \partial\Omega, \tag{2.20}$$

such that

$$\int_{\partial\Omega} j(x)dx = 0. \tag{2.21}$$

where $\mathbf{n}$ is the outward unit normal of u to the boundary $\partial\Omega$. The solution of equation (2.18) subject to Neumann boundary condition (2.20) can be determined for all $x \in \Omega$, up to an additive constant, which could be fixed by choosing the ground such that

$$\int_{\partial\Omega} u(x)dx = 0.$$

or, alternatively

$$u(x_0) = u_0 = \text{const}, \quad x_0 \in \Omega\,.$$

Inverse Problem of EIT

The inverse problem of EIT is to find the electrical admittivity, $\gamma(x)$, for all $x \in \Omega$ satisfying equation (2.18) from measurements of all admissible currents satisfying equation (2.21) and of corresponding voltages on the boundary $\partial\Omega$ of the domain. However, in practice, the number of voltage and current measurements on the boundary is limited and contaminated by noise.

2.5 Electrode Models

In real practice of EIT, current patterns are injected through a finite number of active electrodes placed on the surface of the object under investigation as illustrated in Figure 2.3.

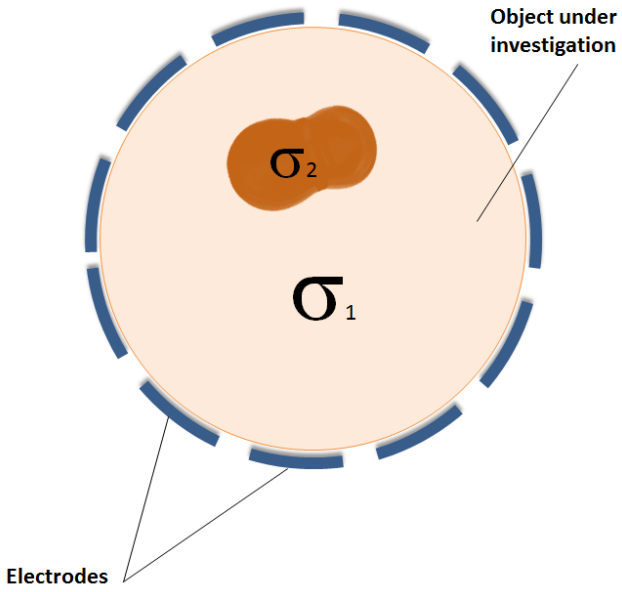

Figure 2.3: Finite number of active electrodes around the surface of the object under investigation.

A common practice in the reconstruction algorithm proposed for EIT was to model the electrodes in contact with skin as point electrodes. This model, however, limits the accuracy of the obtained voltage measurements and, consequently, reduces the inversion estimation, since it does not take into account the actual size of the electrode or the possible shunting effect on the surface of the electrodes caused by a current generated by active regions inside the body flowing through the electrodes back into the skin [88].

The effect of contact impedance between the skin and the electrode is also a critical factor in impedance measurements. This can be an accuracy-limiting factor, especially in the medical applications of EIT [89].

The effect of both the size of electrodes and the contact impedance on the voltage distribution was analysed in [88]. This study showed that, the accuracy of voltage measurements is dependant on the size and the contact impedance of the electrodes. Additionally, it was shown that increasing the number of electrodes does not necessarily enhance the accuracy of the inverse reconstruction. This study demonstrates that a realistic modelling of the electrodes has a significant role in determining the conductivity accurately. This research also provides evidences that, it is important to take into account the actual size of the electrodes, the shunting effect, and the contact impedance between the skin and the surface of the electrodes when modelling the electrodes. The most commonly used electrode models are discussed below.

The ave-gap model

The ave-gap model approximates the current density j by the current I_l on the ℓth electrode e_ℓ divided by the electrode's area A_ℓ, and sets the current density j to zero elsewhere [90, 91], i.e.

$$j(x) = \begin{cases} I_\ell / A_\ell & x \text{ on } e_\ell, \quad \ell = 1, 2, \ldots, L, \\ 0 & \text{elsewhere,} \end{cases}$$

where L is the total number of electrodes. The ave-gap model ignores both the shunting effect of the electrodes and the contact impedance. The advantage of using ave-gap model is due to being mathematically easy to work with [92].

The corresponding voltage U_ℓ measured on the ℓth electrode e_ℓ is approximated by:

$$U_\ell = \frac{1}{A_\ell} \int_{e_\ell} u(x) dx, \tag{2.22}$$

where $u(x)$ is the solution to (2.18).

The laws of the conservation of current and voltages are also considered in the ave-gap model to ensure existence and uniqueness of the results, i.e.

$$\sum_{\ell=1}^{L} I_\ell = 0, \tag{2.23}$$

$$\sum_{\ell=1}^{L} U_\ell = 0. \tag{2.24}$$

The shunt model

The shunt model takes into account the shunting (or shorting) effect of the electrodes as they are in contact with the skin. The electrodes are assumed to be high conductive, offering perfect paths for the current to flow. The potential $u(x)$ is then assumed to be constant on each electrode as

$$u(x) = U_\ell, \quad x \text{ on } e_\ell, \qquad \ell = 1, 2, \cdots, L, \tag{2.25}$$

where U_ℓ are the measured voltages. In this model, the exact current density is not known, but it has to satisfy the following constraints:

1. The total injected current through each electrode is equal to the integral of the current density $j = \sigma \frac{\partial u}{\partial n}$ over e_ℓ:

$$\int_{e_\ell} \sigma(x) \frac{\partial u}{\partial n}\ (x) dx = I_\ell, \qquad x \text{ on } e_\ell, \quad \ell = 1, 2, \ldots, L; \tag{2.26}$$

2. It is assumed that no current flows through areas where no electrodes are present, i.e.

$$\sigma(x) \frac{\partial u(x)}{\partial n}\ (x) = 0, \qquad \text{elsewhere.} \tag{2.27}$$

The complete electrode model

The complete electrode model was firstly developed by Cheng *et al* [93]. As in the shunting model, the same set of conditions (2.25)-(2.26) for the current density are specified. Additionally, it models the interface of the electrode and the medium as a thin layer with surface impedance of z_ℓ. The electrodes are modelled as perfect conductors, i.e. although the quantities of the right-hand side of (2.28) are real-valued functions, the measured potential is a scalar.

$$U_\ell = u(x) + \sigma z_\ell \frac{\partial u}{\partial n}(x) \qquad x \in e_\ell, \quad \ell = 1, 2, \ldots, L. \tag{2.28}$$

Finally, to ensure existence and uniqueness of the solution, the constraints (2.23)-(2.24) are required for the injected current and the measured voltages as in the ave-gap model [91]

2.6 Optimal Current Patterns

The question of optimal current excitation patterns in EIT was first addressed by Seagar [94] were he studied the best placement of a pair of point-electrodes in a planar array to maximize the voltage differences between the measurement of a homogeneous background and an inhomogeneous offset anomaly [95]. A later study suggests maximising the L^2-norm of the difference between the measured and calculated voltages, and constraining the L^2-norm of the current patterns in a multiple drive system [96]. In this way, the power inoculated inside the body was maximised. The researchers pointed out that medical safety regulations restrict the maximum overall current injected inside the patients body to 100μA [97] in order to limit the maximum ohmic power dissipated in the body.

To briefly explain the optimisation problem of the current under these safety regulations, let $\mathbf{V} = (V_1, \cdots, V_k)^T$ be the vector of measured potentials on electrodes, $\mathbf{I} = (I_1, \cdots, I_k)^T$ be the vector of applied currents and k be the number of electrodes. Both the current patterns $\mathbf{I}$ and the measured potentials $\mathbf{V}$ are linearly related by the transfer impedance matrix $\mathbf{R}$ such that:

$$\mathbf{V}{=}\mathbf{R}\mathbf{I} \tag{2.29}$$

If we denote by $\mathbf{V}_c$ the calculated voltages for a given $\mathbf{R}_c$, then the aim is to maximize the L^2-norm of the difference between the measured and calculated voltages, such that:

$$\|\mathbf{V} - \mathbf{V}_c\|_2 = \|(\mathbf{R} - \mathbf{R}_c)\mathbf{I}\|_2 \ .$$

This can be achieved by maximising $\|(\mathbf{R} - \mathbf{R}_c)\mathbf{I}\|_2$ subject to $\|\mathbf{I}\|_2 \leq M$ for some fixed value M. The solution of this optimisation problem is $\mathbf{I}$ which is the eigenvector

of $\mathbf{R} - \mathbf{R}_c$ corresponding to the largest eigenvalue [98].

An important issue in EIT systems is to improve the resolution of the reconstructed images [99]. One criterion for determining the resolution of EIT images was first suggested by Isaacson [100] based on the concept of a quantitative measurement called distinguishability $\delta(j)$, which is the current density's ability to distinguish between two different conductivities σ_1 and σ_2 [101]. The distinguishability, or the ability to detect an object, depends not only on the electric property and the location of the target object, but also on the applied currents used in the EIT system [44]. Mathematically, the distinguishability can be expressed as:

$$\delta(\sigma_1, \sigma_2, j) = \frac{\|V(\sigma_1, j) - V(\sigma_2, j)\|_2}{\|j\|_2}, \tag{2.30}$$

where $V(\sigma_i, j)$ is the measured voltages on the boundary resulting from applying the current density j to a body with conductivity distribution σ_i.

Hence, in order for any EIT system to distinguish between two different conductivities σ_1 and σ_2, the distinguishability $\delta(\sigma_1, \sigma_2, j)$ in (2.30) must be larger than the smallest voltage difference the system can detect [102]. In other words, we can say that two conductivities σ_1 and σ_2 are said to be distinguishable by an EIT system within a measurement of precision ε iff there is current density j for which

$$\delta = \delta(\sigma_1, \sigma_2, j) = \frac{\|V(\sigma_1, j) - V(\sigma_2, j)\|_2}{\|j\|_2} > \varepsilon, \tag{2.31}$$

Similarly we say that two conductivities σ_1 and σ_2 are said to be non-distinguishable by an EIT system within a measurement of precision ε iff there is current density j for which

$$\delta = \delta(\sigma_1, \sigma_2, j) = \frac{\|V(\sigma_1, j) - V(\sigma_2, j)\|_2}{\|j\|_2} \leq \varepsilon, \tag{2.32}$$

For any medical EIT system, the choice of applied current patterns determines its distinguishability. Consequently, a current density j is said to be the best pattern for distinguishing two conductivities, σ_1 and σ_2, if it maximises the distinguishability δ of the EIT system [101,103]. Hence, the distinguishability δ as a function of the best current density j can be mathematically expressed by:

$$[\delta(j)]^2 = \sum_{k=1}^{\infty} |d_k|^2 |\langle \frac{j}{\|j\|_2}, \phi_k \rangle_{L^2}|^2, \tag{2.33}$$

where ϕ_k, are the eigenfunction of $V(\sigma_1, j) - V(\sigma_2, j)$ in (2.30), d_k are the corresponding eigenvalues, the notation $\langle f, g \rangle_{L^2}$ is the L^2 inner product of f, g such that $\langle f, g \rangle_{L^2} = \int_{\partial\Omega} fg$, and k is the number of electrodes.

The experimental results in [78] showed that multiple current sources method yielded the best distinguishability for planar electrode arrays for detecting breast cancer, and had higher distinguishability at all distances than both the SCS and the SVS method. According to the author, distinguishability is a reasonable measuring criterion. However, it is not directly linked with the quality of the reconstructed images. Nevertheless, having a distinguishability higher than a noise or error threshold is essential but not particularly sufficient for improving the accuracy of EIT imaging [78].

2.7 Summary

EIT is a practical realisation of an ill-posed mathematical problem governed by the generalised Laplace equation subject to either Neumann or Dirichlet boundary conditions. EIT has important applications in medicine (breast cancer detection, monitoring of brain activities), in geophysics (detection of underground minerals, detection of leaks in underground storage tanks), and in industry (non-destructive testing, detection of defects in metals).

In EIT systems, the current is injected through discrete number of electrodes equally arranged along the boundary of the object. Therefore, it is important to properly model the electrodes and take into account the size of electrodes, contact impedance and the shunting effects of the current at the surface of the electrodes. The injected current patterns in medical EIT systems should take into account the right safety constraints which limits the amount of power dissipated inside the patients body.

An important criterion for measuring the quality of EIT images is called distinguishability. This is the ability of an EIT system to distinguish between two different conductivities. Therefore, the optimal current pattern is the one that maximise this distinguishability.

The next chapter focuses on EIT as a medical imaging modality for detecting breast cancer with results from clinical trials.

Chapter 3

Electrical Impedance Tomography for Diagnosing Breast Cancer

3.1 Introduction

Early detection of breast cancer is an active research area in medical EIT [50]. Breast cancer is the most occurrent types of cancer in women resulting in high mortality in western societies [104]. It is estimated that one woman in eight is likely to develop breast cancer over her lifetime in countries like UK and USA [17]. The medical treatment for women diagnosed with breast cancer is directly affected by the stage at which the cancer is discovered. Chances of long term recovery are greatly increased for women found with small tumours at early stage.

Periodic X-ray mammographies for women over 40 years of age are the classical diagnostic methods used for detecting breast cancer. The technique has been credited with saving lives and discovering many early breast cancers. However, X-ray mammography has some limitations as a mass screening tool. The cumulative exposure to X-rays beyond a reasonable lifetime quota, although minimal in X-ray mammograms, is dangerous and could itself become a health risk [29], particularly to patients who

are requested to have regular examinations at an early age because of family history. Moreover, X-ray mammography cannot distinguish between benign and malignant tumours. This is due to the fact that malignant tumours in the human breast have nearly the same X-ray attenuation coefficient as benign tissues. When an X-ray mammography test shows a suspicious positive finding, patients are required to undergo biopsies (removal of breast tissue for laboratory examination) for definitive diagnosis. According to clinical statistics, biopsies of breast lesions discovered using X-ray mammography screening are found to be negative in more than 80% of patients. Thus, whilst X-ray mammograms have high sensitivity, they still have a rather low specificity [105].

Another major disadvantage of the X-ray mammography is its inefficiency as a periodic screening for breast cancer among young female population [106]. This is due to the fact that, although young women require exposure to radiation, dense breast tissues which is common in young women make X-ray images difficult to interpret. As a result, unlike women over forty, younger women are not referred to breast imaging unless they are identified as being at high risk [107, 108]. This treatment, unfortunately has lead to the fact that 90% of cancer are detected in young women who had not been identified as being at high risk based on known risk factor (e.g family history) [109].

There are other imaging modalities which can be used to detect breast cancer in its earliest stages. These techniques are mainly used for women who are considered to be at high risk of developing the disease. Similar to X-ray mammography, each of these imaging modalities has its own limitations, and therefore none of them is likely to fully replace X-ray mammography screening.

The most common imaging modalities for detecting breast cancer are discussed bel-

low.

Breast Magnetic Resonance Imaging (MRI)

Breast MRI is an imaging modality which produces highly detailed images of the interior of the breast. It helps to diagnose breast cancer at early stages for women who are more likely to develop malignant tumours. Although breast MRI is more sensitive than X-ray mammography, its increased sensitivity makes normal areas of the breast to appear abnormal in some cases, resulting in an increased number of false positive test results. This may lead to unnecessary biopsies and increased anxiety for many women, especially, that MRI examinations can only differentiate breast lesions from malignant ones if appropriate techniques for injecting paramagnetic contrast agents are used to enhance the detection of cancers and other lesion tissues. [110]. Another disadvantage is that breast MRI examination is more expensive compared to X-ray mammography. Whilst private insurance companies are required to cover the full cost of X-ray mammography every one to two years for women over the age of forty, not all insurance companies cover the coast of breast MRI examination even for women at high risk [111]. In the USA for example, the American Cancer Society suggests that breast MRI is not a replacement for X-ray mammography for high risk women, but it could be used instead as a complementary screening tool. As a result, breast MRI is not used frequently for breast cancer screening.

Breast Ultrasound

Ultrasound, also known as sonography, is another imaging modality which uses sound waves to produce images of the interior of the body. Breast ultrasound is used to examine dense breast tissues [112]. During breast examination, a gel is applied on the surface of the breast and a device called a transducer is moved across the

skin to produce an image of the tissue underneath. The transducer transmits sound waves and records echoes as they bounce back off the breast tissues. The echoes are used afterwards by a computer software to reconstruct ultrasound images. Breast ultrasound examination is not painful, and unlike X-ray mammography and breast MRI, it does not expose the patients to radiation [113]. In addition to detecting breast cancer, ultrasounds are also used to guide the biopsy needle in the cases when a suspicious mass is detected [114]. Moreover, ultrasounds are used to examine the lymph nodes located under the arms in women diagnosed with breast cancer.

Although ultrasound is less sensitive than MRI, some studies considered it to be an important adjunct along with X-ray mammography, mainly because it is non-invasive, and it costs less compared to other imaging modalities [115, 116]. These studies also suggest that using ultrasound along with X-ray mammography can be particularly useful when screening women with dense breast tissue [111]. Despite that, similar to breast MRI, ultrasounds can also miss some cancerous tumours which could be detected by X-ray mammography. They may also show non-cancerous regions as suspicious findings which may lead to unnecessary needle biopsy as well.

Nuclear Imaging

Nuclear imaging works by injecting small amounts of radioactive substances into the body which are then traced by special cameras used to image the emitted gamma radiation [117]. Unlike traditional imaging modalities which image changes in the tissue structure caused by tumours, nuclear medicine scans detect changes in tissue metabolism. By using such technique, different types of abnormalities could be detected depending on the injected substance. Positron Emission Tomography (PET) is one of the scanning techniques in nuclear medicine used for breast imaging. PET scan injects radioactive glucose into the bloodstream. Because cancer cells grow rapidly,

they absorb larger amounts of this radioactive sugar than normal cells would. A PET scanner is then used to image areas with different radioactivity levels in the breast. The ability of PET scans to distinguish between malignant and benign tumours in the breast has been considered by different studies but they were found to be limited as well [111]. For example, PET ability to detect breast cancer depends on the size and histology of the tumour. Moreover, the sensitivity of PET found to be relatively low with 68% when detecting small tumours of a size less than 2cm [118, 119]. Although nuclear medicine is proposed for breast cancer diagnoses as it detects the increased metabolic rate and vascularity of breast cancers which are signs of a tumour growth, the technique is still used with fairly modest success as a screening method [120].

Hybrid Systems

In vivo studies showed that the electrical conductivity of the cancerous tissue can be up to four times the conductivity of the normal breast tissues [121,122]. Hence, the electrical property of the cancer makes it detectable by impedance imaging. To make use of this unique feature, a number of hybrid imaging techniques which combine EIT with other imaging methods were investigated by many research groups.

For example, the team of researchers at Rensselaer Polytechnic Institute proposed a way to combine X-ray mammography with simultaneous EIT measurements of the electrical conductivity, through electrodes attached to the X-ray mammography device. This team claims that the technique could enhance the sensitivity and specificity of the detection of the breast cancer. [123,124]. Other examples include magnetic resonance impedance tomography [125–127], EIT by elastic deformation [128], magneto acoustic imaging and impedance-acoustic tomography [129].

3.2 Medical Tests and Diagnostic Accuracy

A medical test can be defined as the procedure performed to detect, diagnose or monitor diseases and their progress, in addition to determine the best treatment. For any test in general, and medical tests in particular, its accuracy and precision quantify how close the measurements of any property (e.g. the electrical conductivity of the breast tissues) are to the property's actual (true) value [130]. They also measure the degree to which repeated measurements under unchanged conditions yield the same results [131].

If a medical test indicates that a disease is present (positive result), but the disease is not in fact present (the result is false), this represents a **false positive** result. In contrast, a **false negative** result is the case when a medical test indicates that a disease is not present (the result is negative), but in fact the disease is present (the result is false). Similarly, the two possible outcomes associated with a correct results are either a **true positive** or a **true negative**. These are also known in medical tests as true positive and true negative diagnoses, respectively [132, 133].

For a medical test, the accuracy is the percentage of true results (both true positive and true negatives) in a population. It can be used as a statistical measure of how well a test correctly identifies or excludes a disease [134] and is expressed mathematically as [135]:

$$\text{accuracy} = \frac{\text{no. of true positives+true negatives}}{\text{no. of true positives+false positives+false negatives+true negatives}} \times 100\%$$

The precision, on the other hand, is defined as the percentage of the true positives against all the positive results (both true positives and false positives) [136]. It is

expressed mathematically as:

$$\text{precision} = \frac{\text{no. of true positives}}{\text{no. of true positives} + \text{false positives}} \times 100\%$$

As explained by [136], a measurement system can be accurate but not precise, or precise but not accurate. For example, increasing the sample size of an experiment might increase the precision, but does not necessary improve the accuracy due to the systematic errors contained in the measurements. Eliminating systematic errors, however, might improve the accuracy but does not change the overall precision.

3.2.1 Sensitivity and Specificity

The accuracy of a measurement system can be also obtained from other two statistical measures, mainly the sensitivity and the specificity [137]. The sensitivity (also called the true positive rate) measures the percentage of actual positives which are correctly detected. In other words, the percentage of sick people who are correctly identified as having the disease. On the other hand, the specificity (also called the true negative rate) measures the proportion of negatives which are correctly identified. In other words, the percentage of healthy people who are correctly identified as not having the disease. A perfect predictor, is said to be 100% sensitive (i.e. identifying all people from the sick group as sick) and 100% specific (i.e. not identifying anyone from the healthy group as sick). However, theoretically any predictor will contain an error bound referred to as the Bayes error (i.e. the lowest possible error rate given classification problem) [138, 139].

Diagnostic tests usually have a trade-off between sensitive and specific measurements.

A good example is the metal-detectors devices used by airport security. For testing potential threats, the airport scanners could be configured to set the alarm on low-risk items like coins or belt buckles. In this case, the scanners have low specificity and would trigger an alarm when any metal is detected (e.g. coins, key chains, etc.). Although these scanners are not specific in determining whether the detected metal is a real threat or not, at the same time, these scanners also have high sensitivity, as the alarm would trigger any time a metal is detected. This simple example illustrates the situation when a scanner can be sensitive enough to detect any suspicious objects, but at the same time, its specificity is low as it cannot differentiate between safe and risk objects.

For a medical test used to detect a disease, the sensitivity of the test is the proportion of patients known to have the disease. In other words, it is the probability of positive results given that the patient is ill. Mathematically, this can be expressed as:

$$\text{sensitivity} = \frac{\text{no. of true positive}}{\text{no. of true positives} + \text{no. of false negatives}} \times 100\%$$

The specificity of a test refers to the test's ability to eliminate a condition (disease) correctly, i.e. the percentage of people known not to have the disease. In other words, it is the probability of a negative result given that the patient is well. Mathematically, this can also be written as:

$$\text{specificity} = \frac{\text{No. of true negatives}}{\text{No. of true negatives} + \text{No. of false positives}} \times 100\%$$

The efficiency of different medical imaging techniques, particularly X-ray mammography has been considered in many studies. For example, according to [140, 141], the overall sensitivity of X-ray mammography is about 78%. This means that X-ray

mammography can miss-detect about 22% of women who truly have breast cancer. According to these studies, the sensitivity can increase to 83% in women over fifty due to less glandular breasts density. In another study [142], Todd *et al* showed that X-ray mammography has low sensitivity of 74%, and specificity of 60% only. According to [90], this low specificity is the reason why nearly 70% - 80% of women who did a biopsy test are found to have benign lesions.

3.3 *In vivo* and *in vitro* Impedance Measurements of Human Breast Tissues

Biological tissues have significant differences in their electrical properties depending on their morphological structure [143–145]. Human tissues consist of aggregation of cells surrounded by fluids. The biological microstructure of the cell consists of three main components: Extra-Cellular Water (ECW), Intra-Cellular Water (ICW) and the cell membrane. Both the intra-cellular and the extra-cellular fluids and electrolytes (i.e. substances in the body fluids which carry electric charges) are resistive, and they are separated by a thin bipolar membrane made of two layers of lipid (fat) acting as a capacitor with ion-channels allowing leaking in and out the cell. The electrical property determined by such a structure is the impedance of the tissue which may also vary with temperature and time [7].

At low frequencies, the current can only flow through the extracellular fluid. In this case, the cell membranes act as parallel capacitors. At higher frequencies, however, current flows through the total tissue fluid and the cell membranes, which behave like serial resistors. Therefore, the electrical impedance, Z, of the human cell structure contains both resistance and capacitance and hence, it is a complex function which

can be presented by the notation [143–145]:

$$Z = R + iX_c,$$

where R is the resistance, X_c is the reactance and $i = \sqrt{-1}$.

The admittance which is the inverse of the impedance is also a complex function which can be expressed by

$$Y = S + i\omega C,$$

where $Y = 1/Z$ is admittance, S is the conductance, C is the capacitance, and ω is the angular frequency of the applied current.

However, it has been shown that if human tissues are removed from their natural environments, the electrical properties of these living tissues will change [146]. Moreover, dead tissues show even greater changes in their dielectric properties. Therefore, in order to asses the electrical properties of living tissues more accurately, *in vivo* measurements need to be made in a relatively short time to avoid any changes to the tissues resulted by any external applied field.

There are two methods for performing *in vivo* impedance measurements of breast tissues: invasive and non-invasive. In the invasive method needle electrodes are inserted through the skin into the tissue under examination and low frequency alternating current is applied through a pair of electrodes, while voltages responses are measured using an additional pair of needle electrodes. In the non-invasive method, EIT is used to make a large number of impedance measurements from electrodes positioned on the surface of the body [7].

The electrical characteristics of living tissues were investigated by different studies.

It has been shown that electrical properties of tissues vary according to the frequency of the applied current [147]. In a study on the dielectric properties of different breast tissues and other biological fluids at a frequency range from 1Hz to 10Ghz [148], it was shown that the permittivity of the biological tissues decreases as current frequency increases. Moreover, it was shown that cancerous tissues exhibit larger permittivity and conductivity than normal tissue. This is due to the fact that cancerous cells have higher fluid and sodium contents than normal cells [149].

The variation in the electrical properties of the tissues has been associated with current dispersions which occur at three different frequency ranges [150], Alpha-dispersion is associated with the electrical conditions of the double layers of the cell membrane and the ionic effect of the surrounding environment around the cell. Mainly it happens at low frequencies in the range between 10Hz - 10kHz [149]. Beta-dispersion, which is also known as structure relaxation, arises mainly from the capacitive short-out of the membrane resistances and appears in the frequency range between 10kHz - 10MHz [148]. Gamma-dispersion exists at higher frequencies and is only associated with water molecules in the tissue [148]. Since all pathological changes of the normal tissues occur in frequency ranges between 10Hz and 10MHz, only Alpha- and Beta-dispersion regions are of interest to medical applications [147]. Hence, most EIT systems use this current frequency range for medical applications. For example, Singh *et al* obtained the permittivity of recently extirpated kidney using *in vitro* measurements in the Alpha-dispersion range [146]. In other studies, the permittivity of both normal breasts and breasts with malignant tumours were obtained using external electrodes for *in vivo* measurement over the same range [151,152]. Another example of permittivity measurements the Alpha- and Beta-dispersion regions was conducted by Kosterich *et al* [153] on newly excised rat femur bone. In this study, it was observed a fall of the permittivity value from 10^4(F/m) at 10Hz to 100

(F/m) at 1Mhz.

Other examples of *in vivo* and *in vitro* impedance measurements of different mammary tissues are presented below and summarised by Table 3.1.

In a study on fifty four patients with breast tumours, just before biopsy, Morimoto *et al* [154, 155] performed invasive *in vivo* impedance measurement of the breast tissue over a frequency range of 0-200 kHz using needle electrodes inserted into the tumour. In this study, two equivalent electric circuits were used to model the tissue, one with parallel capacitors as shown in Figure 3.1(a) and another model with serial resistors and capacitor as shown in Figure 3.1(b).

It was found that the extracellular resistance (Re) and the intracellular resistance (Ri) of breast cancers were significantly higher than those of benign tumours, and that cell membrane capacitance(Cm) of breast cancers was significantly lower than that of benign tumours. The results summarised in Table 3.1 are the computer-calculated values of the three parameters (Re, Ri, and Cm) for four different breast tissues (normal breast tissue, breast cancer, fibroadenom and fatty tissue).The study concluded that "impedance measurements can be used for differential diagnosis of malignant and benign breast tumour".

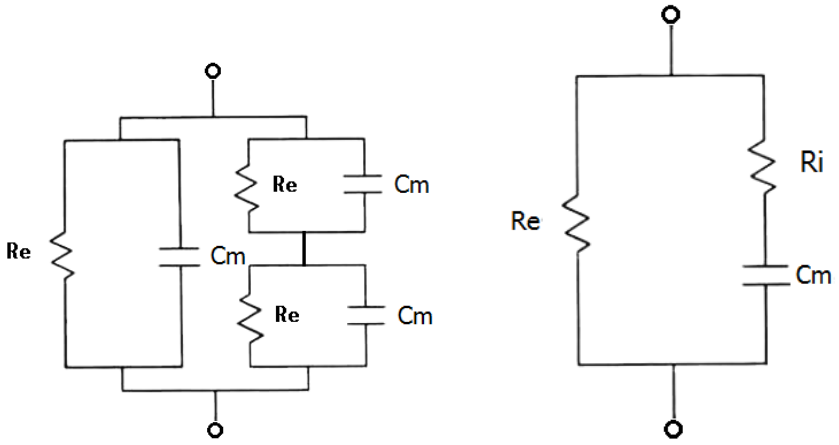

(a) Equivalent electric circuit of breast tissue with parallel capacitors

(b) Equivalent electric circuit with serial resistors.

Figure 3.1: Equivalent electric circuit of the breast tissue [154].

Table 3.1: Electrical parameters of breast diseases [154].

	Three parameters		
Breast Disease	Re (Ω)	Ri (Ω)	Cm (pF)
Breast cancer	1445 ± 586	2493 ± 1490	3525 ± 1879
Fibroadenoma	954 ± 156	1179 ± 446	6171 ± 2536
Normal breast tissue	780 ± 148	1777 ± 1396	6368 ± 2937
Fatty tissue	6044 ± 3388	8622 ± 4210	554 ± 262

In another study by Jossinet [122,150], a collection of 120 impedance measurements of breast tissue were recorded from sixty four patients immediately after breast surgery. The measurements were collected at different frequencies varying from 488Hz - 1 MHz. The impedance readings were arranged into three groups of normal tissues - mammary gland, connective tissue and adipose tissue- and another three groups of pathological tissues - mastopathy (a condition affects the breast tissues in women at the age of childbearing [156]), fibroadenoma (noncancerous tumors composed of fibrous and glandular tissue), and carcinoma. The study showed no significant difference in the electrical properties between normal and benign pathology (mammary gland, mastopathy and fibroadenoma) groups. The third group of carcinoma, however, exhibited a difference from the other two groups mainly by the low resistivity at

frequencies above 125kHz. According to this study, the fact that benign lesions and normal tissue both have the same electrical properties but different from the cancerous tumours is of significant importance that could lead to the ability to distinguish benign lesion from malignant tumours by using EIT [122].

Similar studies [155,157] also showed significant differences in the electrical impedance of benign and malignant breast tumours and concluded that electrical impedance measurements could be used to separate benign from malignant tumours and hence reduce the need for unnecessary needle biopsy.

Although many studies suggest that EIT could be used for breast cancer detection, other studies, however, suggested that the distinction between malignant tumours and benign lesions based on impedance measurements needs further investigation. There are some contradictory results in the literature, for example the study [122] showed that malignant tumours have higher capacitance than benign tumours, while another research [155] demonstrated that malignant tumours have lower capacitance than benign tumours. In [7], Zou explained that these results could be due to a number of factors such as the use of different measurements techniques, or differences in tissues conditions between *in vitro* and *in vivo* measuring methods.

Table 3.2 presents further *in vitro* impedance measurements of human breast tissues from different studies at a range of frequencies between 20kHz - up to 3.2 GHz.

Table 3.2: Different *in vitro* impedance measurements of human breast tissues.

Frequency range	Experimental results
up to 20kHz	A study on a fifty eight patients which included all types of breast tumours. Results show that the capacity of malignant tumours (between 545pF to 2860pF) is consistently larger than that of normal tissues in breast (between 107pF to 583pF) [158].
0.488kHz to 1MHz	The impedance for cancerous tissue is lower than that of adipose subcutaneous fatty tissue or connective tissue. Additionally, it is higher than that of fibroadenoma. No significant difference in impedance between groups of normal tissue and benign pathology (mammary gland, matopathy and fibroadenoma) [122].
0.5kHz to 1MHz	The impedance of malignant tissue is approximately 400 Ω cm at 1 kHz which is lower than that of non-pathogenic surrounding tissue which is nearly 2000 Ω cm [159].
1kHz to 10MHz	At this frequency, the complex conductivity (i.e. admittivity) and the characteristic frequency of the cancerous tissue is the largest. [160].
20kHz to 100MHz	Cancerous tissues show higher conductivity and permittivity compared with surrounding peripheral tissues around the tumour. For the full computed parameters of the breast carcinoma and the surrounding tissues in that range of frequencies, the reader is referred to [36].
3MHz to 3GHz	Results show that the conductivity and permittivity of malignant tissues are higher than those of normal tissues especially for frequencies below 100MHz. The conductivity varies from 1.5mS/cm to 3mS/cm for normal tissues and from 7.5mS/cm to 12mS/cm for the malignant tissues. The permittivity is 10F/m for normal tissues and varies from 50F/m to 400F/m for malignant tissues) [161].
3.2 GHz	At this frequency, there is no significant difference in the conductivity and the permittivity of benign and malignant tumours [162].

3.4 EIT Systems for Breast Cancer in Clinical Trials

Medical EIT Systems, particularly those for detecting breast cancer have been studied and developed by a number of research groups. In the next section, EIT systems developed by different research groups are presented. Later in this chapter, the clinical results of using EIT for detecting breast cancer as stand-alone systems and as adjunct to other medical imaging modalities are discussed.

3.4.1 EIT Systems for Detecting Breast Cancer

T-Scan System also known as TS2000 is the only commercial and FDA (Food and Drug Administration) approved electrical impedance imaging device for adjunctive clinical uses with X-ray mammography. T-Scan is primarily used to reduce uncertain screening results and hence minimise unnecessary biopsies. T-Scan uses a hand-held measuring probe with an array of electrodes arranged on a rectangular grid called surface probe [7, 163]. There are three different probes for breast examination used with the T-Scan: a small one for standard resolution which has an eight by eight electrodes array and a dimension of 32mm by 32mm, a large probe which contains 16 by 16 electrodes array and dimension of 72mm by 72mm and a newer probe which has the same dimensions as the small probe, but with 16 by 16 electrodes array for higher resolution. The distance between the centres of electrodes in the small probe is 4mm, with 1mm spacing between adjacent electrodes.

For examining the breast, the probe is placed on the surface of the skin using a conductive gel. The probe then presses the breast towards the chest-wall [164]. The

T-Scan applies an alternating current between the breast and the patient's arm. A selected AC voltage signal of amplitude from 1V to 2.5V and a frequency range from 100Hz to 100KHz is applied through a cylindrical stainless steel hand-held electrode of 12cm length and 3.4cm diameter [165] and all the other electrodes in the scanning probe are kept at the ground potential. The information about the conductivity distribution inside the breast region beneath the probe is obtained from measurements of the induced current through each electrode in the probe. The admittance data measured at all electrodes in the planar array is presented afterwards as images of the conductivity and permittivity. Any white spots in the reconstructed images are interpreted as possible cancerous lesions inside the examined breast [166].

The first clinical trial on the T-Scan system [167] showed that it cannot detect lesions behind the nipple. This is due to the low impedance of the nipple tissues which appears as a bright white spot. Other major limitations of the T-Scan system are due to interfering bones which also show as bright spots or high conductivity regions and lead to false positive results. Moreover, the maximum measuring distance from the probe is limited to 3-3.5cm in depth, preventing detection of any tumours close to the rib cage. Additionally, the location of suspicious lesions for biopsy cannot be exactly determined. According to the author of [165], TS2000 systems require improvements in both sensitivity and accuracy.

The group at the Institute of Radio-Engineering and Electronics of Russian Academy of Sciences developed a 3D EIT system with planar array of electrodes which can be placed on the surface of the breast under examination [168]. The planar array consists of 256 electrodes for measuring voltages which are arranged over a matrix of a square shape of 12 cm sides. The breast is examined in a similar way as in the T-Scan i.e., the array of electrodes is pressed against the breast in order to flatten the tissue and increase the number of electrodes in contact with the breast. The array

of electrodes is connected to a multiplexer by which the injected current is passed through one electrode in the array. Another multiplexer connects the other electrodes to a unit for measuring potentials. The current flow and potentials are controlled by a computer which determines which electrodes are used to drive the current, and which two adjacent electrodes are used to measure potential differences [169].

The Sussex Electrical Impedance Mammography (EIM) Mk4 System was developed at the University of Sussex. The breast is imaged by inserting it into a 18cm wide cylindrical tank filled with salt water at body temperature [170]. The tank has adjustable depth to fit different breast sizes. In order to minimise the effect of contact impedance, electrodes are placed at the bottom of the tank with no direct contact with the breast. This, however, resulted in another problem caused by air bubbles trapped in the space between the breast and the electrodes. According to Sussex group, this problem was resolved by adding channels which allowed air to escape whilst the breast is pressed towards the bottom of the tank. Breast examination is hence performed with the patient lying in a prone position and one breast placed inside the tank. The base of the tank raises and compresses the breast to maximise sensitivity. For safety requirements, the Mk4 system uses AC current with a maximum amplitude of 1mA. The current frequencies can be chosen from a range between 10kHz to 10MHz. The planar array contains a total of eighty five electrodes arranged in a hexagonal pattern with a distance 1.7cm between adjacent electrodes [170]. Although clinical trials for the Mk4 system took place in 2009 at the John Radcliffe Hospital, Oxford, UK, no results have been released publicly yet [32, 171].

The ACT4 EIT system was the fourth generation of the Adaptive Current Tomography (ACT) system developed by the research group at Rensselaer Polytechnic Institute. The latest EIT System was mainly designed for detecting breast cancer [172]. The ACT4 system uses a frequency range between 3.33kHz up to 1MHz and can also

operate up to seventy two electrodes. Additionally, the system offers the ability to apply current and measure the induced potentials or to fix voltage and measure the current density.

In order to improve the specificity of breast cancer examination, EIT can be combined with X-ray mammography, but it is important that both techniques share the same geometry [173, 174]. Changes in the shape of the breast when it is imaged using EIT and X-ray mammography separately, may result in a difficult and complex mapping between them [174]. Therefore, using the same geometry for EIT and X-ray mammograms would make the analysis of EIT images easier. One way of achieving this is to build special electrodes which allow X-rays to pass through them and place these electrodes on the compressing plates of the mammography unit as illustrated in Figure 3.2. This structure which was firstly introduced in ACT4 system by [172] enables EIT and X-ray mammography data to be taken simultaneously and co-register the images of these two techniques. The arrangement also enables the EIT technique to extend the 2D X-ray mammograms by providing 3D images of the area under examination. As a result, additional information on the location of the tumour can be provided [174]. Detailed information on this topic including a simplified model, a reconstruction algorithm, and the build on the electrodes can be found in [90, 173–175].

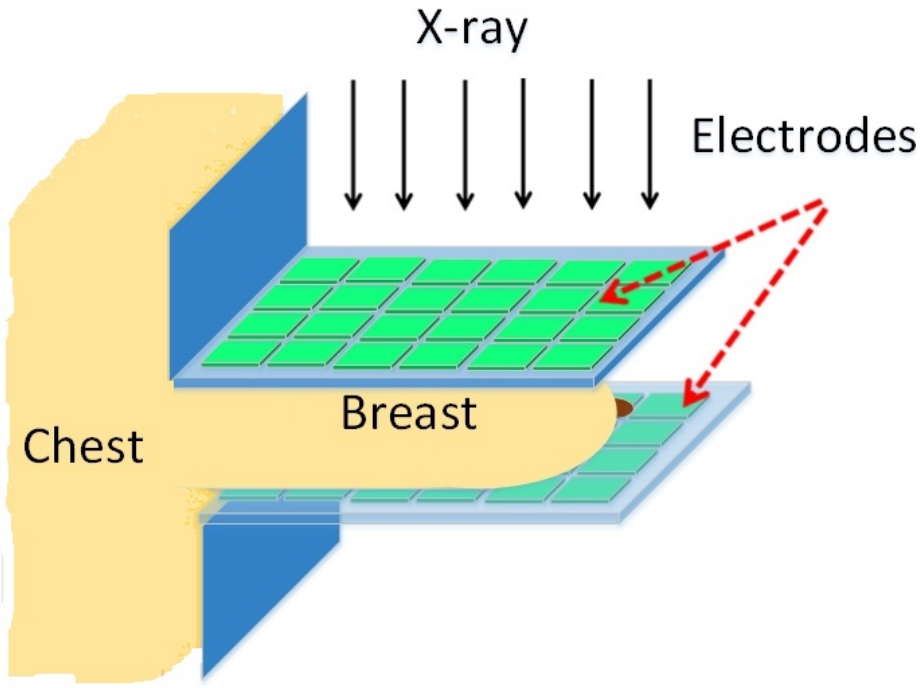

Figure 3.2: X-ray mammography geometry with EIT electrodes.

In the next subsection, the EIT systems developed by the University of Mainz in collaboration with Oxford Brookes University for detecting breast cancer are presented.

3.4.2 EIT Mammograms Developed by the University of Mainz in Collaboration with Oxford Brookes University

The tomographic systems which have been developed by the University of Mainz in collaboration with Oxford Brookes University typically consist of three parts: an electronic device to generate pre-assigned current patterns and to measure the induced potentials, a computer used for data collection and reconstruction of images and a sensing head used for electric measurements [31, 40], see Figure 3.3. For all the designed tomographic versions, the inner electrodes are arranged in a hexagonal

pattern, and all voltage measurements are relative to the system's ground. Moreover, since there are twelve current injecting electrodes, at most eleven linearly independent current can be applied. Further developments in the electronics of the device, however, are planned to allow measurements of electrode-electrode potential differences.

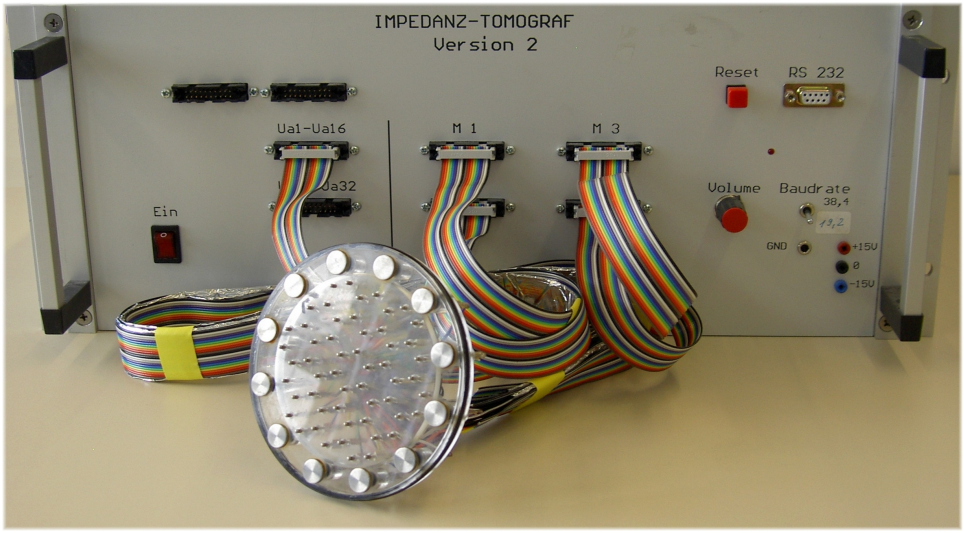

Figure 3.3: The EIT system version 2 developed by Oxford Brookes University in collaboration with University of Mainz [40].

The novelty of these tomographic systems, and hence of the inversion methods, is in the use of two distinct groups of electrodes: active electrodes which are used only for injecting currents and passive electrodes where potential are measured.

In medical EIT systems, electrodes similar to those used by Electrocardiography (ECG) or Electroencephalography (EEG) are placed on the skin with a conducting gel used to improve the skin-electrode contact. When a current is injected, a highly resistive layer is formed at the surface electrode-electrolyte which is due to some electrochemical process inside the gel resulting from converting electron current into ionic current [176]. This conversion takes place at the interface between the metallic surface of the electrode and the ionic gel from one side and the impedance of the stratum corneum layers of the skin. Due to changes in the electrochemical properties

of the gel, changes in sweat ducts during examination, there are large variations in contact impedance of up to 20% or more [89].

Since in EIT, the inverse problem to solve is severely ill-posed and the effect of the uncontrollable contact impedance on the data is sometimes larger than the influence of inhomogeneities which have to be detected, precision is extremely important especially in medical applications where contact impedance uncertainties can result in unknown current densities and potentials under the skin.

In Mainz-Brookes EIT systems, active electrodes through which currents are injected are large to prevent dangerously large current densities at the edges of electrodes. Passive electrodes on the other hand, which are used for measuring potentials are of pin-like design for more measurements precision . If high-impedance voltage measurements are taken, practically no current is driven and the potential on the skin surface underneath each electrode is equal to the potential in the adjacent tissue under the skin. Since no potentials are measured at the active electrodes, the problem of the high and uncontrollable skin-electrode contact impedance is completely eliminated [31, 40]. Moreover, the tomographic devices have a fixed geometry and the coordinates of each electrode are exactly known. Therefore, in addition to overcoming any issues due to the unknown contact impedance, there are no problems related to the boundary shape or the electrode positions.

The earliest sensing head of the mammographs consisted of a planar array of electrodes of circular geometry. There were twelve large outer active electrodes arranged on a ring of radius $R = 44$ mm. This set of electrodes was used to inject external currents. Another set of thirty six inner point-like, high-impedance electrodes were arranged in a hexagonal pattern where the induced potentials were measured, see Figure 3.4.

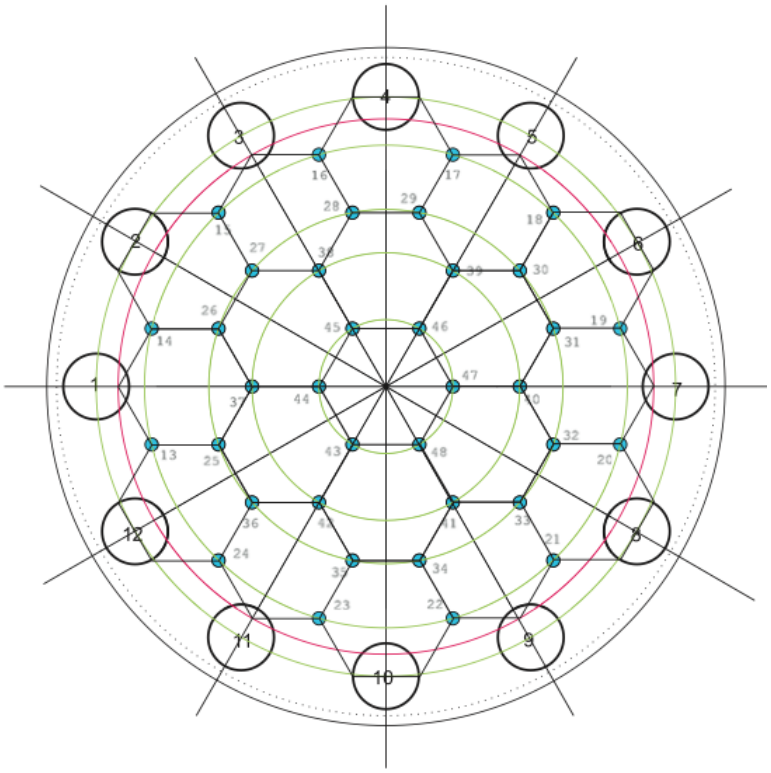

Figure 3.4: The layout of the old sensing head with 12 electrodes for current injection and inner 36 point-like electrodes for potential measurements [177].

A more recent design of the sensing head was similar to the one described above but contained 54 inner voltage measurements electrodes, see Figures 3.5 and 3.6. Two- and three-dimensional reconstruction methods for this design were proposed by [31, 40, 178].

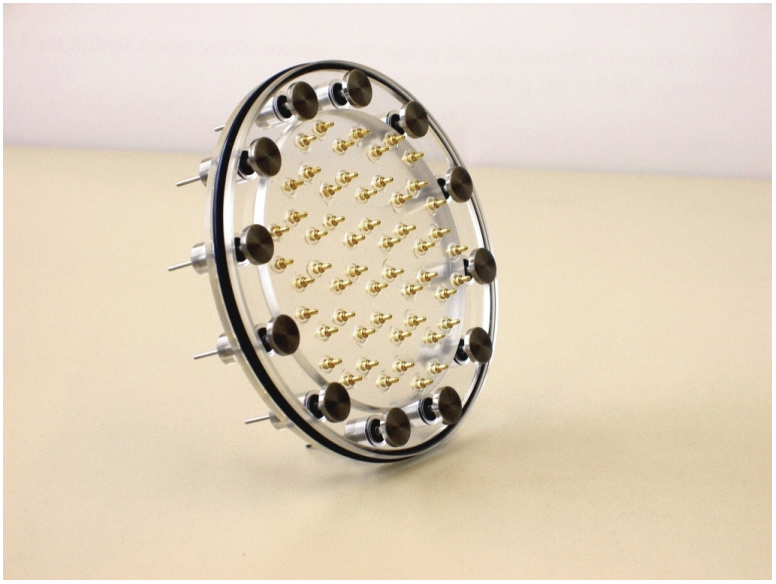

Figure 3.5: The sensing head with twelve large electrodes and fifty four point-like inner-electrodes [40].

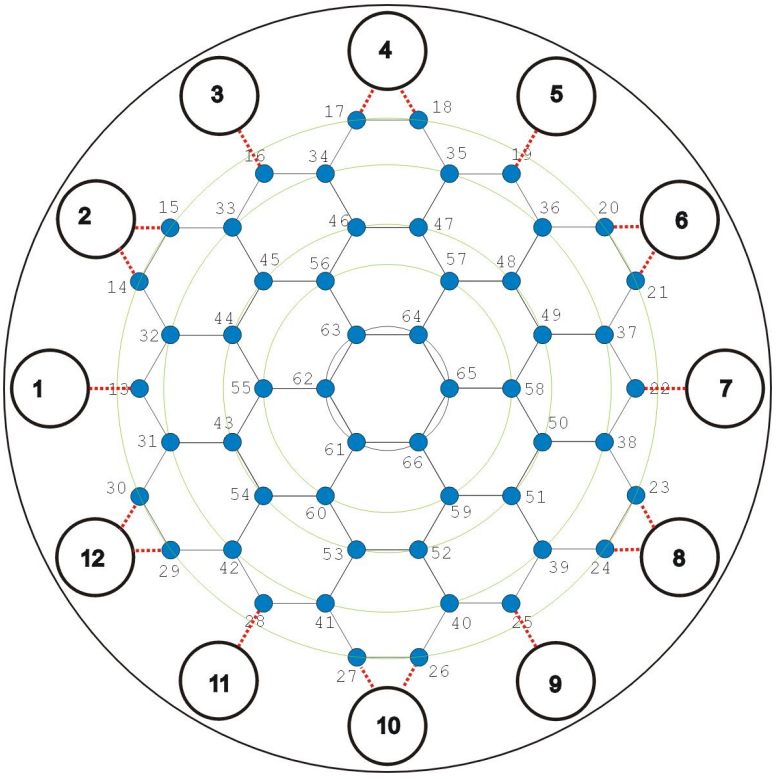

Figure 3.6: The layout of the newer sensing head with twelve outer electrodes for current injection and fifty four point-like inner-electrodes for potential measurements. [40].

3.5 EIT Mammograms in Clinical Trials

As it has been demonstrated by different studies, the conductivity and the permittivity of breast tumours differ significantly from normal or benign tissues. Therefore, EIT is being investigated as a new modality for detecting breast cancer by exploiting these differences as a way to improve the cost-benefits for breast cancer screening, and to identify patients of high risk particularly among younger women [106].

Despite its limitations, many studies used the TS2000 system in clinical trials to asses impedance imaging as a screening method for detecting breast cancer. For example, a study was carried out in seven clinical centres in the USA, Italy and Israel which included 2456 patients, with 882 scheduled for biopsy. The final examinations were conducted on a 504 biopsied breasts with 179 malignant and 325 benign findings [179]. In this study, the TS2000 was used in two different ways: to obtain a stand-alone mammogram, and as an adjunct to X-ray mammography. Results of the clinical trials have revealed that the TS2000 as an adjunct to X-ray mammography improved the specificity of the diagnosis from 39% up to 51%. Additionally, TS2000 also improved the sensitivity of the X-ray mammography from 82% up to 88%. Moreover, the clinical results of examining 273 demographically ambiguous lesions showed that using TS2000 as an adjunct technique increased the examination sensitivity from 41% up to 57% and specificity from 60% up to 82%.

In [106], Alexander *et al* presented a study to evaluate the sensitivity and specificity of electrical impedance measurements in identifying young women who are classified as at high risk of having breast cancer. The clinical trial which was carried out at Walter Reed Army Medical Centre, Washington, DC, USA, was conducted on women aged thirty to forty five years. The aim of the study was to compare both the sensitivity and

the specificity of EIT examination with the conventional clinical breast examination (CBE), i.e. the physical palpation of the breast. The sensitivity test included 189 women prior to scheduled breast biopsy, out of which fifty had verified breast cancer. EIT examination positively identified 19 of them, demonstrating a sensitivity of 38% (19 out of 50). The specificity test included 1361 asymptomatic women visiting the clinic for a routine annual breast examination, out of which sixty seven had positive EIT examination producing a specificity of 95% (1294 out of 1361).

In a different study [167] at the Institute of Diagnostic and Interventional Radiology, Friedrich-Schiller University Jena,Germany, in association with Siemens-Elema, Women's Health and Mobile Generators, Sweden. The purpose of the study was to evaluate the reliability of the electrical impedance scanning (EIS) for differentiating benign from malignant tumours in suspicious lesions, fifty two women with fifty eight mammographically suspicious test results were examined using EIS. All women also underwent biopsy or surgical treatment before the EIT examination. The histopathological test verified twenty nine malignant and twenty nine benign lesions. twenty seven of the twenty nine (sensitivity 93.1 %) malignant lesions were correctly identified using EIS, and nineteen of the twenty nine (specificity 65.5%) benign lesions were identified; ten of twenty nine benign lesions were considered false-positive findings. In total, negative and positive prognostic values of 90.5% and 73.0% were recorded, respectively.

Another clinical examination was also carried out at the Institute of Diagnostic and Interventional Radiology, Friedrich-Schiller University Jena, Germany in association with both the Institute of Diagnostic Radiology, University Zürich, Switzerland and Siemens-Elema Women's Health, Sweden [180]. Using EIS, the study examined 240 women with 280 mammographically suspicious findings. The lesions were all proven histologically as malignant or benign before the EIS examination. The results showed

that 91 out of 113 malignant and 108 out of 167 benign lesions were correctly identified using EIS, resulting in a sensitivity of 80.5% and a specificity of 64.7%.

In a comparative study of different screening modalities for detecting breast cancer [181] (i.e. ultrasound, MRI mammography and EIS), Malich *et al* from the Institute of Diagnostic and Interventional Radiology, Friedrich-Schiller University in Jena, Germany, in collaboration with Siemens Medical Engineering, Special Systems-Women's Health, Sweden, evaluated the accuracy of differentiating benign and malignant lesions to determine if EIS can be used as an adjunct technique for the results obtained by ultrasound examinations or by MRI. In this clinical study, 100 mammographically suspicious lesions were examined by ultrasound, MRI and EIS. With definitive histopathology acquired from either biopsy or surgical operation, the outcomes were as following: fifty out of sixty two malignant lesions were correctly identified using EIS with an overall sensitivity of 81% and twenty four out of thirty eight benign lesions were correctly diagnosed as benign giving a specificity of 63% . Based on these results, the researchers suggested that EIS can be a valuable adjunct for a differentiation of suspicious mammographic lesions. Similar conclusions are also found in [182].

Another study [183] which was carried out at the Center for Early Detection of Breast Cancer (Spanish Association Against Cancer-AECC Madrid), in collaboration with the Service of Pathology, Hospital Nuestra Señora de Sonsoles, and the Department of Morphology, School of Medicine, Autonomous University of Madrid, Spain, also addressed the relationship between the histopathology of breast malignancy (i.e. changes in depth, intensity) and multiplicity, and the capacitance and conductance properties of the tissue. The aim of this study was to examine whether changes in the histopathology of breast malignancy can influence the accuracy of EIS. It was found that EIS had similar rates of false-positive findings compared to X-ray

mammography.

From the results of the clinical trials, Stojadinovic and co-workers in [106], concludes that EIS seems to be a promising technology which provides a relatively high sensitivity for verifying suspicious mammographic lesions. Moreover, EIS can have an important role as a screening technique especially among young women or those of dense breast which require closer attention before they become symptomatic or identified as being at high-risk.

However, according to [180], it is believed that further investigations, especially on the histomorphological characteristics of the cases of false negative and false positive lesions, are still essential in order to acquire more information about bio-dielectric properties of breast tissues .

Recent studies on the other hand, have shown that EIT technology can improve both the sensitivity and the specificity when used as an adjunct method to X-ray mammography and would result in a precise diagnosis [142, 164, 168, 175]. Béqo *et al* [171] also claimed that combining the high resolution images from ultrasound with the parametric data from EIT would increase diagnosis accuracy. Zou *et al* [7], also suggests that because of the low spatial resolution of EIT, combining it with other imaging techniques could improve its applicability in practice.

The role of EIT in hybrid medical imaging techniques was investigated by several studies. For example, during a clinical study, 210 consecutive women with 240 sonographically (using ultrasound) and/or mammographically (using X-ray mammography) suspicious findings were examined using EIS. All lesions were later confirmed histologically. The results published in [8] show that 86 out of 103 malignant and 91 out of 137 benign lesions were correctly identified using EIS (87.8% sensitivity,

66.4% specificity, respectively). By adding EIS to X-ray mammography and ultrasound, the sensitivity improved from 86.4% to 95.1%, whereas the accuracy decreased from 82.3% to 75.7%. A similar study by Fields and colleagues found slightly higher values of sensitivity than this study: 86% sensitivity, 51% specificity, 87% negative predictive value [184] (see Table 3.3).

Table 3.3: Results of EIS as an additional examination [8].

	Mammography/(%) Ultrasound(%)	Adjunctive EIS (%)	Combined methods (%)
Sensitivity	86.4	83.5	95.1
Specificity	78.1	66.4	65.2
Accuracy	82.3	75.0	75.7

3.6 Summary

Several medical technologies are used to diagnose breast cancer. Among those, X-ray mammography is the most widely used and is considered as the standard modality for breast cancer screening in clinical practice nowadays. There are however evidences that improvements are of urgent need.

Current research is aiming at developing alternative imaging techniques to diagnose breast cancer more accurately and possibly earlier. Since *in vivo* studies have shown a difference of three times or more in the specific electrical conductivity between normal and malignant tissues [122, 185], imaging the electrical properties of breast tissues would yield valuable information which can enhance the specificity of the diagnosis. Electric Impedance Mammography (EIM) may therefore be used as an aid to detect breast cancer in its earliest stages of development. Electrical impedance imaging of

the breast cancer is generating interest for several reasons, including comfort to the patient, relatively low cost and relatively high specificity.

The efficiency of electrical impedance tomography as a medical imaging modality for detecting breast cancer was considered in many studies. Several clinical trials have shown that EIT is an effective imaging technique, especially for mammographically dense breasts. In addition to clinical results, many *in vivo* and *in vitro* measurement have also shown significant differences in the electrical bio-impedance properties between normal and malignant breast tissues. According to other studies however, further investigations are still essential.

Next chapter presents a 2D resistor network model with numerical simulations designed for Mainz-Brookes EIT.

Chapter 4

2D Resistor Network Models for a Planar EIT Devices

4.1 Introduction

Conductivity reconstruction using resistor networks methods from boundary measurements, as well as the design of optimal grids attracted researchers' interest during recent years, especially due to their possible implementations in EIT as simple non-iterative and iterative methods [41, 100, 186, 187]. The problem in this case is to find the conductances of resistor network links when measurements are limited to boundary nodes only [188].

The concept of discrete resistor networks arise naturally in the context of EIT [189]. One can think of the human body as an electrical conductive object made of discretised resistive networks. Unlike classical methods which use finite element iterative methods to update the reconstructed image repeatedly by reducing the difference between the measured and simulated values of boundary potentials, the resistor network approaches are simpler and have lower computational costs which is why this technique is sometimes preferred to solve the inverse conductivity problem [190].

4.2 Discrete Resistor Network Model for the Mainz-Brookes Tomographs

For all Mainz-Brookes tomographs, the sensing head contains S active electrodes for injecting currents placed at equal distances on a circle of radius 4.4cm and a number of passive electrodes inside this circle. The positions of the outer electrodes are given by the polar angle $\theta_s = 2\pi s/S$, $s = 1, \ldots, S$. The measurement area can, therefore, be modelled as a network of given resistance patterns depending on the arrangement of the passive electrodes. Let I_s, $s = 1, \ldots, S$, be the injected currents. We define potentials on knots, and currents and resistances on links. The knots (including the outer electrodes) are denoted by an index $k = 0, 1, \ldots, K$ and the potential at the knot k by Φ_k. The knot $k = 0$ is related to the reference potential Φ_0 (ground). Hence, one extra link is added, connecting the first knot of the network to a virtual knot at which the reference potential Φ_0 is fixed. The currents flowing from knot k to knot l are $I_{\{k,l\}}$ and the corresponding resistances $R_{\{k,l\}}$; they satisfy the relations $I_{\{k,l\}} = -I_{\{l,k\}}$ and $R_{\{k,l\}} = R_{\{l,k\}} > 0$, $I_{\{0,1\}} = 0$. If $\Phi_k > \Phi_l$ then $I_{\{k,l\}}$ is positive. We introduce a compound index n to denote the links by

$$n = n(\{k, l\}) = 1, \ldots, N\,, \quad k > l$$

where N is the total number of links.

To find the governing equations of the resistor network we follow the steps below:

1. We apply Kirchhoff's current law at each of the K knots:

$$c_k = \sum_{neighbours\ l} I_{n(\{k,l\})}, \quad k = 1, \ldots, K\,. \tag{4.1}$$

For the outer electrodes, c_k are the external applied currents, $c_k = I_s$ $(k = s = 1, \ldots, S)$; they are ingoing when $c_k \geq 0$. For inner knots, $c_k = 0$.

2. We then apply Ohm's law to all links $n(\{k,l\})$:

$$\Phi_k - \Phi_l = R_{n(\{k,l\})} I_{n(\{k,l\})}. \tag{4.2}$$

3. Finally, we can substitute Ohm's law into Kirchhoff's law to obtain:

$$\sum_{neighbours\ l} (\Phi_k - \Phi_l) S_{n(\{k,l\})} = c_k. \tag{4.3}$$

where $S_{n(\{k,l\})} = \frac{1}{R_{n(\{k,l\})}}$is the conductivity of $n(\{k,l\})$ link

4.2.1 The Forward Problem

The forward problem for the considered resistor network can be formulated as follows: for given known resistances $R_{n(\{k,l\})}$, $n = 1, \ldots, N$, and given external currents I_s, $s = 1, \ldots, S$, we can uniquely determine the potential Φ_k at any knot $k = 1, \ldots, K$, and the internal currents $I_{n(\{k,l\})}$, $n = 1, \ldots, N$, by solving simultaneously equations (4.1)-(4.2). This reduces to solving the following linear system of equations:

$$\mathfrak{K} X = Y\,, \tag{4.4}$$

where the vectors

$$X = (0, I_1, \ldots, I_S, \Phi_1, \ldots, \Phi_K) \quad \text{and} \quad Y = (\Phi_0, 0, \ldots, 0, c_1, \ldots, c_K)$$

are $(1+S+K)$-dimensional, while the $(1+S+K)\times(1+S+K)$ coefficient matrix $\mathfrak{K}$, usually called the Kirchhoff matrix, has the following structure

$$\mathfrak{R} = \begin{pmatrix} R & P^T \\ P & 0 \end{pmatrix} ,$$

where R is the $(1+S)$-dimensional diagonal matrix of the resistances assigned to the outermost links,

$$R = \mathrm{diag}(0, R_1, \ldots, R_S) \tag{4.5}$$

and P is the $(1+S)\times K$-dimensional incidence matrix with

$$P_{k,n} = \begin{cases} +1 & n = n(\{k,l\})(\{k<l\}) \\ -1 & n = n(\{k,l\})(\{k>l\}) \end{cases} , l \in \text{neighbour of knot } k, \tag{4.6}$$

$$P_{k,n} = 0 \quad \text{otherwise}$$

$P_{k1} = 0$ except for the index k which is connected to the external reference potential, where $P_{11} = 1$.
The forward problem is then solved by inverting the matrix $\mathfrak{K}$:

$$X = \mathfrak{K}^{-1} Y \, . \tag{4.7}$$

4.2.2 The Inverse Problem

As mentioned previously, in order to avoid any problems related to the unknown contact impedances, potentials are not measured at the active electrodes. Therefore,

the corresponding inverse problem associated to the considered resistor network can be formulated as follows: for given applied external currents I_s, $s = 1, \ldots, S$, and corresponding potentials Φ_k measured at the inner knots $k = S+1, \ldots, K$, determine the resistances $R_{n(\{k,l\})}$ (or conductances $S_{n(\{k,l\})}$) of the reduced network (see Figure 4.1(b)).

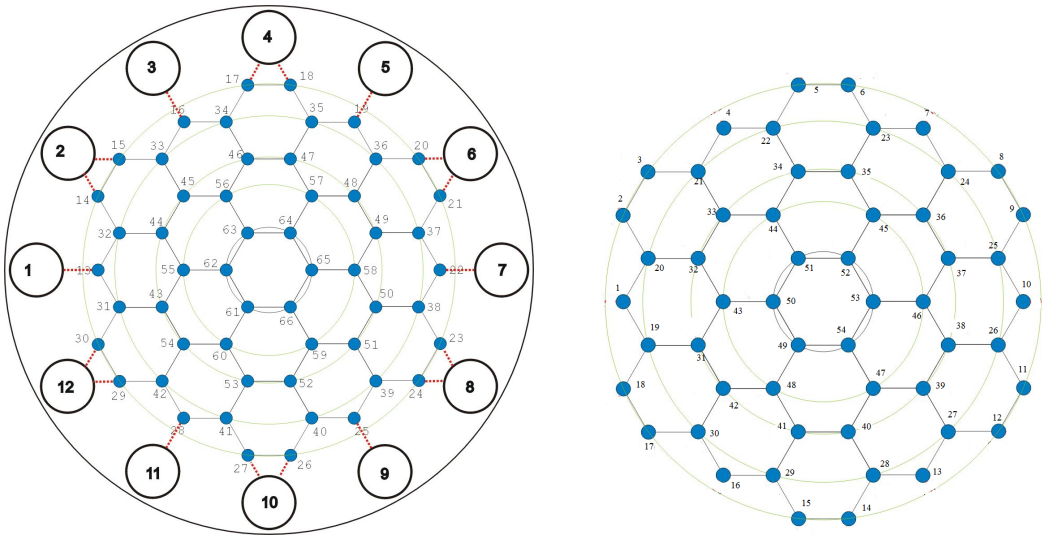

(a) Full resistor network (b) Reduced resistor network

Figure 4.1: Equivalent resistor network models for the sensing heads of one of the EIT prototypes developed at the University of Mainz in collaboration with Oxford Brookes University

Let K_r be the number of inner electrodes and N_r be the number of links in the reduced network. For simplicity, we relabel the inner knots $k = S+1, \ldots, K$ by $\mathfrak{k} = 1, \ldots, K_r$, and the links of the reduced stamp by $\mathfrak{n} = 1, , \ldots, N_r$. To solve the inverse problem, we express equation (4.3) under the matrix form as follows:

$$\begin{pmatrix} U_{1,1} & U_{1,2} & \cdots & U_{1,N_r} \\ U_{2,1} & U_{2,2} & \cdots & U_{2,N_r} \\ \vdots & \vdots & \ddots & \vdots \\ U_{K_r,1} & U_{K_r,2} & \cdots & U_{K_r,N_r} \end{pmatrix} \times \begin{pmatrix} S_1 \\ S_2 \\ \vdots \\ S_{N_r} \end{pmatrix} = \begin{pmatrix} c_1 \\ c_2 \\ \vdots \\ c_{K_r} \end{pmatrix}, \tag{4.8}$$

or, equivalently,

$$US = C\,. \tag{4.9}$$

The coefficient matrix U is a $K_r \times N_r$-dimensional matrix of potential differences $U_{i,n}$ defined as

$$U_{i,\mathfrak{n}} = \begin{cases} \Phi_i - \Phi_{\mathfrak{k}} & \text{with} \quad \mathfrak{n} = \mathfrak{n}(\{i, \mathfrak{k}\}) \quad \text{and} \quad \mathfrak{k} \quad \text{is a neighbour of} \quad i\,, \\ 0 & \text{otherwise}\,, \end{cases} \tag{4.10}$$

$S = (S_1, \ldots, S_{N_r})$ is an N_r-dimensional vector of unknown conductances, and $C = (c_1, \ldots, c_{K_r})$ is the vector of currents entering the reduced network. The system of linear equations (4.9) is undetermined in general since $K_r < N_r$. Therefore, in order to obtain a unique solution, information from repeated measurements with different patterns (α) of injected current has to be added.

In general, for any EIT system with S active electrodes, only $S - 1$ linearly independent trigonometric current patterns of spatial varying frequency type can be applied. The higher the spatial frequency of the current pattern, the less it penetrates inside the object. However, for Mainz-Brookes, only ten standard trigonometric current patterns are applied at the outer electrodes, i.e.

$$I^{(\alpha)}(\theta_s) = \begin{cases} I_0^{(\alpha)} \cos(\alpha\theta_s) & \alpha = 1, \ldots, 5\,, \\ I_0^{(\alpha)} \sin((\alpha - 5)\theta_s) & \alpha = 6, \ldots, 10\,, \end{cases} \tag{4.11}$$

where $\theta_s = 2\pi s/S$ is the angular position of the s-th outer electrode and $I_0^{(\alpha)}$ denotes

the amplitude of the applied current. Consequently, the resulting system of equations

$$\begin{pmatrix} U^{(1)} \\ U^{(2)} \\ \vdots \\ U^{(10)} \end{pmatrix} S = \begin{pmatrix} C^{(1)} \\ C^{(2)} \\ \vdots \\ C^{(10)} \end{pmatrix} \tag{4.12}$$

will be overdetermined if $10 \times K_r > N_r$. $U^{(\alpha)}$ and $C^{(\alpha)}$ correspond to the applied current pattern $I^{(\alpha)}$.

4.2.3 Different Stamps

There are two planar sensing heads of circular geometry designed for Mainz-Brookes Tomograph: an old prototype which has twelve large outer electrodes ($S = 12$) where the external currents are injected, and a set of thirty six point-like high-impedance inner electrodes where the induced potentials are measured ($K_r = 36$). The design of the resistor network is such that it requires the current to split-up into two at each of the outer electrodes. Therefore, additional information needs to be provided to the reconstruction algorithm, i.e. the split-up ratios of the injected current at each outer electrode. Hence, the equivalent resistor network model used for the two-dimensional reconstruction consists of twenty four injected currents ($S_r = 24$) in addition to the thirty six inner electrodes ($K_r = 36$) as shown in Figure 4.2).

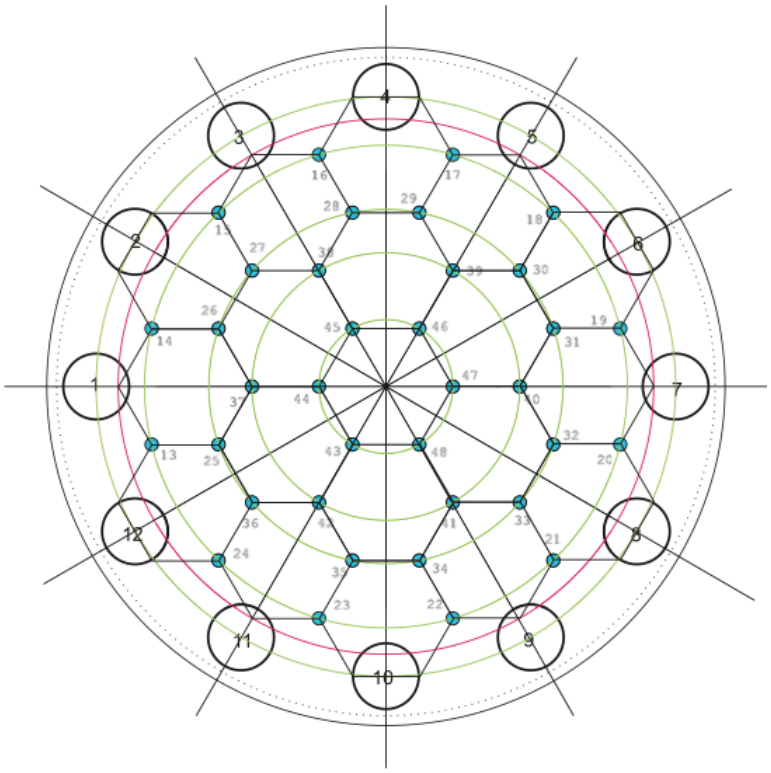

Figure 4.2: The geometry of the old sensing head with twelve outer electrodes ($S = 12$) for current injection splitting into twenty four currents ($S_r = 24$), and thirty six inner point-like electrodes for potential measurements ($K_r = 36$) [177].

For the later sensing head shown in Figure 4.3, there are also twelve large outer electrodes ($S = 12$) where the external currents are injected, and a set of fifty four point-like high-impedance inner electrodes where the induced potentials are measured ($K_r = 54$). For this prototype, the resistor network proposed requires the current to split-up into two components at only six of the twelve current injectors, i.e. at those electrodes which do not lie directly next to the neighbouring inner voltage electrodes. Similarly, for this sensing head, additional information about the eighteen ($= 6 \times 1 + 2 \times 6$) split-up ratios of the injected currents is also required. The equivalent resistor model for this sensing head which is used by the two-dimensional reconstruction algorithm consists of eighteen injected currents ($S_r = 18$) and fifty four inner electrodes ($K_r = 54$).

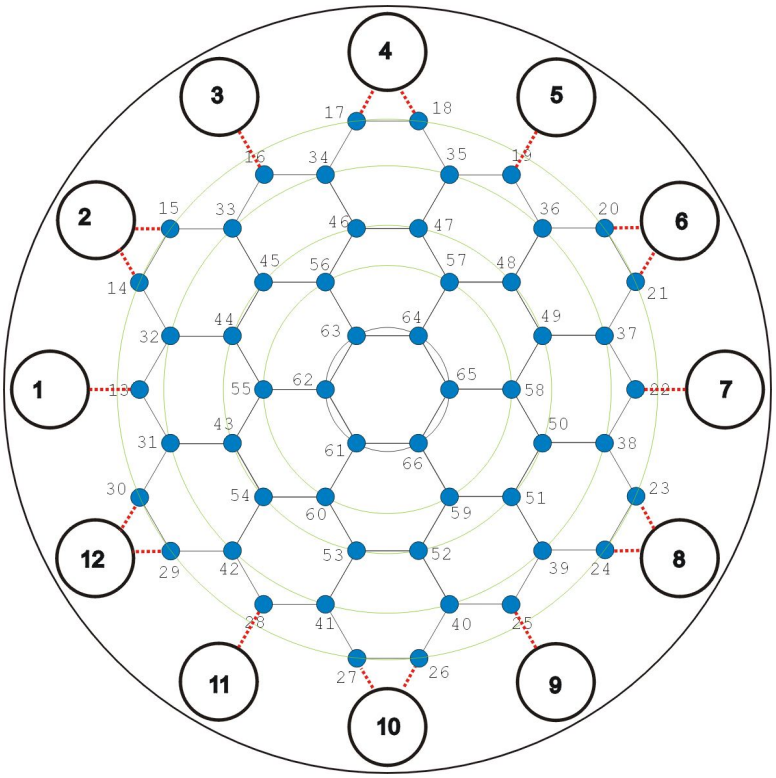

Figure 4.3: The geometry of the later sensing head with twelve outer electrodes for current injection ($S = 12$), eighteen split-ups ($S_r = 18$) and fifty four point-like inner electrodes for potential measurements ($K_r = 54$) [40].

This research investigated two possible ways to modify the later sensing head shown in Figure 4.3 to make the design optimal for breast cancer detection. The first modification was to increase the number of electrodes for injecting currents from twelve to eighteen as depicted in Figure 4.4. The significance of this fundamental modification is in the fact that in the equivalent resistor network for this modified design there are no current split-up at the outer electrodes. This means that no additional assumptions are required by the reconstruction algorithm and, hence, modelling errors from computing the split-up ratio are totally eliminated. In this prototype, the number of inner electrodes remained unchanged (i.e. 54), hence the equivalent resistor network consists of eighteen outer electrodes $S = 18$ and the same number of injected currents $S_r = 18$. The total number of links which corresponds to the number of unknowns in

the forward problem is $N = 90$.

Experimental results from testing the sensing head with eighteen outer electrodes compared to the original design with only twelve electrodes have shown a significant improvement in the sensitivity of the device. The numerical reconstructions and error analysis of this experiment can be found in Section 4.3.2. Table 4.1 summarises the quality of reconstructions for different layouts of the sensing head with different error level (e.g for $\epsilon = 0\%, 2\%, 5\%$) compared to the original design(12/54).

The second modification which was investigated in this research was to increase the number of electrodes for measuring potentials in the sensing head shown in Figure 4.4(b), from fifty four up to seventy three by adding another nineteen electrodes at the centre of each hexagon as depicted in Figure 4.5.

For this new geometry, two resistor network models were considered for the recon-

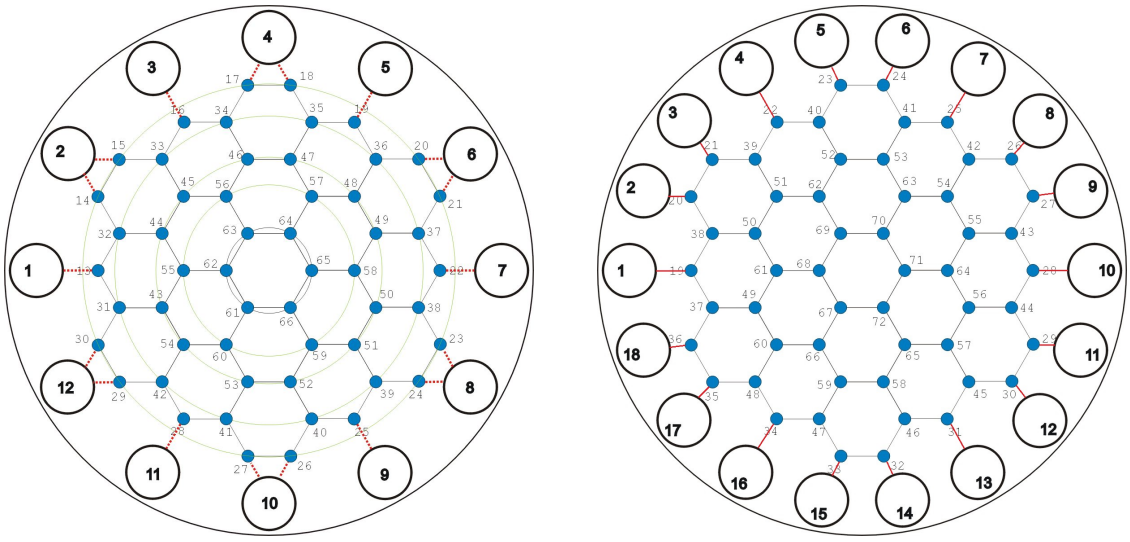

(a) Original design with 12 current injecting electrodes and 54 electrodes for measuring potentials

(b) Modified design with 18 injecting electrodes and 54 electrodes for measuring potentials

Figure 4.4: Modification of the design of the sensing head by increasing the number of current injecting electrodes to 18

Table 4.1: Summary of numerical reconstructions of different sensing head layouts.

Layout		Figures	Qualitative Improvement	Remarks
Name	# Electrodes			
Modified	18/54	4.10	+	Improved both spatial resolution and sensitivity (1 inclusion)
		4.12	+	(2 inclusions)
		4.14	+	(3 inclusions)
Rhombic	18/73	4.15a	-	both spatial resolution and sensitivity decayed (1 inclusion)
		4.15c	-	(2 inclusions)
		4.15e	-	(3 inclusions)
Triangular	18/73	4.15b	-	both spatial resolution and sensitivity severely decayed (1 inclusion)
		4.15d	-	(2 inclusions)
		4.15e	-	(3 inclusions)

struction algorithm: the first one which is shown in Figure 4.6 is a resistor network of triangular pattern, created by linking each of the new electrodes with its six neighbours. In this arrangement, the equivalent resistor network consists of eighteen injected currents $S_r = 18$ and seventy three inner point-like electrodes for potential measurements $K_r = 73$.

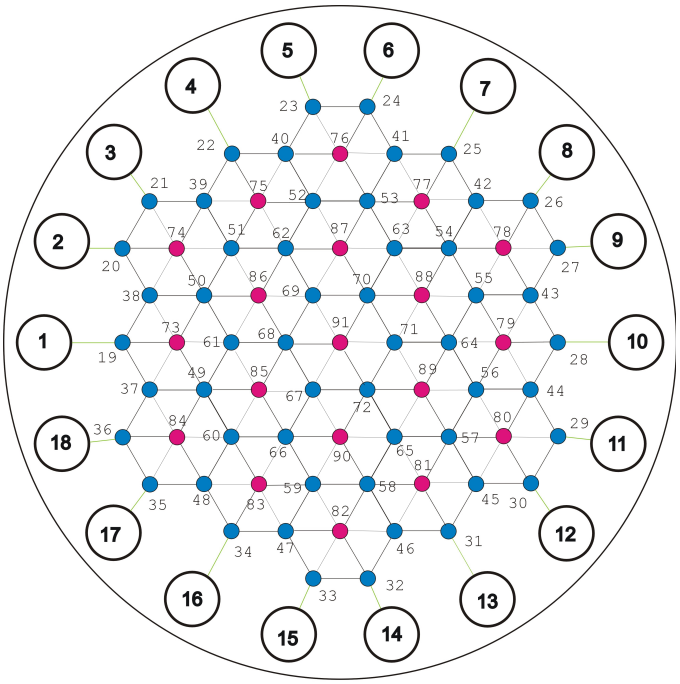

Figure 4.6: The equivalent resistor network of triangular pattern with 18 outer electrodes and 73 inner point-like electrodes for potential measurements.

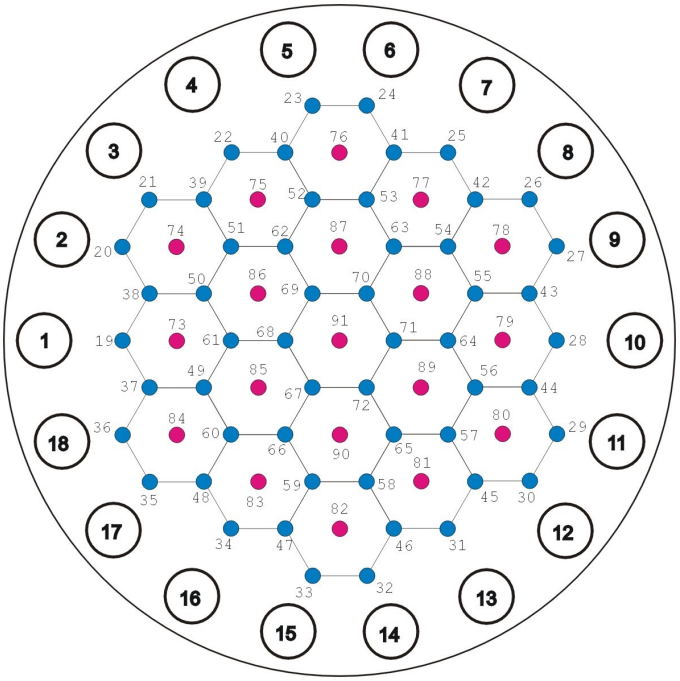

Figure 4.5: Suggested modification of the design of the sensing head with additional nineteen passive electrodes (marked in red) added at the centre of each hexagon.

The second network model for the new geometry has a rhombic pattern. In this network, each of new electrodes was linked to only three neighbours as shown in Figure 4.7. In the equivalent resistor network which is used by the reconstruction algorithm, the number of inner knots is the same as the networks with triangular pattern, i.e. $K_r = 73$. Moreover, both network models have the same number of outer electrodes $S = 18$, and number of injected currents $S_r = 18$. However, the total links in the triangular pattern which corresponds to number of unknowns in the forward problem is $N = 204$, whilst in the rhombic pattern, the number of links is $N = 147$.

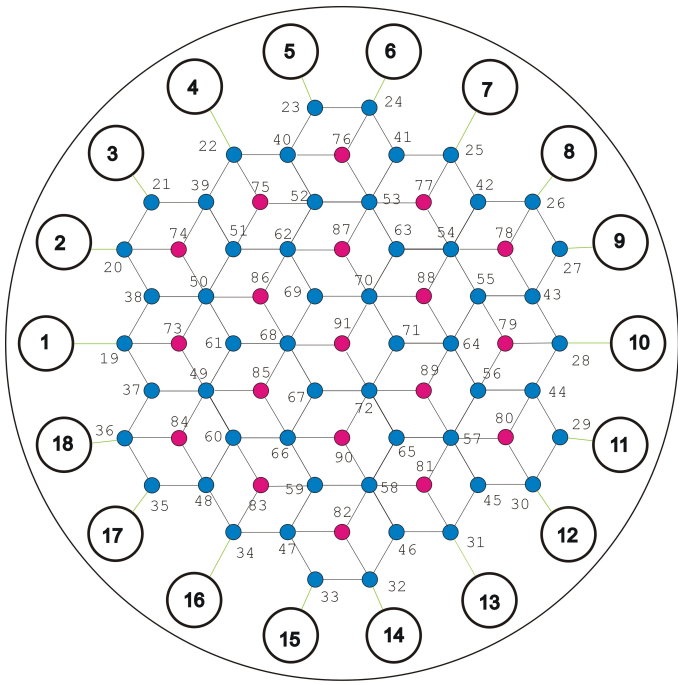

Figure 4.7: The equivalent resistor network of rhombic pattern with 18 outer electrodes and 73 inner point-like electrodes for potential measurements.

The experimental results of testing the rhombic and the triangular networks have shown that the inversion problem in both cases was severely unstable due to accumulative errors. Numerical reconstructions for both is found in Section 4.3.2

4.2.4 Reconstruction Algorithm

To simulate data, the forward problem is solved for a given (known) conductivity distribution either by using the PDE or EIDORS with Matlab (see Subsection 4.3.3). To this end, the geometry of the model needs to be determined first. Next, the Neumann boundary condition is applied which, in this case, corresponds to injecting ten standard varying-frequency input currents. Finally, the model is discretised by a refined triangular mesh across the geometry and simulated potential values are generated by solving the problem numerically at each of the verticies of the triangles.

For all the tomographs, the following step-by-step procedure was implemented in Matlab in an optimised reconstruction algorithm which was developed from scratch during my PhD research.

1. The forward problem for a constant conductivity distribution (e.g. σ_0=1) and the ten standard varying-frequency input currents (4.11) is first solved using the resistor network approach. If needed, the split-up ratios of the currents at the outer electrodes are calculated and stored for later use in the reconstruction.

2. For each of the ten standard varying-frequency input currents (4.11), the estimated split-up ratios (if needed) of currents at the outer electrodes for the constant resistance distribution are then used to calculate the (S_r) currents entering the reduced resistor network.

3. The values of the currents obtained in step (3), together with the simulated values of the potential at the inner electrodes which were obtained in step (2) are used as data to solve the inverse problem for the equivalent resistor network of the sensing head.

To demonstrate the step-by-step procedure above, an academic example including a two-dimensional reconstruction algorithm for a twelve by twelve resistor network simulating a sensing head is included in appendix A.1 with the Matlab code.

4.2.5 Relation Between Discrete Models and Continuum Models

The reconstruction algorithms based on discrete resistor network models, determine the quantities $S_{n(\{k,l\})}$ assigned to the links $n = n(\{k, l\})$. These model the total conductance originating from the areas lying left and right of the corresponding links.

In all our models, the area assigned to a link consists of two isosceles triangles of base ℓ (i.e. the length of the link) and vertex angle β (i.e. $\beta = \pi/3$ for the hexagonal pattern, $\beta = \pi/2$ for the rhombic model and $\beta = 2\pi/3$ for the triangular one). The height of the isosceles triangle (see Figure 4.8) is, therefore, $h = \frac{\ell}{2}\cot(\frac{\beta}{2})$.

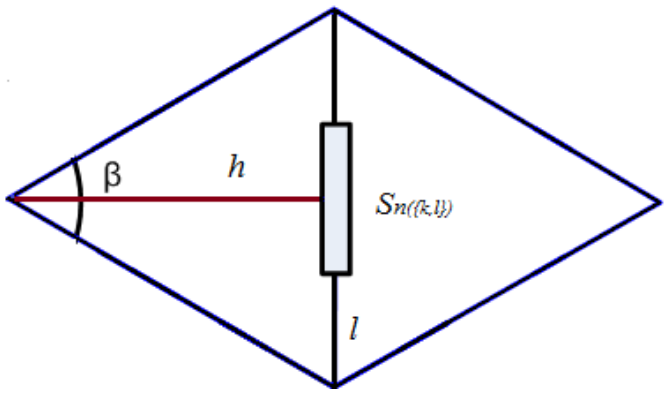

Figure 4.8: Relation between discrete and continuum models

Let $\sigma(x)$ be the conductivity of the area assigned to the link $n(k, l)$ and x be the

centre coordinate of this link. The current density $j(x)$ can be expressed as

$$j(x) = \sigma(x)E(x) = \sigma(x)\frac{I_{n(k,l)}R_{n(k,l)}}{\ell}\,, \tag{4.13}$$

where $E = \frac{I_{n(k,l)}R_{n(k,l)}}{\ell}$ is the electric electric field. By using the identities $j = \frac{I}{2h}$ and $S = \frac{1}{R}$, equation (4.13) yields the relationship between conductivity and conductance

$$S_{n(k,l)} = \frac{2h}{\ell}\sigma(x) = \cot(\frac{\beta}{2})\sigma(x)\,. \tag{4.14}$$

Finally, since estimating the values of the conductivity at any point elsewhere inside the measuring area uses the Matlab griddata interpolation method, therefore, the quality of the reconstructions and hence the spatial resolution of the images depend both on the number of discretisation points and on the accuracy of the Matlab interpolation routine which are used.

4.3 Numerical Experiments and Results

In this section I present numerical reconstructions obtained from using real data collected by the group at the University of Mainz and from simulated numerical data generated at Brookes University. Four sets of numerical reconstructions are included in this section:

- The first one is for testing the modified sensing head when the number of active electrodes is increased from twelve to eighteen.
- The second set is for this latter sensing head when the number of passive elec-

trodes is increased from fifty four to seventy three.

- The third set of reconstructions are obtained from real data collected by the EIT group at Mainz University.

- The fourth set of numerical reconstructions are obtained from simulated numerical data using a three-dimensional EIT model developed in EIDORS.

4.3.1 Reconstructions of 2D Conductivity Distribution Obtained from Simulated Data for Different Designs of Sensing Heads

The first set of numerical tests is used to examine the sensitivity and the spatial resolution of the modified design of the sensing head with eighteen electrodes for injecting current, compared to the original design with only twelve active electrodes. In this experiment both sensing heads were used to reconstruct known two-dimensional conductivity distributions using the two-dimensional resistor network reconstruction algorithm described in Subsection 4.2.4. The reconstructions are followed by an error analysis to compare the sensitivity of both sensing heads. For mammography, only regions of high conductivity are of interest. However, for this experiment, both low and high target continuous conductivities were chosen within a constant background. The chosen target distributions of conductivity can be described mathematically by the following equation:

$$\sigma_n(x, y) = 1.0 + \sum_{i=1}^{n} \delta\sigma_i \exp(-(d_i/\omega_i)^4), \tag{4.15}$$

where

$$d_i = \sqrt{(x - x_{0i})^2 + (y - y_{0i})^2},$$

and

$$\begin{array}{llll} \delta\sigma_1 = 2 & \omega_1 = 5 \text{ mm} & x_{01} = -10 \text{ mm} & y_{01} = -10 \text{ mm}, \\ \delta\sigma_2 = 1 & \omega_2 = 6 \text{ mm} & x_{02} = 10 \text{ mm} & y_{02} = 18 \text{ mm}, \\ \delta\sigma_3 = -0.5 & \omega_3 = 7 \text{ mm} & x_{03} = 22 \text{ mm} & y_{03} = -18 \text{ mm}. \end{array}$$

In equation (4.15) ω_i is a measure of the width of the conductivity distribution, $\delta\sigma_i$ are the magnitudes of target conductivities above or below the background conductivity and x_i and y_i are the coordinates of their centres. The origin of the system of axes is at the centre of the sensing head and $i, n = 1, 2, 3$. The L^2-error presented later in Tables 4.2-4.4 were evaluated numerically as follows:

$$\|\sigma_{rec} - \sigma_i\|_{L^2}^2 = \int_0^R dr\, r \int_0^{2\pi} d\theta (\sigma_{rec}(r,\theta) - \sigma_i(r,\theta))^2 \approx \sum_{k=1}^{172} (\sigma_{rec}(r_k,\theta_k) - \sigma_i(r_k,\theta_k))^2 w_k. \tag{4.16}$$

In EIT a noise level of 1% is acceptable in many situations, even though in many medical applications a better accuracy can be obtained [191]. However, in order to test the robustness of the inversion method, different noise levels ε (i.e. 0%, 2%, and 5%) were applied to both the injected currents and potentials.

For the target two-dimensional conductivity distribution shown in Figure 4.9, the computed errors of the reconstructed conductivity from simulated data with noise levels 0%, 2%, and 5% show that the error produced when using the modified sensing head is significantly less than that when using the original design, i.e. the sensitivity of the modified sensing head is better than that of the old one, see Table 4.2. The numerical reconstructions of this target conductivity distribution are shown in Figure 4.10.

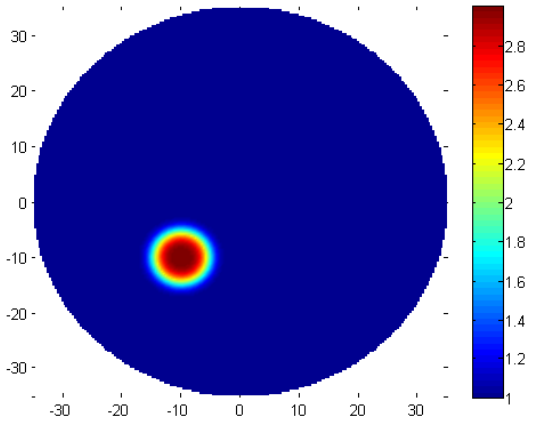

Figure 4.9: Target(exact) conductivity distribution σ_1.

Noise level ε	Original Stamp	Modified Stamp
0%	1.24	0.56
2%	1.26	0.56
5%	1.30	0.63

Table 4.2: The $\|\sigma_{rec} - \sigma_1\|_2$ values in the reconstruction of target conductivity distribution σ_1 for noise levels ε 0%, 2% and 5% by using both the old and the modified design of sensing head.

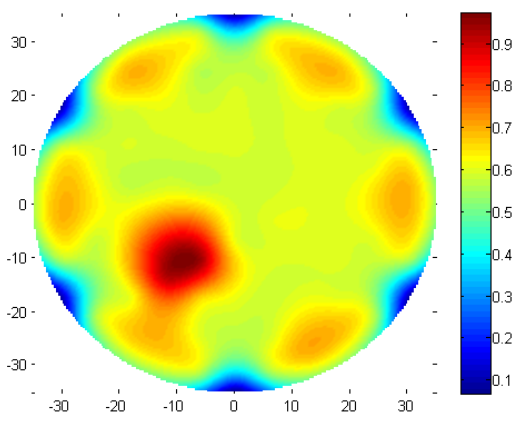

(a) with 0% noise level

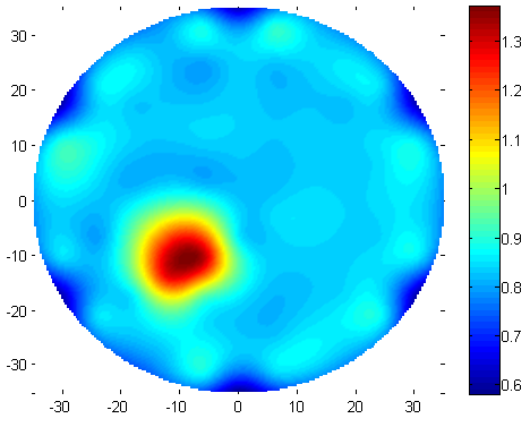

(b) with 0% noise level

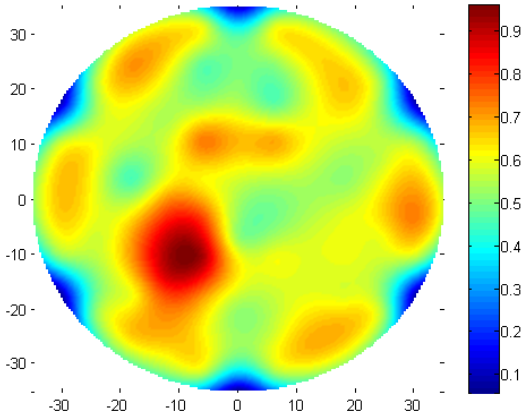

(c) with 2% noise level

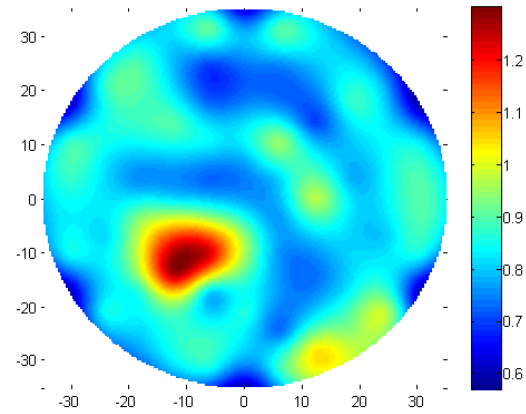

(d) with 2% noise level

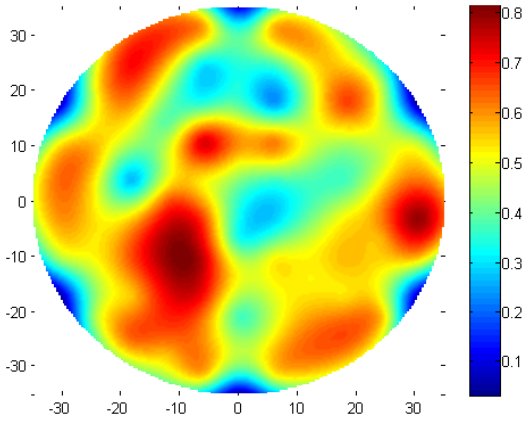

(e) with 5% noise level

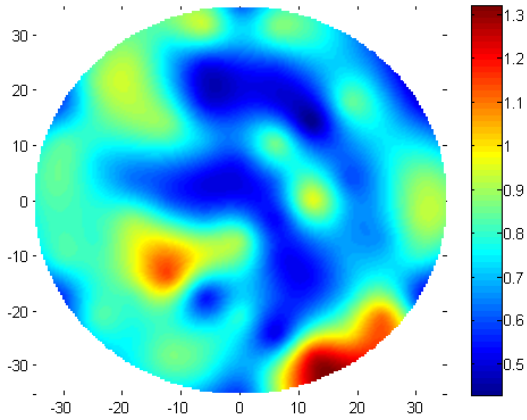

(f) with 5% noise level

Figure 4.10: Numerical reconstructions in the target conductivity distribution σ_1: (a), (c) and (e) using the original design with 12 current injecting electrodes; (b), (d) and (f) using the modified design with 18 current injecting electrodes.

For the target conductivity distribution shown in Figure 4.11, the two-dimensional conductivity reconstructions are presented in Figure 4.12 and the corresponding L^2-errors are summarised in Table 4.3

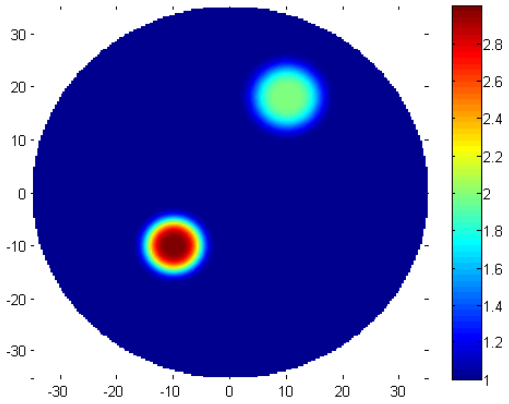

Figure 4.11: Target(exact) conductivity distribution σ_2.

Noise level ε	Old Stamp	Modified Stamp
0%	1.27	0.60
2%	1.29	0.60
5%	1.34	0.69

Table 4.3: The $\|\sigma_{rec} - \sigma_2\|_2$ values in the reconstruction of target conductivity distribution σ_2 for noise levels ε 0%, 2% and 5% by using both the old and the modified design of sensing head.

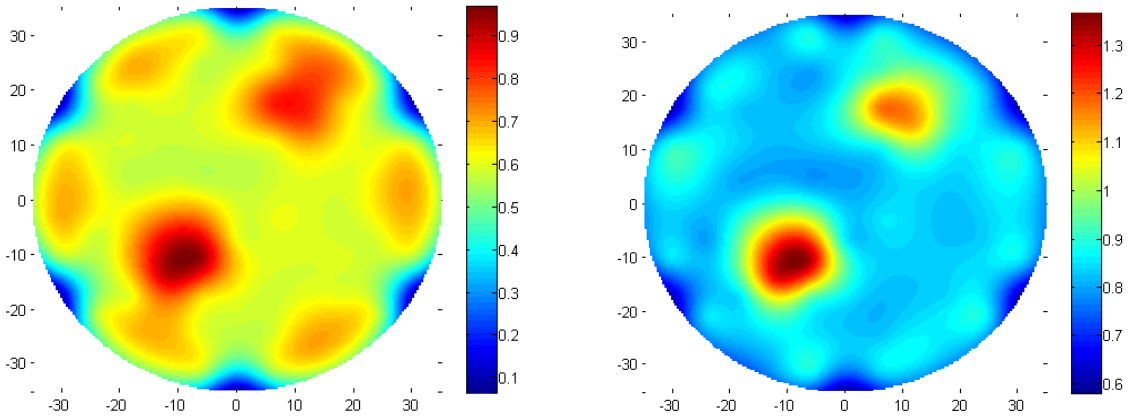

(a) with 0% noise level

(b) with 0% noise level

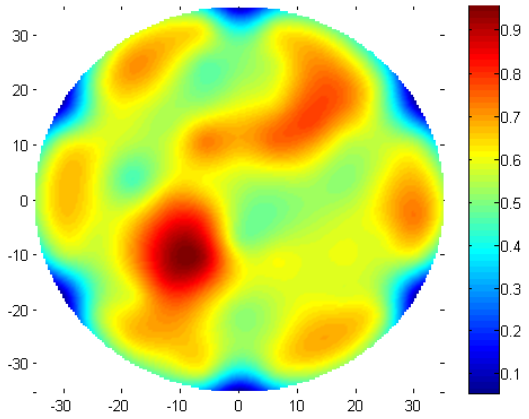

(c) [with 2% noise level

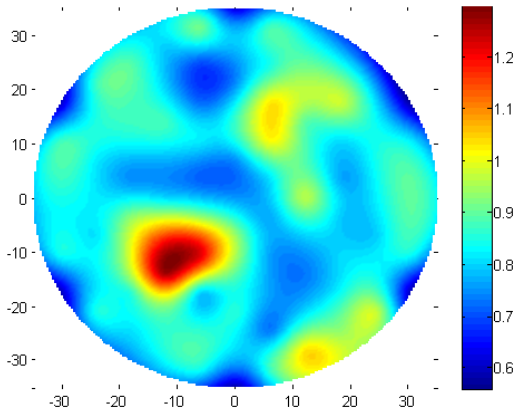

(d) with 2% noise level

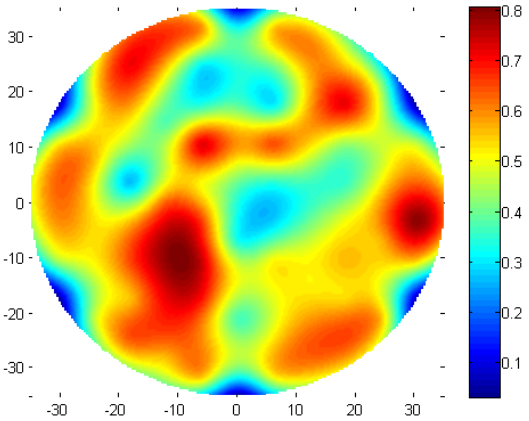

(e) with 5% noise level

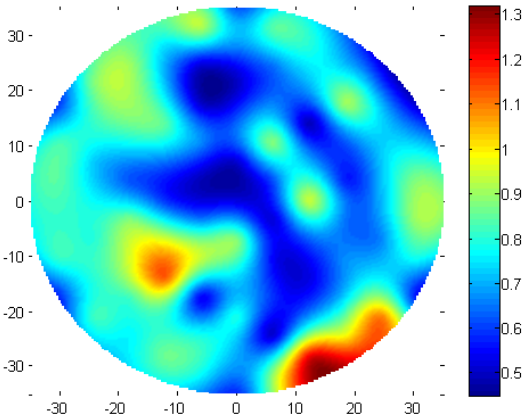

(f) with 5% noise level

Figure 4.12: Numerical reconstructions in the target conductivity distribution σ_2: (a), (c) and (e) using the original design with 12 current injecting electrodes; (b), (d) and (f) using the modified design with 18 current injecting electrodes.

In this final set, the two-dimensional conductivity reconstructions of the target conductivity distribution σ_3 depicted in Figure 4.13 are presented in Figure 4.14 and the corresponding L^2-errors shown in Table 4.4.

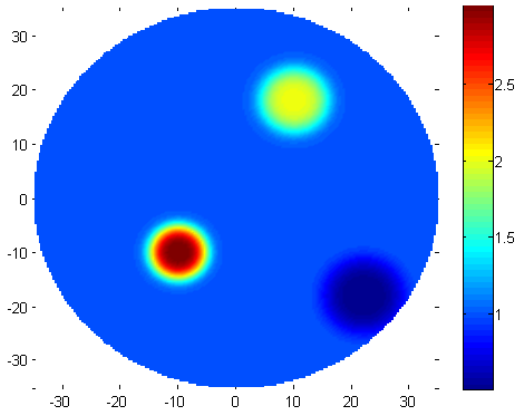

Figure 4.13: Target(exact) conductivity distribution σ_3.

Noise level ε	Old Stamp	Modified Stamp
0%	3.00	2.35
2%	3.03	2.36
5%	2.36	2.43

Table 4.4: The $\|\sigma_{rec} - \sigma_3\|_2$ values in the reconstruction of target conductivity distribution σ_3 for noise levels ε 0%, 2% and 5% by using both the old and the modified design of sensing head.

where (r_k, θ_k) are the polar coordinates of the quadrature points given by Engel [192], while w_k are the corresponding weights. The values of σ_i at these points (r_k, θ_k) were found by using griddata interpolation routine of Matlab.

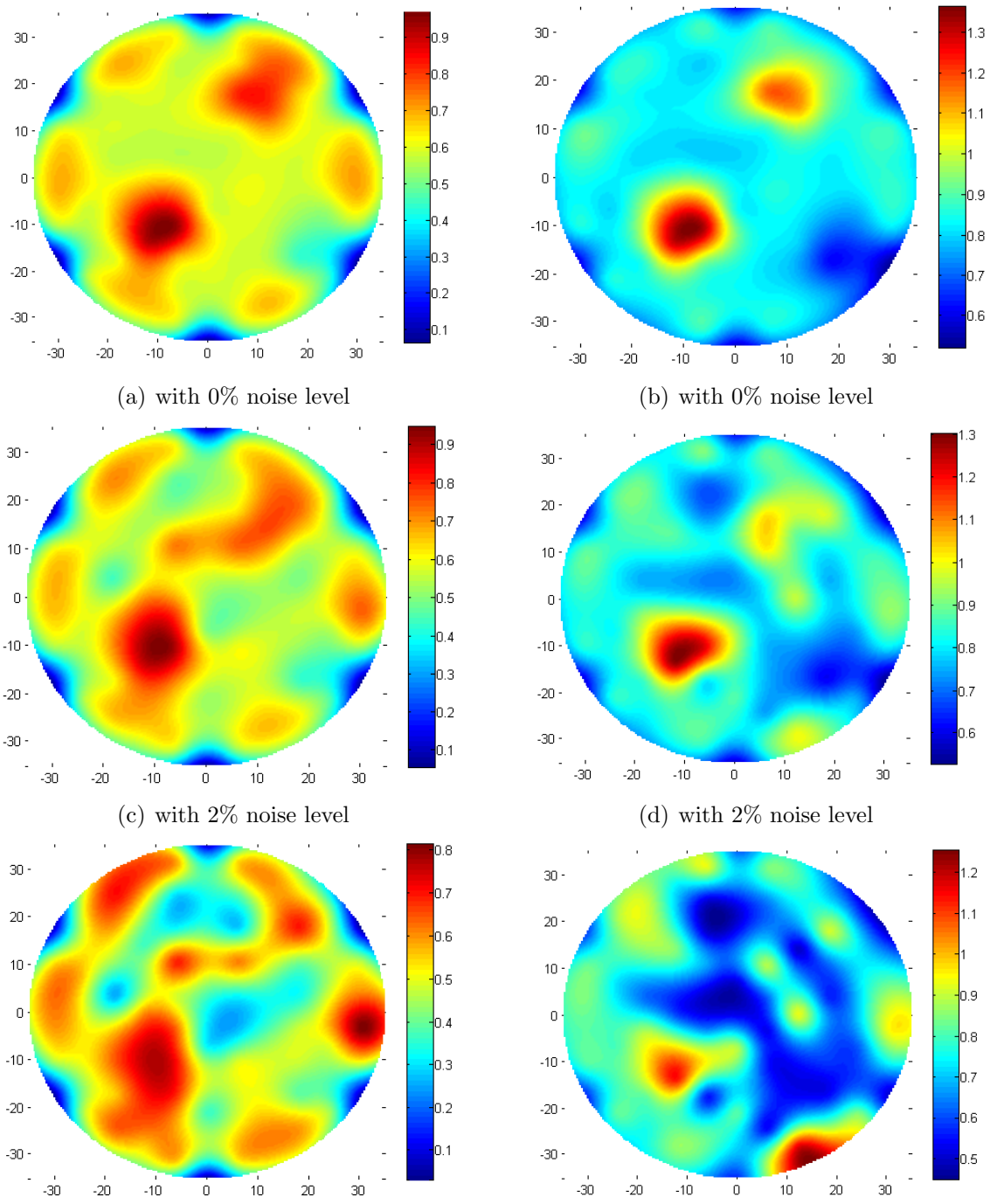

(a) with 0% noise level

(b) with 0% noise level

(c) with 2% noise level

(d) with 2% noise level

(e) with 5% noise level

(f) with 5% noise level

Figure 4.14: Numerical reconstructions in the target conductivity distribution σ_3: (a), (c) and (e) using the original design with 12 current injecting electrodes; (b), (d) and (f) using the modified design with 18 current injecting electrodes.

The second set of numerical tests are to examine the sensitivity and the spatial resolution of the modified design of the sensing head with eighteen active electrodes when the number of passive electrodes are increased from fifty four to seventy three. In this test, two different patterns were proposed for the resistor networks, a rhombic and a triangular one, see Figures 4.6 and 4.7, respectively. The numerical reconstructions of the target conductivity distributions shown in Figure 4.9, 4.11 and in 4.13 at noise level 0% are shown in Figure 4.15

The results from both numerical sets show that increasing the number of passive electrodes has significantly improved the sensitivity of the sensing head. On the other hand, using the proposed rhombic and triangular patterns when the number of passive electrodes are increased to seventy three enlarged dramatically the ill-posedness of the inverse problem, which suggests that, particularly, there is no advantage to increase the number of passive electrodes.

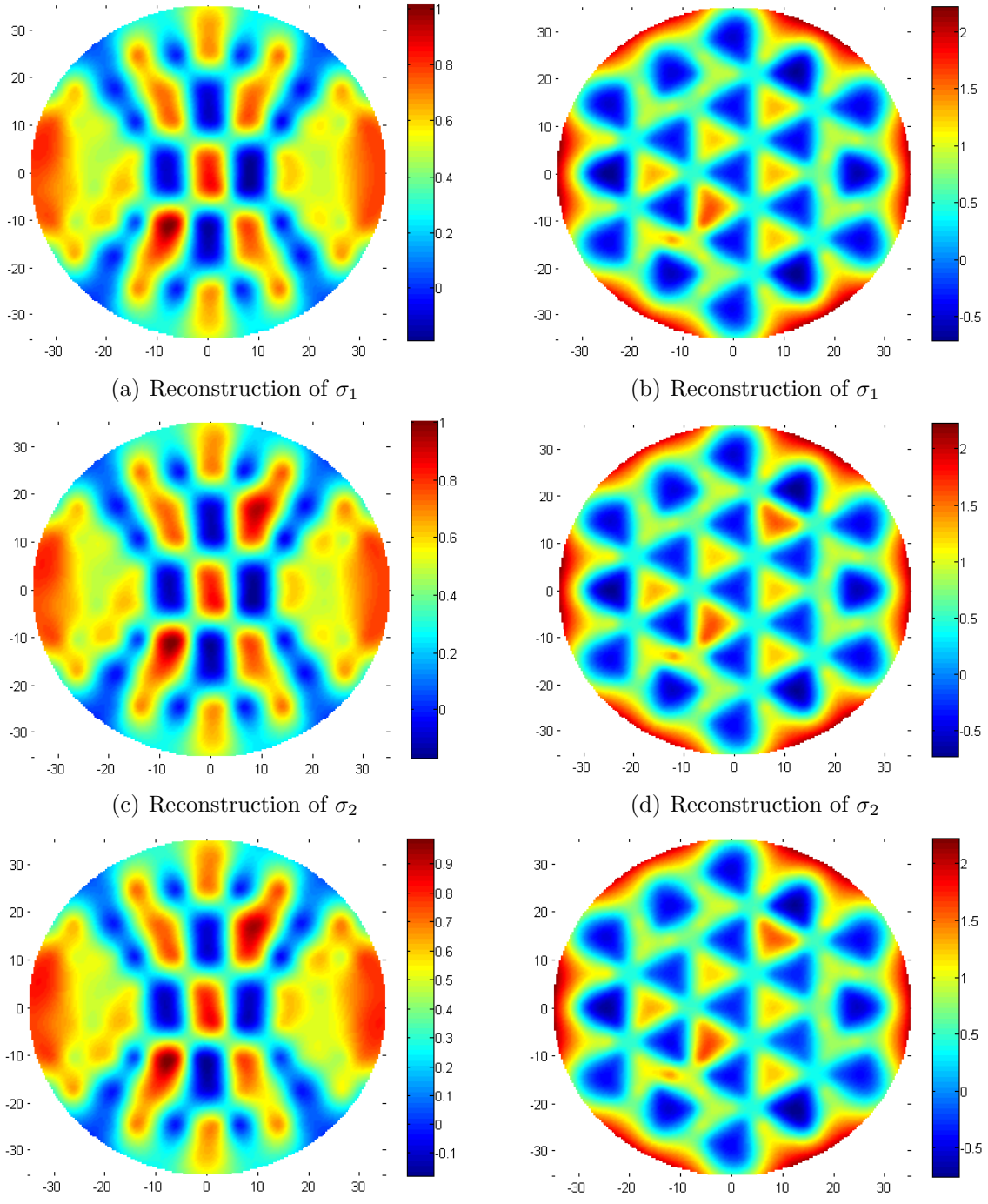

(a) Reconstruction of σ_1

(b) Reconstruction of σ_1

(c) Reconstruction of σ_2

(d) Reconstruction of σ_2

(e) Reconstruction of σ_3

(f) Reconstruction of σ_3

Figure 4.15: Numerical reconstructions of the target conductivity distributions σ_1, σ_2 and σ_3 with 0% noise level: (a), (c) and (e) using the rhombic network pattern; (b), (d) and (f) using triangular network pattern.

4.3.2 Experimental Testing using Real Data of the Old Design of the Sensing Heads

In this subsection, I first explain how the original sensing head shown in Figure 4.3 was tested experimentally at the Institute for Physics, University of Mainz and the experimental set-up of real data collection. Then I present some numerical reconstructions generated by the inversion algorithm using the real data collected at Mainz University.

The data was collected by placing the sensing head at the bottom of a cylindrical tank filled with a conducting saline (salt water) as shown in Figure 4.16.

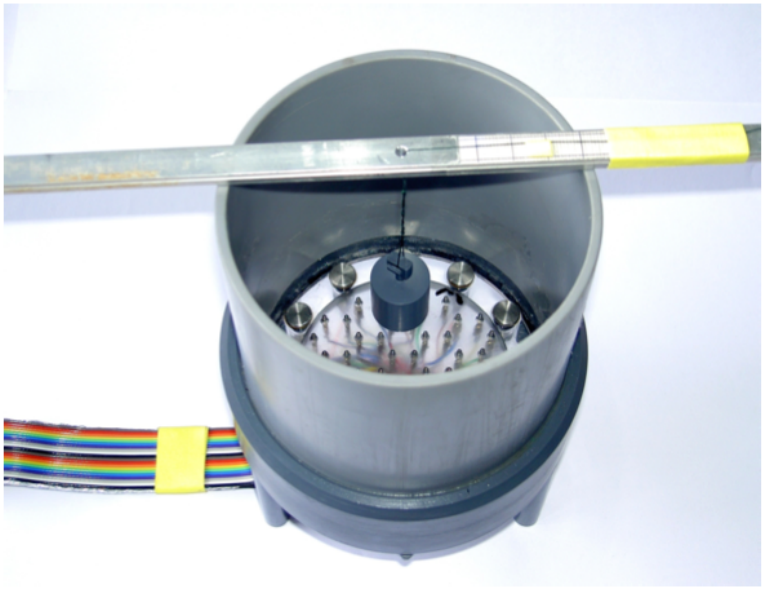

Figure 4.16: Experimental Setup [40].

Metallic objects of different diameters were immersed at various distances z from the sensing head (2mm, 5mm and 10mm). The metallic objects were cylinders of radii 15mm and 20mm. Their heights were equal to their diameters, and objects were placed either at a position in between the inner electrodes (positions 1,2 or 3), on top

of an outer electrode (position 4), on the top of an inner electrode (position 5), or at the centre of the sensing head (position 6). The sizes of the metallic objects used were smaller or larger relative to the sizes of the hexagons of the equivalent resistor network, which have side lengths of approximately 8.1mm. In this arrangement, the detection of the smaller object which covers no electrodes in positions 1,2,3 and 6 tests the spatial resolution of the inversions, while the detection of the larger object which covers six electrodes in position 1, 2, 3 and 6, or four electrodes in position 4 and 5 test the sensitivity of the reconstruction algorithm.

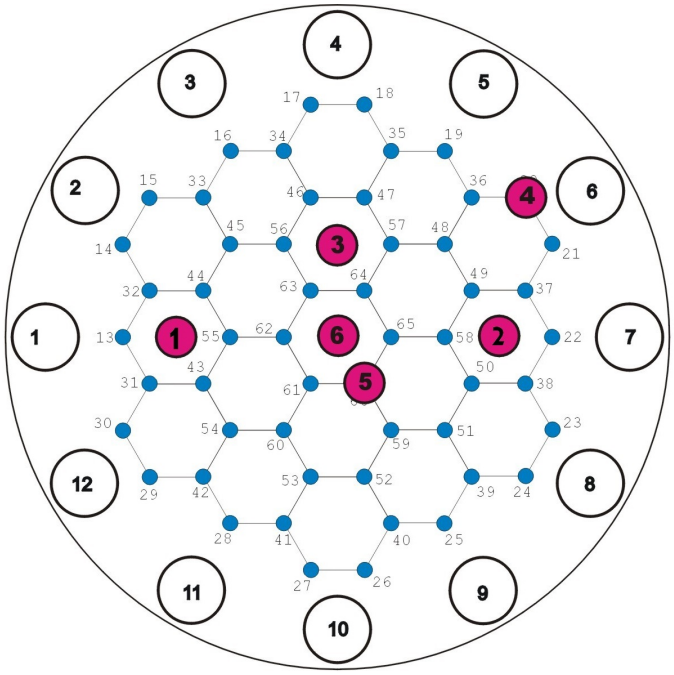

Figure 4.17: Positions of the metallic objects [40].

Figure 4.18, for example, presents the numerical reconstruction of the two-dimensional conductivity distribution in the plane of electrodes of a metallic object of radius 20mm placed in position 1. The experiment was repeated several times by placing the metal object at different positions or by using another metal object of different size as shown

in Figures 4.19 - 4.23.

In addition to reconstructing the conductivity of one metallic object at a time, the two objects with radii 15mm and 20mm were also placed together in the tank at various depths and positions as presented in Figures 4.24 - 4.27. For example, Figure 4.24 shows the reconstructed two-dimensional conductivity distribution for the two metallic objects, the one of radius 15mm placed in position 1 and the other of radius 20mm placed in position 2. Similarly, in Figure 4.25, the two-dimensional conductivity distribution is for the smaller metallic object placed in position 1 and the larger object placed in position 3. In Figures 4.26 - 4.27, the positions of the objects were swapped, i.e. the larger object was placed in position 1 while the smaller object was placed either in position 2 or 3. In these tests, both metallic objects were placed at the same distance from the array of electrodes, either at $z = 2$mm or $z = 5$mm.

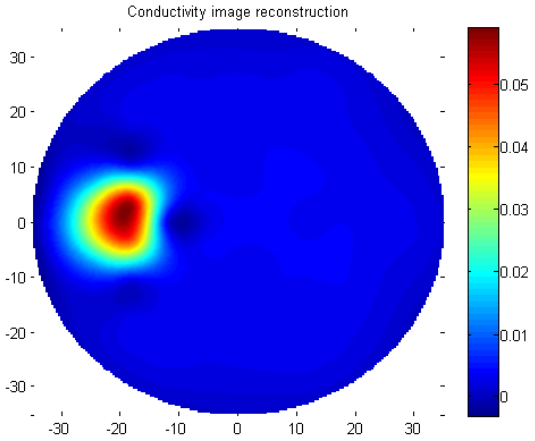

(a) $z = 2$mm

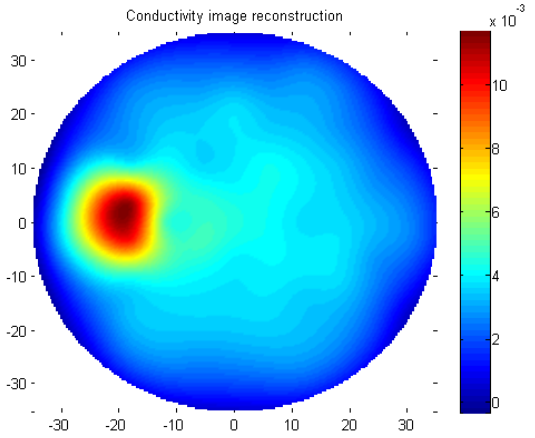

(b) $z = 5$mm

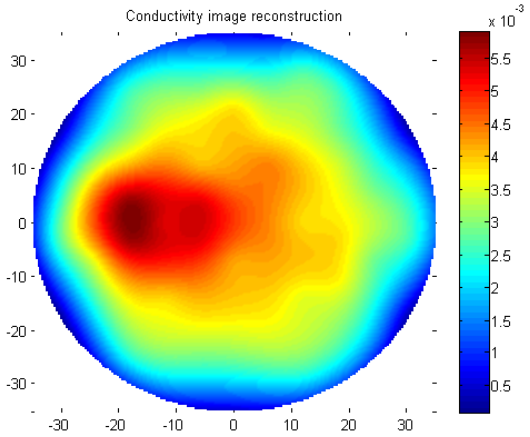

(c) $z = 10$mm

Figure 4.18: Numerical reconstructions of a cylindrical metallic target of radius 20mm in position 1.

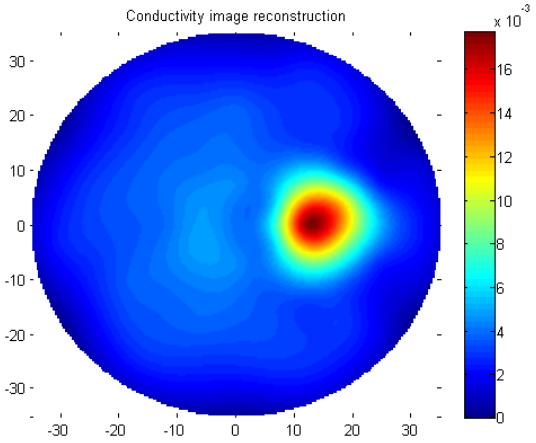

(a) $z = 2$mm

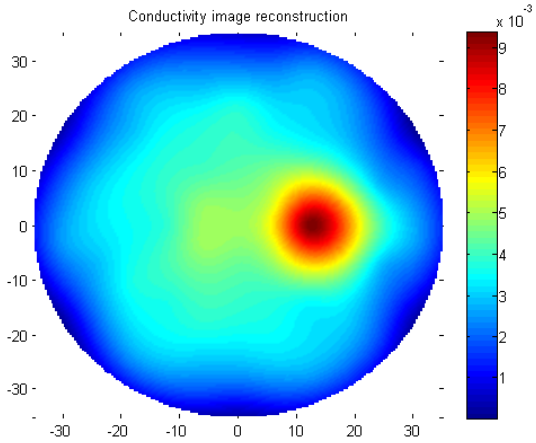

(b) $z = 5$mm

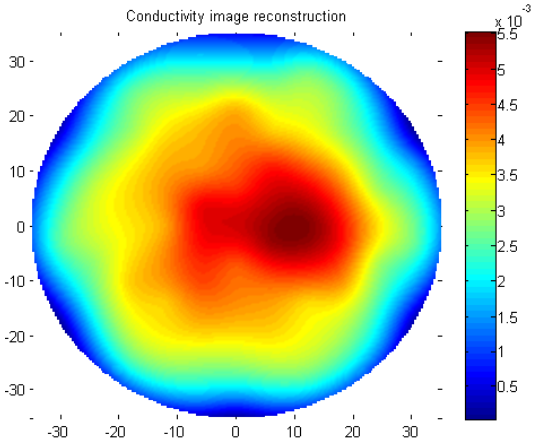

(c) $z = 10$mm

Figure 4.19: Numerical reconstructions of a cylindrical metallic target of radius 15mm in position 2.

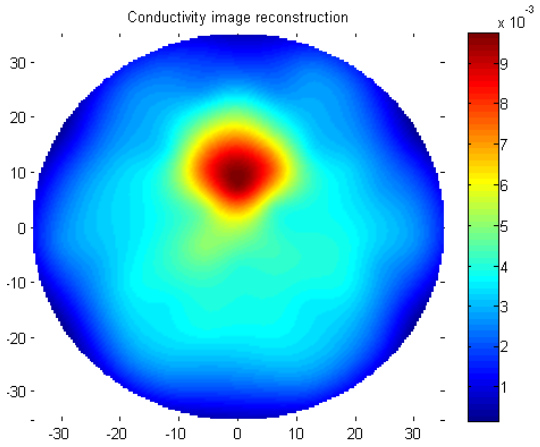

(a) $z = 2$mm

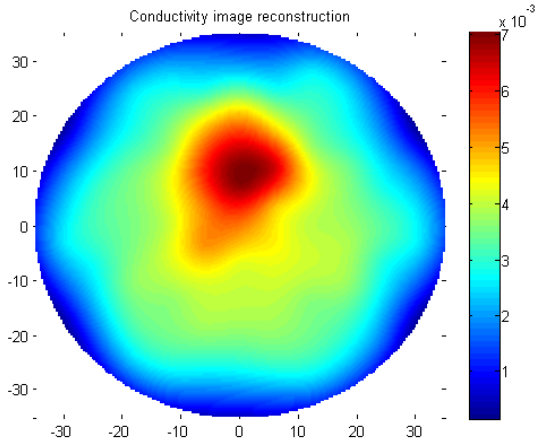

(b) $z = 5$mm

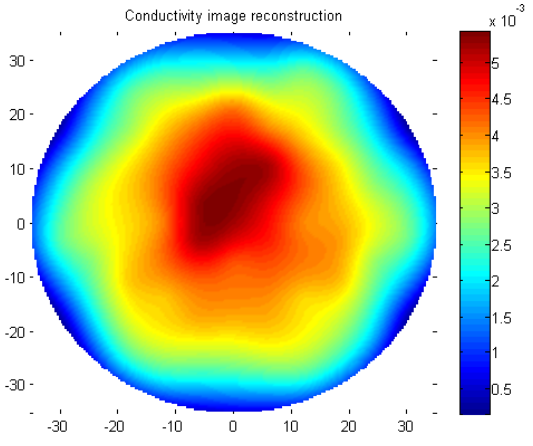

(c) $z = 10$mm

Figure 4.20: Numerical reconstructions of a cylindrical metallic target of radius 15mm in position 3.

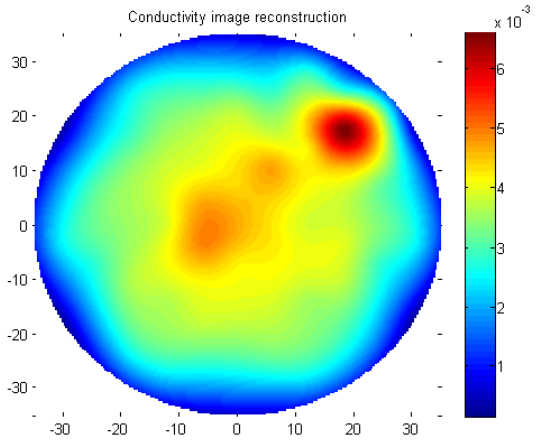

(a) $z = 2$mm

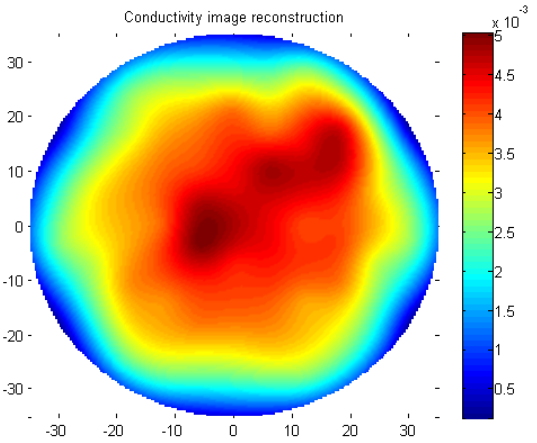

(b) $z = 5$mm

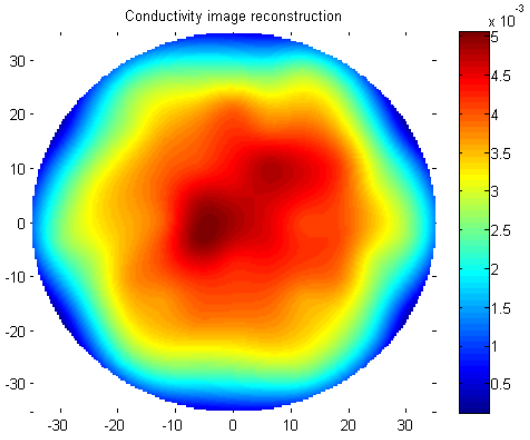

(c) $z = 10$mm

Figure 4.21: Numerical reconstructions of a cylindrical metallic target of radius 15mm in position 4.

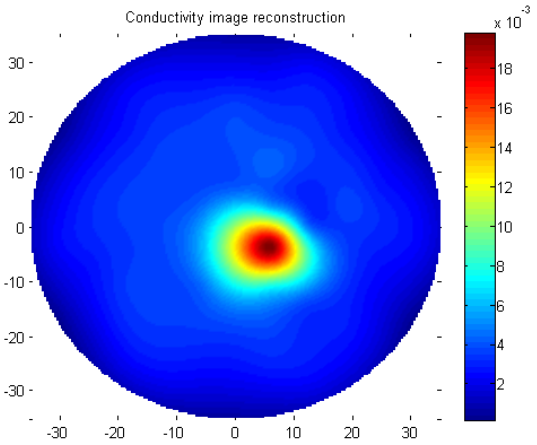

(a) $z = 2$mm

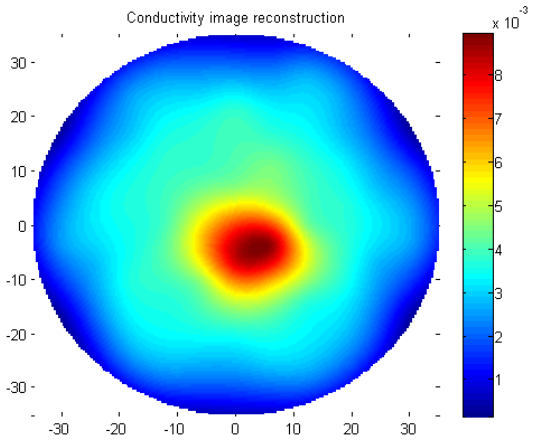

(b) $z = 5$mm

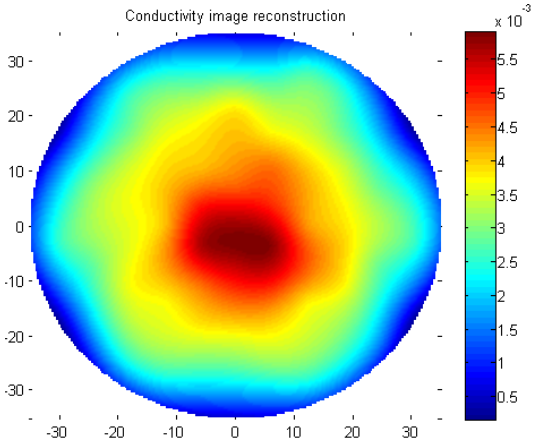

(c) $z = 10$mm

Figure 4.22: Numerical reconstructions of a cylindrical metallic target of radius 15mm in position 5.

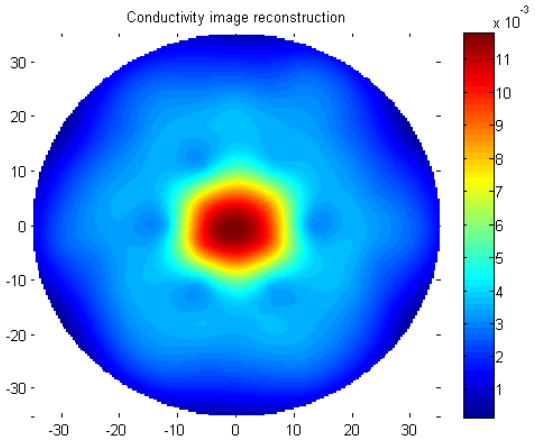

(a) $z = 2$mm

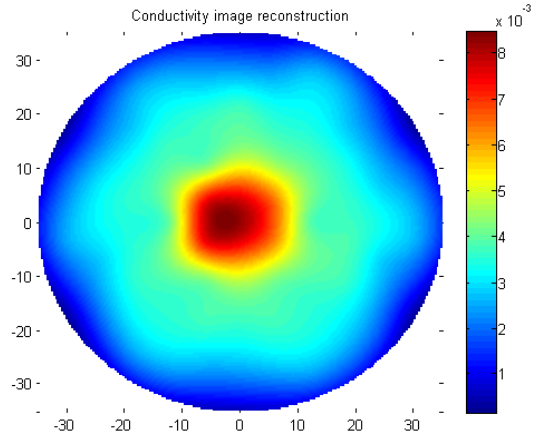

(b) $z = 5$mm

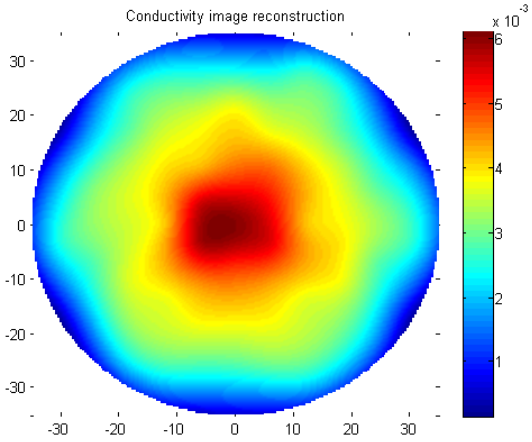

(c) $z = 10$mm

Figure 4.23: Numerical reconstructions of a cylindrical metallic target of radius 15mm in position 6.

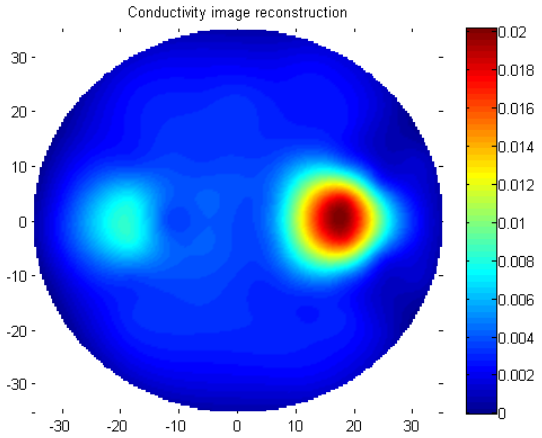

(a) $z = 2$mm

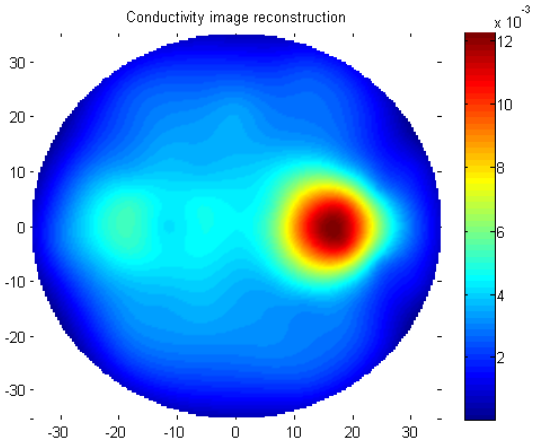

(b) $z = 5$mm

Figure 4.24: Numerical reconstructions of two cylindrical metallic targets of radii 15mm and 20mm in position 1 and 2, respectively.

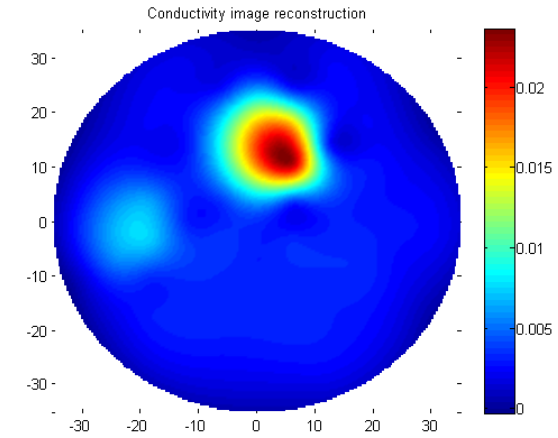

(a) $z = 2$mm

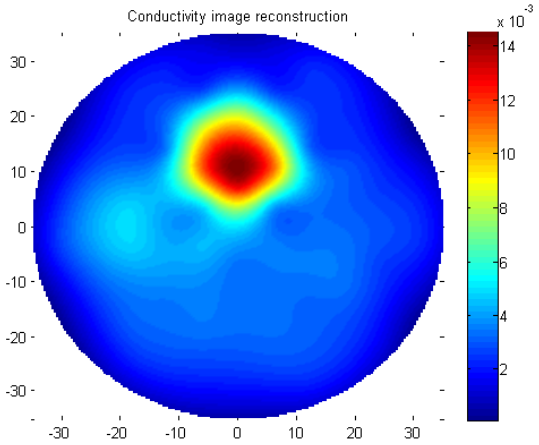

(b) $z = 5$mm

Figure 4.25: Numerical reconstructions of two cylindrical metallic targets of radii 15mm and 20mm in position 1 and 3, respectively.

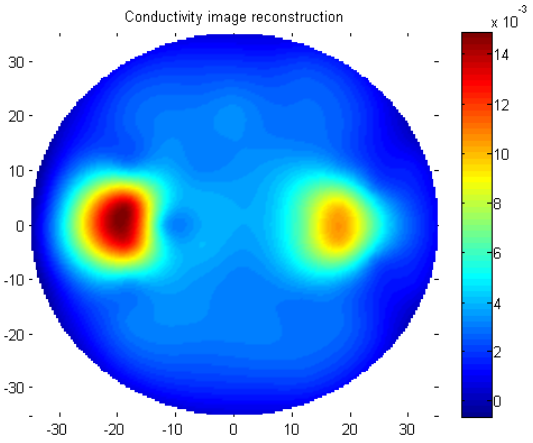

(a) $z = 2$mm

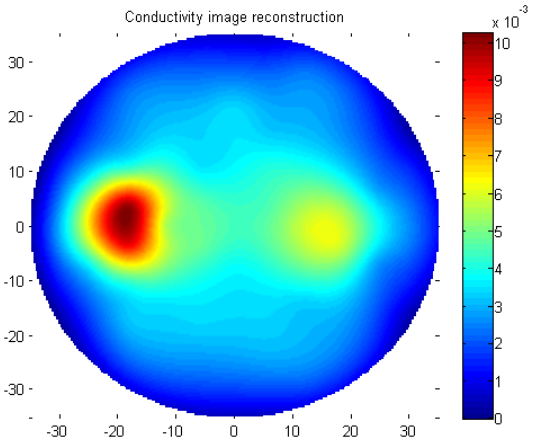

(b) $z = 5$mm

Figure 4.26: Numerical reconstructions of two cylindrical metallic targets of radii 15mm and 20mm in position 2 and 1, respectively.

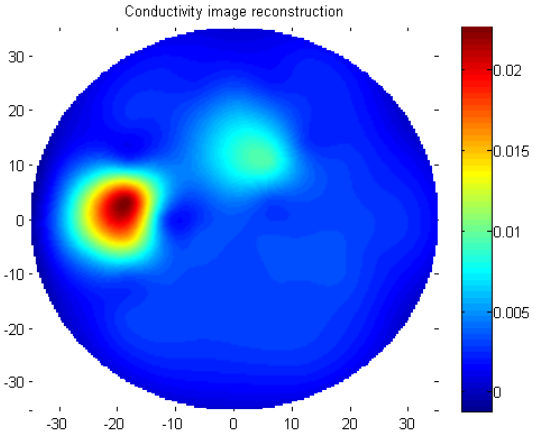

(a) $z = 2$mm

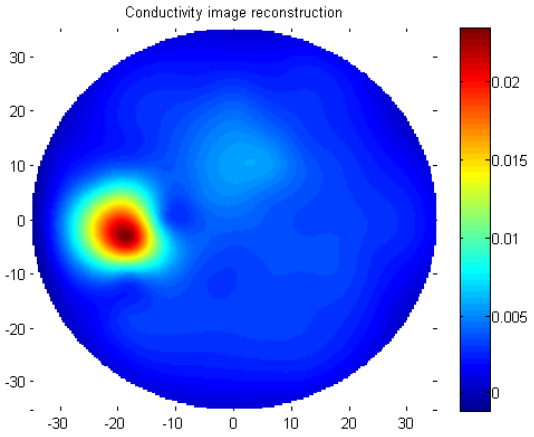

(b) $z = 5$mm

Figure 4.27: Numerical reconstructions of two cylindrical metallic targets of radii 15mm and 20mm in position 3 and 1, respectively.

The presented numerical reconstructions which are of a very good spatial resolution have shown that the inversion algorithm is quite robust and all locations of the metallic objects were correctly identified.

4.3.3 2D Reconstructions Obtained From 3D Numerically Simulated Data Using EIDORS

In this subsection, I present two-dimensional conductivity reconstructions from numerically simulated data generated by using a three dimensional model of the experimental tank obtained in EIDORS.

EIDORS is a Finite Element (FE) software which can be used for forward and inverse modelling for EIT and Diffusion based Optical Tomography, in medical and industrial applications [79,80,193]. In this work, EIDORS is used as a three-dimensional forward solver to mimic the experimental setup used for testing the design of the sensing heads of Mainz-Brookes mammographs. Models similar to the one depicted in Figure 4.28 were developed in EIDORS and used to perform numerical experiments.

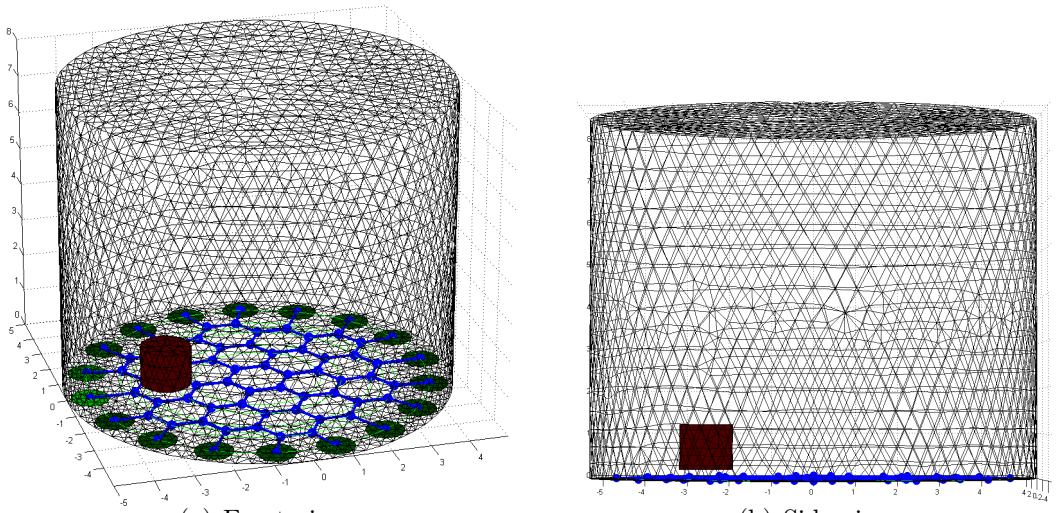

(a) Front view

(b) Side view

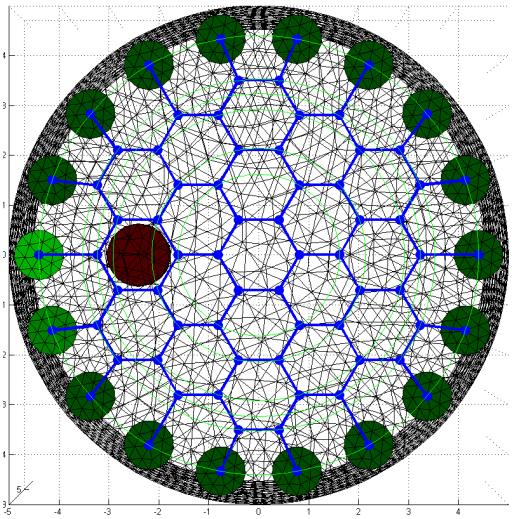

(c) Bottom view

Figure 4.28: Mainz-Brookes EIT 3D model using EIDORS. Numerical inclusion placed at position 1 and $z = 2$mm away from the sensing head.

In this set of reconstructions, the modified sensing head with eighteen active and fifty four passive electrodes was numerically tested using simulated data generated by EIDORS. The exact experimental set-up described in Section 4.3.2 which is used by the EIT group at Mainz University to test the original design of the sensing head was applied in this experiment. Cylindrical inclusion(s) with conductivity four times higher than the background of constant conductivity $\sigma_0 = 1$mS/m and of same sizes

(i.e. radii of 15mm and 20mm) as the metallic objects used by Mainz EIT group were placed at the same depths and positions as in Mainz experimental set-up.

The first group of reconstructions shown in Figures 4.29-4.34 are similar to those obtained from real data shown in Figures 4.18-4.23, i.e. one inclusion was placed at the same positions shown in Figure 4.17. Figure 4.29, for example, shows the conductivity reconstruction of a numerical inclusion of size 20mm with conductivity $\sigma = 4$ placed in position 1 at depths $z = 2$mm, $z = 5$mm or $z = 10$mm. In a similar way, all other two-dimensional reconstructions in this group were obtained.

The second group of the two-dimensional reconstructions shown in Figures 4.35-4.38 are similar to the reconstructions of two metallic objects obtained from real data shown in Figures 4.24-4.27, i.e. two inclusions of radii 15mm and 20mm were placed inside the three-dimensional tank. For example, in Figure 4.35, two numerical inclusions of the same conductivity $\sigma = 4$ but different radii were generated. The first inclusion of size 15mm was placed at position 1 and the other inclusion of size 20mm was placed at position 2 at the same depths where the two metallic objects were placed by Mainz EIT group, i.e. $z = 2$mm, $z = 5$mm and $z = 10$mm.

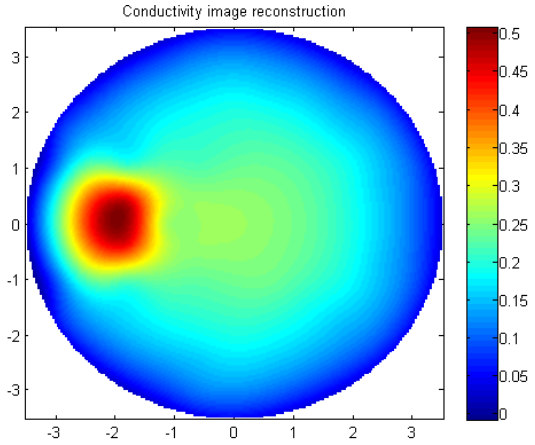

(a) $z = 2$mm

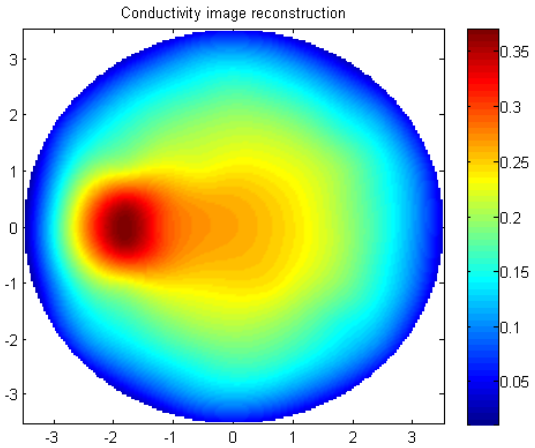

(b) $z = 5$mm

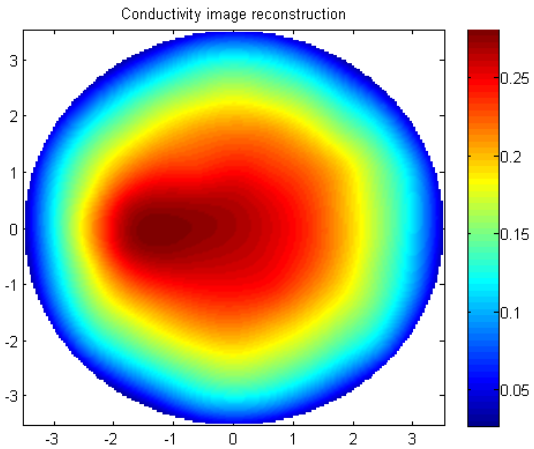

(c) $z = 10$mm

Figure 4.29: Numerical reconstructions of a cylindrical inclusion of radius 20mm in position 1.

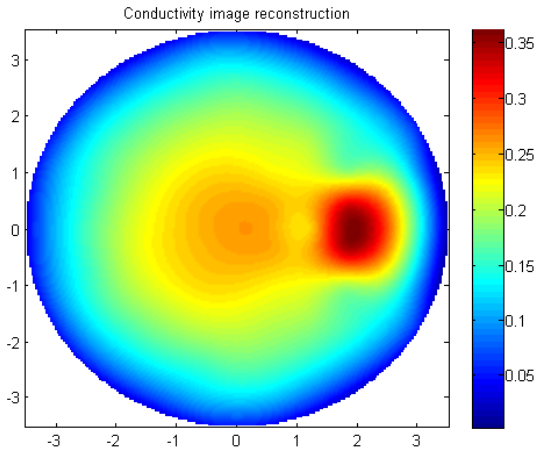

(a) $z = 2$mm

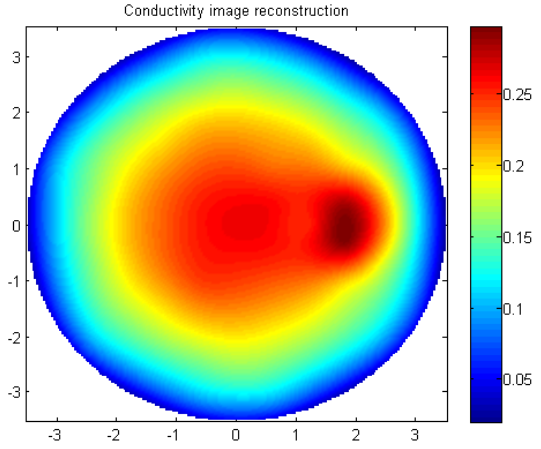

(b) $z = 5$mm

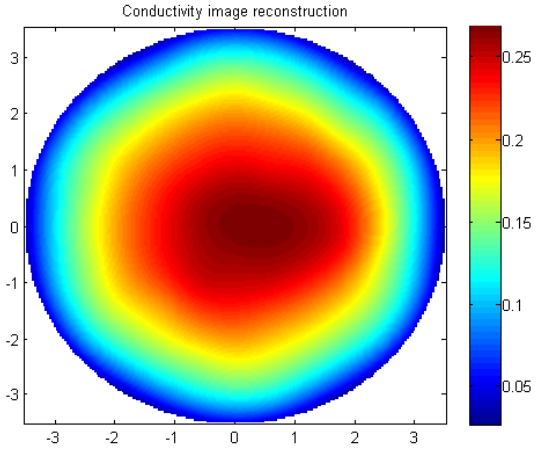

(c) $z = 10$mm

Figure 4.30: Numerical reconstructions of a cylindrical inclusion of radius 15mm in position 2.

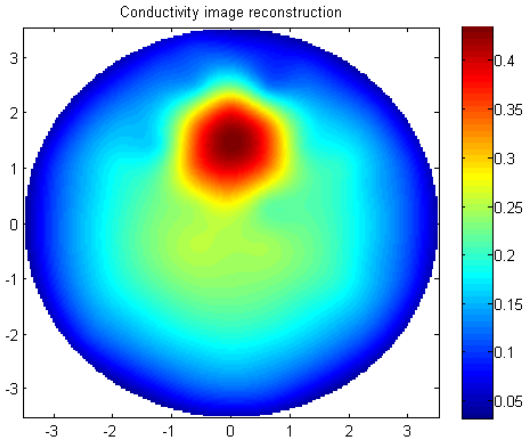

(a) $z = 2$mm

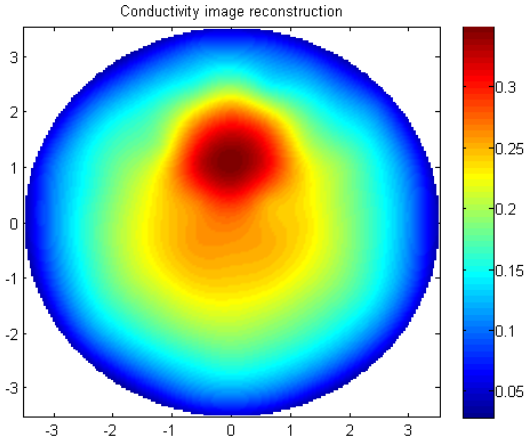

(b) $z = 5$mm

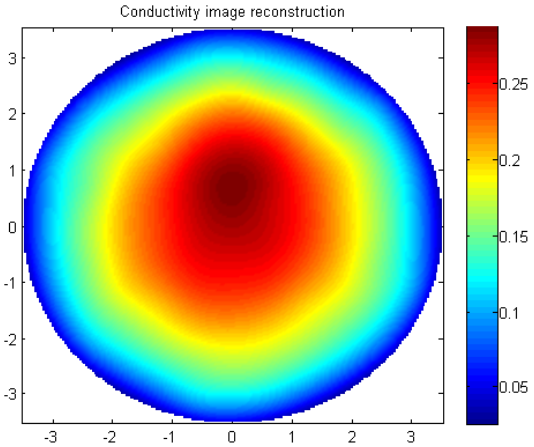

(c) $z = 10$mm

Figure 4.31: Numerical reconstructions of a cylindrical inclusion of radius 15mm in position 3.

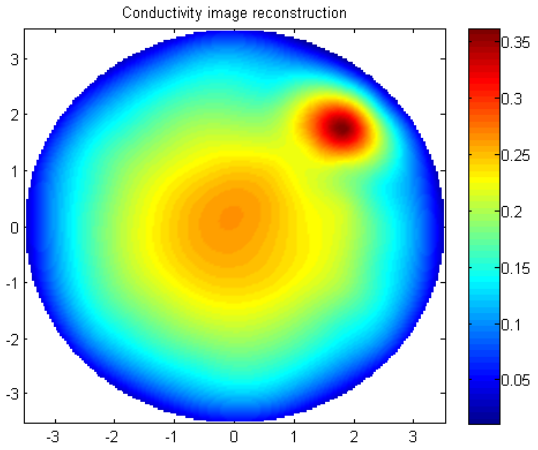

(a) $z = 2$mm

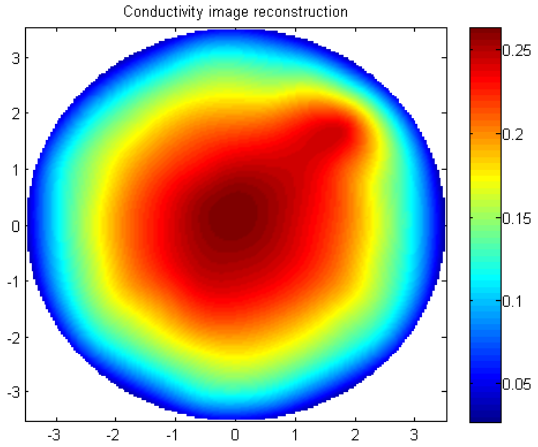

(b) $z = 5$mm

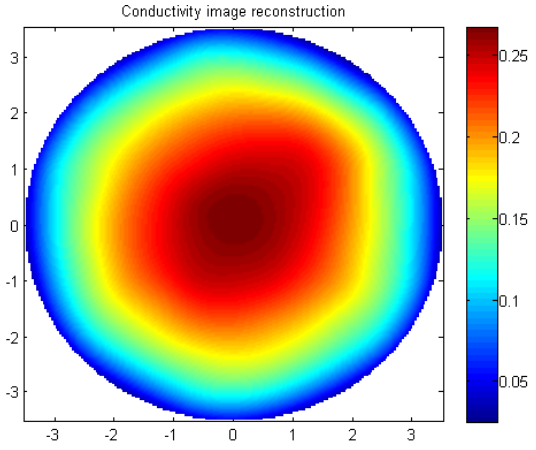

(c) $z = 10$mm

Figure 4.32: Numerical reconstructions of a cylindrical inclusion of radius 15mm in position 4.

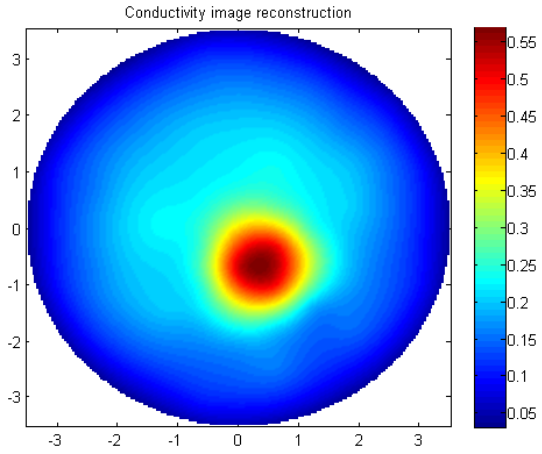

(a) $z = 2$mm

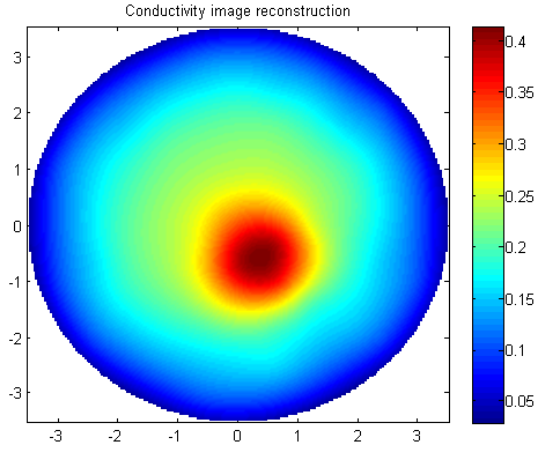

(b) $z = 5$mm

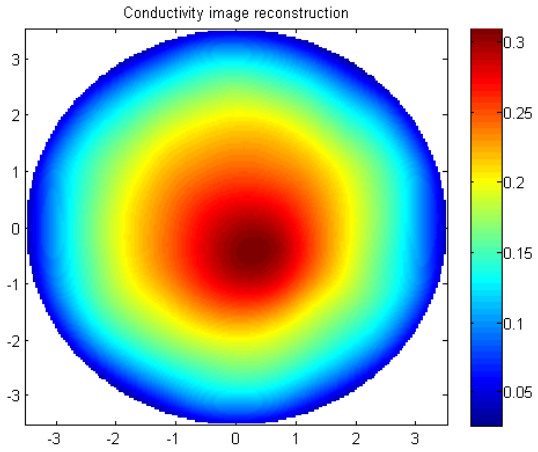

(c) $z = 10$mm

Figure 4.33: Numerical reconstructions of a cylindrical inclusion of radius 15mm in position 5.

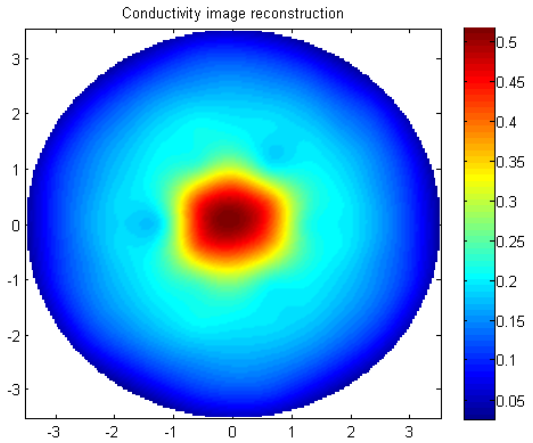

(a) $z = 2$mm

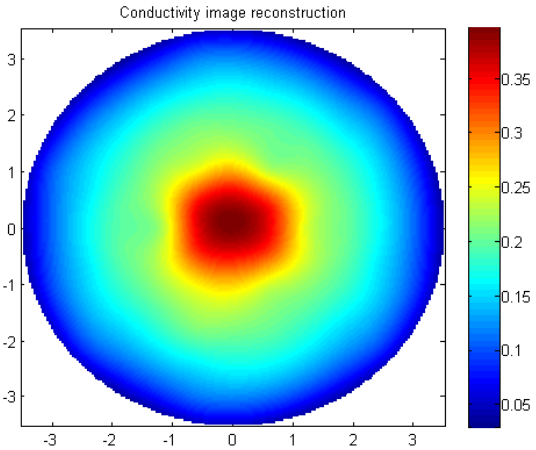

(b) $z = 5$mm

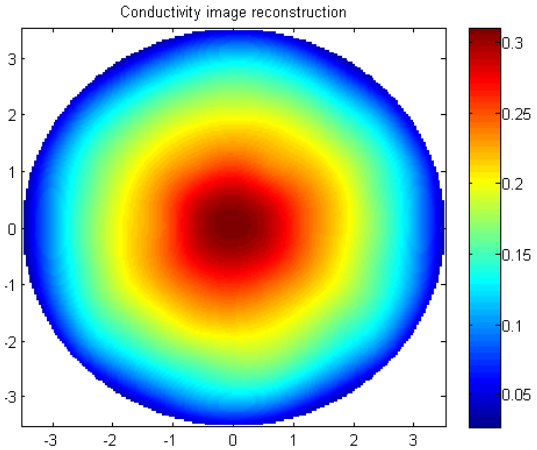

(c) $z = 10$mm

Figure 4.34: Numerical reconstructions of a cylindrical inclusion of radius 15mm in position 6.

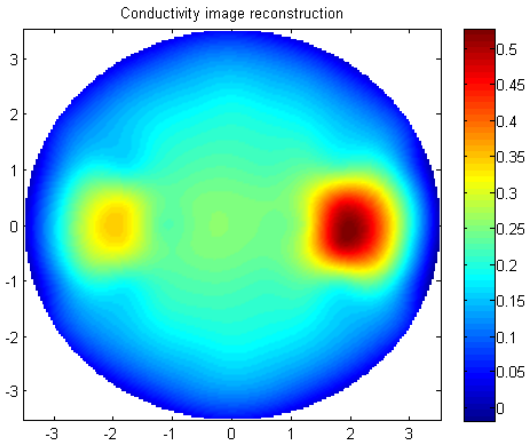

(a) $z = 2$mm

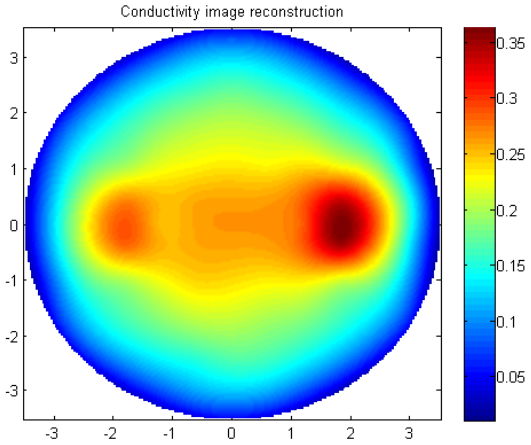

(b) $z = 5$mm

Figure 4.35: Numerical reconstructions of two cylindrical inclusions of radii 15mm and 20mm in position 1 and 2, respectively.

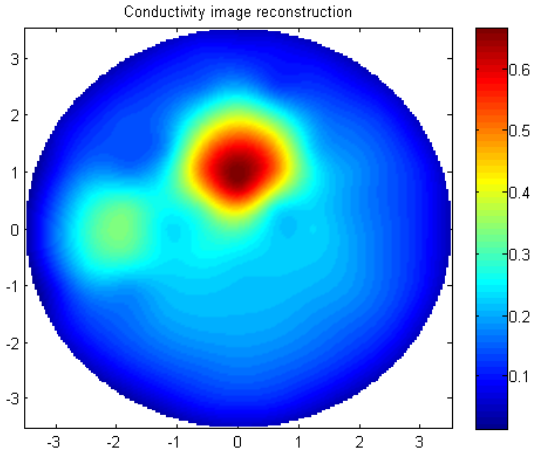

(a) $z = 2$mm

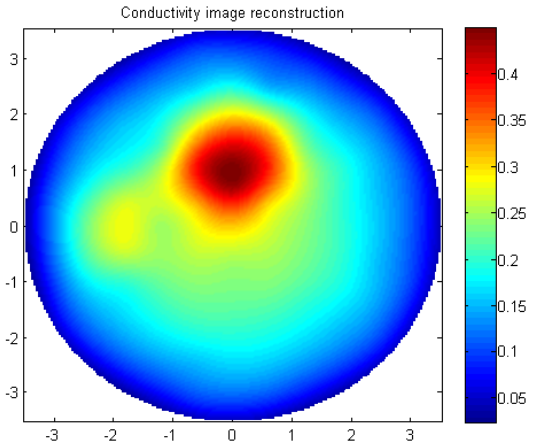

(b) $z = 5$mm

Figure 4.36: Numerical reconstructions of two cylindrical inclusions of radii 15mm and 20mm in position 1 and 3, respectively.

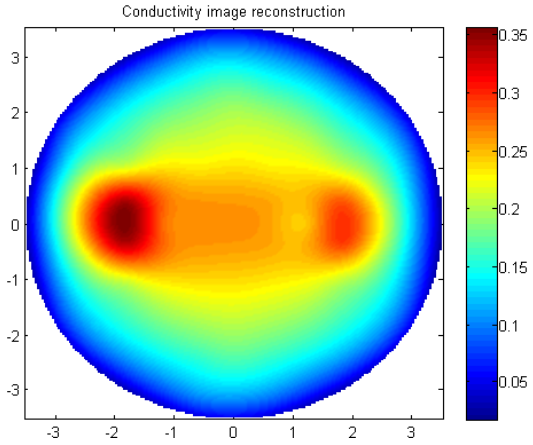

(a) $z = 2$mm

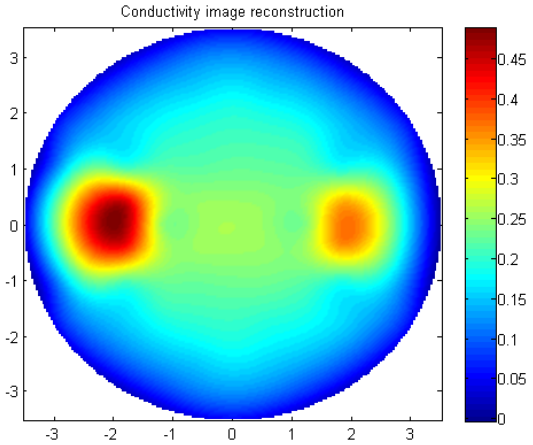

(b) $z = 5$mm

Figure 4.37: Numerical reconstructions of two cylindrical inclusions of radii 15mm and 20mm in position 2 and 1, respectively.

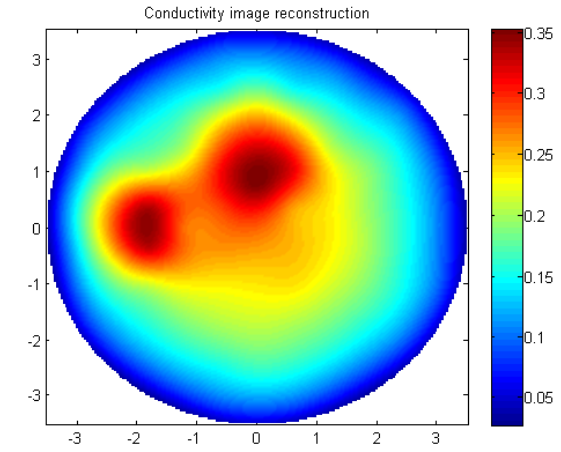

(a) $z = 2$mm

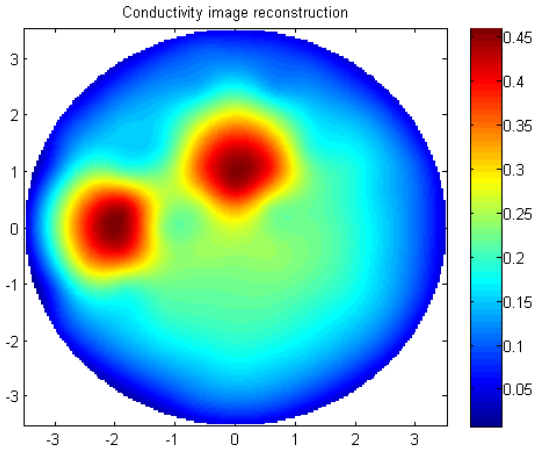

(b) $z = 5$mm

Figure 4.38: Numerical reconstructions of two cylindrical inclusions of radii 15mm and 20mm in position 3 and 1, respectively.

The conductivity distributions shown in group one and two are obtained with noise level $\varepsilon = 0\%$. However, the sensitivity of the sensing head was further tested by repeating the same experiments presented in group one and two with different noise levels. For example, Figures 4.39-4.48 presents the two-dimensional reconstruction using noise level $\varepsilon = 2\%$.

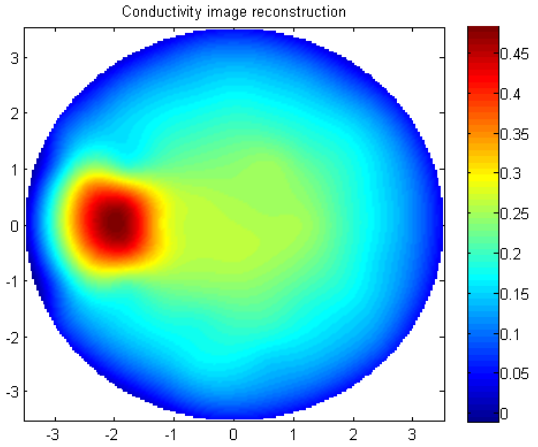

(a) $z = 2$mm

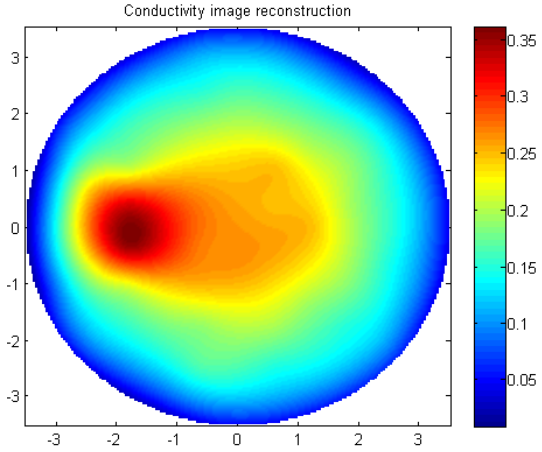

(b) $z = 5$mm

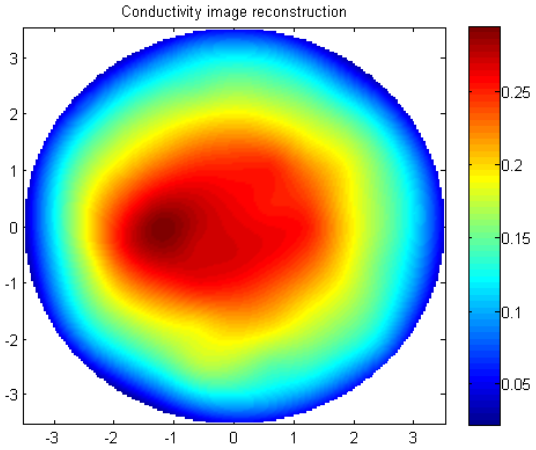

(c) $z = 10$mm

Figure 4.39: Numerical reconstructions of a cylindrical inclusion of radius 20mm in position 1 using noise level $\varepsilon = 2\%$.

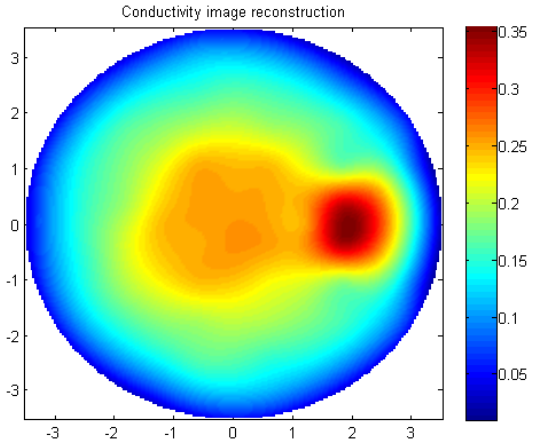

(a) $z = 2$mm

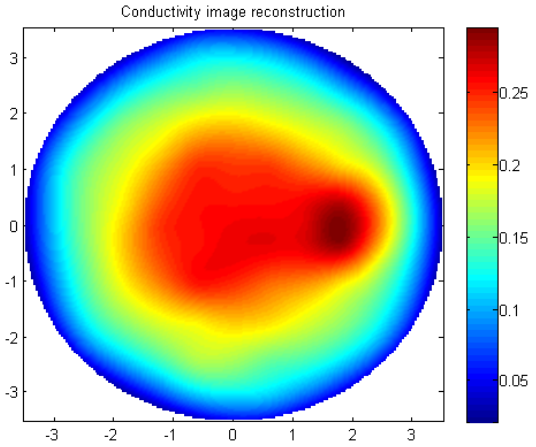

(b) $z = 5$mm

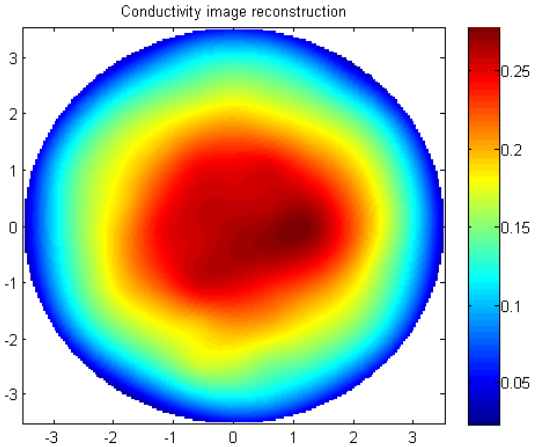

(c) $z = 10$mm

Figure 4.40: Numerical reconstructions of a cylindrical inclusion of radius 15mm in position 2 using noise level $\varepsilon = 2\%$.

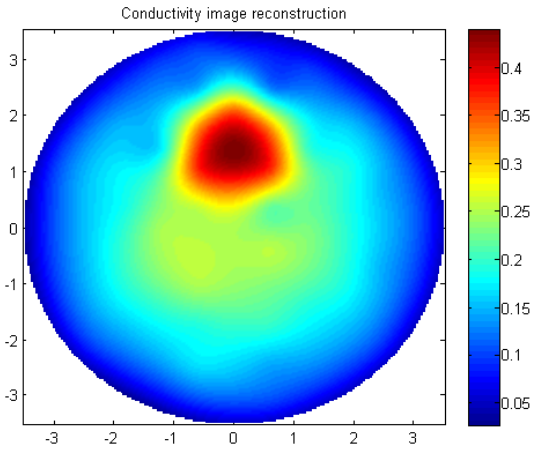

(a) $z = 2$mm

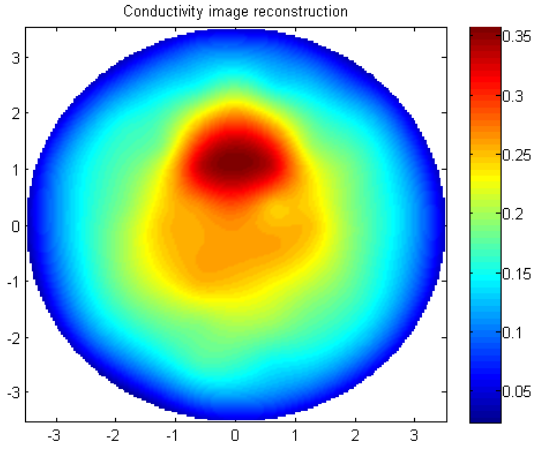

(b) $z = 5$mm

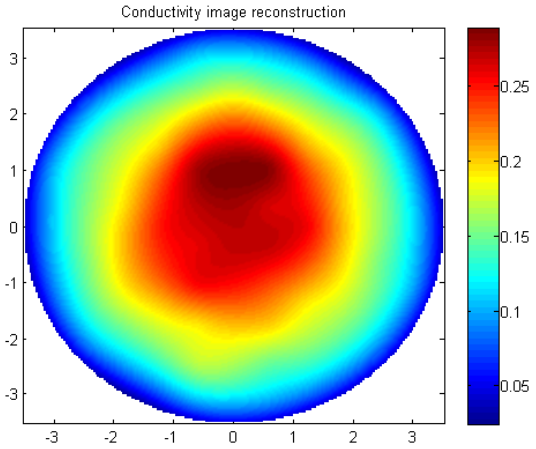

(c) $z = 10$mm

Figure 4.41: Numerical reconstructions of a cylindrical inclusion of radius 15mm in position 3 using noise level $\varepsilon = 2\%$.

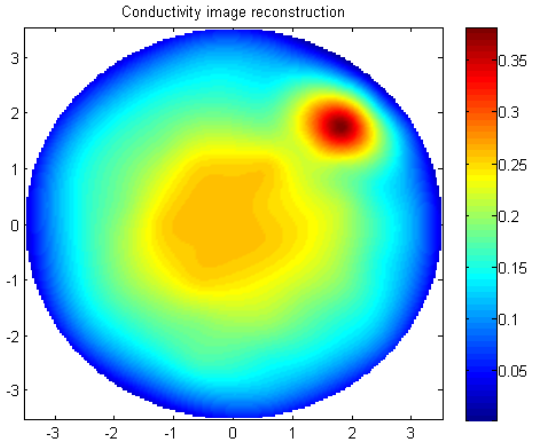

(a) $z = 2$mm

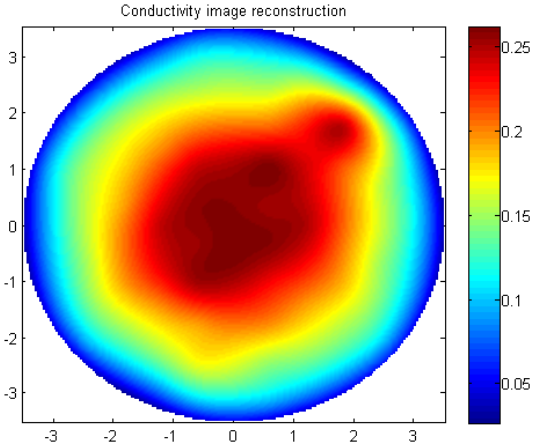

(b) $z = 5$mm

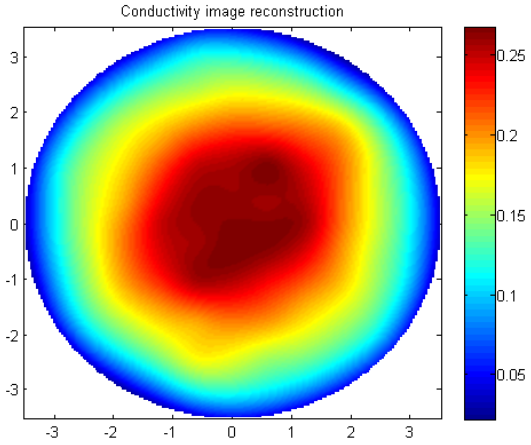

(c) $z = 10$mm

Figure 4.42: Numerical reconstructions of a cylindrical inclusion of radius 15mm in position 4 using noise level $\varepsilon = 2\%$.

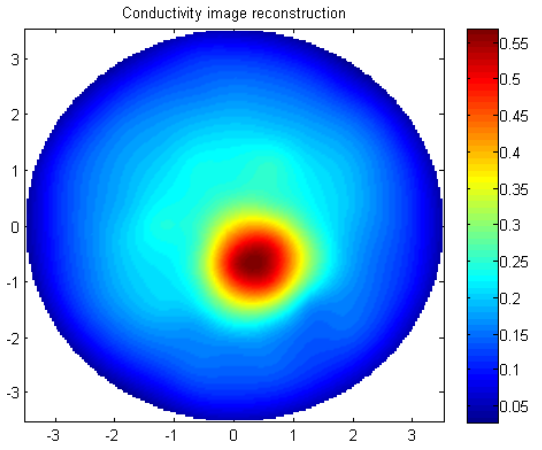

(a) $z = 2$mm

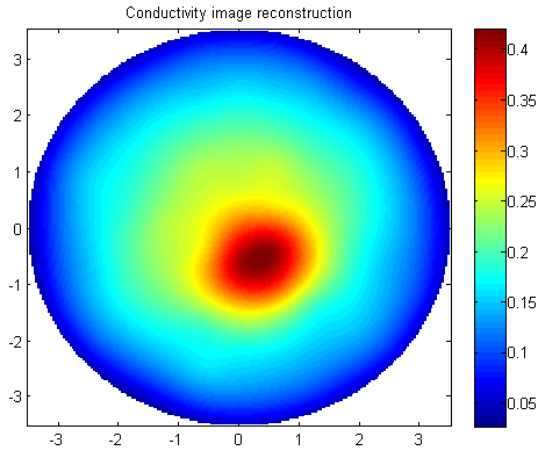

(b) $z = 5$mm

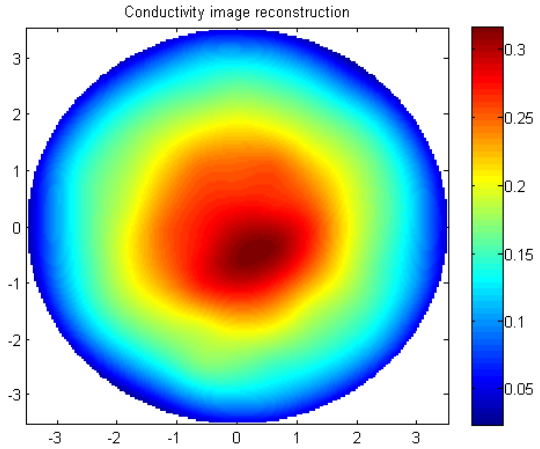

(c) $z = 10$mm

Figure 4.43: Numerical reconstructions of a cylindrical inclusion of radius 15mm in position 5 using noise level $\varepsilon = 2\%$.

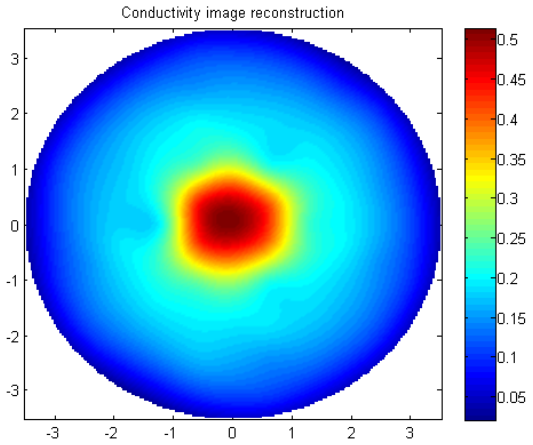

(a) $z = 2$mm

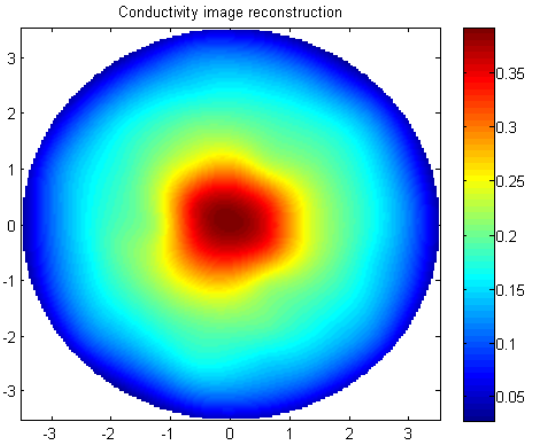

(b) $z = 5$mm

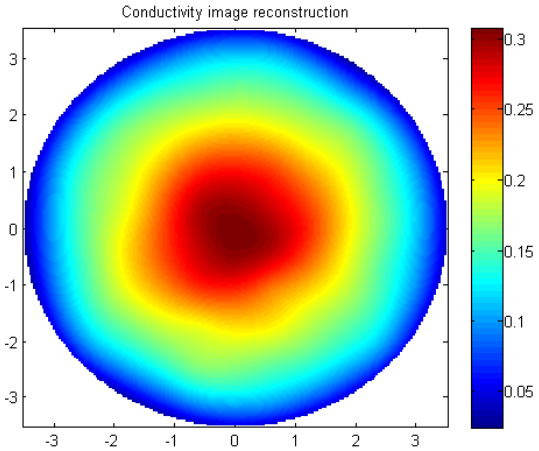

(c) $z = 10$mm

Figure 4.44: Numerical reconstructions of a cylindrical inclusion of radius 15mm in position 6 using noise level $\varepsilon = 2\%$.

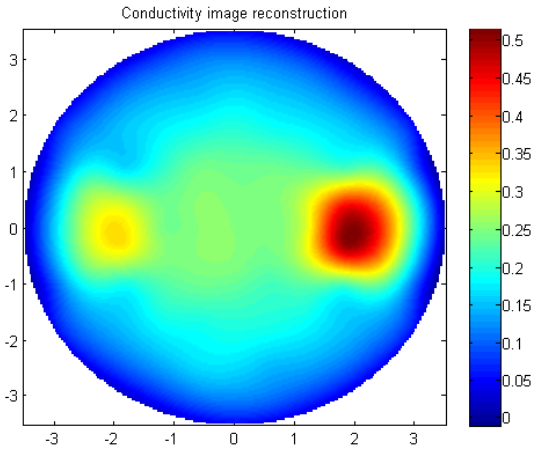

(a) $z = 2$mm

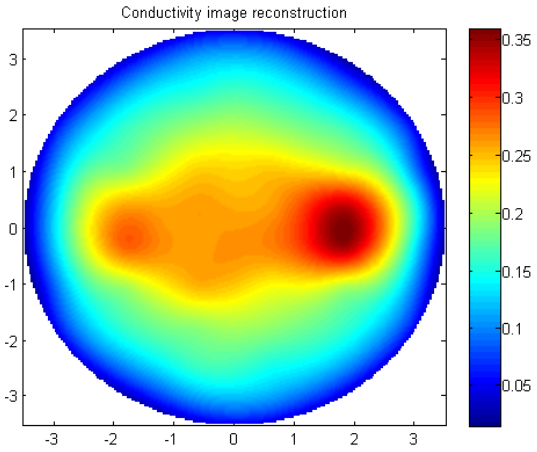

(b) $z = 5$mm

Figure 4.45: Numerical reconstructions of two cylindrical inclusions of radii 15mm and 20mm in position 1 and 2, respectively.

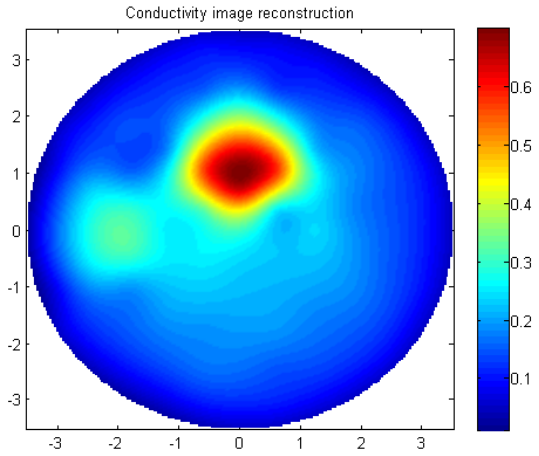

(a) $z = 2$mm

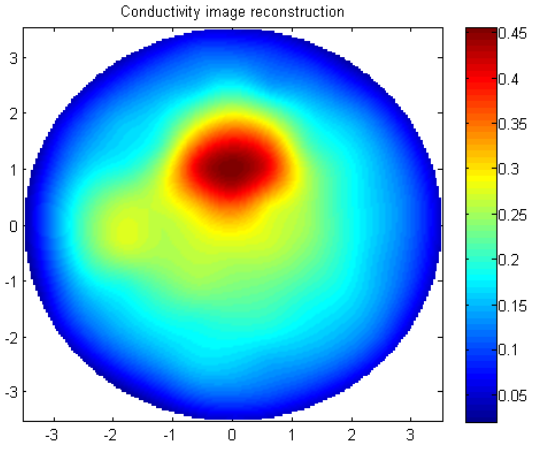

(b) $z = 5$mm

Figure 4.46: Numerical reconstructions of two cylindrical inclusions of radii 15mm and 20mm in position 1 and 3, respectively using noise level $\varepsilon = 2\%$.

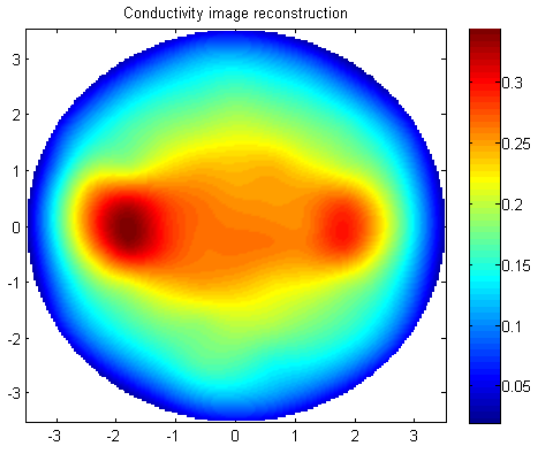

(a) $z = 2$mm

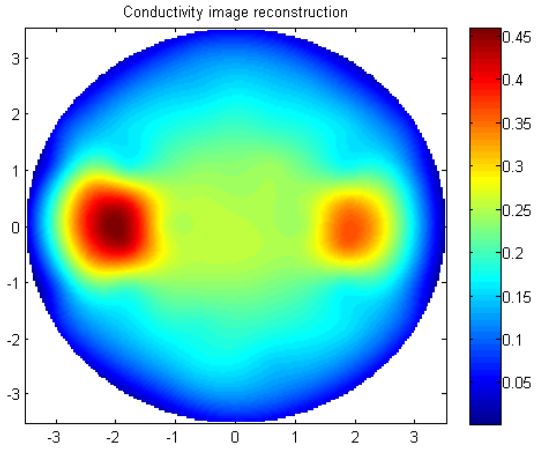

(b) $z = 5$mm

Figure 4.47: Numerical reconstructions of two cylindrical inclusions of radii 15mm and 20mm in position 2 and 1, respectively using noise level $\varepsilon = 2\%$.

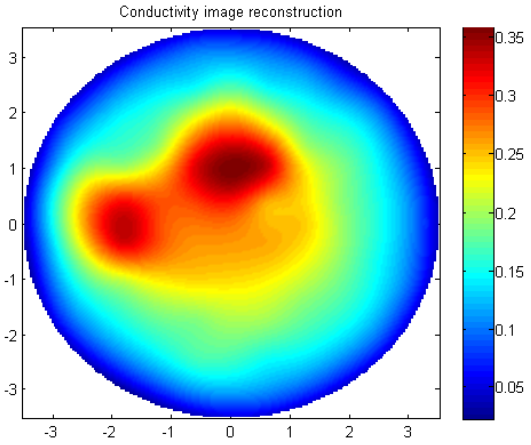

(a) $z = 2$mm

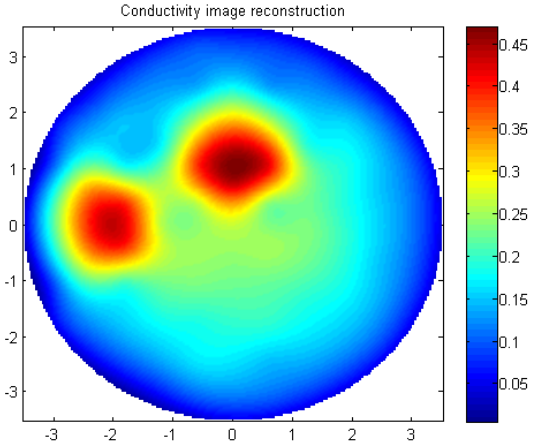

(b) $z = 5$mm

Figure 4.48: Numerical reconstructions of two cylindrical inclusions of radii 15mm and 20mm in position 3 and 1, respectively using noise level $\varepsilon = 2\%$.

Figures 4.49-4.58 presents the two-dimensional reconstruction at noise level $\varepsilon = 5\%$.

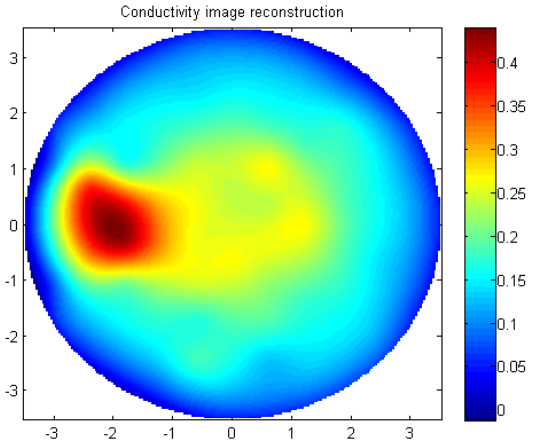

(a) $z = 2$mm

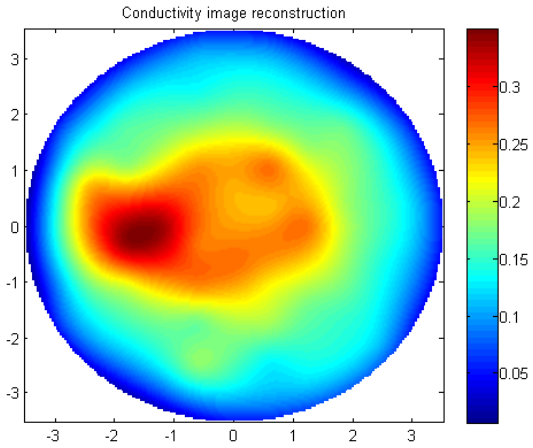

(b) $z = 5$mm

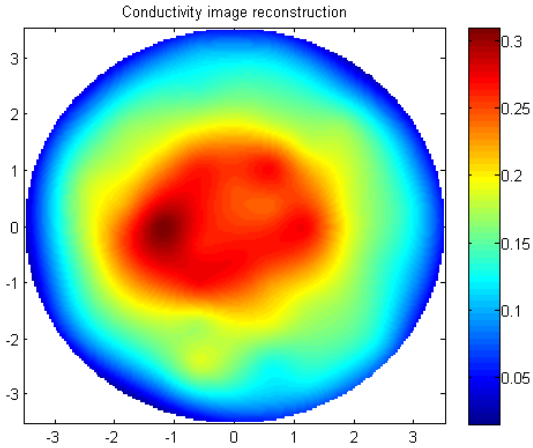

(c) $z = 10$mm

Figure 4.49: Numerical reconstructions of a cylindrical inclusion of radius 20mm in position 1 using noise level $\varepsilon = 5\%$.

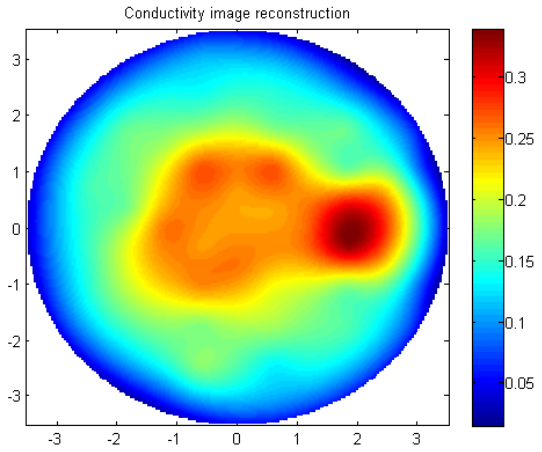

(a) $z = 2$mm

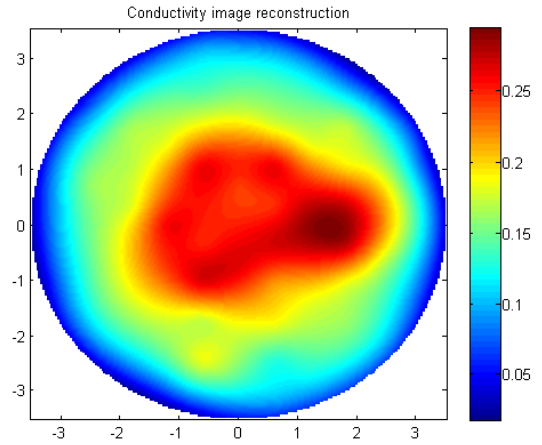

(b) $z = 5$mm

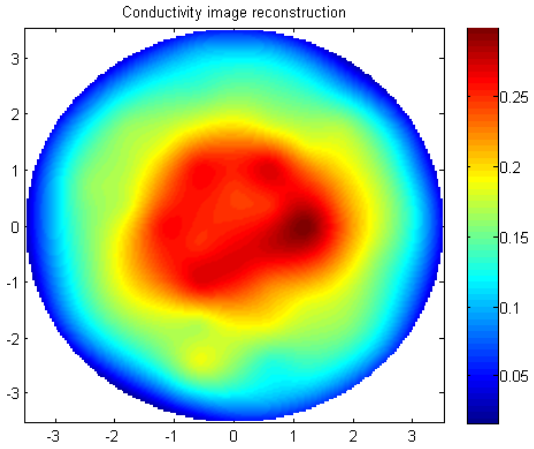

(c) $z = 10$mm

Figure 4.50: Numerical reconstructions of a cylindrical inclusion of radius 15mm in position 2 using noise level $\varepsilon = 5\%$.

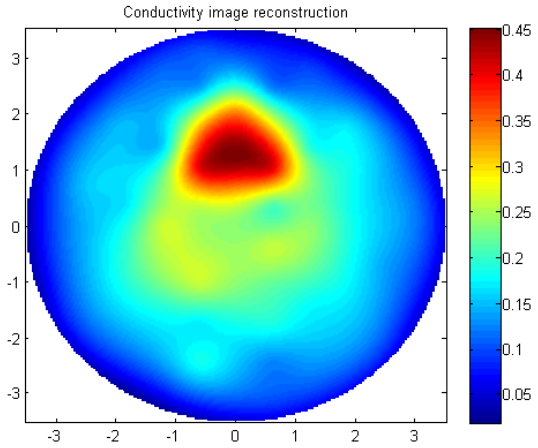

(a) $z = 2$mm

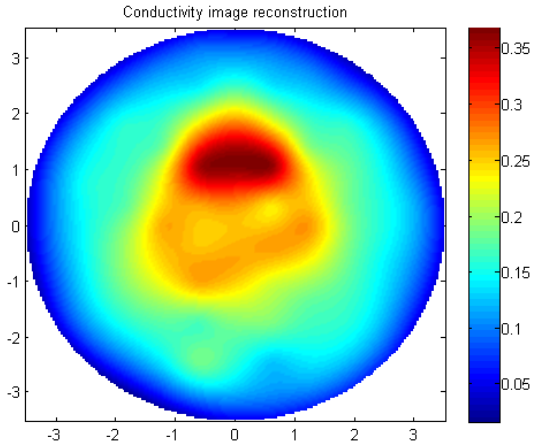

(b) $z = 5$mm

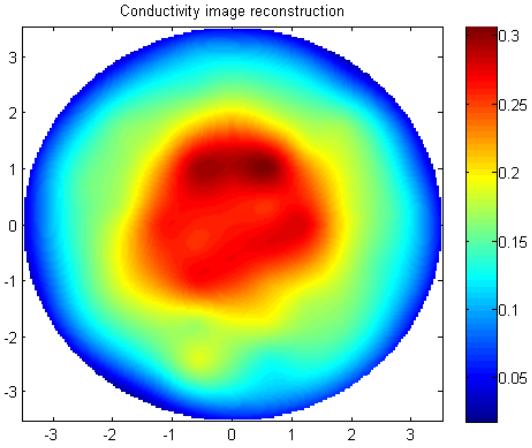

(c) $z = 10$mm

Figure 4.51: Numerical reconstructions of a cylindrical inclusion of radius 15mm in position 3 using noise level $\varepsilon = 5\%$.

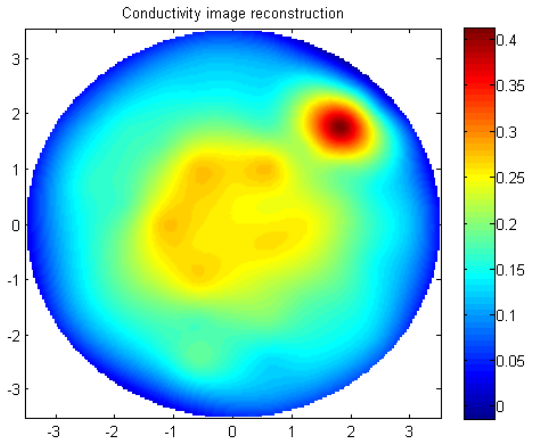

(a) $z = 2$mm

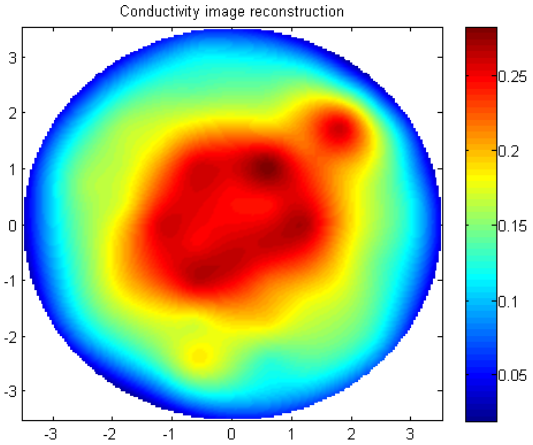

(b) $z = 5$mm

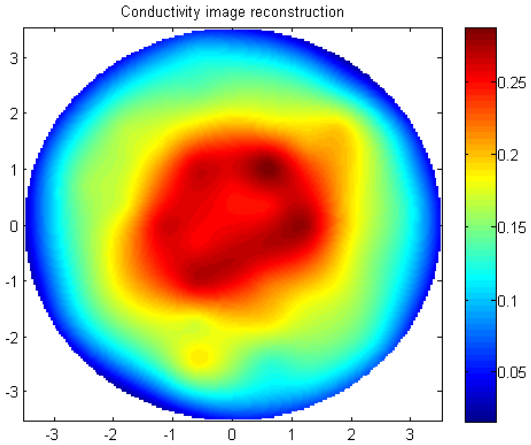

(c) $z = 10$mm

Figure 4.52: Numerical reconstructions of a cylindrical inclusion of radius 15mm in position 4 using noise level $\varepsilon = 5\%$.

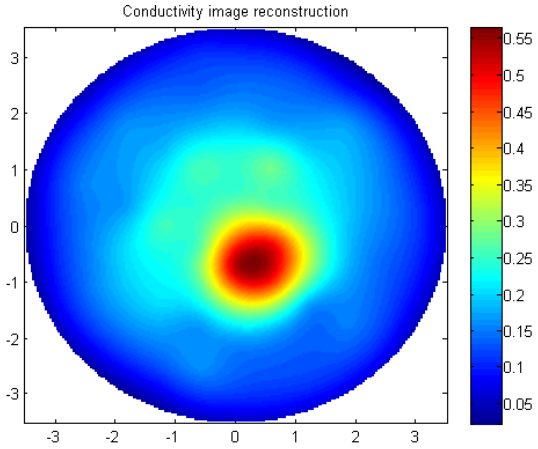

(a) $z = 2$mm

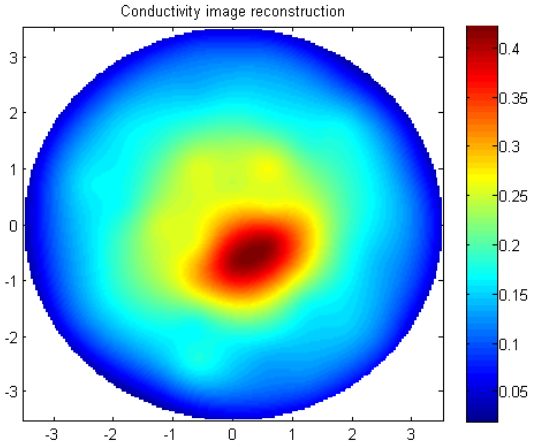

(b) $z = 5$mm

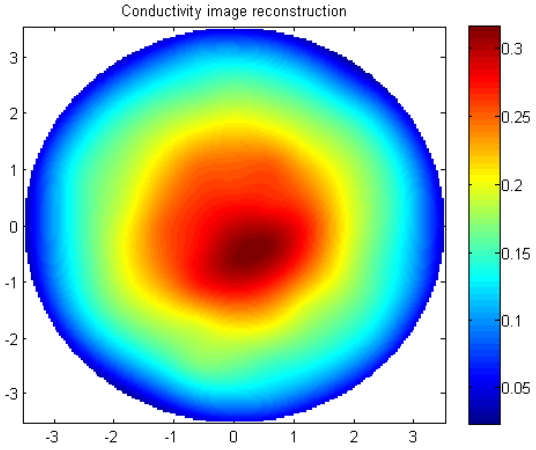

(c) $z = 10$mm

Figure 4.53: Numerical reconstructions of a cylindrical inclusion of radius 15mm in position 5 using noise level $\varepsilon = 5\%$.

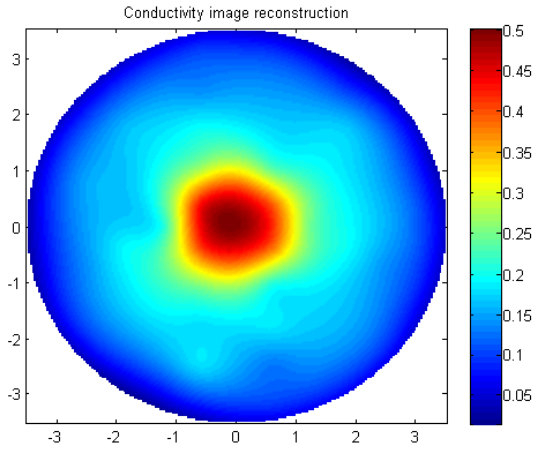

(a) $z = 2$mm

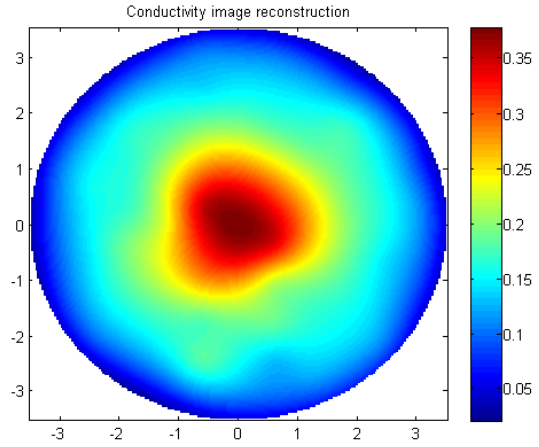

(b) $z = 5$mm

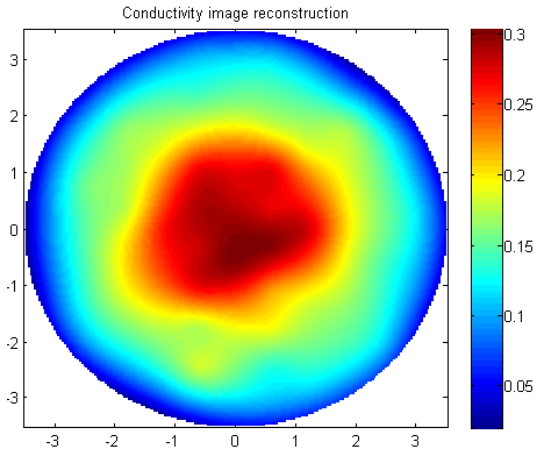

(c) $z = 10$mm

Figure 4.54: Numerical reconstructions of a cylindrical inclusion of radius 15mm in position 6 using noise level $\varepsilon = 5\%$.

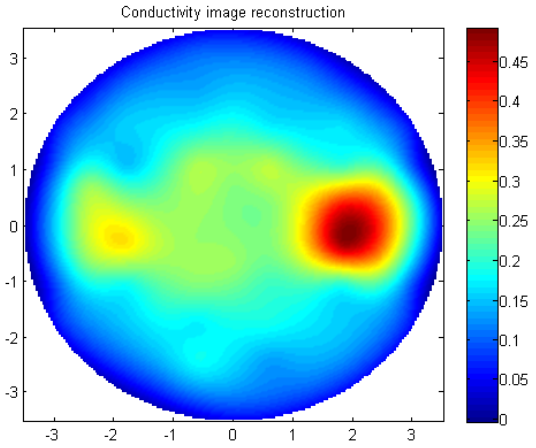

(a) $z = 2$mm

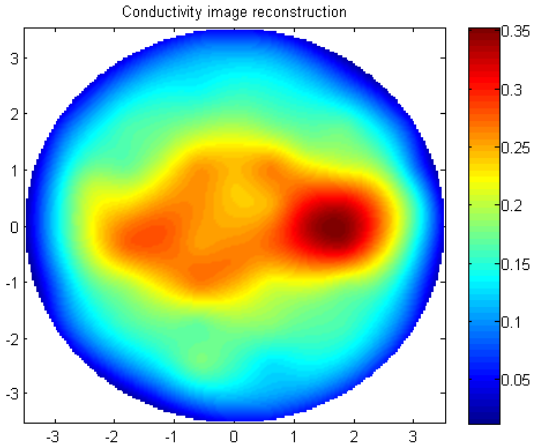

(b) $z = 5$mm

Figure 4.55: Numerical reconstructions of two cylindrical inclusions of radii 15mm and 20mm in position 1 and 2, respectively using noise level $\varepsilon = 5\%$.

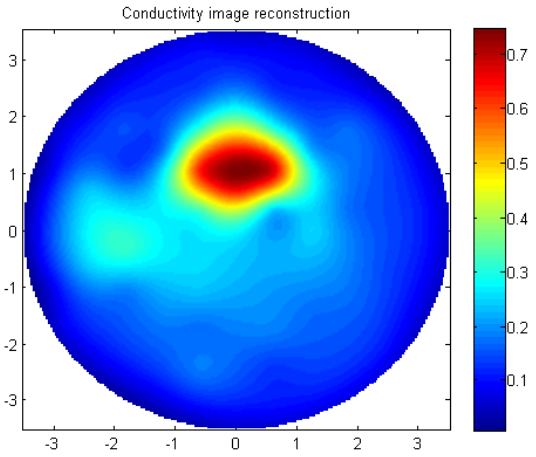

(a) $z = 2$mm

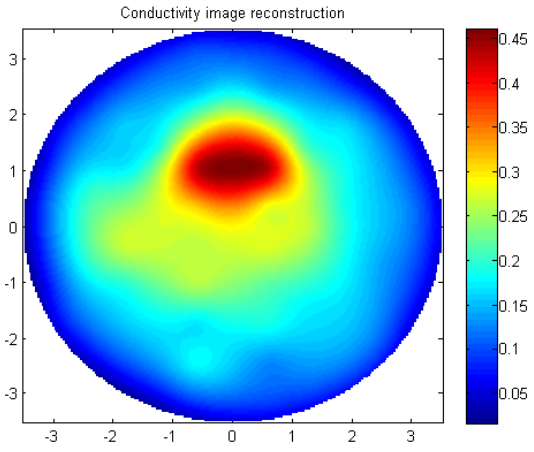

(b) $z = 5$mm

Figure 4.56: Numerical reconstructions of two cylindrical inclusions of radii 15mm and 20mm in position 1 and 3, respectively using noise level $\varepsilon = 5\%$.

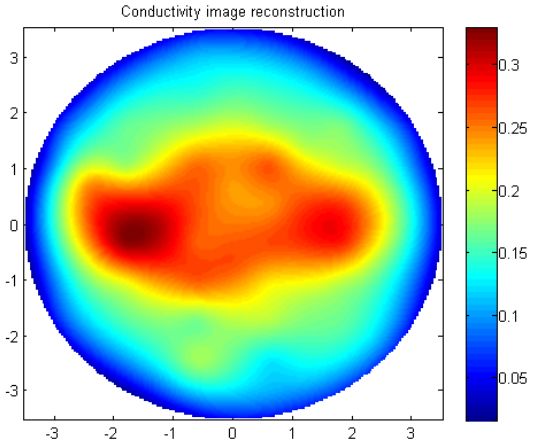

(a) $z = 2$mm

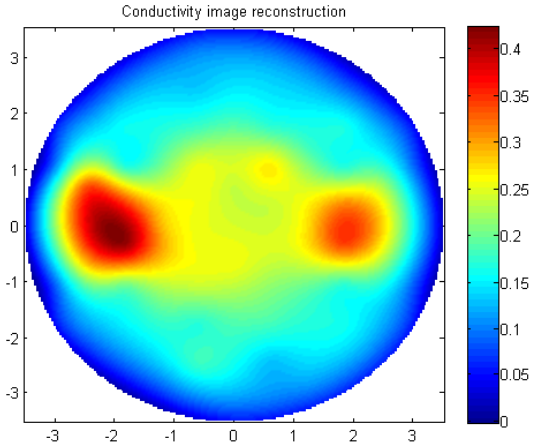

(b) $z = 5$mm

Figure 4.57: Numerical reconstructions of two cylindrical inclusions of radii 15mm and 20mm in position 2 and 1, respectively using noise level $\varepsilon = 5\%$.

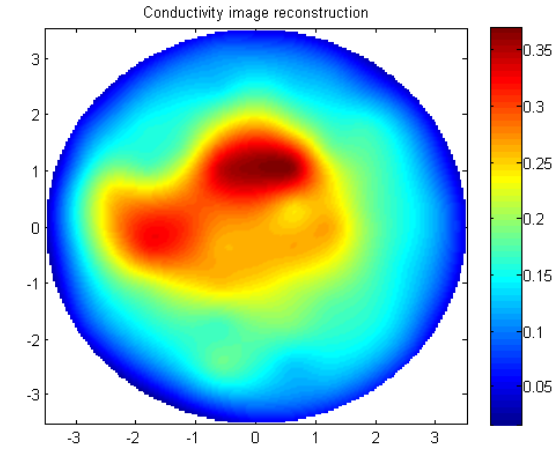

(a) $z = 2$mm

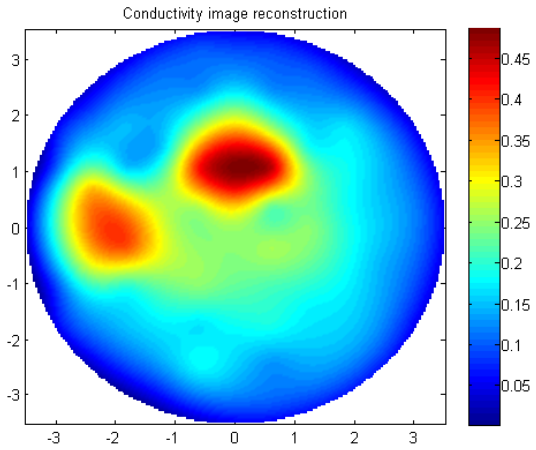

(b) $z = 5$mm

Figure 4.58: Numerical reconstructions of two cylindrical inclusions of radii 15mm and 20mm in position 3 and 1, respectively using noise level $\varepsilon = 5\%$.

All the reconstructions in this set are obtained from simulated data generated numerically by EIDORS. The reconstructions display a good spatial resolution and are very similar to those obtained from real data, although the simulated data was obtained for inclusions of conductivity only four times the background and not for metallic objects which are perfect conductors. This indicates that the sensing head with eighteen active and fifty four passive electrodes could detect tumours not only metallic objects located at distances up to 1cm from the skin surface.

4.4 Summary

Algorithms based on discrete resistor networks are attractive mainly because of their applications in EIT as simple non-iterative reconstruction techniques. These approaches arise naturally in medical EIT, since the human body can be regarded as an electrically conductive object made of a resistive network. This is the reason why one of the two-dimensional reconstruction algorithms developed by Oxford Brookes University in collaboration with University of Mainz for Mainz-Brookes tomographs is based on modelling the measuring area as a resistor network of hexagonal pattern.

There are different prototypes of the Mainz-Brookes mammographs: an old one which has twelve outer electrodes for injecting currents with twenty four current splits, and thirty six inner electrodes where potential are measured, a more recent one which also has twelve electrodes for injecting currents with eighteen splits and fifty four electrodes for measuring potentials, and finally an improved design of the prototype, which is based on increasing the number of the outer electrodes in the previous design. This prototype has eighteen outer electrodes for injecting currents with no splits, and fifty four inner electrodes.

Numerical experiments have shown that increasing the number of electrodes for injecting current has significantly improved the sensitivity of the Mainz-Brookes EIT system. However, increasing the number of electrodes for measuring potentials have resulted in an unstable inverse problem which could not be regularised.

In the next chapter a novel non-iterative three-dimensional reconstruction algorithm proposed for imaging breast cancer will be presented from data collected on a rectangular array.

Chapter 5

A Three-dimensional Image Reconstruction Algorithm for Electrical Impedance Tomography using Planar Electrode Arrays

5.1 Introduction

Several EIT mammographic sensors have been developed recently at the University of Mainz in collaboration with Oxford Brookes University. In contrast to most previous EIT instruments designed for breast cancer detection [7], but similar to devices studied by [32, 42, 56, 168, 194, 195], these mammographic sensors are planar. Detailed descriptions of earlier prototypes can be found in section 4.2.3. The latest design consists of a planar sensing head with thirty six disk electrodes of equal size arranged in a rectangular array of twenty outer (active) electrodes where the external currents are injected, and sixteen inner (passive) electrodes where the induced voltages are measured, see Figure 5.1(a). As in the previous prototypes, to avoid any problems due to the unknown contact impedance, the voltages are not measured at the active electrodes, instead, very high impedance voltage measurements are taken

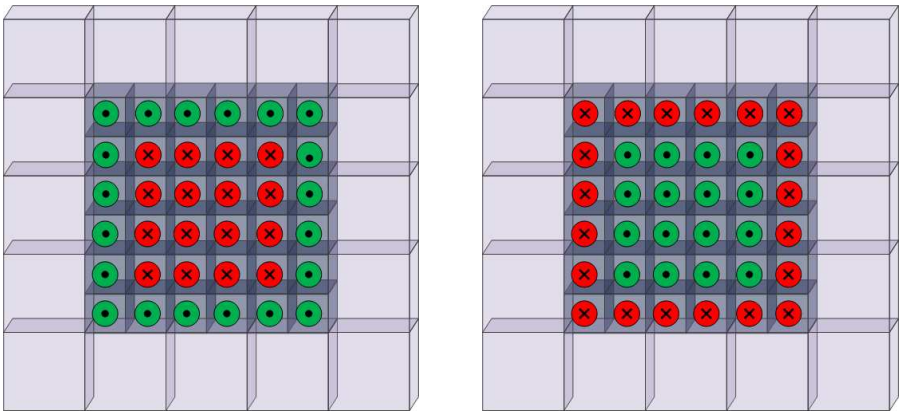

(a) Real experimental setup (b) Thought experimental setup

Figure 5.1: Layout of the rectangular electrode array of the latest prototype developed at the University of Mainz in collaboration with Oxford Brookes University: ● are the active electrodes used for current injection, and ⊗ are the passive electrodes used for potential measurements.

at the sixteen passive electrodes and therefore, the problem of the unknown contact impedance is eliminated. Also, this device has a fixed geometry and the positions of the electrodes are exactly known. Voltage measurements are relative to the systems ground as in the previous devices.

Almost all planar EIT devices [7, 32, 42, 56, 168, 194, 195] use the same electrodes for current injection and voltage measurement. The excitation current is injected (extracted) at one pair of electrodes at a time and the resulting voltage is measured at all or some of the remaining electrodes. The novelty of this EIT device, and hence of the image reconstruction methods proposed consists precisely in the distinct use of active and passive electrodes. The active electrodes are used only for current injection while the passive electrodes only for voltage measurements.

In two-dimensions, two different non-iterative algorithms were developed for imaging the conductivity at the surface using the tomographs designed at the University of Mainz, one based on a discrete resistor network model described in Chapter 4, and an

integral equation formulation approach which is described in [177,196]. In both cases numerical reconstructions had very good spatial resolution, and the algorithms were robust with respect to errors in the data. A three-dimensional iterative reconstruction method that enforced sparsity and used an adapted complete electrode model was also applied to these devices in [178]. Although it produced good images, this iterative procedure proved to be quite demanding computationally and sensitive to the choice of the regularization parameter.

The purpose of the current research is to respond to these issues i.e. the two-dimensional nature of the first two algorithms and the numerical sensitivity of the sparsity algorithm, by developing a simple, direct and rapid three dimensional reconstruction algorithm to image the region beneath the rectangular electrode array. The proposed inversion technique is intended to be used in the future for conductivity imaging using real data collected by the specific EIT device described above. The reconstruction method is similar to an approach described in [197] and is based on linearising the conductivity distribution about a constant approximation in order to reduce the computational demands.

The structure of this chapter is as follows: in Section 5.2 the mathematical formulation of the inverse problem and of the method proposed to image the conductivity are presented. Section 5.3 is dedicated to the numerical implementation of the reconstruction algorithm. The performance of the algorithm is illustrated by showing a number of reconstructions from simulated data in Section 5.4.

5.2 Mathematical Formulation

Since the EIT sensor is much smaller than the human body to which it is applied, and given the rapid decay of the induced potentials as we move away from the top surface (see equation 5.3), the mathematical analysis of breast cancer detection can be considered to be the inverse conductivity problem of EIT on an unbounded domain, specifically the lower half space. Let $\Omega = \{(x, y, z) : z < 0\} \in \mathbb{R}^3$ be a conductive object with boundary $\partial\Omega = \{(x, y, z) : z = 0\}$. Suppose that $\sigma \in L^\infty(\Omega)$ is a strictly positive isotropic scalar electrical conductivity distribution and that there are no current sources inside Ω. A set of L electrodes is placed on $\partial\Omega$ in a rectangular array. Let $\{e_l\}_{l=1}^{M}$ be the set of passive electrodes (voltage measurement) and $\{e_l\}_{l=M+1}^{L}$ be the active electrodes (current injection). If low-frequency currents are applied to the active electrodes, the electric potential u satisfies the following generalized Laplace equation

$$\nabla \cdot (\sigma(x, y, z)\nabla u(x, y, z)) = 0 \quad \text{in} \quad \Omega, \tag{5.1}$$

subject to the boundary condition

$$\sigma(x, y, 0)\frac{\partial u}{\partial z}(x, y, 0) = j(x, y) \quad \text{on} \quad \partial\Omega, \tag{5.2}$$

where j is the induced current density distribution.

In this approach we restrict the analysis to currents $j \in L^2(\partial\Omega)$ and to weak solutions $u \in H^{1,\alpha}(\Omega), (\alpha > 1)$ of equation (5.1) in the lower half-space Ω for which the following point-wise estimates hold uniformly with respect to the direction of $(x, y, z) / \sqrt{x^2 + y^2 + z^2}$:

$$|u(x, y, z)| = \mathcal{O}\left(1/\sqrt{x^2 + y^2 + z^2}\right) \text{ as } \sqrt{x^2 + y^2 + z^2} \to \infty, \tag{5.3}$$

and

$$\left|\frac{\partial u}{\partial \xi}\right| = \mathcal{O}\left(1/\left(x^2+y^2+z^2\right)\right) \text{ as } \sqrt{x^2+y^2+z^2} \to \infty \text{ for } \xi = x, y, z. \tag{5.4}$$

Further details on the definition of the Sobolev spaces $H^{1,\alpha}(\Omega)$ and on the derivation of these asymptotic estimates can be found in [198].

Since in this application the voltages are not measured at the active electrodes, the ave-gap electrode model [90] can be used. Therefore, the current density is assumed to be uniformly distributed over each electrode on the active electrode region and that it is zero outside of the support of all active electrodes. Hence, j is approximated by

$$j(x,y) = \begin{cases} I_l/A_l\,, & (x,y) \quad on \quad e_l\,, \quad l = M+1, \ldots, L \\ 0\,, & \text{otherwise}\,, \end{cases} \tag{5.5}$$

where I_l is the current sent to the lth active electrode e_l and A_l is the area of e_l.

In this experimental setup, a basis of current patterns $\{\mathbf{I}^1, \ldots, \mathbf{I}^{L-M-1}\}$ is applied to the set of $L-M$ active electrodes $\{e_l\}_{l=M+1}^{L}$. For each current pattern $\mathbf{I}^k = \left(I_{M+1}^k, \ldots, I_L^k\right)$, $k = 1, \ldots, L-M-1$, the resulting potentials $\mathbf{U}^k = \left(U_1^k, \ldots, U_M^k\right)$ are measured at the set of M passive electrodes $\{e_l\}_{l=1}^{M}$. The ave-gap model predicts the voltage measured on each electrode as the average of the solution u^k to (5.1), (5.2) and (5.5) with $j = j^k$ over the surface of the electrode:

$$U_l^k = \frac{1}{A_l}\int_{e_l} u^k(x,y)dS\,, \quad l = 1, \ldots, M\,. \tag{5.6}$$

The inverse problem is to estimate the conductivity $\sigma(x,y,z)$ from all $L-M-1$ linearly independent sets of surface measurements.

The proposed reconstruction algorithm is based on the assumption that the spatially varying conductivity is a small perturbation from a constant and known background conductivity σ_0, i.e.

$$\sigma(x, y, z) = \sigma_0 + \delta\sigma(x, y, z)\,, \tag{5.7}$$

and $\sigma = \sigma_0$ near $\partial\Omega$.

For the development of the imaging algorithm, the potentials u_0 and v_0 which are solutions of two theoretical homogeneous forward problems are first introduced. Let u_0 to be the solution of (5.1), (5.2) and (5.5) for $\sigma = \sigma_0$ and let v_0 be the solution of the following boundary value problem:

$$\nabla \cdot (\sigma_0 \nabla v_0(x, y, z)) = 0, \quad \text{in} \quad \Omega, \tag{5.8}$$

$$\sigma_0 \frac{\partial v_0}{\partial z}(x, y, 0) = \tilde{j}(x, y) = \begin{cases} \tilde{I}_l / A_l\,, & (x, y) \quad on \quad e_l\,, \quad l = 1, \ldots, M \\ 0\,, & \text{otherwise}\,, \end{cases} \tag{5.9}$$

where $\tilde{I}_l$ is a simulated current applied at the lth passive electrode. More explicitly, u_0 is the potential created in Ω if it consisted of a material of constant conductivity σ_0, while v_0 is the induced potential when currents are applied to this object of uniform conductivity distribution but reversing the roles of the active and passive electrodes. An illustration of the thought experimental setup corresponding to the second homogeneous forward problem is presented in Figure 5.1(b). There are $M - 1$ linearly independent simulated current patterns $\{\tilde{\mathbf{I}}^1, \ldots, \tilde{\mathbf{I}}^{M-1}\}$, where $\tilde{\mathbf{I}}^i = (I_1^i, \ldots, I_M^i)$, that can be applied to the M passive electrodes.

Let us now consider the following identity:

$$\int_\Omega \left[v_0(\nabla \cdot (\sigma \nabla u) - \nabla \cdot (\sigma_0 \nabla u_0)) - (u - u_0)\, \nabla \cdot (\sigma_0 \nabla v_0) \right] dV = 0\,. \tag{5.10}$$

By applying Gauss's divergence theorem [199] and taking into account the asymptotic behaviour of weak solutions of (5.1) and (5.8) given by equations (5.3)-(5.4), we can express

$$\int_{\Omega} \nabla \cdot (v_0 \sigma \nabla u)\, dV = \int_{\partial\Omega} v_0 \left(\sigma \frac{\partial u}{\partial z}\right) dS \tag{5.11}$$

and, hence, the following identity can be used for the first term in equation (5.10)

$$\int_{\Omega} v_0 \nabla \cdot (\sigma \nabla u)\, dV = \int_{\partial\Omega} v_0 \left(\sigma \frac{\partial u}{\partial z}\right) dS - \int_{\Omega} \sigma \nabla v_0 \cdot \nabla u \, dV\,. \tag{5.12}$$

Similarly, the remaining two terms in equation (5.10) can be rewritten as

$$\int_{\Omega} v_0 \nabla \cdot (\sigma_0 \nabla u_0)\, dV = \int_{\partial\Omega} v_0 \left(\sigma_0 \frac{\partial u_0}{\partial z}\right) dS - \int_{\Omega} \sigma_0 \nabla v_0 \cdot \nabla u_0 \, dV, \tag{5.13}$$

$$\int_{\Omega} (u - u_0) \nabla \cdot (\sigma_0 \nabla v_0)\, dV = \int_{\partial\Omega} (u - u_0) \left(\sigma_0 \frac{\partial v_0}{\partial z}\right) dS - \int_{\Omega} \sigma_0 \nabla v_0 \cdot \nabla (u - u_0)\, dV. \tag{5.14}$$

Consequently, by using identities (5.12)-(5.14) and (5.7) in equation (5.10), it follows that

$$\begin{aligned} \int_{\partial\Omega} \left[v_0 \left(\sigma \frac{\partial u}{\partial z} - \sigma_0 \frac{\partial u_0}{\partial z}\right) \right. &- \left. (u_0 - u) \left(\sigma_0 \frac{\partial v_0}{\partial z}\right) \right] dS \\ &= \int_{\Omega} \left[(\sigma \nabla u - \sigma_0 \nabla u_0) \cdot \nabla v_0 - \sigma_0 \nabla (u - u_0) \cdot \nabla v_0 \right] dV. \end{aligned} \tag{5.15}$$

Since both u and u_0 satisfy the same Neumann boundary condition (5.2), i.e. $j = \sigma \partial u/\partial z = \sigma_0 \partial u_0/\partial z$, the first term under the integral on the left-hand side of (5.15) is zero. Thus, after combining the like terms on the right-hand side, equation (5.15) becomes:

$$\int_{\partial\Omega} (u_0 - u) \left(\sigma_0 \frac{\partial v_0}{\partial z}\right) dS = \int_{\Omega} \delta \sigma \nabla v_0 \cdot \nabla u \, dV\,. \tag{5.16}$$

Linearising the potential u about σ_0 yields:

$$u(x,y,z) = u_0(x,y,z) + \delta u(x,y,z)\,, \tag{5.17}$$

where $\delta u = \mathcal{O}(\delta\sigma)$. Substituting this linearisation in the right-hand side of equation (5.16), the following integral equation can be derived for $\delta\sigma$:

$$\int_{\partial\Omega} (u_0 - u)\left(\sigma_0 \frac{\partial v_0}{\partial z}\right) dS = \int_{\Omega} \delta\sigma \nabla v_0 \cdot \nabla u_0 \, dV + \mathcal{O}(\delta\sigma^2). \tag{5.18}$$

Equation (5.18) is true for any u^k and u_0^k, solutions of equation (5.1) for a given current pattern j^k applied to the active electrodes, and for any v^i, solution of equation (5.8) subject to a current density $\tilde{j}^i$ corresponding to the i-th simulated current pattern $\tilde{\mathbf{I}}^i$ applied at the passive electrodes and given by equation (5.9). Thus,

$$\begin{aligned} \sum_{l=1}^{M} \int_{e_l} \left(u_0^k - u^k\right) \tilde{j}^i \, dS \;\; &\approx \;\; \int_{\Omega} \delta\sigma \nabla v_0^i \cdot \nabla u_0^k \, dV\,, \\ & \qquad k = 1, \ldots, L - M - 1 \quad \text{and} \quad i = 1, \ldots, M - 1 \end{aligned} \tag{5.19}$$

Using the ave-gap model for the electrodes, the inverse problem becomes that of finding the perturbation $\delta\sigma$ satisfying the following system of equations

$$\begin{aligned} \sum_{l=1}^{M} \left(U_{0,l}^k - U_l^k\right) \tilde{I}_l^i \;\; &= \;\; \int_{\Omega} \delta\sigma \nabla v_0^i \cdot \nabla u_0^k \, dV\,, \\ & \qquad k = 1, \ldots, L - M - 1 \quad \text{and} \quad i = 1, \ldots, M - 1\,, \end{aligned} \tag{5.20}$$

where

$$U_{0,l}^k = \frac{1}{A_l} \int_{e_l} u_0^k(x,y) dS\,. \tag{5.21}$$

The left-hand side of (5.20) contains only measured and simulated quantities, U_l^k and

$U^k_{0,l}$, respectively, and will be denoted by $B(i,k)$, i.e.

$$B(i,k) = \sum_{l=1}^{M} \left(U^k_{0,l} - U^k_l\right) \tilde{I}^i_l \,. \tag{5.22}$$

A further simplification that can be introduced to aid the image reconstruction process comes from the fact that the objective is to identify a small object(tumour) of uniform conductivity lying within a region (breast tissue) of uniform, but different and known, conductivity. It can therefore be assumed that the conductivity is piecewise constant. In this case the half-space can be approximated by voxels, $\{V_n\}_{n=1}^{\infty}$, and thus

$$\delta\sigma(x,y,z) = \sum_{n=1}^{\infty} \delta\sigma_n \chi_n(x,y,z)\,,$$

where χ_n is the characteristic function over the nth voxel, i.e.

$$\chi_n(x,y,z) = \begin{cases} 1\,, & (x,y,z) \in V_n\,, \\ 0\,, & \text{otherwise}\,, \end{cases}$$

However, in practice, a finite number of measurements are possible and, hence, only conductivities of a finite number N of voxels, where $N \leq (L-M-1)\times(M-1)$ can be reconstructed. In this case, equation (5.20) reduces to an over-determined linear system of equations

$$B(i,k) = \sum_{n=1}^{N} A(i,k,n)\delta\sigma_n\,, \quad k = 1,\ldots,L-M-1 \quad \text{and} \quad i = 1,\ldots,M-1\,, \tag{5.23}$$

where

$$A(i,k,n) = \int_{V_n} \nabla v^i_0 \cdot \nabla u^k_0 \, dV\,. \tag{5.24}$$

Note that the matrix $\mathbf{A}$ is independent of the measured voltage data and it can

be computed in advance and stored for use with other reconstructions in the same geometry.

Since, the linearized system of equations (5.23) inherits ill-posedness from the original nonlinear inverse conductivity problem, the matrix $\mathbf{A}$ is ill-conditioned and regularization is required. The system of equations (5.23) is therefore solved by means of generalized inverse and truncated singular value decomposition was used as the regularization scheme [200]. In this way very small singular values (i.e. smaller than a certain threshold ϵ) will be neglected and will not enter in the reconstruction.

5.3 Numerical Implementation

5.3.1 Electrode and Voxel Configuration

As described earlier, the planar array of electrodes is rectangular and consists of $L\,(=36)$ circular electrodes of radius $r_l\,(=3.5\text{mm})$, $l = 1, \ldots, L$, which are equally spaced. The distance between the centres of two adjacent electrodes is $d\,(=12\text{mm})$. There are $M\,(=16)$ passive (inner) electrodes and $L-M\,(=20)$ active (outer) electrodes. The terms outer and inner are relative to the positions of the electrodes in the array. As seen in Figure 5.1(a), all the electrodes located on the boundary of the rectangular array are active, while the remaining ones are passive. At this point, it is important to note that this electrode configuration not only provides a simpler geometry than the hexagonal pattern of the earlier prototypes in [177, 196], but for some electrical impedance imaging problems in geophysics, archaeology, medical diagnosis and industrial plant control, an appropriate electrode geometry may be that of a rectangular array of electrodes placed on a surface plane. For example, rect-

angular electrode configurations have been employed before for medical applications such as: breast cancer detection [56, 164, 168, 197], respiratory monitoring, functional imaging of the digestive system and peripheral venography [201], or for engineering and environmental studies (e.g. [202] and the references therein).

For the numerical implementation of the algorithm, a layered voxel configuration is used, similar to the one introduced in [197] and it is depicted in Figure 5.2(b). There are 52 voxels in each layer:

36 small inner voxels aligned immediately under the electrodes of dimensions 12mm $\times$ 12mm $\times$ 2mm, and

16 outer large voxels arranged around the boundary of the electrode array of dimensions 24mm $\times$ 24mm $\times$ 2mm (i.e. the same height, 2mm, but four times the volume of a small voxel).

Although the interest is to image the conductivity in the region under the electrode array, the voxel configuration has to model, nevertheless, an unbounded domain. The reason for introducing the outer large voxels is to achieve this in a practical manner. As mentioned earlier, the total number of voxels should satisfy $N \leq (L - M - 1) \times (M - 1) = 285$. Hence, since there are 52 voxels per layer, no more than 5 layers of voxels can be considered (i.e. $N = 5 \times 52 = 260 \leq 285$). Note that the number of voxels per layer is determined by the geometry of the electrode array, while the total number of layers is constrained by the number of active and passive electrodes, i.e. the total number (=285) of possible combinations of measured and simulated currents. The height of each voxel layer, however, is not fixed and it can be adjusted to allow conductivity reconstructions up to the required depths. Most of breast tumours are located near the skin surface [203]. The results of a clinical study of single-breast

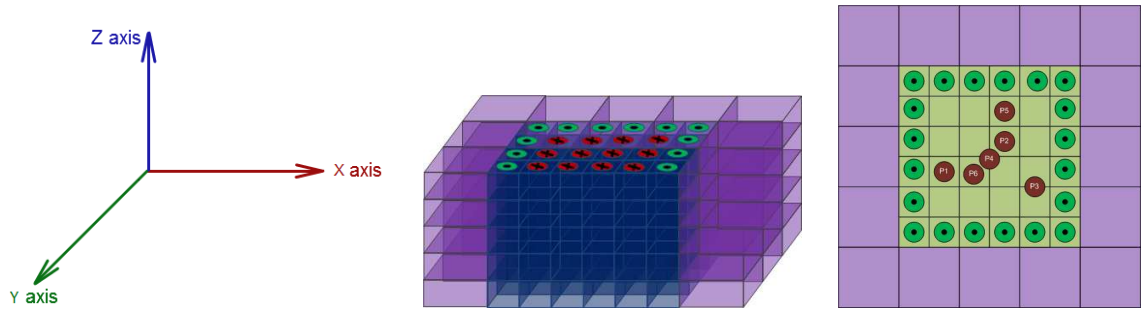

(a) x-y-z plan (b) Three-dimensional view (c) Two-dimensional view

Figure 5.2: Voxel configuration: ● are the active electrodes, ⊗ are the passive electrodes, and $P1 - P5$ denote the positions in the xy-plane where inclusions were placed in the numerical simulations.

lesions located at least 0.5cm from the skin surface and pectoralis margin and at least 2.0cm from the nipple showed that the mean distance from the skin surface to the lesion was 0.9cm (range, $0.5 - 1.7$cm) [204]. Therefore, in this approach the chosen voxel configuration allows reconstructions up to a depth of 1cm (=5 layers×2mm).

5.3.2 Computation of Matrix A

Before discussing the construction of matrix $\mathbf{A}$ in (5.24), the problem of computing the potentials u_0 and v_0 for a homogeneous medium is first addressed.

Let $P = (x, y, z)$ be an interior point in Ω, $Q_0 = (x', y', 0)$ be a point on the boundary $\partial\Omega$ and $Q_l = (x_l, y_l, 0)$ be the centre of lth electrode. For a constant conductivity distribution σ_0, the solutions of the two theoretical forward problems, defined by (5.1),

(5.2) and (5.5) with $j = j^i$ and (5.8)-(5.9) with $\tilde{j} = \tilde{j}^k$, are straightforward [199]:

$$\begin{aligned} u_0^k(x,y,z) &= \frac{1}{2\pi\sigma_0}\int_{\partial\Omega}\frac{1}{r_{PQ_0}}j^k(x',y')\,dx'\,dy' \\ &= \frac{1}{2\pi\sigma_0}\sum_{l'=M+1}^{L}\frac{I_{l'}^k}{A_{l'}}\int_{e_{l'}}\frac{1}{r_{PQ_0}}\,dx'\,dy'\,, \quad k=1,\ldots,L-M-1\,, \end{aligned} \tag{5.25}$$

and, respectively,

$$\begin{aligned} v_0^i(x,y,z) &= \frac{1}{2\pi\sigma_0}\int_{\partial\Omega}\frac{1}{r_{PQ_0}}\tilde{j}^i(x',y')\,dx'\,dy' \\ &= \frac{1}{2\pi\sigma_0}\sum_{l=1}^{M}\frac{\tilde{I}_l^i}{A_l}\int_{e_l}\frac{1}{r_{PQ_0}}\,dx'\,dy'\,, \quad i=1,\ldots,M-1\,, \end{aligned} \tag{5.26}$$

where $r_{PQ_0} = |P - Q_0| = \sqrt{(x-x')^2 + (y-y')^2 + z^2}$.

In order to compute the entries of the matrix $\mathbf{A}$, the volume integral in (5.24) is fist discretized. To this end, the same approach as in [197] is followed and each of the voxels is divided into m subvoxels V_n^j ($j = m = 1$ for the inner voxels and $j = 1, ..., m = 4$ for the outer ones). Thus, there will be 100 subvoxels of equal volume per layer. The volume of the jth subvoxel of the nth voxel V_n^j is, therefore, $Vol_n^j = 12 \times 12 \times 2 = 288\text{mm}^3$. Using this dicretization, and the expressions for u_0^k and v_0^i given by equations (5.25) and (5.26), the following expression is obtained for the entries of the matrix $\mathbf{A}$ by evaluating the integral (5.24) at the points P_n^j, the centres of subvoxels V_n^j:

$$\begin{aligned} A(i,k,n) = \quad & \sum_{j=1}^{m}\frac{Vol_n^j}{(2\pi\sigma_0)^2}\sum_{l=1}^{M}\sum_{l'=M+1}^{L}\frac{\tilde{I}_l^i I_{l'}^k}{A_l A_{l'}} \times \\ & \left[\nabla_P\int_{e_l}\frac{1}{r_{PQ_0}}dx'\,dy'\right]_{P=P_n^j}\cdot\left[\nabla_P\int_{e_{l'}}\frac{1}{r_{PQ_0}}dx'\,dy'\right]_{P=P_n^j}. \end{aligned} \tag{5.27}$$

In order to evaluate these entries, the following quantity has to be is computed:

$$\nabla_P \int_{e_l} \frac{1}{r_{PQ_0}} dx'\, dy' = \nabla_P \int_{e_l} \frac{1}{|(P - Q_l) - (Q_0 - Q_l)|} dx'\, dy' \,, \quad \text{for} \quad l = 1, \ldots, L \tag{5.28}$$

These expressions were computed analytically by converting the integrals to cylindrical coordinates as follows. Let (r, θ, z) and $(s, \vartheta, 0)$ be the cylindrical coordinates of $\tilde{P} = P - Q_l$ and $\tilde{Q} = Q_0 - Q_l$, respectively. Specifically, $\tilde{Q} = (\tilde{x}, \tilde{y}, 0)$, where $\tilde{x} = x' - x_l = s\cos(\vartheta)$ and $\tilde{y} = y' - y_l = s\sin(\vartheta)$. Then, r_{PQ_0} can be expressed in cylindrical coordinates as

$$r_{PQ_0} = |\tilde{P} - \tilde{Q}| = \sqrt{r^2 + s^2 - 2rs\cos(\vartheta - \theta) + z^2} \,. \tag{5.29}$$

It is clear from symmetry that the following integral is independent of the polar angle θ, i.e.

$$\begin{aligned} \int_{e_l} \frac{1}{r_{PQ_0}} dx'\, dy' &= \int_0^{r_l} \int_0^{2\pi} \frac{1}{\sqrt{r^2 + s^2 - 2rs\cos(\vartheta - \theta) + z^2}} s\, ds\, d\vartheta \\ &= \int_0^{r_l} \int_0^{2\pi} \frac{1}{\sqrt{r^2 + s^2 - 2rs\cos\vartheta + z^2}} s\, ds\, d\vartheta \,. \end{aligned} \tag{5.30}$$

Hence,

$$\nabla_P \int_{e_l} \frac{1}{r_{PQ_0}} dx'\, dy' = \left(\mathbf{e}_r \frac{\partial}{\partial r} + \mathbf{e}_z \frac{\partial}{\partial z} \right) \int_0^{r_l} \int_0^{2\pi} \frac{1}{r_{PQ_0}} s\, ds\, d\vartheta \,, \tag{5.31}$$

with

$$\begin{aligned} \frac{\partial}{\partial r} \int_0^{r_l} \int_0^{2\pi} \frac{1}{r_{PQ_0}} s\, ds\, d\vartheta = \frac{2}{r} \sqrt{(r + r_l)^2 + z^2} \Bigg[& E\left(\frac{4rr_l}{(r + r_l)^2 + z^2} \right) \\ & - \frac{r^2 + r_l^2 + z^2}{(r + r_l)^2 + z^2} K\left(\frac{4rr_l}{(r + r_l)^2 + z^2} \right) \Bigg] \end{aligned} \tag{5.32}$$

and

$$\begin{aligned}\frac{\partial}{\partial z}\int_0^{r_l}\int_0^{2\pi}\frac{1}{r_{PQ_0}}s\,ds\,d\vartheta &= \frac{1}{\sqrt{(r+r_l)^2+z^2}}\times\left[4zK\left(\frac{4rr_l}{(r+r_l)^2+z^2}\right)\right.\\ &- 2i\times\left((r-r_l-iz)\Pi\left(\frac{2r_l}{r+r_l-iz}\middle|\frac{4rr_l}{(r+r_l)^2+z^2}\right)\right.\\ &+ \left.\left.(-r+r_l-iz)\Pi\left(\frac{2r_l}{r+r_l+iz}\middle|\frac{4rr_l}{(r+r_l)^2+z^2}\right)\right)\right]\end{aligned} \tag{5.33}$$

where $K(k)$, $E(k)$ and $\Pi(n|k)$ are the complete elliptic integrals of first, second and third kind, respectively. Further details about these special functions can be found in [205]. Both the r-component and the z-component of the gradient given by equations (5.32) and (5.33), respectively, are real valued functions. However, due to numerical inaccuracies in the computer algorithms used to evaluate these functions, there are always some residual imaginary parts in the order of the machine precision. To overcome this issue, only their real parts are considered in further computations.

Note that although in our implementation we preferred to use the above closed form expressions, all these integrals could also be evaluated to great accuracy by using a numerical quadrature method such as boundary elements (see, for example, [206]). This would be more consistent with the numerical experiments where the forward model is a bounded domain but at the cost of increased computation time.

5.3.3 Construction of Matrix B

For the construction of matrix **B** given by equation (5.22), the measured and simulated voltages, U_l^k and $U_{0,l}^k$, respectively are needed.

In practice, the voltages U_l^k are known experimental data. However, as no real data is yet available, instead, the measured voltages are simulated numerically as explained in Section 5.4.

In order to find the values of the simulated voltages $U_{0,l}^k$ given by equation (5.21), firstly $u_0^k(x,y) = u_0^k(x,y,z=0)$ has to be computed by evaluating the expression in equation (5.25) at $z=0$. To this end, the same change of variables as in subsection 3.2 and equation (5.30) is used. Note that due to the symmetry considerations of the integral (5.30), the solution u_0^k is also independent of the polar angle θ. Hence, $u_0^k(r,\theta,z=0) = u_0^k(r)$, and the following expression is obtained

$$u_0^k(r) = \frac{1}{2\pi\sigma_0} \sum_{l'=M+1}^{L} \frac{I_{l'}^k}{A_{l'}} \int_0^{r_{l'}} \int_0^{2\pi} \frac{1}{\sqrt{r^2+s^2-2rs\cos\vartheta}} s\, ds\, d\vartheta\,, \quad k = 1,\ldots,L-M-1\,. \tag{5.34}$$

The integral in equation (5.34) can be computed analytically, i.e.

$$\int_0^{r_{l'}} \int_0^{2\pi} \frac{1}{\sqrt{r^2+s^2-2rs\cos\vartheta}} s\, ds\, d\vartheta = 2\,(r+r_{l'})\, E\left(\frac{4\,r\,r_{l'}}{(r+r_{l'})^2}\right) - 2\,(r-r_{l'})\, K\left(\frac{4\,r\,r_{l'}}{(r+r_{l'})^2}\right)\,. \tag{5.35}$$

Once the currents applied at the active electrodes $I_{l'}^k$ are known from measurements, u_0^k can be estimated in a straightforward way using equations (5.34)-(5.35) at different points on the surfaces of passive electrodes e_l, $l = 1,\cdots,M$, and then obtain $U_{0,l}^k$ by evaluating numerically the integral in equation (5.21).

The simulated currents $\tilde{\mathbf{I}}^i = \left(I_1^k,\ldots,I_{16}^k\right)$, $i = 1,\ldots,M = 15$, are assumed to be standard trigonometric linearly independent current patterns, i.e.

$$\tilde{\mathbf{I}}_l^i = \begin{cases} \cos\left(i\,(l-1)\,\frac{2\pi}{M}\right), & i = 1,\ldots,\lfloor\frac{M}{2}\rfloor, \\ \sin\left(\left(i-\lfloor\frac{M}{2}\rfloor\right)(l-1)\,\frac{2\pi}{M}\right), & i = \lfloor\frac{M}{2}\rfloor,\ldots,M-1. \end{cases} \tag{5.36}$$

5.4 Numerical Examples

In this section, I present some reconstructions obtained by applying the above reconstruction algorithm to simulated data. The setup of the numerical tests mimicked closely the laboratory experiments presented in [40, 178]. A rectangular tank of length $L\,(= 15\text{cm})$, width $W\,(= 15\text{cm})$ and height $H\,(= 7.5\text{cm})$ is considered, which contained an isotropic medium of conductivity approximately equal to that of healthy breast tissue, $\sigma_0 = 200\text{mS/m}$. The rectangular array of electrodes was placed at the centre of the top of the tank (i.e. $z = 0\text{cm}$). The dimensions of the tank were much larger than those of the electrode array ($0.72\text{cm}\times 0.72\text{cm}$) and of the voxel configuration ($12\text{cm}\times 12\text{cm}\times 1\text{cm}$) used for conductivity reconstructions, thus approximating an infinite half space.

Cylindrical inclusions of radii $R_{15} = 1.5\text{mm}$, $R_{25} = 2.5\text{mm}$ and/or $R_{35} = 3.5\text{mm}$, heights $h = 5\text{mm}$ and conductivities $\sigma = 800\text{mS/m}$ or 600mS/m were then placed on below positions $P1 - P5$ in the xy-plane (see Figure 5.2(c)) and at different depths z. Note that the largest cylindrical object R_{35} has the same radius as the electrodes, while the other two, R_{25} and R_{15}, have much smaller radii. $P1$, $P2$ and $P5$ in Figure 5.2(c) are positions directly below a passive electrode, while $P4$ and $P5$ are positions between the passive electrodes.

To simulate the measured values of the potential on the boundary, the direct problem (5.1), (5.2) and (5.5) was first solved. In order to avoid inverse crimes and to test the robustness of the inversion techniques, EIDORS [207] was used as a forward solver. EIDORS is a finite element software package which has no connection with the reconstruction method under consideration. Current patterns similar to those defined in equation 5.36 were applied at the active electrodes, $\mathbf{I}^k = \left(I_{21}^k, \ldots, I_{36}^k\right)$, $k =$

$1, \ldots, L-M-1 = 19$. The direct problem was solved for each of the nineteen different current patterns and the values of the corresponding voltages were obtained at the passive electrodes $\mathbf{U}^k = \left(U_1^k, \ldots, U_{20}^k\right)$, $k = 1, \ldots, 19$, by interpolating the numerical solution at points on the surface of the electrodes and evaluate numerically the integral in equation (5.6). This was the data used by the reconstruction algorithm. The conductivities of all $N = 260$ voxels were obtained by inverting the over-determined linear system of equations (5.23). In the numerical examples considered, singular values smaller than $\epsilon = 10^{-5}$ were cut off (i.e. 35 singular values were used in the reconstructions).

As mentioned earlier, in EIT a noise level of 1% is reasonable in many circumstances, but in some medical applications greater accuracy can be achieved [191]. However, since the reconstruction method is quite stable with respect to the noise level in the data, in all the numerical examples discussed below, reconstruction results obtained from data with 2% additive Gaussian random errors are shown. Note that in all figures presented below the colour ranges are the same for each subplot. Moreover, the homogeneity properties of the proposed algorithm are good. As shown in Figure 5.3, it was possible to reconstruct an uniform distribution of conductivity of 200mS/m using simulated data for the tank with no inclusions.

In Figures 5.4, 5.5 and 5.6, I present the conductivity reconstructions for the medium size cylindrical object of radius R_{25} and conductivity 800mS/m (i.e. four times higher than the background conductivity) placed below position $P1$ (i.e. below an electrode and next to an active electrode) and at depths $z = -2$, -3 and -6mm, respectively, from the array of electrodes. The position of the inclusion in the xy-plane was successfully recovered in all three cases but the reconstructed conductivity values were smaller than the actual conductivity values. This difficulty in recovering the amplitude of high contrast conductivities is a common feature of EIT linearisation methods,

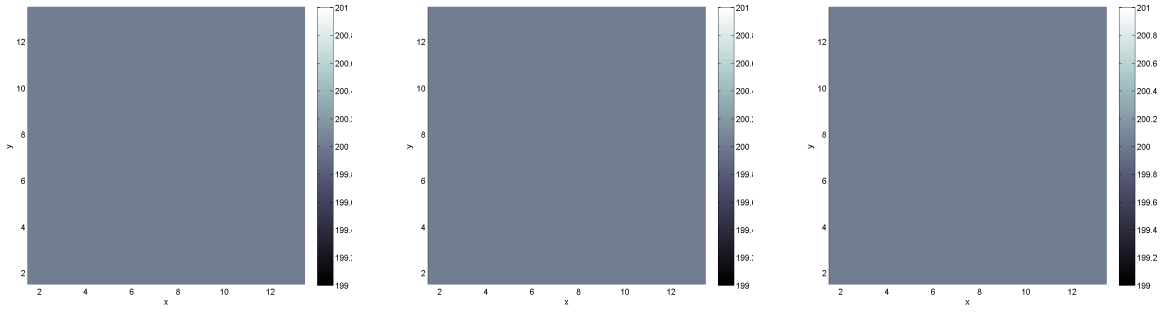

(a) Voxel Layer 1 (b) Voxel Layer 2 (c) Voxel Layer 3

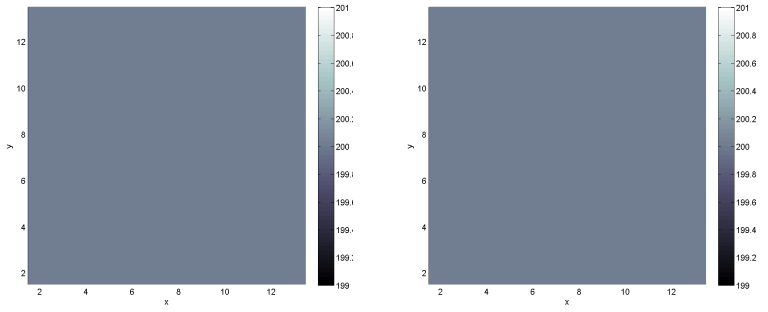

(d) Voxel Layer 4 (e) Voxel Layer 5

Figure 5.3: The reconstruction of an uniform distribution of conductivity of 200mS/m using simulated data for the tank with no inclusions.

see for example [177, 197, 208]. It was also found that estimating the depth of the inhomogeneity was more ill-posed than reconstructing its position in the xy-plane. For an inclusion placed at this position, the values of the reconstructed conductivities at position $P1$ were larger in the upper voxel layers with a maximum value attained in the second layer irrespective of the depths of the inclusions. However, the deeper the object, the smaller the values of the reconstructed conductivity. This suggests that some information about the depth location of the inclusions is present in the data, but as seen from Figures 5.4(f) and 5.5(f) there is limited information about objects' heights as it seems as if the inclusion extends over all five voxel layers. This conclusion is in agreement with the findings in [178].

To test the spatial resolution of the algorithm, I placed cylindrical inclusions of conductivity 800mS/m and of different radii R_{35}, R_{25} and R_{15} at position $P2$ (i.e. below an electrode, but further away from the active electrodes) and depth $z = -3$mm. The numerical results can be found in Figures 5.7, 5.8 and 5.9, respectively. Similar to the previous numerical experiments, the position of the inclusion in the plane of electrodes was well characterized. The values of the reconstructed conductivities at position $P2$ were also smaller than the true ones, but overall larger in the upper voxel layers with a maximum value attained in the first layer in this case. Moreover, as expected, the smaller the size of the inhomogeneity, the smaller were the values of the reconstructed conductivity. Note that, by using the electrode array and the experimental setup under consideration as well as the proposed three-dimensional reconstruction algorithm, I managed to detect inhomogeneities which are much smaller in size (i.e. a cylinder of radius R_{15} and height 5mm whose conductivity is only four times higher than the background) and up to larger depths than in [178, 196, 197].

When a cylindrical inhomogeneity of radius R_{25} and of conductivity 800mS/m was placed on a position between two electrodes, $P3$, or in the middle of four neighbouring

electrodes, $P4$, then the conductivity of all two or four adjacent voxels was much larger than that of the background, see Figures 5.10 and 5.11.

Next I demonstrate that the detection of a small conductive inhomogeneity is not affected by the presence of a more resistive tissue layer (i.e. the skin) at the surface. To this end, I included a 2mm thick resistive layer of conductivity 50mS/m layer directly under the surface. A cylindrical object of radius R_{35} was positioned at $P1$ and $z = -4$mm. As seen from the numerical reconstructions presented in Figure 5.12, the presence of the object is visible and its position in the xy-plane is well characterized.

The final simulations included in this Chapter consist of reconstructions of two conductive objects of radii R_{25} and R_{15} placed at positions $P5$ and $P6$, respectively, and at the same depth ($z = -3$mm). Firstly, in Figure 5.13 I present the results obtained when the two inclusions have the same conductivity (800mS/m). In this case, the presence of the smaller cylindrical object (R_{15}) is slightly shielded by the larger object (R_{25}). Then, in Figure 5.14 I show the reconstructions of objects of different conductivities (600mS/m and 800mS/m, respectively) when the presence of the smaller object is more pronounced.

5.5 Summary

In this Chapter I presented a three-dimensional non-iterative reconstruction algorithm developed for conductivity imaging with real data collected on a planar rectangular array of electrodes. Such an electrode configuration as well as the proposed

imaging technique are intended to be used for breast cancer detection. The algorithm is based on linearizing the conductivity about a constant value and allows real-time reconstructions. The performance of the algorithm was tested on numerically simulated data and I successfully detected small inclusions with conductivities three or four times the background lying beneath the data collection surface. The results were fairly stable with respect to the noise level in the data and displayed very good spatial resolution in the plane of electrodes.

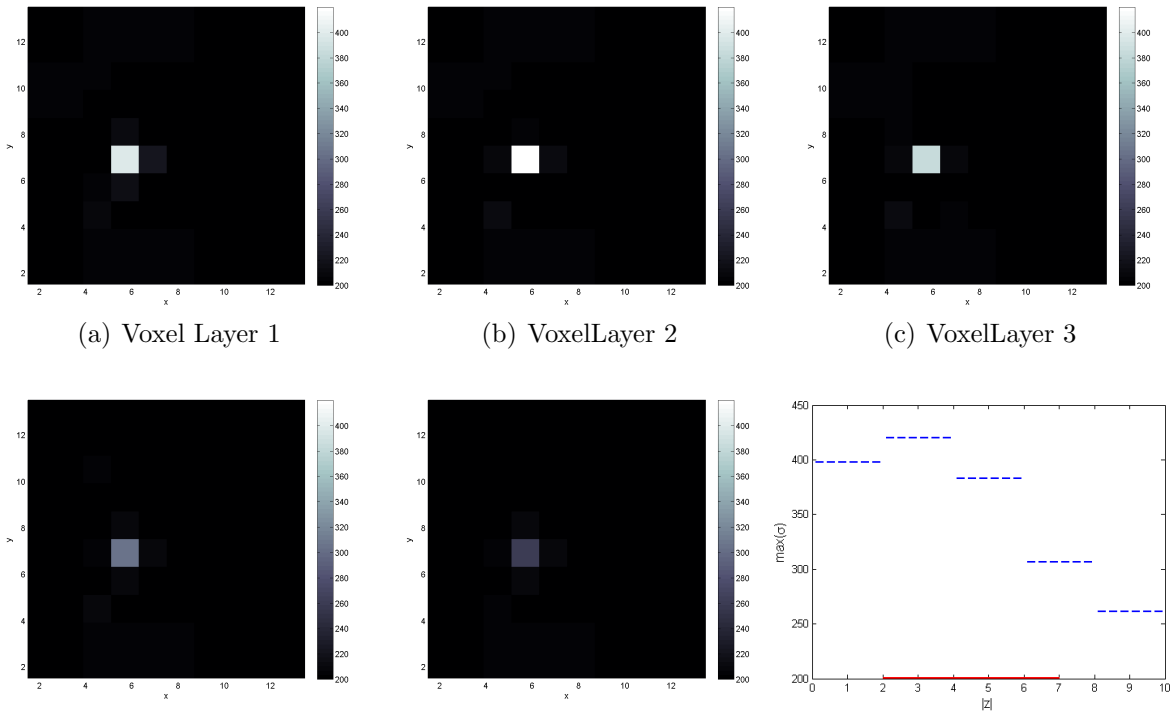

(a) Voxel Layer 1 (b) VoxelLayer 2 (c) VoxelLayer 3

(d) VoxelLayer 4 (e) VoxelLayer 5 (f) $\sigma(|z|)$ at $P1$

Figure 5.4: Conductivity reconstructions for a cylindrical object of radius R_{25} of conductivity 800mS/m placed at position $P1$ and $z = -2$mm. The thick continuous line in (e) marks the position and the height of the inclusion along the z-axis.

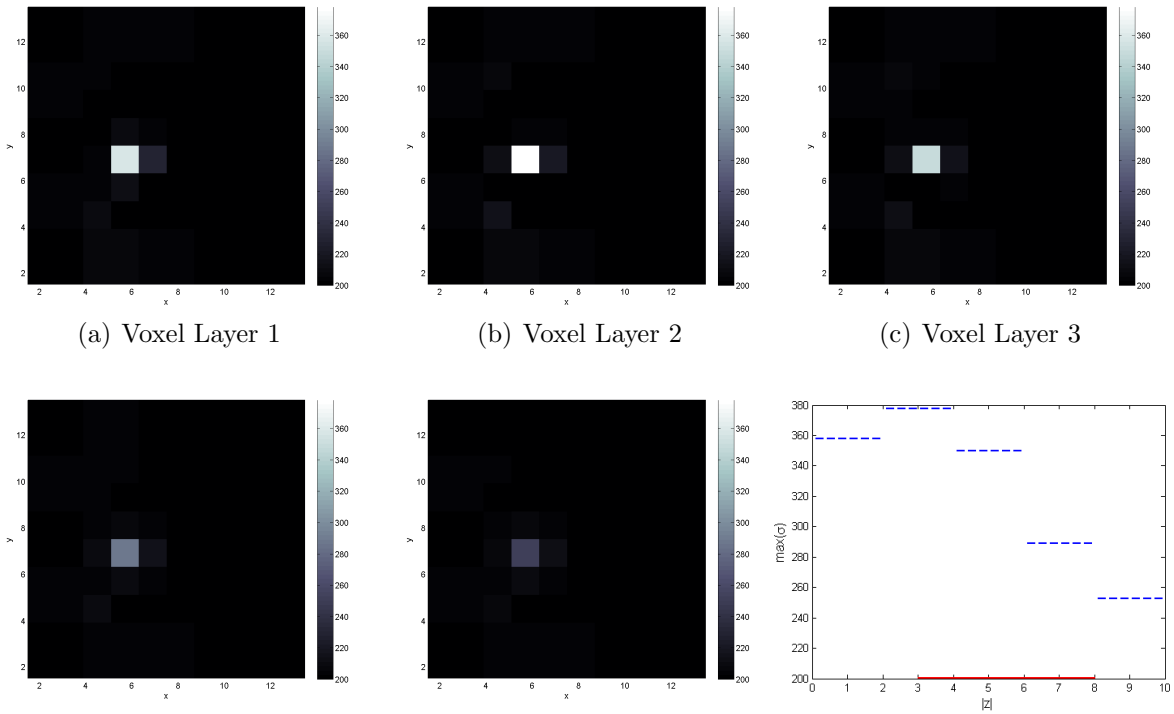

(a) Voxel Layer 1 (b) Voxel Layer 2 (c) Voxel Layer 3

(d) Voxel Layer 4 (e) Voxel Layer 5 (f) $\sigma(|z|)$ at $P1$

Figure 5.5: Conductivity reconstructions for a cylindrical object of radius R_{25} of conductivity 800mS/m placed at position $P1$ and $z = -3$mm. The thick continuous line in (e) marks the position and the height of the inclusion along the z-axis.

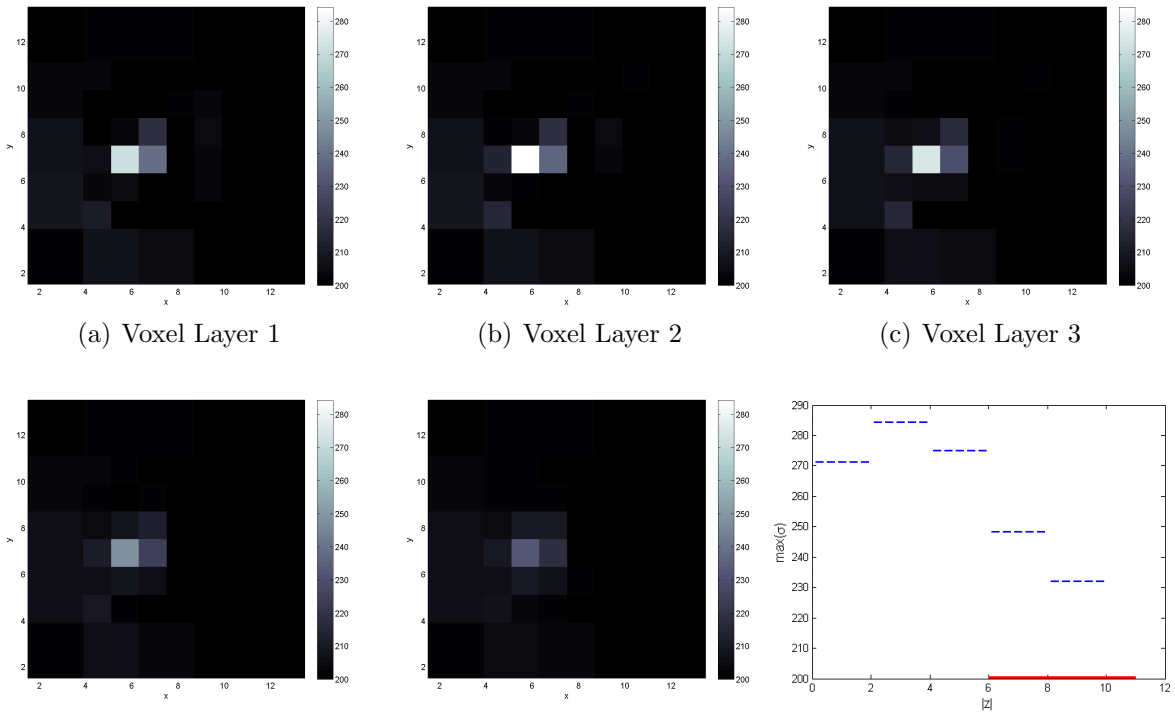

(a) Voxel Layer 1 (b) Voxel Layer 2 (c) Voxel Layer 3

(d) Voxel Layer 4 (e) Voxel Layer 5 (f) $\sigma(|z|)$ at $P1$

Figure 5.6: Conductivity reconstructions for a cylindrical object of radius R_{25} of conductivity 800mS/m placed at position $P1$ and $z = -6$mm. The thick continuous line in (e) marks the position and the height of the inclusion along the z-axis.

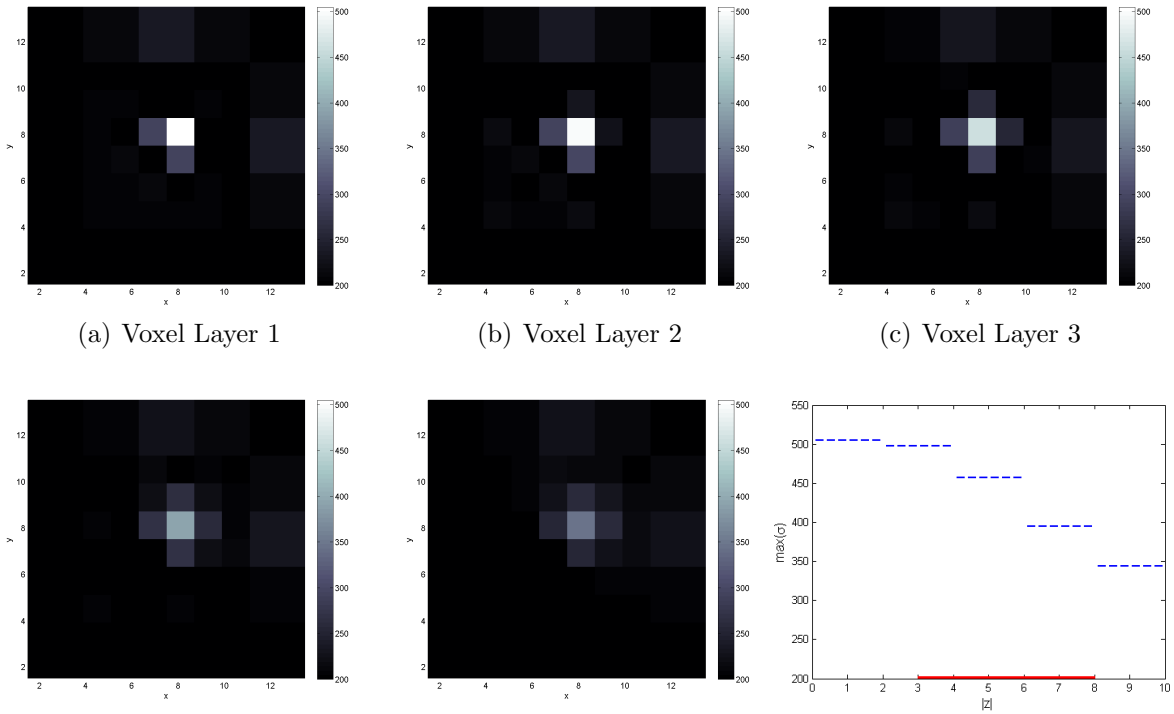

(a) Voxel Layer 1 (b) Voxel Layer 2 (c) Voxel Layer 3

(d) Voxel Layer 4 (e) Voxel Layer 5 (f) $\sigma(|z|)$ at $P2$

Figure 5.7: Conductivity reconstructions for a cylindrical object of radius R_{35} of conductivity 800mS/m placed at position $P2$ and $z = -3$mm. The thick continuous line in (e) marks the position and the height of the inclusion along the z-axis.

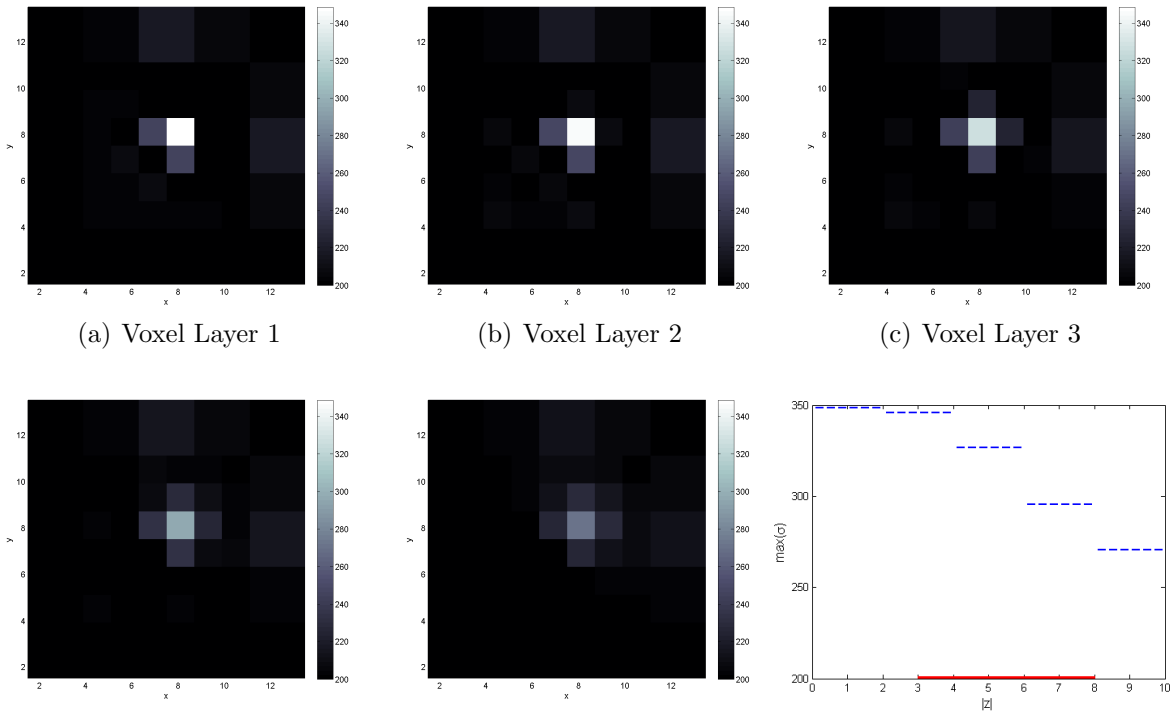

(a) Voxel Layer 1 (b) Voxel Layer 2 (c) Voxel Layer 3

(d) Voxel Layer 4 (e) Voxel Layer 5 (f) $\sigma(|z|)$ at $P2$

Figure 5.8: Conductivity reconstructions for a cylindrical object of radius R_{25} of conductivity 800mS/m placed at position $P2$ and $z = -3$mm. The thick continuous line in (e) marks the position and the height of the inclusion along the z-axis.

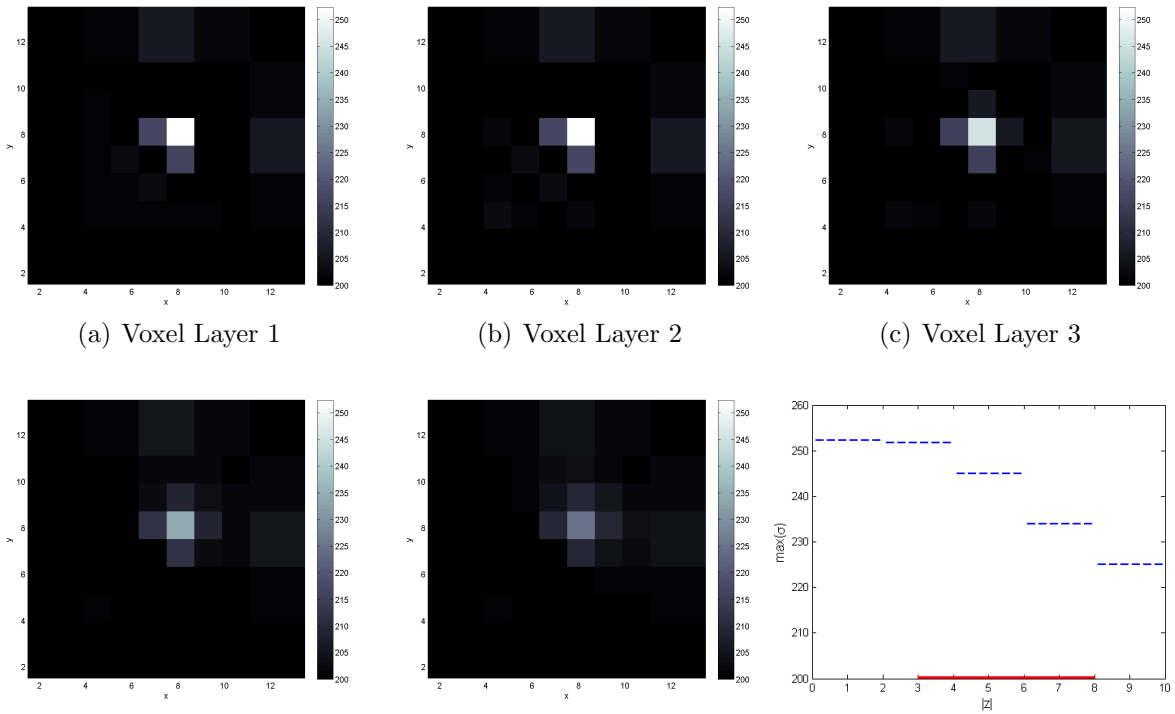

(a) Voxel Layer 1 (b) Voxel Layer 2 (c) Voxel Layer 3

(d) Voxel Layer 4 (e) Voxel Layer 5 (f) $\sigma(|z|)$ at $P2$

Figure 5.9: Conductivity reconstructions for a cylindrical object of radius R_{15} of conductivity 800mS/m placed at position $P2$ and $z = -3$mm. The thick continuous line in (e) marks the position and the height of the inclusion along the z-axis.

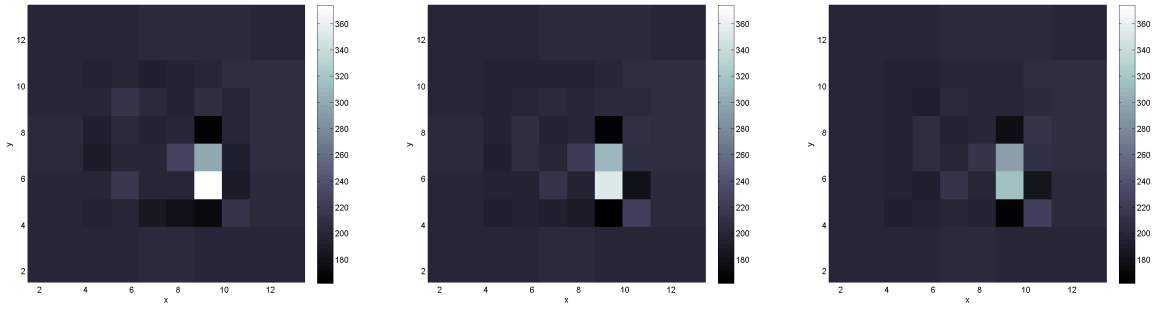

(a) Voxel Layer 1 (b) Voxel Layer 2 (c) Voxel Layer 3

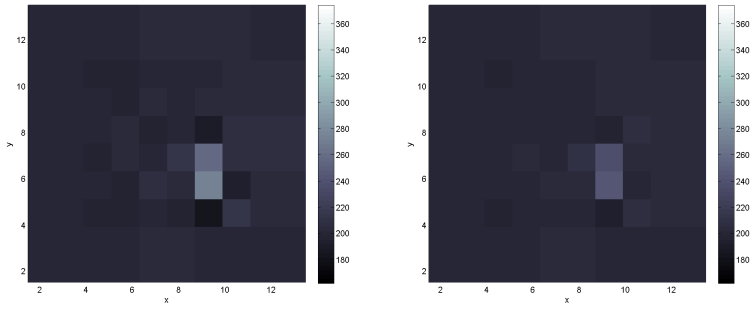

(d) Voxel Layer 4 (e) Voxel Layer 5

Figure 5.10: Conductivity reconstructions for a cylindrical object of radius R_{25} of conductivity 800mS/m placed at position $P3$ and $z = -3$mm.

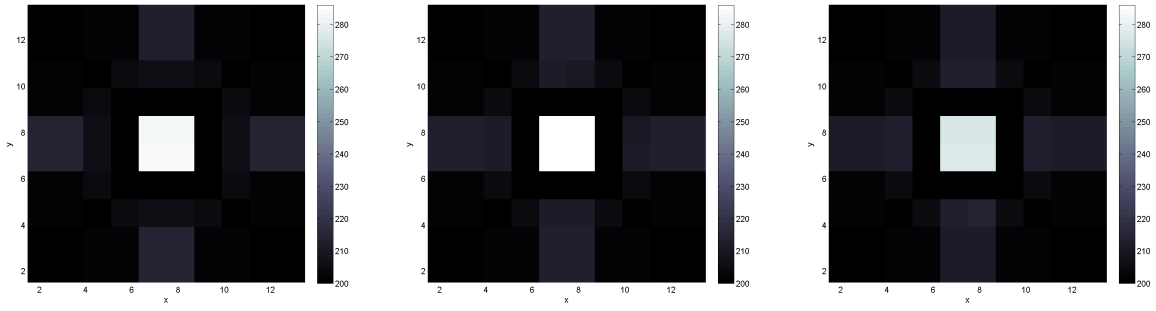

(a) Voxel Layer 1 (b) Voxel Layer 2 (c) Voxel Layer 3

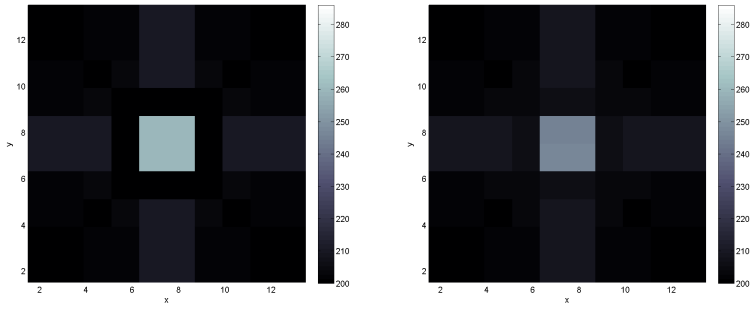

(d) Voxel Layer 4 (e) Voxel Layer 5

Figure 5.11: Conductivity reconstructions for a cylindrical object of radius R_{25} of conductivity 800mS/m placed at position $P4$ and $z = -3$mm.

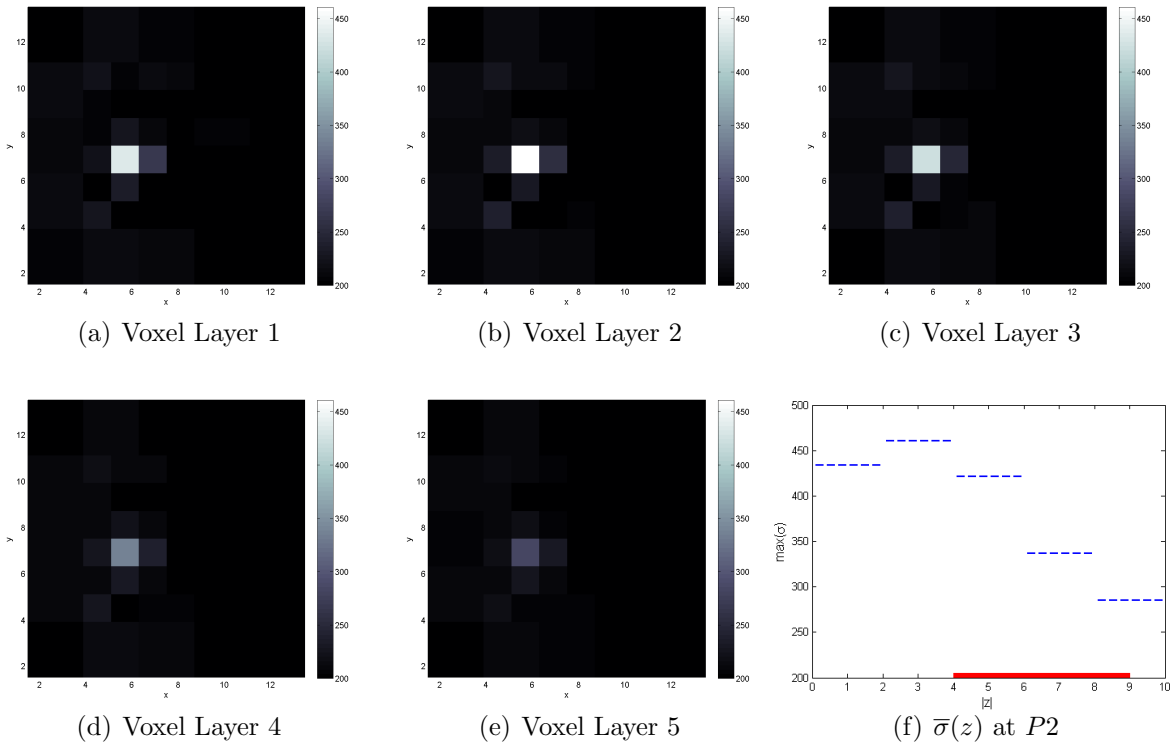

(a) Voxel Layer 1 (b) Voxel Layer 2 (c) Voxel Layer 3

(d) Voxel Layer 4 (e) Voxel Layer 5 (f) $\overline{\sigma}(z)$ at $P2$

Figure 5.12: Conductivity reconstructions for a cylindrical object of radius R_{35} of conductivity 800mS/m placed at position $P1$ and $z = -4$mm in the presence of a resistive medium (50mS/m) in Voxel Layer 1. The thick continuous line in (e) marks the position and the height of the inclusion along the z-axis.

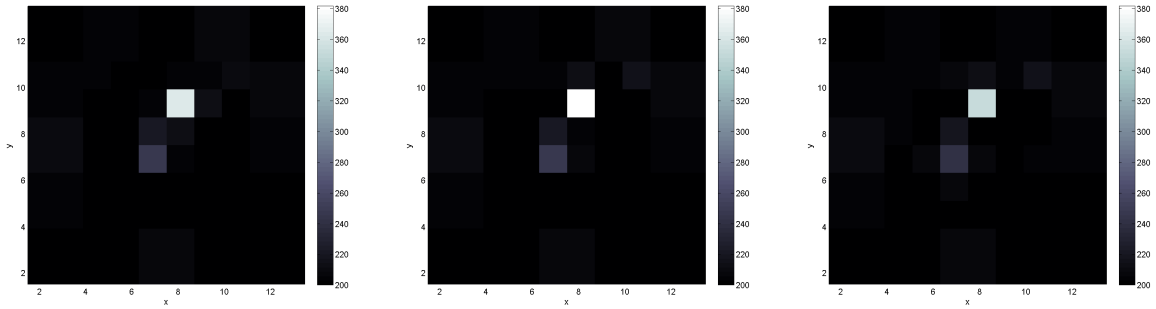

(a) Voxel Layer 1 (b) Voxel Layer 2 (c) Voxel Layer 3

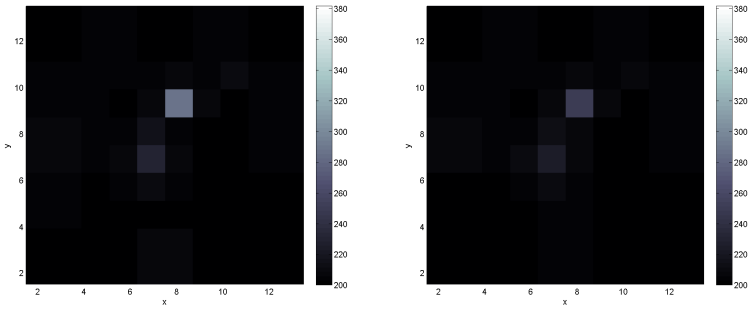

(d) Voxel Layer 4 (e) Voxel Layer 5

Figure 5.13: Conductivity reconstructions for two cylindrical objects of radii R_{25} and R_{15} of conductivities 800mS/m placed at positions $P5$ and $P6$, respectively, and $z = -3$mm.

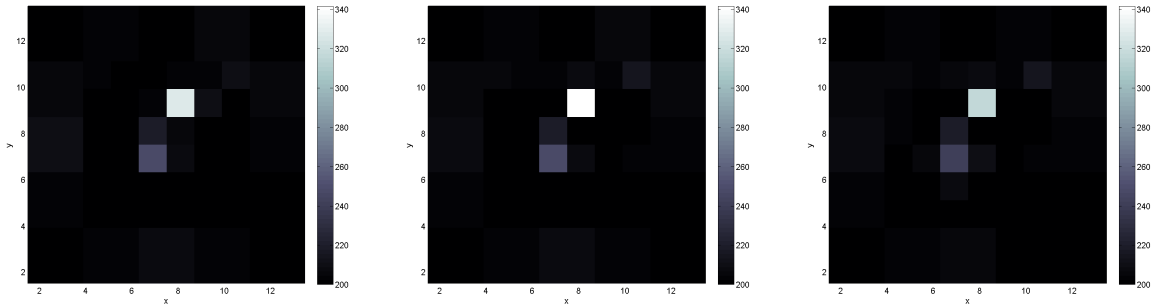

(a) Voxel Layer 1 (b) Voxel Layer 2 (c) Voxel Layer 3

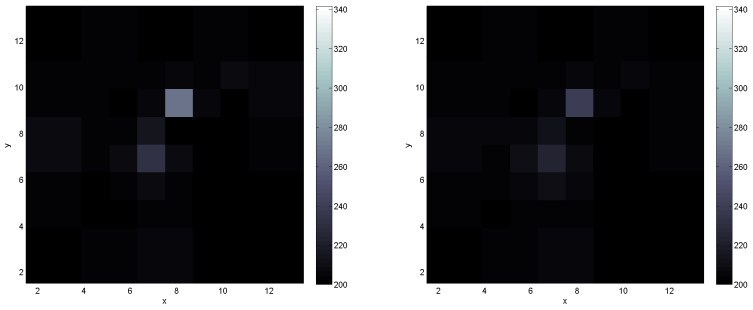

(d) Voxel Layer 4 (e) Voxel Layer 5

Figure 5.14: Conductivity reconstructions for two cylindrical objects, one of radius R_{25} and of conductivity 600mS/m, and the other of radius R_{15} and of conductivity 800mS/m, placed at positions $P5$ and $P6$, respectively, and $z = -3$mm.

Chapter 6

Conclusions and Future Work

In the first part of this thesis, reconstructions of the conductivity of a two-dimensional circular domain from boundary measurements of currents and interior measurements of the potential were carried out. The two-dimensional conductivity reconstructions presented in Chapter four were obtained from data generated numerically using the finite element solvers PDE and EIDORS toolboxes for Matlab, and from real data measured by a planar EIT device developed for early detection of breast cancer at the University of Mainz in collaboration with Oxford Brookes University. The real data was obtained at the Institut für Physik, Universität, Mainz, by placing a planar array of electrodes at the bottom of a tank filled with saline water, and then by immersing metal objects, with various sizes, at different depths and positions from the sensing head.

All Mainz-Brookes sensing heads have S electrodes for injecting current (twelve in the old prototypes and eighteen in the latest proposed one), which are arranged at equal distances on the outer ring of a disk with radius 4.4cm. In the resistor network model, the old prototype included twenty four current splits, while the later version contained only eighteen. In the latest modified design, however, the proposed geometry is such

that there are no current splits. There are K_r inner electrodes for measuring potentials (thirty six in the old design and fifty four in the later ones) arranged in a hexagonal pattern. The equivalent resistor network of each prototype also has N links (sixty six in the old prototype and ninety in latest ones) where currents and resistances are specified.

The novelty in the design of Mainz-Brookes sensing heads is in the use of two distinct groups of electrodes: active, for injecting current patterns only, and point-like high impedance passive electrodes where the induced potentials are measured, hence no issues related to the contact impedance arise. The devices also have fixed geometry, and the positions of the electrodes are exactly known. When the measuring area of those sensing heads is modelled as a resistor network, a map of the reconstructed conductivity at the surface to which the EIT device is applied could provide valuable information on the existence, location and size of breast tumours situated at shallow depths.

In order to carry out numerical reconstructions of different depths, sizes, positions and number of inclusions, a finite elements model which mimics the experimental setup of Mainz group was numerically designed using EIDORS and Matlab. A three-dimensional finite element forward solver was then used to simulate data to further test the robustness of the inversion algorithm and the sensitivity of different sensing heads. In these numerical reconstructions, presented in Chapter four, it has been shown that the positions of the metallic objects could be detected up to distances from the sensing head which are approximately equal to their diameters.

In the second part of this thesis, the geometry of an optimal planar array of electrodes was determined for the design of a new sensing head for Mainz-Brookes mammographs. The new design which has eighteen electrodes for injecting currents, with

no current splits is a modification of an old sensing head which has only twelve electrodes for injecting current and eighteen current splits. Both however had fifty four electrodes for measuring potentials. The equivalent resistor network for this sensing head consists of $S = 18$ electrodes for injecting currents, which are also arranged at equal distances on the outer ring of a disk of radius $R = 4.4$cm. The number of inner electrodes for measuring potentials which are arranged in a hexagonal pattern is similar to the previous design with $K_r = 54$ knots. The number of links in this sensing head where currents and resistances are specified is $N = 90$ as mentioned earlier. The significance of this new design lies in the fact that the current splits which existed in all old prototypes and required additional information for the reconstruction algorithm have been totally eliminated. Thus, modelling errors from computing the split-up ratio has been also excluded.

The third and final part of this thesis presents a novel three-dimensional non-iterative reconstruction method for conductivity imaging in breast cancer detection using numerically generated data from a planar EIT device developed at the University of Mainz in collaboration with Oxford Brookes University. The head of the sensor contains both active electrodes, where standard trigonometric current patterns are applied, and passive electrodes, where the induced voltages are measured, arranged in a rectangular array. A finite region beneath the surface was discretised into voxels of different sizes depending on their position relative to the electrode array and their conductivities were determined from the data measured on the electrode array. The reconstruction algorithm is based on linearizing the conductivity about a constant value. It is simple, direct and fast, and it allows reconstructions in real-time.

The performance of the algorithm was tested on numerically simulated data. Small inclusions of various conductivities placed at several depths were detected and their positions in the plane of the electrode array were successfully recovered. Although

the depth resolution is rather poor, the reconstructions have good spatial resolution in the xy-plane and are quite stable with respect to the noise level in the data. The most relevant feature is the fact that it can detect smaller objects up to larger depths than the other two-dimensional non-iterative approaches developed for similar planar EIT devices.

Hence, my research started by establishing adequate knowledge and understanding of the application specifications, followed by a comprehensive evaluation of available EIT imaging systems for breast cancer and their associated challenges. The research continued by an investigation of various network grids for modelling the measurement area in planar arrays, which led to determining the optimal geometry for the sensing head. Moreover, analysis of different mathematical models for the three-dimensional imaging problem has also led to developing a novel inversion algorithm.

The thesis was divided into six chapters. Chapter one began by providing a brief insight into medical imaging and fundamental principles of Electrical Impedance Tomography, followed by an overview of the inverse conductivity problem and its ill-posedness nature.

Chapter two presented the fundamental principles and specifications of EIT systems, followed by a list of medical and industrial applications of this technique. Next, the mathematical formulation of EIT including the forward and inverse problem of the continuum model and a description of some known electrodes modelling were introduced. This chapter also established the relation between optimal currents and the distinguishabilty, a criterion used to measure the ability of an EIT system to differentiate between two conductivities.

Chapter three was devoted to EIT mammographs. This chapter also included termi-

nologies related to medical examination such as accuracy, specificity, and sensitivity. Additionally, *in vitro* and *in vivo* methods for measuring the human breast tissues were explained with some experimental results giving various measurements of the electrical property of different human tissues. The chapter also presented results of clinical trials of EIT for detecting breast cancer, with a focus on evaluating the sensitivity and specificity. The chapter concluded with clinical trials using EIT as an adjunct to other imaging modalities (mainly X-ray mammography).

According to these clinical trials, it was shown that popular screening modalities lack specificity, which results in a high false-positive results of up to 80%. However, when using EIT as an adjunct technique for detecting breast cancer, the accuracy of the examination improved. Moreover, a number of research studies have also showed that EIT has an advantage over other imaging techniques in its ability to differentiate between benign and malignant tumours.

In Chapter four, a two-dimensional reconstruction algorithm based on discrete resistor model is presented followed by numerical results. An academic example was included at the end of the thesis which explains the inversion method based on resistor networks.

Chapter five presented the three-dimensional novel reconstruction algorithm for electrical impedance imaging. A simple implementation of the algorithm and reconstructions from simulated data obtained using EIDORS was also provided in this chapter. The results showed very good spatial resolution, and the algorithm was robust with respect to errors in the data.

To summarise, the following major stages were accomplished in this research project:

1. Review and analysis of relevant literature which included, Electrical Impedance Tomography (EIT), information about other existing screening modalities and their practicality in detecting breast cancer as well as results of clinical trials for using different imaging modalities.

2. Implementation of a two-dimensional reconstruction method based on discrete resistor networks in Matlab, for Mainz-Brookes tomographs intended to be used for detecting breast cancer.

3. Numerical tests of the geometry of an optimal planar array of electrodes for the design of a new sensing head of the Mainz-Brookes EIT devices.

4. Finite Element specialist software (PDE and EIDORS) with Matlab were used to generate synthetic data for the forward problem of Mainz-Brookes EIT system. This data, together with the implemented two-dimensional reconstruction method based on resistor networks were used to test the geometry of an optimal planar array of electrodes, and to test the robustness of the inversion technique.

5. Design of a novel three-dimensional reconstruction method which is suitable for breast cancer imaging from surface measurements of voltages and currents.

6. Generation of synthetic data using EIDORS and Matlab to reconstruct the conductivity inside a rectangular tank in order to test the three-dimensional inversion.

6.1 Future Work

Although the reconstructions from simulated data are promising first results, in order to determine whether Mainz-Brookes mammographs and their proposed inver-

sion techniques will prove effective for breast cancer detection, there are still further yet significant lab experiments and clinical trials to be carried out.

With the promising first numerical results from the novel three-dimensional reconstruction algorithm, the groups at Oxford Brookes and Mainz Universities are currently considering possible ways to adapt the Mainz-Brookes mammographs in order to enable the three-dimensional imaging. Furthermore, it is planned to obtain reconstructions from real data and try to improve the depth resolution of the algorithm by possibly imposing *a priori* and/or *a posteriori* sparsity constraints on the reconstructed conductivity values in each voxel.

The groups at both universities are currently improving the electronics of the EIT device in order to measure the voltages at the inner electrodes more accurately as this would increase depth at which tumours can be detected.

In addition to our research on EIT for breast cancer, current studies on EIT for detecting skin cancer are taking place. The initial investigation to determine the optimal geometry for this application has already been conducted during my research. Further work is still ongoing.

References

[1] S. R. Arridge and J. C. Hebden, "Optical imaging in medicine: II. modelling and reconstruction," *Physics in Medicine and Biology*, vol. 42, no. 5, p. 841, 1997.

[2] P. C. Gøtzsche and K. J. Jørgensen, "Screening for breast cancer with mammography," *Cochrane Database Syst Rev*, vol. 6, no. 6, 2013.

[3] R. S. Cobbold, *Foundations of biomedical ultrasound*. Oxford University Press on Demand, 2007.

[4] G. T. Herman, *Fundamentals of computerized tomography: image reconstruction from projections*. Springer Science & Business Media, 2009.

[5] H. Ammari, *An introduction to mathematics of emerging biomedical imaging*, vol. 62. Springer, 2008.

[6] H.-Y. Wei and M. Soleimani, "Electromagnetic tomography for medical and industrial applications: Challenges and opportunities [point of view]," *Proceedings of the IEEE*, vol. 101, no. 3, pp. 559–565, 2013.

[7] Y. Zou and Z. Guo, "A review of electrical impedance techniques for breast cancer detection," *Medical Engineering & Physics*, vol. 25, no. 2, pp. 79–90, 2003.

[8] A. Malich, T. Böhm, M. Facius, M. Freessmeyer, M. Fleck, R. Anderson, and W. Kaiser, "Additional value of electrical impedance scanning: experience of 240 histologically-proven breast lesions," *European Journal of Cancer*, vol. 37, no. 18, pp. 2324–2330, 2001.

[9] U. Schaumlöffel-Schulze, S. Heywang-Köbrunner, C. Alter, D. Lampe, and J. Buchmann, "Diagnostische vakuumbiopsie der brust ergebnisse von 600 patienten," *Fortschr Röntgenstr*, vol. 170, p. S72, 1999.

[10] J. G. Elmore, M. B. Barton, V. M. Moceri, S. Polk, P. J. Arena, and S. W. Fletcher, "Ten-year risk of false positive screening mammograms and clinical breast examinations," *New England Journal of Medicine*, vol. 338, no. 16, pp. 1089–1096, 1998.

[11] D. B. Kopans and D. Kopans, *Breast imaging*, vol. 1. Lippincott Williams & Wilkins Philadelphia, PA, 2007.

[12] J. E. Martin, M. Moskowitz, and J. R. Milbrath, "Breast cancer missed by mammography," *American Journal of Roentgenology*, vol. 132, no. 5, pp. 737–739, 1979.

[13] M. Kejariwal, K. Kaster, J. Jurist, and J. Pakanati, "Breast cancer detection using electrical impedance tomography: spice simulation," in *Engineering in Medicine and Biology Society, 1993. Proceedings of the 15th Annual International Conference of the IEEE*, pp. 64–65, 1993.

[14] N. Polydorides, *Image Reconstruction Algorithm for Soft-Field Tomography*. PhD thesis, School of Science and Technology, University of Manchester, 2002.

[15] W. Breckon, *Electrical Impedance Tomography*. PhD thesis, School of Computing and Matghematical Sciences, Oxford Polytechnic, 1990.

[16] L. Borcea, "Electrical impedance tomography," *Institute of Physics Publisihing*, vol. 18, pp. 99–136, 2002.

[17] B. M. Graham, *Enhancements in Electrical Impedance Tomography (EIT) Image Reconstruction for 3D Lung Imaging*. PhD thesis, School of Informtation Technology, University of Ottawa, 2007.

[18] A. Morimoto, E. Yasuno, Y. Kinouchi, Y. Ohmine, A. Tangoku, and T. Morimoto, "Spatial resolution in the electrical impedance tomography for the local tissue," in *27th Annual International Conference of the Engineering in Medicine and Biology Society, 2005. IEEE-EMBS 2005.*, pp. 6638–6641, 2005.

[19] S. Zlochiver, M. Arad, D. Barak-Shinar, and S. Abboud, "A portable bio-impedance system for monitoring lung resistivity," *Medical Engineering & Physics*, vol. 29, no. 1, pp. 93 – 100, 2007.

[20] H. Brown, "Electrical impedance tomography a review," *Journal of Mecidal Engineering & Technology*, vol. 27, no. 4, pp. 97 –108, 2008.

[21] E. L. Costa, R. G. Lima, and M. B. Amato, "Electrical impedance tomography," in *Intensive Care Medicine*, pp. 394–404, Springer, 2009.

[22] J. Karsten, K. Krabbe, H. Heinze, K. Dalhoff, T. Meier, and D. Drömann, "Bedside monitoring of ventilation distribution and alveolar inflammation in community-acquired pneumonia," *Journal of clinical monitoring and computing*, vol. 28, no. 4, pp. 403–408, 2014.

[23] T. Meier, H. Luepschen, J. Karsten, T. Leibecke, M. Großherr, H. Gehring, and S. Leonhardt, "Assessment of regional lung recruitment and derecruitment during a peep trial based on electrical impedance tomography," *Intensive Care Medicine*, vol. 34, no. 3, pp. 543–550, 2008.

[24] S. Lindgren, H. Odenstedt, C. Olegård, S. Söndergaard, S. Lundin, and O. Stenqvist, "Regional lung derecruitment after endotracheal suction during volume-or pressure-controlled ventilation: a study using electric impedance tomography," *Intensive Care Medicine*, vol. 33, no. 1, pp. 172–180, 2007.

[25] E. L. Costa, C. N. Chaves, S. Gomes, M. A. Beraldo, M. S. Volpe, M. R. Tucci, I. A. Schettino, S. H. Bohm, C. R. Carvalho, H. Tanaka, *et al.*, "Real-time detection of pneumothorax using electrical impedance tomography," *Critical Care Medicine*, vol. 36, no. 4, pp. 1230–1238, 2008.

[26] G. Hahn, A. Just, T. Dudykevych, I. Frerichs, J. Hinz, M. Quintel, and G. Hellige, "Imaging pathologic pulmonary air and fluid accumulation by functional and absolute EIT," *Physiological Measurement*, vol. 27, no. 5, p. S187, 2006.

[27] A. P. Calderón, "On an inverse boundary value problem, seminar on numerical analysis and its applications to continuum physics," *Brasileira de Mathematica*, 1980.

[28] G. Uhlmann, "Electrical impedance tomography and Calderón's problem," *Inverse Problems*, vol. 25, no. 12, p. 123011, 2009.

[29] D. Holder, *Electrical impedance tomography : methods, history and applications*. Bristol: Institute of Physics, 2004.

[30] C. Toumazou, F. J. Lidgey, and D. Haigh, *Analogue IC design : the current-mode approach*. IEE circuits and systems series, London, U.K.: Peregrinus on behalf of the Institution of Electrical Engineers, 1990.

[31] C. Hähnlein, K. Schilcher, C. Sebu, and H. Spiesberger, "Conductivity imaging with interior potential measurements," *Inverse Problems in Science and Engineering*, vol. 19, no. 5, pp. 729–750, 2011.

[32] G. Sze, *Detection of breast cancer with electrical impedance mammography*. PhD thesis, School of Engineering and Informatics, University of Sussex, 2012.

[33] D. Liu, V. Kolehmainen, S. Siltanen, A. Seppanen, *et al.*, "Estimation of conductivity changes in a region of interest with electrical impedance tomography," *Inverse Problems and Imaging*, vol. 1, no. 9, pp. 211–229, 2015.

[34] K. Krishnan, J. Liu, and K. Kohli, "Feature-space assessment of electrical impedance tomography coregistered with computed tomography in detecting multiple contrast targets," *Medical Physics*, vol. 41, no. 6, p. 061903, 2014.

[35] O. K. Lee, H. Kang, J. C. Ye, and M. Lim, "A non-iterative method for the electrical impedance tomography based on joint sparse recovery," *Inverse Problems*, vol. 31, no. 7, p. 075002, 2015.

[36] A. J. Surowiec, S. S. Stuchly, J. R. Barr, and A. Swarup, "Dielectric properties of breast carcinoma and the surrounding tissues," *Biomedical Engineering on IEEE Transactions*, vol. 35, no. 4, pp. 257–263, 1988.

[37] F. Santosa and M. Vogelius, "A backprojection algorithm for electrical impedance imaging," *SIAM Journal on Applied Mathematics*, vol. 50, no. 1, pp. 216–243, 1990.

[38] M. Cheney and D. Isaacson, "An overview of inversion algorithms for impedance imaging," *Contemp. Math*, vol. 122, pp. 29–39, 1991.

[39] M. Cheney, D. Isaacson, J. Newell, S. Simske, and J. Goble, "Noser: An algorithm for solving the inverse conductivity problem," *International Journal of Imaging Systems and Technology*, vol. 2, no. 2, pp. 66–75, 1990.

[40] K.-H. Georgi, C. Hähnlein, K. Schilcher, C. Sebu, and H. Spiesberger, "Conductivity reconstructions using real data from a new planar electrical impedance tomography device," *Inverse Problems in Science and Engineering*, vol. 21, no. 5, pp. 801–822, 2013.

[41] L. Borcea, V. Druskin, A. Mamonov, and F. G. Vasquez, "Pyramidal resistor networks for electrical impedance tomography with partial boundary measurements," *Inverse Problems*, vol. 26, no. 10, p. 105009, 2010.

[42] J. L. Mueller, S. Siltanen, and D. Isaacson, "A direct reconstruction algorithm for electrical impedance tomography," *Medical Imaging on IEEE Transactions*, vol. 21, no. 6, pp. 555–559, 2002.

[43] Z. G. Y. Zou, "A review of electrical impedance techniques for breast cancer detection," *Medical Engineering & Physics*, vol. 25, p. 7990, 2003.

[44] J. Mueller and S. Siltanen, *Linear and nonlinear inverse problems with practical applications*. Computational science and engineering series, 2012.

[45] M. Lastovickova, "Laboratory measurements of electrical-properties of rocks and minerals," *Geophysical Surveys*, vol. 6, no. 1-2, pp. 201–213, 1983.

[46] L. P. G. Telford, W. M. and R. E. Sheriff., *Applied Geophysics*. Cambridge University Press, 1990.

[47] S. I. Karato and D. Wang, "Electrical conductivity of minerals and rocks," *Physics and Chemistry of the Deep Earth*, pp. 145–182, 2012.

[48] M. Soleimani and R. H. Bayford, "New and emerging tomographic imaging techniques in medical and industrial applications," *Philosophical Transactions of the Royal Society A: Mathematical, Physical and Engineering Sciences*, vol. 367, no. 1900, pp. 3017–3019, 2009.

[49] S. R. H. Hoole, S. Subramaniam, R. Saldanha, J.-L. Coulomb, and J.-C. Sabonnadiere, "Inverse problem methodology and finite elements in the identification of cracks, sources, materials, and their geometry in inaccessible locations," *Magnetics on IEEE Transactions*, vol. 27, no. 3, pp. 3433–3443, 1991.

[50] C. Roobottom, G. Mitchell, and G. Morgan-Hughes, "Radiation-reduction strategies in cardiac computed tomographic angiography," *Clinical Radiology*, vol. 65, no. 11, pp. 859 – 867, 2010.

[51] P. Sabatier and C. Sebu, "On the resolving power of electrical impedance tomography," *Inverse Problems*, vol. 23, no. 5, p. 1895, 2007.

[52] T. Tidswell, A. Gibson, R. H. Bayford, and D. S. Holder, "Three-dimensional electrical impedance tomography of human brain activity," *Neuroimage*, vol. 13, no. 2, pp. 283–294, 2001.

[53] D. S. Holder, "Electrical impedance tomography of brain function," in *Automation Congress, 2008. WAC 2008. World*, pp. 1–6, IEEE, 2008.

[54] J. Laufer, E. Zhang, G. Raivich, and P. Beard, "Three-dimensional noninvasive imaging of the vasculature in the mouse brain using a high resolution photoacoustic scanner," *Applied Optics*, vol. 48, no. 10, pp. D299–D306, 2009.

[55] V. Cherepenin, Y. Gulyaev, A. Korjenevsky, S. Sapetsky, and T. Tuykin, "An electrical impedance tomography system for gynecological application git with a tiny electrode array," *Physiological Measurement*, vol. 33, no. 5, p. 849, 2012.

[56] V. A. Cherepenin, A. Y. Karpov, A. V. Korjenevsky, V. N. Kornienko, Y. S. Kultiasov, M. B. Ochapkin, O. V. Trochanova, and J. D. Meister, "Three-dimensional EIT imaging of breast tissues: system design and clinical testing," *IEEE Transactions on Medical Imaging*, vol. 21, no. 6, pp. 662–667, 2002.

[57] H. McCann, *Process imaging for automatic control*. Boca Raton, Fla: Taylor & Francis, 2005.

[58] R. A. Williams, *Process tomography : principles, techniques, and applications*. Oxford Boston: Butterworth-Heinemann, 1995.

[59] Y. Ma, Y. Lai, M. Wang, and J. Jia, "Experimental validation of over-zero switching method," in *What, where, when: multi-dimensional advances for industrial process monitoring international symposium (W3MDM). Leeds (UK)*, 2009.

[60] W. Wightman, F. Jalinoos, P. Sirles, and K. Hanna, "Application of geophysical methods to highway related problems," tech. rep., 2004.

[61] P. Kearey, *An introduction to geophysical exploration*. Oxford England Boston: Blackwell Scientific Publications, 1991.

[62] F. Dickin, R. Waterfall, R. Williams, C. Xie, M. Beck, S. Huang, B. Hoyle, A. Hunt, C. Lenn, *et al.*, "Tomographic imaging of industrial process equipment: techniques and applications," *IEE Proceedings G (Circuits, Devices and Systems)*, vol. 139, no. 1, pp. 72–82, 1992.

[63] J. G. Zhang and F. C. Ma, "Application of electrical resistance tomography to ice-water two-phase flow parameters measurement," *Key Engineering Materials*, vol. 562, pp. 686–690, 2013.

[64] G. Niu, Z. Jia, and J. Wang, "Void fraction measurement in oil-gas transportation pipeline using an improved electrical capacitance tomography system," *Chinese Journal of Chemical Engineering*, vol. 12, no. 4, pp. 476–481, 2004.

[65] A. A. Bery, R. Saad, E. T. Mohamad, M. Jinmin, I. Azwin, N. M. A. Tan, and M. Nordiana, "Electrical resistivity and induced polarization data correlation with conductivity for iron ore exploration," *Electronic Journal of Geotechnical Engineering*, vol. 17, pp. 3323–3337, 2012.

[66] S. Ward, "Induced polarisation methods in mineral exploration," *Geoexploration*, vol. 9, no. 2, p. 79, 1971.

[67] J. Kiberu, "Induced polarization and resistivity measurements on a suite of near surface soil samples and their empirical relationship to selected measured engineering parameters," *Interntional Institute for Geo-information Science and Earth Observation, Enschede, The Netherlands*, 2002.

[68] L. Tarassenko, *Electrical Impedance Technique for Study of the Cerebral Circulation and Cranial Imaging in the Newborn*. PhD thesis, School of Computing and Mathematical Sciences, University of Oxford, 1985.

[69] E. Bor-Seng-Shu, W. S. Kita, E. G. Figueiredo, W. S. Paiva, E. T. Fonoff, M. J. Teixeira, and R. B. Panerai, "Cerebral hemodynamics: concepts of clinical importance," *Arquivos de neuro-psiquiatria*, vol. 70, no. 5, pp. 352–356, 2012.

[70] R. P. Henderson and J. G. Webster, "An impedance camera for spatially specific measurements of the thorax," *Biomedical Engineering on IEEE Transactions*, vol. 25, no. 3, pp. 250–254, 1978.

[71] D. Barber and B. Brown, "Applied potential tomography," *Journal of Physics. E. Scientific Instruments*, vol. 17, no. 9, pp. 723–733, 1984.

[72] D. Barber, B. Brown, and I. Freeston, "Imaging spatial distributions of resistivity using applied potential tomographyapt," in *Information Processing in Medical Imaging*, pp. 446–462, Springer, 1984.

[73] P. H. tech medicine, *MEIK Electro Impedance Computer Mammograph*.

[74] T. K. Bera and J. Nagaraju, "A LabVIEW based data acquisition system for electrical impedance tomography (EIT)," *Advances in Intelligent Systems and Computing Proceedings of the Third International Conference on Soft Computing for Problem Solving*, pp. 377–89, 2014.

[75] S. Zlochiver and M. Arad, "A portable bio-impedance system for monitoring lung resistivity," *Medical Engineering and Physics*, vol. 29, pp. 93–100, 2007.

[76] B. Medicalsham, *Differential Diagnosis of Abdominal Pain*.

[77] A. Romsauerova, A. McEwan, and D. Holder, "Identification of a suitable current waveform for acute stroke imaging," *Physiological Measurement*, vol. 27, no. 5, p. S211, 2006.

[78] T. J. Kao, J. Newell, G. Saulnier, and D. Isaacson, "Distinguishability of inhomogeneities using planar electrode arrays and different patterns of applied excitation," *Physiological Measurement*, vol. 24, no. 2, p. 403, 2003.

[79] M. Vauhkonen, W. R. Lionheart, L. M. Heikkinen, P. J. Vauhkonen, and J. P. Kaipio, "A matlab package for the eidors project to reconstruct two-dimensional eit images," *Physiological Measurement*, vol. 22, no. 1, p. 107, 2001.

[80] A. Adler and W. R. Lionheart, "Uses and abuses of eidors: an extensible software base for EIT," *Physiological Measurement*, vol. 27, no. 5, p. S25, 2006.

[81] R. Harikumar, R. Prabu, and S. Raghavan, "Electrical impedance tomography (EIT) and its medical applications: A review," *International Journal of Soft Computing and Engineering*, vol. 3, no. 4, pp. 193–198, 2013.

[82] J. L. Mueller and S. Siltanen, *Linear and nonlinear inverse problems with practical applications*, vol. 10. Siam, 2012.

[83] T. E. Kerner, D. B. Williams, K. S. Osterman, F. R. Reiss, A. Hartov, and K. D. Paulsen, "Electrical impedance imaging at multiple frequencies in phantoms," *Physiological measurement*, vol. 21, no. 1, p. 67, 2000.

[84] D. Griffiths, *Introduction to electrodynamics*. Upper Saddle River, N.J: Prentice Hall, 1999.

[85] D. A. Fleisch, *A student's guide to Maxwell's equations*. Cambridge, UK ; New York: Cambridge University Press, 2008.

[86] D. M. Cook, *The theory of the electromagnetic field*. Courier Corporation, 1975.

[87] J. Jackson, *Classical electrodynamics*. New York: Wiley, 1999.

[88] J. O. Ollikainen, M. Vauhkonen, P. A. Karjalainen, and J. P. Kaipio, "Effects of electrode properties on EEG measurements and a related inverse problem," *Medical Engineering & Physics*, vol. 22, no. 8, pp. 535–545, 2000.

[89] R. Cardu, P. H. Leong, C. T. Jin, and A. McEwan, "Electrode contact impedance sensitivity to variations in geometry," *Physiological Measurement*, vol. 33, no. 5, p. 817, 2012.

[90] M. H. Choi, T.-J. Kao, D. Isaacson, G. Saulnier, and J. C. Newell, "A reconstruction algorithm for breast cancer imaging with electrical impedance tomography in mammography geometry," *Biomedical Engineering on IEEE Transactions*, vol. 54, no. 4, pp. 700–710, 2007.

[91] B. S. Kim, G. Boverman, J. C. Newell, G. J. Saulnier, and D. Isaacson, "The complete electrode model for EIT in a mammography geometry," *Physiological measurement*, vol. 28, no. 7, p. S57, 2007.

[92] E. Somersalo, M. Cheney, and D. Isaacson, "Existence and uniqueness for electrode models for electric current computed tomography," *SIAM Journal on Applied Mathematics*, vol. 52, no. 4, pp. 1023–1040, 1992.

[93] K.-S. Cheng, D. Isaacson, J. Newell, and D. G. Gisser, "Electrode models for electric current computed tomography," *Biomedical Engineering, IEEE Transactions on*, vol. 36, no. 9, pp. 918–924, 1989.

[94] A. D. Seagar, "Probing with low frequency electric currents.," 1983.

[95] V. Cheverda, F. Clement, V. Khaidukov, and V. Kostin, "Linearized inversion of data of multi-offset data for vertically inhomogeneous background," *Journal of Inverse and Ill-posed Problems*, vol. 6, no. 5, pp. 453–484, 1998.

[96] D. Gisser, D. Isaacson, and J. Newell, "Current topics in impedance imaging," *Clinical Physics and Physiological Measurement*, vol. 8, no. 4A, p. 39, 1987.

[97] W. R. Lionheart, J. Kaipio, and C. N. McLeod, "Generalized optimal current patterns and electrical safety in eit," *Physiological Measurement*, vol. 22, no. 1, p. 85, 2013.

[98] W. R. Lionheart, J. Kaipio, and C. N. McLeod, "Generalized optimal current patterns and electrical safety in EIT," *Physiological measurement*, vol. 22, no. 1, p. 85, 2001.

[99] E. Demidenko, A. Hartov, N. Soni, and K. D. Paulsen, "On optimal current patterns for electrical impedance tomography," *Biomedical Engineering on IEEE Transactions*, vol. 52, no. 2, pp. 238–248, 2005.

[100] D. Isaacson, "Distinguishability of conductivities by electric current computed tomography," *Medical Imaging on IEEE Transactions*, vol. 5, no. 2, pp. 91–95, 1986.

[101] M. Cheney and D. Isaacson, "Issues in electrical impedance imaging," *Computational Science & Engineering, IEEE*, vol. 2, no. 4, pp. 53–62, 1995.

[102] D. G. Gisser, D. Isaacson, and J. C. Newell, "Electric current computed tomography and eigenvalues," *SIAM Journal on Applied Mathematics*, vol. 50, no. 6, pp. pp. 1623–1634, 1990.

[103] A. Allers and F. Santosa, "Stability and resolution analysis of a linearized problem in electrical impedance tomography," *Inverse Problems*, vol. 7, no. 4, p. 515, 1991.

[104] C. C. Boring, T. S. Squires, T. Tong, and S. Montgomery, "Cancer statistics, 1994," *CA: A Cancer Journal for Clinicians*, vol. 44, no. 1, pp. 7–26, 1994.

[105] R. Burns, "Image-guided breast biopsy," *American Journal of Surgery*, vol. 173, pp. 9–11, JAN 1997.

[106] A. Stojadinovic, O. Moskovitz, Z. Gallimidi, S. Fields, A. D. Brooks, R. Brem, R. N. Mucciola, M. Singh, M. Maniscalco-Theberge, H. E. Rockette, *et al.*, "Prospective study of electrical impedance scanning for identifying young women at risk for breast cancer," *Breast Cancer Research and Treatment*, vol. 97, no. 2, pp. 179–189, 2006.

[107] R. A. Smith, D. Saslow, K. A. Sawyer, W. Burke, M. E. Costanza, W. Evans, R. S. Foster, E. Hendrick, H. J. Eyre, and S. Sener, "American cancer society guidelines for breast cancer screening: update 2003," *CA: A Cancer Journal For Clinicians*, vol. 53, no. 3, pp. 141–169, 2003.

[108] C. K. Kuhl, "High-risk screening: multi-modality surveillance of women at high risk for breast cancer (proven or suspected carriers of a breast cancer susceptibility gene).," *Journal of Experimental & Clinical Cancer Research: CR*, vol. 21, no. 3 Suppl, pp. 103–106, 2002.

[109] E. E. Penhoet, D. B. Petitti, J. E. Joy, *et al.*, *Saving Women's Lives:: Strategies for Improving Breast Cancer Detection and Diagnosis*. National Academies Press, 2005.

[110] D. Saslow, C. Boetes, W. Burke, S. Harms, M. O. Leach, C. D. Lehman, E. Morris, E. Pisano, M. Schnall, S. Sener, *et al.*, "American cancer society guidelines for breast screening with mri as an adjunct to mammography," *CA: A Cancer Journal For Clinicians*, vol. 57, no. 2, pp. 75–89, 2007.

[111] C. K. Kuhl, S. Schrading, C. C. Leutner, N. Morakkabati-Spitz, E. Wardelmann, R. Fimmers, W. Kuhn, and H. H. Schild, "Mammography, breast ultrasound, and magnetic resonance imaging for surveillance of women at high familial risk for breast cancer," *Journal of Clinical Oncology*, vol. 23, no. 33, pp. 8469–8476, 2005.

[112] K. M. Kelly, J. Dean, W. S. Comulada, and S.-J. Lee, "Breast cancer detection using automated whole breast ultrasound and mammography in radiographically dense breasts," *European Radiology*, vol. 20, no. 3, pp. 734–742, 2010.

[113] C. H. Lee, D. D. Dershaw, D. Kopans, P. Evans, B. Monsees, D. Monticciolo, R. J. Brenner, L. Bassett, W. Berg, S. Feig, *et al.*, "Breast cancer screening with imaging: recommendations from the society of breast imaging and the acr on the use of mammography, breast mri, breast ultrasound, and other technologies for the detection of clinically occult breast cancer," *Journal of the American College of Radiology*, vol. 7, no. 1, pp. 18–27, 2010.

[114] G. J. Whitman, B. Erguvan-Dogan, W. T. Yang, J. Wilson, P. Patel, and S. Krishnamurthy, "Ultrasound-guided breast biopsies," *Ultrasound Clinics*, vol. 1, no. 4, pp. 603–615, 2006.

[115] D. Lister, A. Evans, H. Burrell, R. Blamey, A. Wilson, S. Pinder, I. Ellis, C. Elston, and J. Kollias, "The accuracy of breast ultrasound in the evaluation of clinically benign discrete, symptomatic breast lumps," *Clinical Radiology*, vol. 53, no. 7, pp. 490–492, 1998.

[116] W. Teh and A. Wilson, "The role of ultrasound in breast cancer screening. a consensus statement by the european group for breast cancer screening," *European Journal of cancer*, vol. 34, no. 4, pp. 449–450, 1998.

[117] H. Anger, "A new instrument for mapping gamma-ray emitters," *Biology and Medicine Quarterly Report UCRL*, vol. 3653, p. 38, 1957.

[118] S. K. Yang, N. Cho, and W. K. Moon, "The role of pet/ct for evaluating breast cancer," *Korean Journal of Radiology*, vol. 8, no. 5, pp. 429–437, 2007.

[119] L. K. Griffeth, "Use of pet/ct scanning in cancer patients: technical and practical considerations," *Proceedings (Baylor University. Medical Center)*, vol. 18, no. 4, p. 321, 2005.

[120] S. L. Edell and M. D. Eisen, "Current imaging modalities for the diagnosis of breast cancer," *Delaware Medical Journal*, vol. 71, no. 9, pp. 377–82, 1999.

[121] A. Surowiec, S. Stuchly, J. Barr, and A. Swarup, "Dielectric properties of breast carcinoma and the surrounding tissues," *Biomedical Engineering, IEEE Transactions on*, vol. 35, pp. 257–263, April 1988.

[122] J. Jossinet, "Variability of impedivity in normal and pathological breast tissue," *Medical and Biological Engineering and Computing*, vol. 34, no. 5, pp. 346–350, 1996.

[123] B. S. Kim, D. Isaacson, H. Xia, T. J. Kao, J. C. Newell, and G. J. Saulnier, "A method for analyzing electrical impedance spectroscopy data from breast cancer patients," *Physiological Measurement*, vol. 28, no. 7, pp. S237–46, 2007.

[124] T.-J. Kao, G. Boverman, B. seok Kim, D. Isaacson, G. Saulnier, J. Newell, M. Choi, R. Moore, and D. Kopans, "Regional admittivity spectra with tomosynthesis images for breast cancer detection: Preliminary patient study," *Medical Imaging on IEEE Transactions*, vol. 27, no. 12, pp. 1762–1768, 2008.

[125] O. Kwon, E. J. Woo, J.-R. Yoon, and J. K. Seo, "Magnetic resonance electrical impedance tomography (MREIT): simulation study of j-substitution algorithm," *Biomedical Engineering on IEEE Transactions*, vol. 49, no. 2, pp. 160–167, 2002.

[126] S. H. Oh, B. I. Lee, E. J. Woo, S. Y. Lee, M. H. Cho, O. Kwon, and J. K. Seo, "Conductivity and current density image reconstruction using harmonic Bz algorithm in magnetic resonance electrical impedance tomography," *Physics in Medicine and Biology*, vol. 48, no. 19, p. 3101, 2003.

[127] E. J. Woo and J. K. Seo, "Magnetic resonance electrical impedance tomography (mreit) for high-resolution conductivity imaging," *Physiological Measurement*, vol. 29, no. 10, p. R1, 2008.

[128] H. Ammari, E. Bonnetier, Y. Capdeboscq, M. Tanter, M. Fink, *et al.*, "Electrical impedance tomography by elastic deformation," *SIAM Journal on Applied Mathematics*, vol. 68, no. 6, pp. 1557–1573, 2008.

[129] B. Gebauer and O. Scherzer, "Impedance-acoustic tomography," *SIAM Journal on Applied Mathematics*, vol. 69, no. 2, pp. 565–576, 2008.

[130] I. BIPM, I. IFCC, I. ISO, and O. IUPAP, "The international vocabulary of metrologybasic and general concepts and associated terms (vim), jcgm 200: 2008," 2008.

[131] J. Taylor, *Introduction to error analysis, the study of uncertainties in physical measurements*, vol. 1. 1997.

[132] K. Ivanov, *Quality-control of information: on the concept of accuracy of information in data-banks and in management information systems*. Royal Institute of Technology, Department of Information Processing Computer Science [Reproduced byU. S. National Technical Information Service], 1972.

[133] T. Holmes and H. Littlejohn, "The serum diagnosis of typhoid fever.," *British Medical Journal*, vol. 1, 1897.

[134] W. Zhu, N. Zeng, N. Wang, *et al.*, "Sensitivity, specificity, accuracy, associated confidence interval and roc analysis with practical sas® implementations," *NESUG proceedings: Health Care and Life Sciences, Baltimore, Maryland*, pp. 1–9, 2010.

[135] C. E. Metz, "Basic principles of roc analysis," in *Seminars in nuclear medicine*, vol. 8, pp. 283–298, Elsevier, 1978.

[136] J. R. Taylor, "An introduction to error analysis: The study of uncertainties in physical measurements," 1996.

[137] E. J. Boyko, "Ruling out or ruling in disease with the most sensitiue or specific diagnostic test short cut or wrong turn?," *Medical Decision Making*, vol. 14, no. 2, pp. 175–179, 1994.

[138] K. Fukunaga, *Introduction to statistical pattern recognition*. Academic Press, 2013.

[139] K. Tumer and J. Ghosh, "Estimating the bayes error rate through classifier combining," in *Proceedings of the 13th International Conference on Pattern Recognition, 1996.*, vol. 2, pp. 695–699, IEEE, 1996.

[140] M. A. Rawashdeh, W. B. Lee, R. M. Bourne, E. A. Ryan, M. W. Pietrzyk, W. M. Reed, R. C. Heard, D. A. Black, and P. C. Brennan, "Markers of good performance in mammography depend on number of annual readings," *Radiology*, vol. 269, no. 1, pp. 61–67, 2013.

[141] I. Théberge, S.-L. Chang, N. Vandal, J.-M. Daigle, M.-H. Guertin, É. Pelletier, and J. Brisson, "Radiologist interpretive volume and breast cancer screening accuracy in a canadian organized screening program," *Journal of the National Cancer Institute*, p. djt461, 2014.

[142] T. E. Kerner, K. D. Paulsen, A. Hartov, S. K. Soho, and S. P. Poplack, "Electrical impedance spectroscopy of the breast: clinical imaging results in 26 subjects," *Medical Imaging on IEEE Transactions*, vol. 21, no. 6, pp. 638–645, 2002.

[143] O. Al-Surkhi, P. Riu, F. Vazquez, and J. Ibeas, "Monitoring cole-cole parameters during haemodialysis (hd)," in *Engineering in Medicine and Biology Society, 2007. EMBS 2007. 29th Annual International Conference of the IEEE*, pp. 2238–2241, IEEE, 2007.

[144] O. Al-Surkhi, P. Riu, and M. Jaffrin, "Monitoring body fluid shifts during haemodialysis (hd) using electrical bioimpedance measurments," in *2011 1st Middle East Conference on Biomedical Engineering (MECBME)*, pp. 108–113, IEEE, 2011.

[145] P. Riu and F. Vazquez, "Monitoring fluid shifts during haemodialysis using local tissue bioimpedance measurement," in *4th European Conference of the International Federation for Medical and Biological Engineering*, pp. 1334–1338, Springer, 2009.

[146] B. Singh, C. Smith, and R. Hughes, "In vivo dielectric spectrometer," *Medical and Biological Engineering and Computing*, vol. 17, no. 1, pp. 45–60, 1979.

[147] C. T.-S. Ching, T.-P. Sun, S.-H. Huang, C.-S. Hsiao, C.-H. Chang, S.-Y. Huang, Y.-J. Chen, C.-S. Cheng, H.-L. Shieh, and C.-Y. Chen, "A preliminary study of the use of bioimpedance in the screening of squamous tongue cancer," *International Journal of Nanomedicine*, vol. 5, p. 213, 2010.

[148] R. Pethig, "Dielectric properties of body tissues," *Clinical Physics and Physiological Measurement*, vol. 8, no. 4A, p. 5, 1987.

[149] B. Blad and B. Baldetorp, "Impedance spectra of tumour tissue in comparison with normal tissue; a possible clinical application for electrical impedance tomography," *Physiological Measurement*, vol. 17, no. 4A, p. A105, 1996.

[150] J. Jossinet, "The impedivity of freshly excised human breast tissue," *Physiological measurement*, vol. 19, no. 1, p. 61, 1998.

[151] J.-M. Kim, D. Oh, J. Yoon, S. Cho, N. Kim, J. Cho, Y. Kwon, C. Cheon, and Y.-K. Kim, "In vitro and in vivo measurement for biological applications using micromachined probe," *Microwave Theory and Techniques, IEEE Transactions on*, vol. 53, pp. 3415–3421, Nov 2005.

[152] G. Qiao, W. Duan, C. Chatwin, A. Sinclair, and W. Wang, "Electrical properties of breast cancer cells from impedance measurement of cell suspensions," in *Journal of Physics: conference series*, vol. 224, p. 012081, IOP Publishing, 2010.

[153] J. D. Kosterich, K. R. Foster, and S. R. Pollack, "Dielectric permittivity and electrical conductivity of fluid saturated bone," *Biomedical Engineering on IEEE Transactions*, no. 2, pp. 81–86, 1983.

[154] T. Morimoto, S. Kimura, Y. Konishi, K. Komaki, T. Uyama, Y. Monden, D. Y. Kinouchi, and D. T. Iritani, "A study of the electrical bio-impedance of tumors," *Investigative Surgery*, vol. 6, no. 1, pp. 25–32, 1993.

[155] T. Morimoto, Y. Kinouchi, T. Iritani, S. Kimura, Y. Konishi, N. Mitsuyama, K. Komaki, and Y. Monden, "Measurement of the electrical bio-impedance of breast tumors," *European Surgical Research*, vol. 22, no. 2, pp. 86–92, 1990.

[156] S. L. NORWOOD, "Fibrocystic breast disease an update and review," *Journal of Obstetric, Gynecologic, & Neonatal Nursing*, vol. 19, no. 2, pp. 116–121, 1990.

[157] Y. Ohmine, T. Morimoto, Y. Kinouchi, T. Iritani, M. Takeuchi, and Y. Monden, "Noninvasive measurement of the electrical bioimpedance of breast tumors.," *Anticancer Research*, vol. 20, no. 3B, pp. 1941–1946, 1999.

[158] H. Fricke and S. Morse, "The electric capacity of tumors of the breast," *The Journal of Cancer Research*, vol. 10, no. 3, pp. 340–376, 1926.

[159] J. Jossinet, A. Lobel, C. Michoudet, and M. Schmitt, "Quantitative technique for bio-electrical spectroscopy," *Journal of biomedical engineering*, vol. 7, no. 4, pp. 289–294, 1985.

[160] J. Stelter, J. Wtorek, A. Nowakowski, A. Kopacz, and T. Jastrzembski, "Complex permittivity of breast tumor tissue," in *Proceedings of 10th International Conference on Electrical Bio-Impedance, Barcelona*, pp. 59–62, 1998.

[161] S. Chaudhary, R. Mishra, A. Swarup, and J. M. Thomas, "Dielectric properties of normal & malignant human breast tissues at radiowave & microwave frequencies.," *Indian Journal of Biochemistry & Biophysics*, vol. 21, no. 1, p. 76, 1984.

[162] A. Campbell and D. Land, "Dielectric properties of female human breast tissue measured in vitro at 3.2 ghz," *Physics in Medicine and Biology*, vol. 37, no. 1, p. 193, 1992.

[163] M. Choi, T.-J. Kao, D. Isaacson, G. Saulnier, and J. Newell, "A simplified model of mammography geometry for breast cancer imaging with electrical impedance tomography," in *Engineering in Medicine and Biology Society, 2004. IEMBS '04. 26th Annual International Conference of the IEEE*, vol. 1, pp. 1310 –1313, 2004.

[164] M. Assenheimer, O. Laver-Moskovitz, D. Malonek, D. Manor, U. Nahaliel, R. Nitzan, and A. Saad, "The t-scantm technology: electrical impedance as a diagnostic tool for breast cancer detection," *Physiological Measurement*, vol. 22, no. 1, p. 1, 2001.

[165] H. Ammari, O. Kwon, J. K. Seo, and E. J. Woo, "T-scan electrical impedance imaging system for anomaly detection," *SIAM Journal on Applied Mathematics*, vol. 65, no. 1, pp. 252–266, 2004.

[166] M. H. Choi, T.-J. Kao, D. Isaacson, G. Saulnier, and J. Newell, "A reconstruction algorithm for breast cancer imaging with electrical impedance tomography in mammography geometry," *Biomedical Engineering, IEEE Transactions on*, vol. 54, no. 4, pp. 700 –710, 2007.

[167] A. Malich, T. Fritsch, R. Anderson, T. Boehm, M. Freesmeyer, M. Fleck, and W. Kaiser, "Electrical impedance scanning for classifying suspicious breast lesions: first results," *European Radiology*, vol. 10, no. 10, pp. 1555–1561, 2000.

[168] V. Cherepenin, A. Karpov, A. Korjenevsky, V. Kornienko, A. Mazaletskaya, D. Mazourov, and D. Meister, "A 3d electrical impedance tomography (EIT) system for breast cancer detection," *Physiological Measurement*, vol. 22, no. 1, p. 9, 2001.

[169] A. Cherepenin and A. Karpov, "Three-dimensional EIT imaging of breast tissues: system design and clinical testing," *IEEE Transactions on Medical Imaging*, vol. 20, p. 662667, 2002.

[170] G. Sze, *Detection of breast cancer with electrical impedance mammography*. PhD thesis, school of engineering and design university of sussex brighton uk, May 2012.

[171] N. Béqo, G. Sze, N. Huber, and W. Wang, "The flexible and configurable sussex eim mk4 using pci extensions for instrumentation (pxi)," in *Journal of Physics: Conference Series*, vol. 224, p. 012164, IOP Publishing, 2010.

[172] G. J. Saulnier, N. Liu, C. Tamma, H. Xia, T.-J. Kao, J. Newell, and D. Isaacson, "An electrical impedance spectroscopy system for breast cancer detection," in *Engineering in Medicine and Biology Society, 2007. EMBS 2007. 29th Annual International Conference of the IEEE*, pp. 4154–4157, IEEE, 2007.

[173] M. H. Choi, T.-J. Kao, D. Isaacson, G. Saulnier, and J. C. Newell, "A simplified model of mammography geometry for breast cancer imaging with electrical impedance tomography," in *Engineering in Medicine and Biology Society, 2004. IEMBS'04. 26th Annual International Conference of the IEEE*, vol. 1, pp. 1310–1313, IEEE, 2004.

[174] T. J. Kao, G. J. Saulnier, H. Xia, C. Tamma, J. Newell, and D. Isaacson, "A compensated radiolucent electrode array for combined EIT and mammography," *Physiological Measurement*, vol. 28, no. 7, p. S291, 2007.

[175] D. Ardrey, E. Murphy, D. Isaacson, G. Saulnier, and J. Newell, "Electrical impedance tomography using the finite element method in the mammography geometry," in *Bioengineering Conference (NEBEC), 2011 IEEE 37th Annual Northeast*, pp. 1–2, IEEE, 2011.

[176] E. McAdams, J. Jossinet, A. Lackermeier, and F. Risacher, "Factors affecting electrode-gel-skin interface impedance in electrical impedance tomography," *Medical and Biological Engineering and Computing*, vol. 34, no. 6, pp. 397–408, 1996.

[177] C. Hähnlein, K. Schilcher, C. Sebu, and H. Spiesberger, "Conductivity imaging with interior potential measurements," *Inverse Problems in Science and Engineering*, vol. 19, no. 5, pp. 729–750, 2011.

[178] M. Gehre, T. Kluth, C. Sebu, and P. Maass, "Sparse 3d reconstructions in electrical impedance tomography using real data," *Inverse Problems in Science and Engineering*, vol. 22, no. 1, pp. 31–44, 2014.

[179] U. Food, D. Administration, *et al.*, "Summary of safety and effectiveness data for t-scan breast scanner," *URL: http://www. fda. gov/cdrh/pdf/p970033b. pdf*, 1999.

[180] A. Malich, T. Böhm, M. Facius, I. Kleinteich, M. Fleck, D. Sauner, R. Anderson, and W. Kaiser, "Electrical impedance scanning as a new imaging modality in breast cancer detectiona short review of clinical value on breast application, limitations and perspectives," *Nuclear Instruments and Methods in Physics Research Section A: Accelerators, Spectrometers, Detectors and Associated Equipment*, vol. 497, no. 1, pp. 75–81, 2003.

[181] A. Malich, T. Boehm, M. Facius, M. Freesmeyer, M. Fleck, R. Anderson, and W. Kaiser, "Differentiation of mammographically suspicious lesions: evaluation of breast ultrasound, mri mammography and electrical impedance scanning as adjunctive technologies in breast cancer detection," *Clinical Radiology*, vol. 56, no. 4, pp. 278–283, 2001.

[182] D. Pak, N. Rozhkova, M. Kireeva, M. Ermoshchenkova, A. Nazarov, D. Fomin, and N. Rubtsova, "Diagnosis of breast cancer using electrical impedance tomography," *Biomedical Engineering*, vol. 46, no. 4, pp. 154–157, 2012.

[183] G. Martín, R. Martín, M. Brieva, and L. Santamaría, "Electrical impedance scanning in breast cancer imaging: correlation with mammographic and histologic diagnosis," *European Radiology*, vol. 12, no. 6, pp. 1471–1478, 2002.

[184] S. Fields, M. Rossman, and P. E, "Adjunctive improvement of mammographic accuracy using electrical impedance scanning(eis)," pp. 272–273, 1998,.

[185] B. Rigaud, J.-P. Morucci, and N. Chauveau, "Bioelectrical impedance techniques in medicine. part i: Bioimpedance measurement. second section: impedance spectrometry.," *Critical Reviews in Biomedical Engineering*, vol. 24, no. 4-6, pp. 257–351, 1995.

[186] F. Lorussi, W. Rocchia, E. P. Scilingo, A. Tognetti, and D. De Rossi, "Wearable, redundant fabric-based sensor arrays for reconstruction of body segment posture," *Sensors Journal, IEEE*, vol. 4, no. 6, pp. 807–818, 2004.

[187] D. Gisser, D. Isaacson, and J. Newell, "Electric current computed tomography and eigenvalues," *SIAM Journal on Applied Mathematics*, vol. 50, no. 6, pp. 1623–1634, 1990.

[188] P. Zegarmistrz and Z. Galias, "On reconstruction of conductances in resistor grids from boundary measurements," in *ECCTD 2007. 18th European Conference on Circuit Theory and Design, 2007.*, pp. 783–786, IEEE, 2007.

[189] L. Borcea, V. Druskin, F. Vasquez, and A. Mamonov, "Resistor network approaches to electrical impedance tomography," *arXiv preprint arXiv:1107.0343*, 2011.

[190] J. Yong and L. Min, "Electrical impedance tomography on a resistive network with internal currents." 2010.

[191] N. Terzopoulos, K. Hayatleh, B. Hart, F. Lidgey, and C. McLeod, "A novel bipolar-drive circuit for medical applications.," *Physiological Measurement*, vol. 26, no. 5, pp. N21–7, 2005.

[192] F. Grund, "Engels, h., numerical quadrature and cubature, computational mathematics and applications," *ZAMM-Journal of Applied Mathematics and Mechanics*, vol. 62, no. 7, pp. 355–355, 1982.

[193] A. Adler and W. R. Lionheart, "Eidors: Towards a community-based extensible software base for EIT," in *Proc. of the 6th Conf. on Biomedical Applications of Electrical Impedance Tomography (London, UK, 22–24 June 2005)*, pp. 1–4, 2005.

[194] R. Bilal, *Investigation of undesired errors relating to the planar array system of electrical impedance mammography for breast cancer detection*. PhD thesis, University of Sussex, 2012.

[195] M. Azzouz, M. Hanke, C. Oesterlein, and K. Schilcher, "The factorization method for electrical impedance tomography data from a new planar device," *International Journal of Biomedical Imaging*, vol. 2007, 2007.

[196] K. Georgi, C. Hähnlein, K. Schilcher, C. Sebu, and H. Spiesberger, "Conductivity reconstructions using real data from a new planar electrical impedance tomography device," *Inverse Problems in Science and Engineering*, vol. 21, no. 5, pp. 801–822, 2013.

[197] J. L. Mueller, D. Isaacson, and J. C. Newell, "A reconstruction algorithm for electrical impedance tomography data collected on rectangular electrode arrays," *Biomedical Engineering on IEEE Transactions*, vol. 46, no. 11, pp. 1379–1386, 1999.

[198] M. Lukaschewitsch, P. Maass, M. Pidcock, and C. Sebu, "The asymptotic behaviour of weak solutions to the forward problem of electrical impedance tomography on unbounded three-dimensional domains," *Mathematical Methods in The Applied Sciences*, vol. 32, no. 2, pp. 206–222, 2009.

[199] J. Kevorkian, *Partial differential equations: Analytical solution techniques*, vol. 6. Springer Science & Business Media, 2000.

[200] P. C. Hansen, "Regularization tools: A matlab package for analysis and solution of discrete ill-posed problems," *Numerical Algorithms*, vol. 6, no. 1, pp. 1–35, 1994.

[201] C. Kotre, "Subsurface electrical impedance imaging: measurement strategy, image reconstruction and in vivo results," *Physiological measurement*, vol. 17, no. 4A, p. A197, 1996.

[202] A. Kemna, A. Binley, and L. Slater, "Crosshole ip imaging for engineering and environmental applications," *Geophysics*, vol. 69, no. 1, pp. 97–107, 2004.

[203] B. Tutt, "New partial-breast radiation therapy regimen uses protons.," *OncoLog*, vol. 58, no. 1, pp. 11–12, 2013.

[204] D. E. March, B. F. Coughlin, R. B. Barham, R. A. Goulart, S. V. Klein, M. E. Bur, J. L. Frank, and G. Makari-Judson, "Breast masses: Removal of all us evidence during biopsy by using a handheld vacuum-assisted deviceinitial experience 1," *Radiology*, vol. 227, no. 2, pp. 549–555, 2003.

[205] D. Zwillinger, *Table of integrals, series, and products*. Elsevier, 2014.

[206] C. Brebbia, J. Telles, and L. Wrobel, *Boundary element techniques: theory and applications in engineering*. Springer Berlin etc., 1984.

[207] A. Adler, W. Lionheart, and N. Polydorides, "Eidors-electrical impedance tomography and diffuse optical tomography reconstruction software," *EIDORS3d.sourceforge. net*, 2008.

[208] K. Knudsen, M. Lassas, J. Mueller, and S. Siltanen, "Reconstructions of piecewise constant conductivities by the d-bar method for electrical impedance tomography," in *Journal of Physics: Conference Series*, vol. 124, p. 012029, IOP Publishing, 2008.

Appendix A

An Academic Example

A.1 Introduction

Due to the complex nature of the resistor networks corresponding to the actual Mainz-Brookes tomographs, this example shows how Ohm's and Kirchoff's laws can be applied to solve both the forward and the inverse problem for a simpler resistor network consisting of 12 electrodes (e.g 8 outer-electrodes for current injection, 4 inner-electrodes for potential measurements and 12 links). The mathematical formulations of the problems are generic and the equations derived can be easily adapted to more complex resistor networks.

Example A.1.1. Consider the resistor network model shown in Figure A.2, Find the conductivity from given currents $I_0, \cdots, I_8$

Solution.

Let $s = 1, \ldots, 8$, be the electrodes used for current injection and I_s, $s = 1, \ldots, 8$ be the injected currents. The potentials are defined on knots, while currents and resistances on links. The knots (including the outer electrodes) are denoted by an index $k = 0, 1, \ldots, 12$ and the potential at the knot k by Φ_k. The knot $k = 0$ refers to the reference potential Φ_0 (ground). As depicted in Figure A.2 one extra link is added, connecting the network to the virtual knot at which the reference potential Φ_0 is fixed. The currents flowing from knot k to knot l are $I_{\{k,l\}}$ and the corresponding

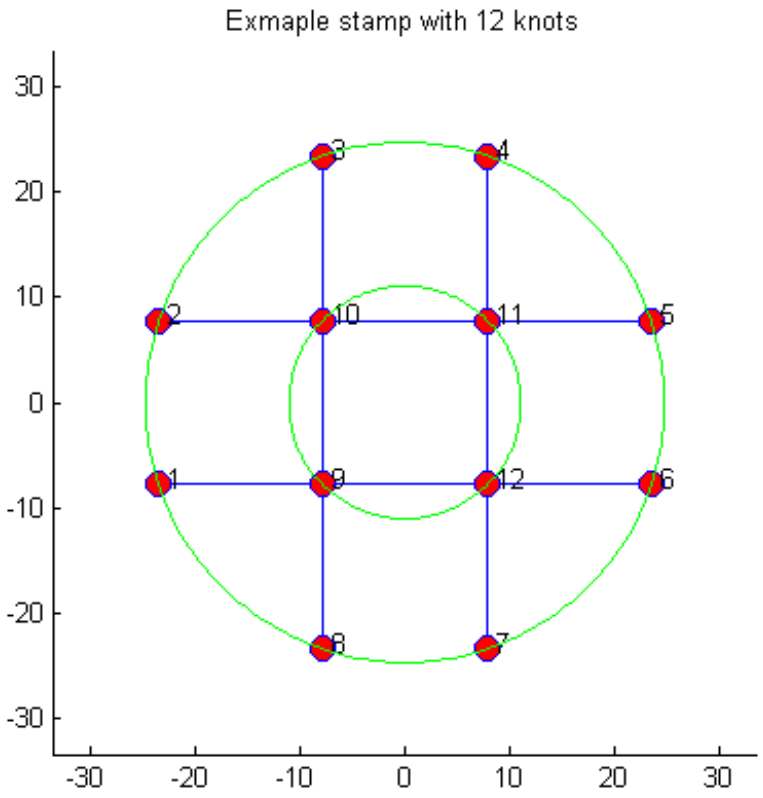

Figure A.1: A Stamp with 12 knots and 12 links

resistances $R_{\{k,l\}}$ satisfy the relations $I_{\{k,l\}} = -I_{\{l,k\}}$ and $R_{\{k,l\}} = R_{\{l,k\}} > 0$, $I_{\{0,1\}} = 0$. If $\Phi_k > \Phi_l$ then $I_{\{k,l\}}$ is positive. A compound index n is substituted to denote the links by

$$n = n(\{k,l\}) = 0, \ldots, 12\,, \quad k > l\,.$$

Further details about the use of this compound index are given in Table A.1 on page 204.

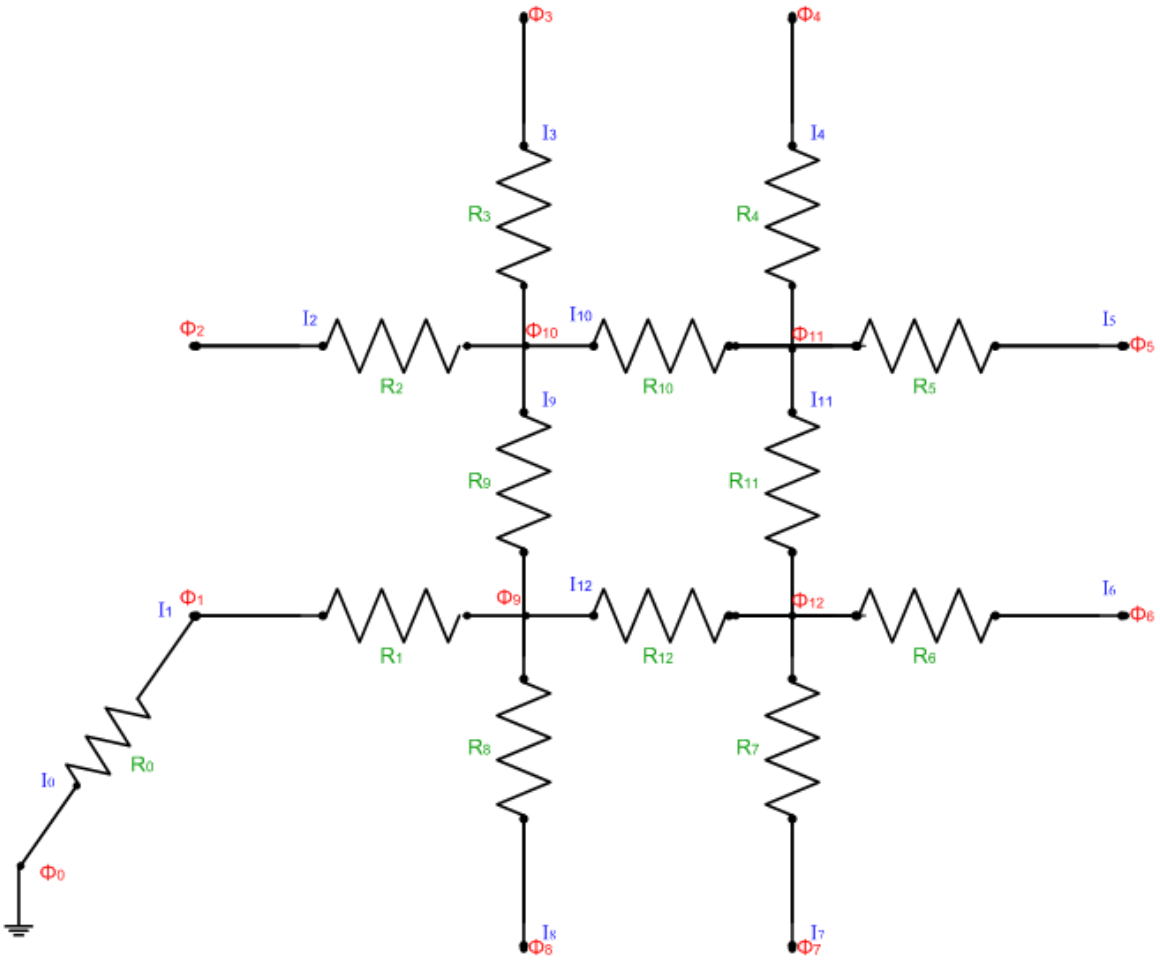

Figure A.2: A resistor network with 12 knots and 12 links

From Ohm's law, we determine the following equations:

$$\begin{aligned}
\Phi_1 - \Phi_0 &= I_0 R_0 \quad = 0 \\
\Phi_9 - \Phi_1 &= I_1 R_1 \\
\Phi_{10} - \Phi_2 &= I_2 R_2 \\
\Phi_{10} - \Phi_3 &= I_3 R_3 \\
\Phi_{11} - \Phi_4 &= I_4 R_4 \\
\Phi_{11} - \Phi_5 &= I_5 R_5 \\
\Phi_{12} - \Phi_6 &= I_6 R_6 \\
\Phi_{12} - \Phi_7 &= I_7 R_7 \\
\Phi_9 - \Phi_8 &= I_8 R_8 \\
\Phi_{10} - \Phi_9 &= I_9 R_9 \\
\Phi_{11} - \Phi_{10} &= I_{10} R_{10} \\
\Phi_{12} - \Phi_{11} &= I_{11} R_{11} \\
\Phi_{12} - \Phi_9 &= I_{12} R_{12}
\end{aligned} \tag{A.1}$$

Kirchhoff's current law applied to the knots $k = 9\,, 10\,, 11$ and 12 leads to the set

Table A.1: Compound index values

{k,l}	n({k,l})
{1,0}	0
{9,1}	1
{10,2}	2
{10,3}	3
{11,4}	4
{11,5}	5
{12,6}	6
{12,7}	7
{9,8}	8
{10,9}	9
{11,10}	10
{12,11}	11
{12,9}	12

of equations:

$$\begin{aligned} -I_1 - I_8 + I_9 + I_{12} &= 0 \\ -I_2 - I_3 - I_9 + I_{10} &= 0 \\ -I_4 - I_5 - I_{10} + I_{11} &= 0 \\ -I_6 - I_7 - I_{11} - I_{12} &= 0 \end{aligned} \tag{A.2}$$

A.1.1 Forward Problem

As synthetic data need to be generated for using in the inverse problem, the forward problem has to be considered first: for given known resistances $R_{n(\{k,l\})}$, $n = 0, \ldots, 12$ and given external currents I_s, $s = 1, \ldots, 8$, determine the potential Φ_k (up to a constant Φ_0) at any knot $k = 1, \ldots, 12$, and the internal currents $I_{n(\{k,l\})}$, $n = 9, \ldots, 12$. This can be achieved by solving the system of equations (A.3) and

(A.2). To this aim we rearrange equations (A.3) and (A.2) as follows:

$$
\begin{aligned}
\Phi_1 &= \Phi_0 \\
R_1 I_1 + \Phi_1 - \Phi_9 &= 0 \\
R_2 I_2 + \Phi_2 - \Phi_{10} &= 0 \\
R_3 I_3 + \Phi_3 - \Phi_{10} &= 0 \\
R_4 I_4 + \Phi_4 - \Phi_{11} &= 0 \\
R_5 I_5 + \Phi_5 - \Phi_{11} &= 0 \\
R_6 I_6 + \Phi_6 - \Phi_{12} &= 0 \\
R_7 I_7 + \Phi_7 - \Phi_{12} &= 0 \\
R_8 I_8 + \Phi_8 - \Phi_9 &= 0 \\
R_9 I_9 + \Phi_9 - \Phi_{10} &= 0 \\
R_{10} I_{10} + \Phi_{10} - \Phi_{11} &= 0 \\
R_{11} I_{11} + \Phi_{11} - \Phi_{12} &= 0 \\
R_{12} I_{12} + \Phi_9 - \Phi_{12} &= 0 \\
-I_1 - I_8 + I_9 + I_{12} &= 0 \\
-I_2 - I_3 - I_9 + I_{10} &= 0 \\
-I_4 - I_5 - I_{10} + I_{11} &= 0 \\
-I_6 - I_7 - I_{11} - I_{12} &= 0
\end{aligned}
\tag{A.3}
$$

and the system of linear equation above, can be express by a matrix representation as:

$$
\begin{pmatrix}
R_0 & 0 & 0 & 0 & 0 & 0 & 0 & 0 & 0 & 0 & 0 & 0 & 0 & 1 & 0 & 0 & 0 & 0 & 0 & 0 & 0 & 0 & 0 & 0 & 0 \\
0 & R_1 & 0 & 0 & 0 & 0 & 0 & 0 & 0 & 0 & 0 & 0 & 0 & 1 & 0 & 0 & 0 & 0 & 0 & 0 & 0 & -1 & 0 & 0 & 0 \\
0 & 0 & R_2 & 0 & 0 & 0 & 0 & 0 & 0 & 0 & 0 & 0 & 0 & 0 & 1 & 0 & 0 & 0 & 0 & 0 & 0 & 0 & -1 & 0 & 0 \\
0 & 0 & 0 & R_3 & 0 & 0 & 0 & 0 & 0 & 0 & 0 & 0 & 0 & 0 & 0 & 1 & 0 & 0 & 0 & 0 & 0 & 0 & -1 & 0 & 0 \\
0 & 0 & 0 & 0 & R_4 & 0 & 0 & 0 & 0 & 0 & 0 & 0 & 0 & 0 & 0 & 0 & 1 & 0 & 0 & 0 & 0 & 0 & 0 & -1 & 0 \\
0 & 0 & 0 & 0 & 0 & R_5 & 0 & 0 & 0 & 0 & 0 & 0 & 0 & 0 & 0 & 0 & 0 & 1 & 0 & 0 & 0 & 0 & 0 & -1 & 0 \\
0 & 0 & 0 & 0 & 0 & 0 & R_6 & 0 & 0 & 0 & 0 & 0 & 0 & 0 & 0 & 0 & 0 & 0 & 1 & 0 & 0 & 0 & 0 & 0 & -1 \\
0 & 0 & 0 & 0 & 0 & 0 & 0 & R_7 & 0 & 0 & 0 & 0 & 0 & 0 & 0 & 0 & 0 & 0 & 0 & 1 & 0 & 0 & 0 & 0 & -1 \\
0 & 0 & 0 & 0 & 0 & 0 & 0 & 0 & R_8 & 0 & 0 & 0 & 0 & 0 & 0 & 0 & 0 & 0 & 0 & 0 & 1 & -1 & 0 & 0 & 0 \\
0 & 0 & 0 & 0 & 0 & 0 & 0 & 0 & 0 & R_9 & 0 & 0 & 0 & 0 & 0 & 0 & 0 & 0 & 0 & 0 & 0 & 1 & -1 & 0 & 0 \\
0 & 0 & 0 & 0 & 0 & 0 & 0 & 0 & 0 & 0 & R_{10} & 0 & 0 & 0 & 0 & 0 & 0 & 0 & 0 & 0 & 0 & 0 & 1 & -1 & 0 \\
0 & 0 & 0 & 0 & 0 & 0 & 0 & 0 & 0 & 0 & 0 & R_{11} & 0 & 0 & 0 & 0 & 0 & 0 & 0 & 0 & 0 & 0 & 0 & 1 & -1 \\
0 & 0 & 0 & 0 & 0 & 0 & 0 & 0 & 0 & 0 & 0 & 0 & R_{12} & 0 & 0 & 0 & 0 & 0 & 0 & 0 & 0 & 1 & 0 & 0 & -1 \\
1 & 1 & 0 & 0 & 0 & 0 & 0 & 0 & 0 & 0 & 0 & 0 & 0 & 0 & 0 & 0 & 0 & 0 & 0 & 0 & 0 & 0 & 0 & 0 & 0 \\
0 & 0 & 1 & 0 & 0 & 0 & 0 & 0 & 0 & 0 & 0 & 0 & 0 & 0 & 0 & 0 & 0 & 0 & 0 & 0 & 0 & 0 & 0 & 0 & 0 \\
0 & 0 & 0 & 1 & 0 & 0 & 0 & 0 & 0 & 0 & 0 & 0 & 0 & 0 & 0 & 0 & 0 & 0 & 0 & 0 & 0 & 0 & 0 & 0 & 0 \\
0 & 0 & 0 & 0 & 1 & 0 & 0 & 0 & 0 & 0 & 0 & 0 & 0 & 0 & 0 & 0 & 0 & 0 & 0 & 0 & 0 & 0 & 0 & 0 & 0 \\
0 & 0 & 0 & 0 & 0 & 1 & 0 & 0 & 0 & 0 & 0 & 0 & 0 & 0 & 0 & 0 & 0 & 0 & 0 & 0 & 0 & 0 & 0 & 0 & 0 \\
0 & 0 & 0 & 0 & 0 & 0 & 1 & 0 & 0 & 0 & 0 & 0 & 0 & 0 & 0 & 0 & 0 & 0 & 0 & 0 & 0 & 0 & 0 & 0 & 0 \\
0 & 0 & 0 & 0 & 0 & 0 & 0 & 1 & 0 & 0 & 0 & 0 & 0 & 0 & 0 & 0 & 0 & 0 & 0 & 0 & 0 & 0 & 0 & 0 & 0 \\
0 & 0 & 0 & 0 & 0 & 0 & 0 & 0 & 1 & 0 & 0 & 0 & 0 & 0 & 0 & 0 & 0 & 0 & 0 & 0 & 0 & 0 & 0 & 0 & 0 \\
0 & -1 & 0 & 0 & 0 & 0 & 0 & 0 & -1 & 1 & 0 & 0 & 1 & 0 & 0 & 0 & 0 & 0 & 0 & 0 & 0 & 0 & 0 & 0 & 0 \\
0 & 0 & -1 & -1 & 0 & 0 & 0 & 0 & 0 & -1 & 1 & 0 & 0 & 0 & 0 & 0 & 0 & 0 & 0 & 0 & 0 & 0 & 0 & 0 & 0 \\
0 & 0 & 0 & 0 & -1 & -1 & 0 & 0 & 0 & 0 & -1 & 1 & 0 & 0 & 0 & 0 & 0 & 0 & 0 & 0 & 0 & 0 & 0 & 0 & 0 \\
0 & 0 & 0 & 0 & 0 & 0 & -1 & -1 & 0 & 0 & 0 & -1 & -1 & 0 & 0 & 0 & 0 & 0 & 0 & 0 & 0 & 0 & 0 & 0 & 0
\end{pmatrix}
\times
\begin{pmatrix}
0 \\ I_1 \\ I_2 \\ I_3 \\ I_4 \\ I_5 \\ I_6 \\ I_7 \\ I_8 \\ I_9 \\ I_{10} \\ I_{11} \\ I_{12} \\ \Phi_1 \\ \Phi_2 \\ \Phi_3 \\ \Phi_4 \\ \Phi_5 \\ \Phi_6 \\ \Phi_7 \\ \Phi_8 \\ \Phi_9 \\ \Phi_{10} \\ \Phi_{11} \\ \Phi_{12}
\end{pmatrix}
=
\begin{pmatrix}
\Phi_0 \\ 0 \\ 0 \\ 0 \\ 0 \\ 0 \\ 0 \\ 0 \\ 0 \\ 0 \\ 0 \\ 0 \\ 0 \\ I_1 \\ I_2 \\ I_3 \\ I_4 \\ I_5 \\ I_6 \\ I_7 \\ I_8 \\ 0 \\ 0 \\ 0 \\ 0
\end{pmatrix}
$$

Note that a few extra trivial (for this example only) equations were added to get a symmetrical structure for the coefficient matrix, e.g. $I_1 = I_1$. For simplicity, we choose $R_0 = 0$ and $\Phi_0 = 0$. For a compact notation we introduce two $(1 + 12 + 12)$-dimensional vectors:

$$X = (0\,, I_1\,, \ldots\,, I_{12}\,, \Phi_1\,, \ldots\,, \Phi_{12}) \quad \text{and} \quad Y = (\Phi_0\,, 0\,, \ldots\,, 0\,, I_1\,, \ldots\,, I_8\,, 0\,, 0\,, 0\,, 0)\,,$$

and a $(1+12+12)\times(1+12+12)$ Kirchoff matrix

$$\mathfrak{K} = \begin{pmatrix} R & P^T \\ P & 0 \end{pmatrix}. \tag{A.4}$$

In equation (A.4) R is the $(1+12)$-dimensional diagonal matrix of the resistances assigned to the outermost links

$$R = \mathrm{diag}(0, R_1, \ldots, R_{12}),$$

and P the $(1+12)\times 12$-dimensional incidence matrix with

$$P_{k,n+1} = \begin{cases} +1 & \text{for } n = n(\{k,j\}) \quad (k<j) \\ -1 & \text{for } n = n(\{j,k\}) \quad (j>k) \end{cases}, \quad j \in \text{neighbors of knot } k,$$
$$P_{k,n+1} = 0, \quad \text{otherwise.}$$

$P_{k,1} = 0$ except for the index $k = 1$ which is connected to the external reference potential, where $P_{1,1} = 1$. The forward problem is then solved by inverting the matrix $\mathfrak{K}$:

$$X = \mathfrak{K}^{-1} Y .$$

In this way data for potentials and internal currents can be generated for given resistances and given external currents. These data could then be used as synthetic input for testing our inversion algorithm.

A.1.2 Inverse Problem

In practice, in order to avoid any problems related to the contact impedance, potentials are not measured at the electrodes used for current injection. The corresponding inverse problem for the resistor network presented in Figure A.2 on page 203 can be formulated as follows: for given applied external currents, $I_1, \cdots, I_8$ and corresponding potentials Φ_k measured at the inner knots $k = 9, \ldots, 12$, determine the resistors $R_9, R_{10}, R_{11}, R_{12}$. To solve this inverse problem the last four equations in (A.3) are used and rearranged as:

$$\begin{aligned} I_9 &= (\Phi_{10} - \Phi_9)\tfrac{1}{R_9}, \\ I_{10} &= (\Phi_{11} - \Phi_{10})\tfrac{1}{R_{10}}, \\ I_{11} &= (\Phi_{12} - \Phi_{11})\tfrac{1}{R_{11}}, \\ I_{12} &= (\Phi_{12} - \Phi_9)\tfrac{1}{R_{12}}. \end{aligned} \tag{A.5}$$

Substituting equations (A.5) into equations (A.2) we obtain:

$$\begin{array}{rcl}(\Phi_9-\Phi_{10})S_9+(\Phi_9-\Phi_{12})S_{12} &=& -I_1-I_8\,,\\ (\Phi_{10}-\Phi_9)S_9+(\Phi_{10}-\Phi_{11})S_{10} &=& -I_2-I_3\,,\\ (\Phi_{11}-\Phi_{10})S_{10}+(\Phi_{11}-\Phi_{12})S_{11} &=& -I_4-I_5\,,\\ (\Phi_{12}-\Phi_{11})S_{11}+(\Phi_{12}-\Phi_9)S_{12} &=& -I_6-I_7\,,\end{array} \tag{A.6}$$

where $S_n = 1/R_n$ for $n = 8\,,\ldots\,,12$ are the corresponding conductances.

The inner knots $k = 9,\ldots,12$ are relabel by $\mathfrak{k} = 1,\ldots,K_r$, where $K_r = 4$ is the total number of inner knots, and the corresponding links $n(\{k,l\}) = 9\,,\ldots\,,12$ by $\mathfrak{n} = 1,,\ldots\,,N_r$, where $N_r = 4$, and let c_i be the currents entering the reduced network as illustrated in Figure A.3, i.e.

$$\begin{aligned}c_1 &= -I_1 - I_8\\ c_2 &= -I_2 - I_3\\ c_3 &= -I_4 - I_5\\ c_4 &= -I_7 - I_6\end{aligned} \tag{A.7}$$

Consequently, the system of equations (A.6) now reads:

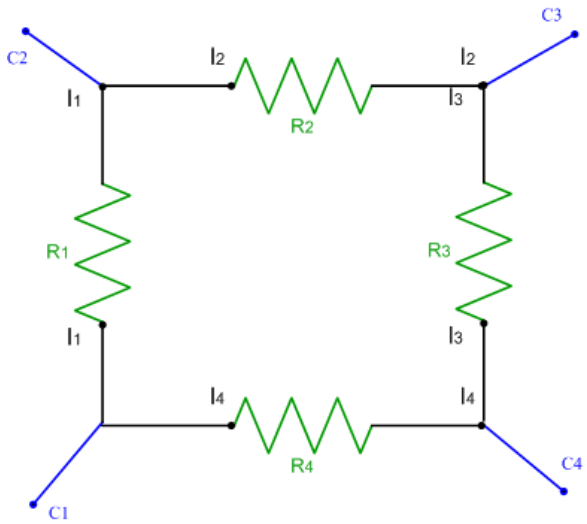

Figure A.3: Reduced resistor network.

$$\begin{array}{rcl}(\Phi_1-\Phi_2)S_1+(\Phi_1-\Phi_4)S_4 &=& c_1\\ (\Phi_2-\Phi_1)S_1+(\Phi_2-\Phi_3)S_2 &=& c_2\\ (\Phi_3-\Phi_2)S_2+(\Phi_3-\Phi_4)S_3 &=& c_3\\ (\Phi_4-\Phi_3)S_3+(\Phi_4-\Phi_1)S_4 &=& c_4\end{array} \tag{A.8}$$

We now introduce the 4-dimensional (i.e. N_r-dimensional) vector of conductances $\Sigma = (S_1,\, S_2,\, S_3,\, S_4)$, the 4-dimensional (i.e. K_r-dimensional) vector of applied currents $C = (c_1,\, c_2,\, c_3,\, c_4)$, and the 4×4 (i.e. $K_r \times N_r$ matrix of potential differences

$$U_{i,\mathfrak{n}} = \begin{cases} \Phi_i - \Phi_{\mathfrak{k}} & \text{with} \quad \mathfrak{n} = \mathfrak{n}(\{i, \mathfrak{k}\}) \quad \text{and} \quad \mathfrak{k} \quad \text{is a neighbour of} \quad i \\ 0 & \text{otherwise.} \end{cases} \tag{A.9}$$

The only non-zero entries of the matrix U are given explicitely below:

$$\begin{aligned} U_{1,1} &= \Phi_1 - \Phi_2 \\ U_{1,4} &= \Phi_1 - \Phi_4 \\ U_{2,1} &= \Phi_2 - \Phi_1 \\ U_{2,2} &= \Phi_2 - \Phi_3 \\ U_{3,2} &= \Phi_3 - \Phi_2 \\ U_{4,3} &= \Phi_4 - \Phi_3 \\ U_{4,4} &= \Phi_4 - \Phi_1 \end{aligned} \tag{A.10}$$

Finally, the system of equations (A.8), can be rewritten in a compact form as:

$$U \cdot \Sigma = C\,. \tag{A.11}$$

Although this is a system of 4 equations for 4 unknowns, due to the total law of current conservation (i.e. $\sum_{s=1}^{8} I_s = \sum_{k=1}^{4} c_k = 0$) only 3 equations are linearly independent. Hence, the system is under-determined and in order to find a unique solution we need to add data from repeated measurements (at least from two different linearly independent current patterns applied at the 8 outer electrodes).

A.2 Matlab Code for the Academic Example

A.2.1 Forward Solver Code

```
%==========================================================================
% The forward solver for the simple stamp of the academic example
% Number of Knots 12
% Number of links 12
%==========================================================================
%======================== Initialisation ==================================

clc;
clear all;
close all;

%==========================================================================
%======================== Stamp Specifications ============================
%%
disp('Sample stamp with 12 Knots and 12 links');
disp(' ');
stamp = xlsread('smallStampK12N12.xls');
    N = 12;                 %Number of links
    K = 12;                 %Number of Knotes
    S = 8;                  %Number active electrodes
    Sj = 8;                 %Number of split currents
    resistors = [0 9 10 8 4 6 2 10 9 9 3 6 1];
    r=sqrt(stamp([1,9],4).^2+stamp([1,9],5).^2);
    name = 'Example stamp with 12 knots';

%==========================================================================
%======================== Construct Links =================================
zStamp = size(stamp);
NP = 10;                                        %Number of current patterns
selection = [N,K,S,Sj,NP];
tPair = zeros(1,2);                          %Temporary pairs for comparison
J0=1;                                             %Injected current Amplitude
Y =  zeros(1+N+K,1);          %Vector containing injected currents and zeros
R = [0 ones(1,N)];                                  %Initialising resistors
resistances = diag(R);                                %The resistors matrix
theta=0:pi/6:(S-1)*pi/6;        %Angular position of the external electrode
links = zeros(N,15);
P = zeros(K,N);
NP = 10;                                                %Number of patterns
%==========================================================================

linkNumber = 0;
for i = 1 : length(stamp)
    tKnote = stamp(i,2);
    j=6;                              %Where the neighbours of the node start
    while stamp(i,j) ~= 0
        tPair(1,1) = tKnote;
          tPair(1,2) = stamp(i,j);
            isInCol2  = ismember(links(:,2:3), tPair, 'rows');
          isInCol3=ismember(fliplr(links(:,2:3)), tPair,'rows');
    if ~(isInCol2|isInCol3)
        linkNumber = linkNumber + 1;
        links(linkNumber,1) = linkNumber;
           links(linkNumber,2:3) = tPair;
```

```
          links(linkNumber,4:5) = stamp(i,4:5);
         vi =find(stamp(:,2)==(tPair(1,2)));
        links(linkNumber,6:7) = stamp(vi,4:5);
        links(linkNumber,8) = (links(linkNumber,4) +
links(linkNumber,5))/2;
        links(linkNumber,9) = (links(linkNumber,6) + links(linkNumber,7))/2;
    end

    j=j+1;
    end
end

%=========================================================================
%======================== Build the Links List ===========================

%%
%We take each node from i = 1 to K, and check if it is in Link(:,2) means
%it is smaller so the link between it and the neighbour in Link(:,3) is
%positive. we repeat this for link(:,3) and compare with neighbours in
%link(:,2). link(:,1) represents the links number.
%The P routine has been inspected one by one and is 100% Correct

for i = 1:K                                                 % Number of Nodes
    for  j = 1 : N;                                         % Number of Links
        if (links(j,2) == i) && (links(j,2) < links(j,3))
            P(links(j,2),links(j,1)) = 1;
        else
            if (links(j,2) == i) && (links(j,2) > links(j,3))
                P(links(j,2),links(j,1)) = -1;
            end
        end
    end
end

for i = 1:K                                                 % Number of Nodes
    for  j = 1 : N;                                         % Number of Links
        if (links(j,3) == i) && (links(j,3) > links(j,2))
            P(links(j,3),links(j,1)) = -1;
        else
            if (links(j,3) == i) && (links(j,3) < links(j,2))
                P(links(j,3),links(j,1)) = 1;
            end
        end
    end
end
%%
%=========================================================================
%======================== Create Current Patterns ========================

 for col = 1: 5
    colp = col+5;
      cp(:,col) = J0*sin(theta*col);   %sin Current patterns
    cp(:,colp)= J0*cos(theta*colp);  %cos Current patterns
 end
```

```
%=============================================================================
%======================== Construct the matrix ===========================

KA(2:N+1,N+2:1+N+K) = P';
  KA(1+N+1:1+N+K,2:1+N) = P;
   KA(1:1+N,1:1+N) = resistances;
 KA(1,N+2) = 1;
KA(N+2,1) = 1;

for col = 1 : NP                                    %NP is Number of Patterns
    Y(1+N+1: 1+N+S,1) = cp(:,col);
    X = KA\Y;
   %X = pinv(KA)*Y;

  I(:,col) = X([2:Sj+1]);     % Add Currents readings to a column matrix Ci
Pt(:,col) = X([N+2+S:end]); %Potentials for the reduced stamp (inner links)
end


%=============================================================================
%======================== Checking KCL and KVL laws ======================

display('Checking Kirchhoff's law for conservation of currents, please
wait...');
KCL = zeros(K,4);
for  i = 1:K
    KCL(i,1) = i;
    KCL(i,2) = KCL(i,2) +X(links(i,1)+1,1);
end
for  i = 1:K
     KCL(i,3) = KCL(i,3) -X(links(i,1)+1,1);
end
for  i = 1:K
     KCL(i,4) = KCL(i,2) + KCL(i,3);
     if KCL(i,4) ~= 0
         fprintf(1,'Error at Knot %i \n',KCL(i,1));
         fprintf(1,'The current does not sum to zero .\n');
     end
end

display('Checking ... DONE!');
display('Checking Kirchhoff's law for conservation of voltages around a
closed loop');
KVL = zeros(N,3);                                   %Kirchhoff's Voltage low
for  i = 1:N
    KVL(i,1) = i;
    KVL(i,2) = resistances(links(i,1)+1,links(i,1)+1)*X(links(i,1)+1,1);
    KVL(i,3) = -X(links(i,2)+1+N,1)+X(links(i,3)+1+N,1);
end
for  i = 1:N
     KVL(i,4) = KVL(i,2) - KVL(i,3);
     if KVL(i,4) > 1e-10
         fprintf(1,'Error at Knot %i \n',KVL(i,1));
         fprintf(1,'Check potential or current readings .\n');
    end
```

```
end
display('Checking ... DONE!');




%=========================================================================
%======================== Plot The Stamp ================================

figure;
    axis equal
    title(name);
    xlim([min(links(:,4))-10 max(abs(links(:,4)))+10]);
    ylim([min(links(:,5))-10 max(abs(links(:,5)))+10]);
    sizeStamp = size(stamp);
    sizeLinks= size(links);
for  i = 1: sizeLinks(1)
        line([stamp(links(i,3),4) stamp(links(i,2),4)], ...
        [stamp(links(i,3),5) stamp(links(i,2),5)],'Marker','o',...
        'MarkerFaceColor','r','MarkerSize',10,'LineWidth',1);

end
% To Print the values of the nodes

for i=1:1:sizeStamp(1)
        text(stamp(i,4)+1,stamp(i,5)+0.5,int2str(stamp(i,2)));
end
hold on
%To plot the circles we need a lot of close points
angle=0:pi/100:2*pi;
for i=1:length(r)
plot(r(i)*cos(angle),r(i)*sin(angle),'g')
end

%%
%=========================================================================
%======================== Save Variables ================================

save('selection','selection');
save('links','links');
save('currents','I');
save('potentials','Pt');

%=========================================================================
%======================== End of program ================================
```

A.2.2 Inversion Solver Code

```
%=========================================================================
%======================== Inverse Problem ================================
% This code solves the inverse problem for the simple stamp with 12 links
% and 12 nodes using 8 injected currents.
%=========================================================================

clc;
close all;
clear all;

%=========================================================================
%====================== Selected stamp initialisation ====================


selection = load ('selection.mat');
N = selection.selection(1); % Number of links in the selected stamp
K = selection.selection(2); % Number of knots in the selected stamp
C = selection.selection(3); % Number of active electrodes in the selected
stamp
Cj = selection.selection(4);% Number current of splits in the selected stamp
NP = selection.selection(5);% Number of current patterns applied
rN = N - Cj;                % Reduced links
rK = K - C;                 % Reduced Knots

links = load('links.mat');                              % Load the links file
rLinks = (links.links(Cj+1:end,1:3));                % Remove outer electrodes
rLinks(:,1) = rLinks(:,1)-Cj;                        %Reset links numbers to 1
rLinks(:,2:3) = rLinks(:,2:3)-C;%Reset nodes numbers and adjacent neighbour
I = load('currents.mat');      % Currents for the reduced resistor network
rI = I.I;
Pt = load('potentials.mat');            % Potential for the reduced network
rPt = Pt.Pt;

%%
%=========================================================================
%====================== Construct the U Matrix ===========================
% Link = rLinks(i,2)
% Knote = rLinks(i,2) or rLinks(i,3)
% Neighbour = rLinks(i,3), when Knote is (Knote = rLinks(i,2)) and
% Neighbour = rLinks(i,2) when Knote is (Knote = rLinks(i,3))
% U(Knote,link) = Phi(Knote) - Phi(Neighbour)
%=========================================================================

U = [];
for j = 1:NP
for i = 1: rN
    tU(rLinks(i,2),rLinks(i,1)) = -rPt(rLinks(i,2),j)+rPt(rLinks(i,3),j);
    tU(rLinks(i,3),rLinks(i,1)) = -rPt(rLinks(i,3),j)+rPt(rLinks(i,2),j);
end
U=[U;tU];                                       % Append an exisiting matrix
end
%%
%=========================================================================
%=================== Generate Currents and  Solve for S ==================
```

```
tCi(1,:) = rI(1,:)+rI(end,:);
 k = 2;                                          % Index for increasing rI by 2
     for i = 2:Cj/2;
         tCi(i,:) = rI(k,:)+rI(k+1,:);    % Loop to increase Ci from 2 to 12
         k = k+2;
     end

%=========================================================================
%======================== New Stamp Initialisation =======================
global tCi;
tCi = [tCi;zeros((length(U)/NP)-size(tCi),NP)];% Append the matrix in zeros
Ci=tCi(:);         % converts a multi-column matrix into a one-column matrix
S = U\Ci;
%%
%=========================================================================
%======================== Display Results ================================
results(:,1)=S;
 results(:,2)=S.^-1;
results

%=========================================================================
%======================== End of program =================================
```

Appendix B

Publications By the Author

[1] **H. Perez**, M. Pidcock and C. Sebu, *A 3D Image Reconstruction Algorithm for Electrical Impedance Tomography Data Collected on Planar Electrode Arrays*, Inverse Problems in Science and Engineering,2016, DOI:10.1080/17415977.2016.1169279

[2] **H. Perez**, M. Pidcock, C. Sebu and S. Sivanesan, *3D Image Reconstruction Algorithm for Electrical Impedance Tomography Data Collected on Planar Electrode Arrays*, Proceedings of the 8th International Conference on Inverse Problems in Engineering: Theory and Practice (ICIPE 2014)